

*Defect analysis of semiconductor thin films for photovoltaic  
applications using photo-luminescence and photo-  
conductivity*

*Thesis submitted to*

*Cochin University of Science and Technology*

*in partial fulfillment of the requirements  
for the award of the degree of*

*Doctor of Philosophy*

*by*

*R. Jayakrishnan*

*Thin Film Photovoltaic Division*

*Department of Physics*

*Cochin University of Science and Technology*

*Cochin – 682 022, Kerala, India*

*APRIL 2008*

**Defect analysis of semiconductor thin films for photovoltaic applications using photo-luminescence and photo-conductivity**

PhD thesis in the field of Material Science

*Author:*

R. Jayakrishnan  
Thin Film Photovoltaic Division  
Department of Physics  
Cochin University of Science and Technology  
Cochin – 682 022, Kerala, India  
email: [rjayakrishnan2002@yahoo.co.in](mailto:rjayakrishnan2002@yahoo.co.in)

*Supervising Guide:*

Prof. K. P. Vijayakumar  
Thin Film Photovoltaic Division  
Department of Physics  
Cochin University of Science and Technology  
Cochin – 682 022, Kerala, India  
email: [kpvcusat.ac.in](mailto:kpvcusat.ac.in)

Cochin University of Science and Technology  
Cochin-682022, Kerala, India

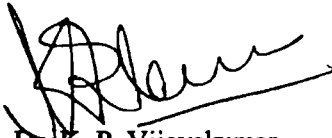
APRIL 2008

**Dr. K. P. Vijayakumar**  
Professor  
Department of Physics  
Cochin University of Science and Technology  
Cochin – 682 022

---

## *Certificate*

Certified that the work presented in this thesis entitled “*Defect analysis of semiconductor thin films for photovoltaic applications using photo-luminescence and photo-conductivity*” is based on the authentic record of research done by Mr. R. Jayakrishnan under my guidance in the Department of Physics, Cochin University of Science and Technology, Cochin – 682 022 and has not been included in any other thesis submitted for the award of any degree.

  
Dr. K. P. Vijayakumar  
(Supervising Guide)

Date: 23/4/08

---

Phone: +91 484 2577404 extn 33. Fax: 91 484 2577595. Email: [kpv@cusat.ac.in](mailto:kpv@cusat.ac.in)

## Declaration

Certified that the work presented in this thesis entitled “*Defect analysis of semiconductor thin films for photovoltaic applications using photoluminescence and photo-conductivity*” is based on the original research work done by me under the supervision and guidance of *Prof. K. P. Vijayakumar*, Department of Physics, Cochin University of Science and Technology, Cochin-682022 and has not been included in any other thesis submitted previously for the award of any degree.

Cochin – 22

Date: 23/4/08



R. Jayakrishnan

---



## *Acknowledgments*

*First of all I would like to thank my family for standing by me in this endeavor of mine*

*The foremost acknowledgement goes to my philosopher and guide Prof. K.P.Vijayakumar who entrusted me this problem. His views and opinions on each problem always lead to possible solutions which inspired me to indulge in long arguments and discussions with him. Many moments remain with me as they built a different character in me. In the few years of association with him I have imbibed many of his characters and often I feel I am imitating his style of thought & execution.*

*My gratitude remains to Dr. C. Sudha Kartha who stood along as a supervisor in establishing the base of my thesis work. Her sharp vision for perfection and knowledge in fluorescence spectroscopy were a blessing to my work. At times of distress her actions and suggestions have been exemplary.*

*I would like to thank the Head and all the teaching staff of the department who have been very helpful in discussing and suggesting alternatives to the problems discussed with them. Their cooperation, understanding and willingness to help are rare qualities one comes across.*

*I would like to thank Dr. V. Ganesan, UGC-DAE, Consortium for Scientific Research, Indore for inspiring me to work on at a different pace and his words on a cold night will remain always engraved in me. I would also like to thank the center director of UGC-DAE for extending me with local hospitality during my periods of stay at the centre.*

*Next I would to thank Dr. Teny Theresa John, Mrs. Tina Sebastian and Ms. K.G. Deepa with whom I have had long discussions. I feel rewarded from their actions and remain obliged to them.*

*I would like to thank Dr. S. Ramkumar, Dr. Paulraj Mani, Dr. Ratheesh Kumar P.M., Mr. A. Sreekumar, Ms. Beena Mary John, Mr. V.C. Kishore, Mr. R. Sreekumar, Mrs. Meril Lijoy, Mr. T.V. Vimal Kumar, Ms. Pramitha, Mrs. Anitha*

*Warrier, Mrs. Angel Susan, Mr. T.H. Sajeesh, Mr. Rajesh Menon, Mr. C.S.Rajesh, Mr. Rajesh Mon, Mr. Jafar, Mr. Subin, Mr. Vinay Raj & Ms. Poornima whose presence in my life has always lightened the harsher feelings I have had during my days of work. This team has always been my backbone on which I have tried to excel in every aspect of research and living. I would like to name many more of the research scholars of the Department of Physics and Chemistry who have always been there around me to support me in this journey of mine and whose friendship I would like to maintain for a lifetime.*

*My gratitude remains to Defence Research and Development Organisation (DRDO) (ER & IPR) and to Hind High Vacuum India Pvt. Ltd for the financial support extended to me to complete my work,*

*I would also like to thank the administrative staff of the Department of Physics, the planning section, the academic section and audit section with whom I have had to interact equally as to my thesis problem. Their wishes and support have been most supportive in the period of my work,*

*Lastly I would like to thank my room mate Mr. R. S. Ajimsha and my friend who were there with me in my ups and downs, to hear all that I had to say and patiently reply. To all those fruitful and fruitless, subjective and objective, days and nights I spent with them*

*&*

*To god to whom I pray....*

*Lead me from untruth to truth  
From darkness to light  
And from death to immortality*

# CONTENTS

Abbreviations.....	v
Preface .....	vii
Publication.....	xi

## *Chapter 1: Photo-luminescence and Photo-conductivity in Analysis of Semiconductors*

<b>1.1 An introduction to photo-electronic properties in semiconductors.....</b>	<b>1</b>
1.1.1 Optical absorption in semiconductor.....	2
1.1.1A Intrinsic optical absorption.....	2
1.1.1B Extrinsic optical absorption.....	4
<b>1.2 Recombination in semiconductors .....</b>	<b>5</b>
1.2.1 Radiative recombination-by emitting photons: Photo- luminescence.....	6
1.2.2 Exciton photo-luminescence.....	12
1.2.2A Free excitons .....	12
1.2.2B Bound excitons .....	14
1.2.2C Excitonic molecules .....	15
1.2.3 Photo-luminescence due to band-to-band recombination.....	17
1.2.3A Direct transitions .....	18
1.2.3B Indirect transitions.....	18
1.2.3C Effect of doping.....	19
1.2.3D Carrier interaction assisted emission.....	20
1.2.4 Photo-luminescence due to transitions between a band and impurity level .....	21
1.2.4A Shallow transitions.....	22
1.2.4B Deep transitions .....	22
1.2.4C Transitions to deep levels .....	24
1.2.5 Luminescence due to donor-acceptor pair recombination.....	24
1.2.5A Spectral features .....	24
1.2.5B Emission energy dependence on time .....	27
1.2.5C Emission energy dependence on excitation intensity .....	27
1.2.5D Luminescence due to iso-electronic traps .....	28
1.2.6 Intra-band luminescence.....	28
<b>1.3 Photo-conductivity.....</b>	<b>29</b>
1.3.1 Theoretical background.....	29
1.3.2 Measure of photosensitivity .....	30

1.3.4 Effect of traps .....	34
1.3.4A Decrease in speed of response .....	34
1.3.4B Decrease in mobility .....	35
1.3.4C Decrease in photosensitivity .....	35
1.3.4D Temperature dependence of photo-conductivity .....	36
1.3.4E Effect of excitation intensity on photo-conductivity.....	36
1.3.5 Fermi level in photoconductor .....	37
1.4 PL in analysis of semiconductors .....	38
1.5 PC in analysis of semiconductors.....	47
1.6 Conclusions .....	51
1.7 Reference.....	52

## ***Chapter 2: A System for Low Temperature Photo-luminescence and Photo-conductivity Studies***

<b>2.1 Characterization using photo-luminescence and photo-conductivity: An introduction.....</b>	<b>59</b>
<b>2.2 Requirements for the fabrication of a PL mapping and PC measurement system .....</b>	<b>61</b>
<b>2.3 Schematic of the low temperature photo-luminescence scanning and photo-conductivity set up.....</b>	<b>68</b>
<b>2.4 On the assembled opto-electronic characterization unit .....</b>	<b>71</b>
2.4.1 Excitation Sources .....	72
2.4.1A He-Cd laser .....	72
2.4.1B Ar ion laser.....	72
2.4.1C Solid state diode pumped green laser.....	72
2.4.1D He-Ne laser.....	72
2.4.1E Xenon arc lamp .....	73
2.4.2 Detection system.....	74
2.4.2A Spectrophotometer for UV-VIS-IR region .....	74
2.4.2B Optical fibers.....	75
2.4.2C Software package.....	75
2.4.3 Closed cycled liquid He cryostat-A cooling system.....	76
2.4.3A Modifications for signal collection.....	76
2.4.4 Mechanical translator system .....	77
2.4.5 The PL scanning system.....	78
<b>2.5 Integration of photo-conductivity experiment.....</b>	<b>81</b>

2.5.1 DC photo-conductivity .....	81
2.5.2 AC photo-conductivity .....	82
<b>2.6 Conclusions .....</b>	<b>82</b>
<b>2.7 Reference .....</b>	<b>83</b>

### *Chapter 3: Photo-luminescence in Analysis of CuInS<sub>2</sub> Thin Films*

<b>3.1 Introduction .....</b>	<b>86</b>
<b>3.2 Photo-luminescence of CuInS<sub>2</sub> .....</b>	<b>92</b>
<b>3.3 Sprayed CuInS<sub>2</sub> thin films for photovoltaic application.....</b>	<b>94</b>
3.3.1 Preparation of CuInS <sub>2</sub> thin films using Chemical Spray Pyrolysis .....	95
3.3.2 Structural, optical and chemical analysis of CuInS <sub>2</sub> thin films .....	97
<b>3.4 On the exciton emissions in CuInS<sub>2</sub> thin films.....</b>	<b>100</b>
<b>3.5 Spatially resolved PL mapping .....</b>	<b>110</b>
<b>3.6 Broad band defect related PL emissions in CuInS<sub>2</sub> thin films .....</b>	<b>113</b>
<b>3.7 Effect of substrate temperature on the PL emissions in CuInS<sub>2</sub> thin films.....</b>	<b>118</b>
<b>3.8 Conclusions .....</b>	<b>122</b>
<b>3.9 Reference.....</b>	<b>124</b>

### *Chapter 4: Photoluminescence Studies on CuInSe<sub>2</sub> Thin Films*

<b>4.1 Introduction .....</b>	<b>128</b>
<b>4.2 PL of CuInSe<sub>2</sub> .....</b>	<b>132</b>
<b>4.3 Sequential layer deposition of CuInSe<sub>2</sub> thin films for photovoltaic application .....</b>	<b>135</b>
4.3.1 Preparation of CuInSe <sub>2</sub> thin films .....	136
4.3.2 Structural and optical studies .....	137
<b>4.4 PL from SEL deposited CuInSe<sub>2</sub> thin films .....</b>	<b>139</b>
4.4.1 CuInSe <sub>2</sub> thin films grown using Se layer deposited employing CBD .....	139
4.4.2 CuInSe <sub>2</sub> thin films grown by diffusing Cu into In <sub>2</sub> Se <sub>3</sub> .....	143
4.4.3 CuInSe <sub>2</sub> thin films grown by vacuum evaporation.....	147
4.4.4 Radiative donor-acceptor pair recombination in CuInSe <sub>2</sub> thin films .....	155
<b>4.5 Donor-Acceptor and free-to-bound transitions in CuInSe<sub>2</sub>/ITO hetero-structure .....</b>	<b>161</b>

<b>4.6 Conclusions .....</b>	<b>165</b>
<b>4.7 Reference .....</b>	<b>168</b>

***Chapter 5: Opto-electronic Characterization of  $\beta$ - In<sub>2</sub>S<sub>3</sub> Thin Films***

<b>5.1 Introduction .....</b>	<b>173</b>
5.1.1 Crystal structure of $\beta$ -In <sub>2</sub> S <sub>3</sub> .....	175
5.1.2 The band structure .....	177
5.1.3 $\beta$ - In <sub>2</sub> S <sub>3</sub> an optoelectronic material .....	179
<b>5.2 Structural and morphological studies on In<sub>2</sub>S<sub>3</sub> thin films .....</b>	<b>181</b>
<b>5.3 Optical absorption of <math>\beta</math>-In<sub>2</sub>S<sub>3</sub> thin films .....</b>	<b>184</b>
<b>5.4 Defect analysis of <math>\beta</math>-In<sub>2</sub>S<sub>3</sub> thin films using PL.....</b>	<b>187</b>
<b>5.5 Effect of above band gap and sub-band gap excitation on the PL.....</b>	<b>195</b>
<b>5.6 Effect of annealing in vacuum and air .....</b>	<b>199</b>
5.6.1 Effect of rapid thermal quenching.....	201
<b>5.7 Photo-conductivity in <math>\beta</math>-In<sub>2</sub>S<sub>3</sub> thin films.....</b>	<b>202</b>
5.7.1 General properties .....	202
5.7.2 On the photo-conductivity in $\beta$ -In <sub>2</sub> S <sub>3</sub> thin films.....	205
<b>5.8 The role of Cl impurity on the opto-electronic properties.....</b>	<b>216</b>
<b>5.9 Conducting grain boundaries of <math>\beta</math>-In<sub>2</sub>S<sub>3</sub> .....</b>	<b>219</b>
<b>5.10 Conclusions .....</b>	<b>228</b>
<b>5.11 Reference .....</b>	<b>229</b>

***Chapter 6: Summary and Outlook***

<b>6.1 Summary .....</b>	<b>235</b>
<b>6.2 Future outlook .....</b>	<b>239</b>
<b>6.3 Reference .....</b>	<b>240</b>

## *Abbreviations*

Atomic Force Microscopy	AFM
Band Gap Energy	$E_g$
Bound Exciton	BE
Cartesian Coordinate	CC
Chalcopyrite	Ch-
Charge Coupled Device	CCD
Chemical Bath Deposition	CBD
Chemical Spray Pyrolysis	CSP
Chemical Vapor Deposition	CVD
Conductance Atomic Force Microscopy	C-AFM
Conduction Band	CB
$CuInSe_2$	CISe
$CuInS_2$	CIS
Donor-Acceptor Pair	DAP
Electron-Hole Pair	EHP
Energy Dispersive Analysis using X-rays	EDAX
Free Exciton	FE
Full Width at Half Maximum	FWHM
Infrared	IR
Optical Resolution	OR
Photo-conductivity	PC
Photo-luminescence	PL
Photo Multiplier Tube	PMT
Photovoltaic	PV
Physical Vapor Deposition	PVD
Scanning Electron Microscopy	SEM
Sequential Elemental Layer	SEL
Shockley-Read-Hall	SRH
Sub-Miniature Version A	SMA
Thermally Stimulated Current	TSC
Valence Band	VB
X-ray Diffraction	XRD
X-ray Photoelectron Spectroscopy	XPS

## Preface

Semiconductors have emerged as the most promising class of materials that can convert sunlight directly into electrical energy. Currently, a wide range of semiconductors are being explored for their potential use in photovoltaic (PV) applications. Lowering the cost of solar cell production is one of the most important intentions in PV research. Recent developments in solar cell research proved that  $\text{CuInSe}_2$  (and its alloys) and  $\text{CuInS}_2$  are promising absorber layers for high efficiency large area solar cells. Efficiency up to 19.2% has been achieved with  $\text{ZnO/CdS/CuInGaSe}_2$  (CIGS) cell structure. Commercially available solar cells use CdS as the buffer layer which is toxic and carcinogenic. A lot of research is going on for the replacement of the CdS buffer layer by Cd-free, wide band gap materials like  $\text{In}_x(\text{OH,S})_y$ , ZnO, ZnSe,  $\text{In}_2\text{Se}_3$  and  $\text{In}_2\text{S}_3$ .  $\text{In}_2\text{S}_3$  films deposited using Atomic Layer Chemical Vapor Deposition (ALCVD) yielded an efficiency of 16.4% in CIGS based cells.

In batch or large area thin film growth process reliability, repeatability and uniformity require robust non-destructive tools which can be used *in-situ* so that material, time and labor loss on defective wafers can be avoided. Growth techniques evolve towards obtaining defect free materials. Photo-luminescence (PL) is one such tool which is now being used industrially and has shown tremendous usefulness to the light emitting device (LED) and PV industry. Defects are useful because they provide alternative routes to probe the materials band structure by acting as radiative recombination centers or as traps or as donor/acceptor levels. Their presence affects the carrier generation-recombination paths and effectively modulates carrier lifetime which is the most important parameter for device application. The opto-electronics industry that drives most of the material investigations is concerned with optical and electronic properties. PL spectroscopy provides optical characterization and is a selective and extremely sensitive probe of discrete electronic states.

**Chapter 1** provides an introduction to the general theory of PL and PC in semiconductors, its characteristics and its application in the semiconductor opto-electronic industry. The chapter begins with the description of various kinds of PL, their characteristics and their temperature and excitation intensity dependence. The effect of recombination centers and shallow traps on the PL



and PC is described. A detailed review on the application of PL and PC as a diagnostic tool for semiconductor devices and thin films is presented as separate sections in the chapter. The chapter concludes with a discussion on the impact of simultaneously using PL and PC studies for characterization, quality and failure analysis in the opto-electronic industry.

**Chapter 2** describes the setting up of a Low Temperature Opto-electronic characterization unit for PL mapping and PC studies which was the starting point of this thesis work. A low temperature fiber optic laser induced PL and PC set up was assembled by integrating the required components. This system primarily consists of five subsystems: optical excitation system, cooling system, opto-electronic system, mechanical system, and data acquisition system. The resolution of the PL system was found to be 1.67 nm in the 350-900 nm wavelength range while it was found to be 2.34 nm in the 900-1730 nm wavelength range.

Chemical Spray Pyrolysis (CSP) technique is suitable for solar cell production, because of the possibility of large-area deposition of thin films in any required shape, convenience in doping and/or variation of atomic ratio and economic nature of the technique. **Chapter 3** describes the analysis of  $\text{CuInS}_2$  thin films deposited by CSP technique using PL. PL was studied on  $\text{CuInS}_2$  thin film samples grown as a function of the exact composition in terms of the deviation from molecularity and stoichiometry. The near band edge (exciton) emissions were investigated for various material compositions as a function of temperature. From these investigations the exciton ionization energy (20 meV) was determined. The peak position of the "A" free exciton transition was found to be directly related to the composition of the film. For Indium rich films the "A" free exciton emission was located around  $\sim 1.559$  eV, for Copper rich films it was located at  $\sim 1.535$  eV and for stoichiometric films it was located at  $\sim 1.550$  eV. Based on temperature (12-300 K) and excitation intensity dependent measurements, donor-acceptor transitions were identified. In this chapter defect levels of vacancy of Sulphur ( $V_s$ ), vacancy of Copper ( $V_{\text{Cu}}$ ), vacancy of Indium ( $V_{\text{In}}$ ) and Copper interstitials ( $\text{Cu}_i$ ) / Copper at Sulphur sites ( $\text{Cu}_s$ ) has been identified using dependence of PL on film stoichiometry in  $\text{CuInS}_2$  thin films. The critical dependence of substrate temperature on film composition was identified by carrying out PL study of samples prepared by spraying the same molar ratio solution on to substrates maintained at different temperatures. Samples obtained with substrate temperature maintained at  $350^\circ\text{C}$  and with spray precursor solution containing Cu/In molar ratio of 1 and S/Cu molar ratio

of 5, showed band edge emission at room temperature indicating very good crystalline quality and absence of defects in the films. Thus precursor solution and substrate temperature could be standardized for the spray pyrolysis of  $\text{CuInS}_2$  thin films.

**Chapter 4** describes the PL studies on  $\text{CuInSe}_2$  thin films. In the search for a simple, eco-friendly low temperature thin film deposition process for stoichiometric  $\text{CuInSe}_2$  thin films, PL was used as a tool to identify a standard deposition process for the growth of stoichiometric films.  $\text{CuInSe}_2$  thin films grown using Selenium deposited by Chemical Bath Deposition (CBD) showed free-to-bound emission involving the  $V_{\text{Cu}}$  acceptor level, bound-to-free emission involving the  $V_{\text{Se}}$  donor level and donor-acceptor pair (DAP) recombination involving  $\text{In}_{\text{Cu}}$  donor levels and deep acceptors. When the films were grown using Physical Vapor Deposition (PVD) technique sharper PL emission lines were recorded which indicated improvement in crystallinity and decrease in defect density. Also in these films the PL intensity was lower compared to films grown using the former technique. The number of emission lines was also reduced in films deposited using this technique. Stoichiometric films grown, showed only bound-to-free transitions with the smallest full width at half maximum. Ease of stoichiometry control in films grown by this process enabled the identification of defects like Copper interstitial ( $\text{Cu}_i$ ), Copper at Indium anti-site ( $\text{Cu}_{\text{In}}$ ), vacancy of Selenium ( $V_{\text{Se}}$ ) and vacancy of Indium ( $V_{\text{In}}$ ).

**Chapter 5** describes the defect analysis on  $\beta\text{-In}_2\text{S}_3$  thin films; an III<sub>2</sub>-VI<sub>3</sub> semiconductor prepared using CSP technique using PL and PC studies. The study showed the material to be highly luminescent and thus the potential to use this material in a wide variety of opto-electronic device application was realized. The material was found to show two luminescence bands one in the green region  $\sim 540$  nm and another in the red region  $\sim 690$  nm. The luminescence at these regions could be quenched when the film stoichiometry was changed and in effect PL tuning was achieved. Temperature and excitation intensity dependent studies revealed that the PL emissions were DAP kind. PC complements PL and hence PC studies were carried out to understand the defects in this material. Excitation energy, excitation intensity, illumination time and temperature dependent PC studies were carried out. The films were found to highly photosensitive and the speed of response was found to be controlled by the defects.  $\beta\text{-In}_2\text{S}_3$  was found to possess two defect bands: one spread from 0.82 eV to 0.89 eV above the valence band and another spread from  $\sim 0.21$  to 0.51 eV

below the conduction band (CB) edge. Based on the PL and PC studies this material was identified to possess defect bands within the forbidden band gap.

**Chapter 6** is a summary of the entire work. The defect band model for  $\text{CuInS}_2$ ,  $\text{CuInSe}_2$  and  $\text{In}_2\text{S}_3$  is proposed in this chapter based on the results obtained from the PL and PC studies of the samples. The chapter ends with future scope of the present work.

# *Publications*

## **Journal Papers related to the thesis**

1. Do the grain boundaries of  $\beta$ - $\text{In}_2\text{S}_3$  thin films have a role in sub band gap photosensitivity to 632.8 nm? Jayakrishnan, R., Teny Theresa John, Sudha Kartha, C. Vijayakumar, K. P., Deepthi Jain, Sharath Chandra, L. S. and Ganesan, V., J. Appl. Phys. **103**, 053106 (2008).
2. Photoconductivity in Sprayed  $\beta$ - $\text{In}_2\text{S}_3$  thin films under sub band gap excitation of 1.96 eV, Jayakrishnan, R., Tina Sebastian, Teny Theresa John, Sudha Kartha, C. and Vijayakumar, K. P., J. Appl. Phys. **102**, 043109 (2007).
3. Surface topology using laser back scattering and photoluminescence on Cu- and In- rich  $\text{CuInSe}_2$  thin films, Jayakrishnan, R., Ratheesh Kumar P. M., Sudha Kartha, C. and Vijayakumar, K. P., Meas. Sci. Technol. **17**, 3301 (2006).
4. Tuning Donor-Acceptor and Free-bound transitions in  $\text{CuInSe}_2/\text{ITO}$  heterostructure. Jayakrishnan, R., Deepa, K. G., Sudha Kartha, C., and Vijayakumar. K. P., J. Appl. Phys. **100**, 046104 (2006).
5. Room temperature photo-luminescence surface mapping. Jayakrishnan, R., Tina Sebastian, Sudha Kartha, C. and Vijayakumar, K. P., Journal of Physics: Conference Series **28**, 62 (2006).
6. Defect analysis of sprayed  $\beta$ - $\text{In}_2\text{S}_3$  thin films using photo-luminescence studies. Jayakrishnan, R., Teny Theresa John, Sudha Kartha, C., Vijayakumar, K. P., Abe, T. and Kashiwaba, Y., Semicon. Sci. Technol. **20**, 1162 (2005)

## **Conference Papers:**

### **International:**

1. Room temperature photo-luminescence surface mapping, Jayakrishnan, R., Tina Sebastian, Sudha Kartha, C. and Vijayakumar, K.P., International Conference on Materials for Advanced Technologies, Symposium Y: Optical Spectroscopic Techniques, 3–8 July, Singapore (2005).

2. Temperature and Temporal dependence of Photosensitivity of  $\beta$ - $\text{In}_2\text{S}_3$  thin films under sub band gap excitation of 2.33 eV, Jayakrishnan, R., Teny Theresa John, Sudha Kartha, C. and Vijayakumar, K. P., International Conference on Materials for Advanced Technologies, Symposium J: Materials for Advanced Sensors and Detectors, 1–6 July, Singapore (2007).
3. Role of intermediate bands of sprayed  $\beta$ - $\text{In}_2\text{S}_3$  in sprayed  $\text{CuInS}_2/\text{In}_2\text{S}_3$  solar cells, Jayakrishnan, R., Teny Theresa John, Sudha Kartha, C. and Vijayakumar, K. P., Proceedings of the International Conference on Solar Cells (IC-SOLACE), 21-23 Jan, Cochin. p. 188 (2008).

### **National:**

1. Analysis of sprayed  $\beta$ - $\text{In}_2\text{S}_3$  thin films using photo-luminescence studies, Jayakrishnan, R., Teny Theresa John, Sudha Kartha, C., Vijayakumar, K. P., Solid State Physics Symposium held by DAE-BRNS at Guru Nanak Dev University, Punjab (2004).
2. PL surface scan of sprayed  $\text{CuInS}_2$  thin films, Jayakrishnan, R., Tina Sebastian, Sudha Kartha, C. and Vijayakumar, K. P., Proceedings of National Conference on Luminescence Application (NCLA), Vol XVII, p. 130 (2005).
3. Defect studies on SEL deposited  $\text{CuInSe}_2$  thin films, Jayakrishnan, R., Deepa, K. G., Sudha Kartha, C. and Vijayakumar, K. P., Presented at the MRSI conference held at NCL, Pune (2005).
4. Low temperature laser induced photo-luminescence set up, Jayakrishnan, R., Deepa, K. G., Teny Theresa John, Sudha Kartha, C. and Vijayakumar, K. P., Proceedings of the National Conference on Luminescence Application (NCLA), Vol XVIII, p. 187 (2006).
5. Tunable photo-detectors based on  $\beta$ - $\text{In}_2\text{S}_3$  thin films, Jayakrishnan, R., Tina Sebastian, Sudha Kartha, C. and Vijayakumar, K. P., Proceedings of National Conference on “Smart Structures and MEMS Systems for Aerospace application, “ISSS-MEMS 2006”, RCI Hyderabad (2006).
6. Photoluminescence in  $\beta$ - $\text{In}_2\text{S}_3$  based thin film devices, Jayakrishnan, R., Sudha Kartha, C. and Vijayakumar, K. P., Proceedings of the National Conference on Luminescence Application (NCLA), p. 269 (2006).
7. Chemical spray pyrolysed  $\beta$ - $\text{In}_2\text{S}_3$  thin films for sensor and energy conversion applications, Jayakrishnan, R., Teny Theresa John, Tina

Sebastian, Meril Mathew, C.Sudha Kartha and K.P.Vijayakumar, Souvenir and Abstracts of the 18<sup>th</sup> Annual General meeting of MRSI, p. 42 (2007).

8. Fractal analysis of chemical spray pyrolysed  $\beta$ -In<sub>2</sub>S<sub>3</sub> thin films, Jayakrishnan, R., Tina Sebastian, Sudha Kartha, C. and Vijayakumar, K. P., Deepthi Jain, Sharath Chandra, L. S. and Ganesan, V., Proceeding of the National Conference on Smart Materials and Recent Technologies, p. 142 (2007).
9. Where does photo-current flow in  $\beta$ -In<sub>2</sub>S<sub>3</sub> Thin Films? Jayakrishnan, R., Teny Theresa John, Sudha Kartha, C., Vijayakumar, K. P., Deepthi Jain, Sharath Chandra, L. S. and Ganesan, V., Proceedings of the National Conference on Current Trends in Material Science p. 155 (2007).

### **Other Contributions to Journal Papers**

1. Enhancement of band gap and photoconductivity in gamma indium selenide due to swift heavy ion irradiation, Sreekumar, R., Jayakrishnan, R., Sudha Kartha, C. Vijayakumar, K. P., Khan, S. A. and Avasthi, D. K., J. Appl. Phys. **103**, 023709 (2008).
2. Anomalous behavior of silver doped indium sulfide thin films. Meril Mathew, Jayakrishnan, R., Ratheesh Kumar P. M., Sudha Kartha, C., Vijayakumar, K. P., Abe, T. and Kashiwaba, Y., J. Appl. Phys. **100**, 033504 (2006).
3. Anomalous Photoconductivity in In<sub>2</sub>Se<sub>3</sub> thin films. Sreekumar, R., Jayakrishnan, R., Sudha Kartha, C., Vijayakumar, K. P., J. Appl. Phys. **100**, 033707 (2006).
4. Different phases of indium Selenide prepared by annealing In /Se bilayer at various temperatures: Characterization studies. Sreekumar, R., Jayakrishnan, R., Sudha Kartha, C., Vijayakumar, K. P., Kashibawa, Y. and Abe, T., Sol. Energy Mat. Sol. Cells. **90**, 2908 (2006)

### **Other Conference Papers:**

#### **International:**

- 1) Comparative study of Cu rich and In rich CuInS<sub>2</sub> Thin Films prepared Using Automated Spray System, Tina Sebastian, Teny Theresa John, Jayakrishnan, R., Vijayakumar, K. P., Sudha Kartha, C., Deepthi Jain and Ganesan, V., International Conference on Optoelectronic Materials and Thin Films OMTAT-2005, 24-26<sup>th</sup> October, Cochin, India (2005).

**National:**

- 1) Preparation of device quality CuInS<sub>2</sub> using Chemical Spray Technique for PV applications, Tina Sebastian, Jayakrishnan, R., Manju Gopinath, Sudha Kartha, C. and Vijayakumar, K. P., Souvenir and Abstracts of the 18<sup>th</sup> Annual General meeting of MRSI, p. 105 (2007).
- 2) Raman analysis of sequentially evaporated CuInSe<sub>2</sub> thin films, Deepa, K. G., Jayakrishnan, R., Sathae, V., Phase, D. M., Vijayakumar, K. P. and Sudha Kartha, C., Souvenir and Abstracts of the 18<sup>th</sup> Annual General meeting of MRSI, p. 154 (2007).
- 3) Defect analysis of CuInS<sub>2</sub> thin films using TSC technique, Manju Gopinath, Tina Sebastian, Jayakrishnan, R., Sudha Kartha, C. and Vijayakumar, K. P., Proceeding of the National Conference on Smart Materials and Recent Technologies, p. 128 (2007).

# CHAPTER 1

## Photo-luminescence and Photo-conductivity in Analysis of Semiconductors

---

*Most semiconductor devices operate by the creation of charge carriers in excess of thermal equilibrium. These excess carriers can be generated by optical excitation or electron bombardment or injection across a forward biased p-n junction. When the excess carriers arise, they can dominate the conduction process in the semiconductor material. This chapter deals with the creation of excess carriers by optical absorption and the resulting properties of photo-luminescence and photo-conductivity. A detailed study on the different mechanisms of electron-hole pair recombination as well as effect of carrier trapping and temperature on these physical processes are included in this chapter. Finally, a discussion on the possible application of these effects in the opto-electronic industry for characterization and application is attempted.*

### **1.1 An introduction to photo-electronic properties in semiconductors**

Opto-electronics deals with interaction of electronic processes with light. Such a process is accompanied by an energy conversion (either electrical to optical or vice-versa). Devices which can interact in this way are made with semiconductors and the present work aims at understanding these properties in some of the binary and ternary compound semiconductors. Semiconductors are materials having electrical resistivity in the range  $10^{-2}$  to  $10^9$  ohm-cm, intermediate between good conductors ( $10^{-6}$  ohm-cm) and insulators ( $10^{14}$  to  $10^{22}$  ohm-cm).<sup>1</sup> The characteristic feature that distinguishes semiconductors from metals and insulators is their band gap. The electrons in semiconductors can have energies only within certain *bands* lying between a ground state, [corresponding to electrons tightly bound to the atomic nuclei of



the material] and the free electron energy, [corresponding to the energy needed by an electron to escape from the interactions inside the atoms]. Each 'energy band' corresponds to a large number of discrete and closely packed quantum states of valence electrons. In most semiconductors, the bands are filled up to a particular one called valence band (VB), above which the bands are almost empty at low energy conditions. The band lying just above the VB is called the conduction band (CB). Energy difference between the two bands is referred to as the band gap of the material. If energy greater than the band gap of the material is supplied to electrons, the electrons in the VB can cross the band gap and reach the CB.

### *1.1.1 Optical absorption in semiconductors*

Optical absorption is described qualitatively through the absorption coefficient  $\alpha$ . In the simplest case, neglecting reflection or interference effects, if light of intensity  $I_0$  is incident on a material of thickness  $d$  with absorption coefficient  $\alpha$ , the intensity of the transmitted light  $I$  is given approximately by Beer's law as<sup>2</sup>

$$I = I_0 \exp(-\alpha d) \quad (1.1)$$

The phenomenon of optical absorption in semiconductors can be divided into two: 1) Intrinsic and 2) Extrinsic optical absorptions.

#### *1.1.1A Intrinsic optical absorption*

Intrinsic optical absorption corresponds to photo-excitation of an electron from the VB to the CB. If the minimum of the CB is at the same position as the maximum of the VB in the  $k$ -space, a vertical transition takes place, involving the absorption of a photon only (Fig. 1.1). Such a transition is called 'direct optical transition'. The minimum photon energy for absorption is given by  $\hbar\omega = E_{GD}$ , where  $E_{GD}$  represents the direct band gap of the material and the change in  $k$  upon making the transition, is given as  $\Delta k = 0$ . This is because the momentum associated with the photon is very small compared to the width of the Brillouin zone and can effectively be neglected.

According to quantum mechanical calculation, during direct absorption, the effect of light is treated as a first order perturbation. For a direct absorption, the transition probability depends on the square of the matrix element involving only the interaction of light with electrons and hence it is a first order process. The variation of the absorption coefficient  $\alpha$  is given by<sup>3</sup>

$$\alpha^2 = (\hbar\omega - E_{GD}) \quad (1.2)$$

A plot of  $\alpha^2$  versus  $\hbar\omega$  gives a straight line whose intercepts with the  $\hbar\omega$  axis corresponds to  $E_{GD}$ . Direct optical transitions are characterized by a rapid increase in the value of  $\alpha$  when incident energy becomes greater than the band gap. If the minimum of the conduction band is at a different k-value compared with the highest point in the VB (Fig. 1.1), the process should involve the absorption of a photon and simultaneous emission or absorption of a phonon. In this case,  $E_{GI} = \hbar\omega_{\min} \pm E_{\text{phonon}}$  where  $E_{GI}$  is the indirect band gap of the material and  $E_{\text{phonon}}$  is the energy of the phonon involved in the process. Here a positive sign corresponds to phonon absorption while negative sign corresponds to phonon emission. The change in 'k' upon an indirect optical transition is given by  $\Delta k = k_{\text{phonon}}$ . In this case, the matrix element depends on the interaction of photons and phonons with electrons and hence is a second order process. The magnitude of  $\alpha$  is smaller than that obtained in direct optical absorption.

Figure 1.1(a) shows a typical plot of  $\alpha^2$  vs.  $\hbar\omega$  for a direct band gap material. The point of intersection of the straight line with the  $\hbar\omega$  axis corresponds to the band gap of the material above which the optical absorption increases many fold. Figure 1.1(b) shows a typical plot of  $\alpha^{1/2}$  vs.  $\hbar\omega$  for an indirect band gap material. For the indirect band gap material the plot gives two straight lines. If these two straight lines intersect the  $\hbar\omega$  axis at  $\hbar\omega_1$  and  $\hbar\omega_2$  with  $\hbar\omega_1 < \hbar\omega_2$ , then

$$E_{GI} = (\hbar\omega_1 + \hbar\omega_2)/2 \text{ and}$$

$$E_{\text{phonon}} = (\hbar\omega_2 - \hbar\omega_1)/2 \quad (1.3)$$

Several effects dependent on the type of optical excitation may be summarized as follows<sup>3</sup>

1. For direct band gap materials (GaAs, CdTe etc) optical absorption occurs near the surface of the material; for indirect band gap material light penetrates much deeper into the material.
2. For direct band gap materials the magnitude of intrinsic photo-conductivity (PC) depends critically on the surface lifetime; in indirect band gap materials surface lifetime is less important
3. If a direct band gap material is used in a p-n junction type of device, where junction collection of photo-excited carriers is important, a shorter diffusion length is required for carrier collection by the junction.

In an indirect band gap material a larger length is necessary if all excited carriers are to be collected.

4. Direct band gap materials are associated with greater luminescence efficiency because of a shorter radiative recombination lifetime whereas indirect ones have lower intrinsic luminescence efficiency due to longer radiative recombination lifetime, which allows other competing non-radiative process to become important.

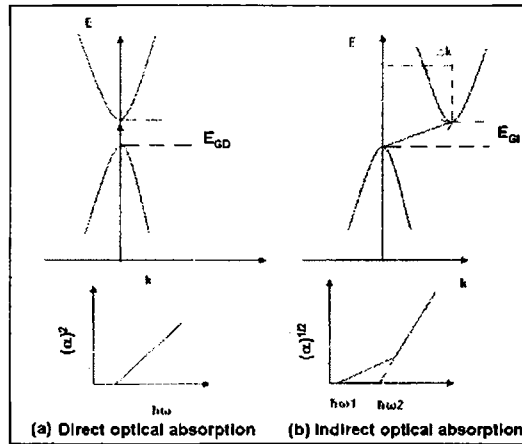


Fig. 1.1: Optical absorption in semiconductors (a) Direct and (b) Indirect.

### 1.1.1B Extrinsic optical absorption

In semiconductors, imperfections in the crystal may introduce in the forbidden energy gap, discrete energy levels with localized wave functions. Absorption involving such imperfection levels are called 'extrinsic optical absorption'. The optical absorption can raise the electrons from the valence band to these localized states or from these states into the conduction band. The absorption constant is proportional to the density of absorbing centers,  $N$  by relation <sup>3</sup>

$$\alpha = S_0 N \tag{1.4}$$

where  $S_0$  is called the optical cross section for the absorption process. Optical absorption coefficient reaches appreciable value at energies corresponding to the transitions taking place between the levels or imperfections situated within the band gap. The magnitude and dependence on photon energy on  $S_0$  have been calculated by a variety of quantum mechanical approximation.

## 1.2 Recombination in semiconductors

Many interesting photo-electronic phenomena are associated with semiconductors. It includes optical absorption, by which free carriers are created, electrical transport by which free carriers contribute to electrical conductivity of semiconductors and capture of free carriers leading to recombination or trapping. The different photo-electronic processes associated with semiconductors are illustrated in the Fig. 1.2. Intrinsic optical absorption (a) corresponds to the raising of an electron from the VB to the CB; Extrinsic optical absorption (b) & (c) corresponds to raising of an electron from an imperfection to the CB or raising of an electron from the VB to an imperfection; (d) & (e) represent capture and recombination of electrons and holes; (f) represents trapping and de-trapping. A study of all these processes is very important as they all contribute to the photo-electronic analysis of materials. Such methods are useful in the investigation and analysis of the properties of materials dominated with imperfections, replacing standard approaches as photo-Hall, photo-thermoelectric and photo-capacitance measurements.<sup>2</sup>

The excess electrons and holes created by optical absorption are eliminated by the recombination. It is therefore the recombination process which determines the lifetime of free carriers. Recombination processes can be classified according to the answers of the following two questions: (1) How is the energy of the excited carriers dissipated in the recombination process? (2) Is the recombination direct or indirect?

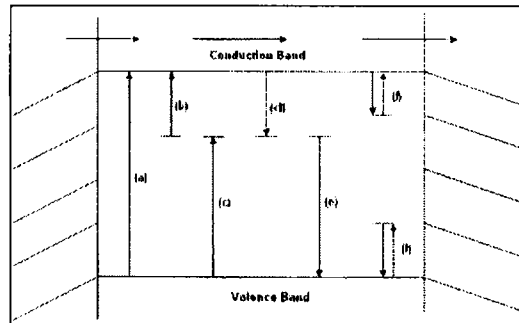


**Fig. 1.2:** Photo-electronic processes in semiconductors.

When an electron or hole is photo-excited to a higher energy state, there are three fundamental processes by which the energy can be given up when the carrier returns to its thermal equilibrium state: (1) Radiative recombination: by emitting photons, commonly called 'luminescence'; the energy of the emitted photon is equal to the energy difference between the two carriers before

recombination (2) Non-radiative recombination: emitting phonons either simultaneously or sequentially and (3) raising other free carriers to higher energy states: another non radiative effect, called Auger recombination, after which they may relax by the emission of phonons which is a three body collision process.

### ***1.2.1 Radiative recombination-by emitting photons: Photo-luminescence***

The term luminescence was first introduced by Eilhardt Wiedemann in 1888 and comes from the Latin word *lumen*, which means light. Physicists, chemists and biologists think and talk about 'light induced processes' which can be used to study systems / materials, because of the wealth of information that can be extracted from such experiments. When electron-hole pairs (EHP) are generated in a semiconductor, or when excess carriers are excited into higher impurity levels from which they fall to their equilibrium states, light can be given off by the material. Many of the semiconductors are well suited for light emission, particularly with direct band gaps. The general property of light emission is called luminescence. The category can be sub-divided based on the excitation mechanism: if carriers are excited by photon absorption, the radiation resulting from the recombination of the excited carriers is called photo-luminescence (PL); if the excited carriers are generated by high energy electron bombardment of the material, the mechanism is called cathode-luminescence (CL); if the excitation occurs by the introduction of current into the sample, the resulting luminescence is called electro-luminescence (EL). Figure 1.3 shows a typical energy-level scheme used in PL. The emitting system is raised by optical excitation from the ground state *f* to the excited state *e*. The system returns to the ground state with the emission of light at time  $\tau$  after excitation,  $\tau$  being the lifetime of the excited state.

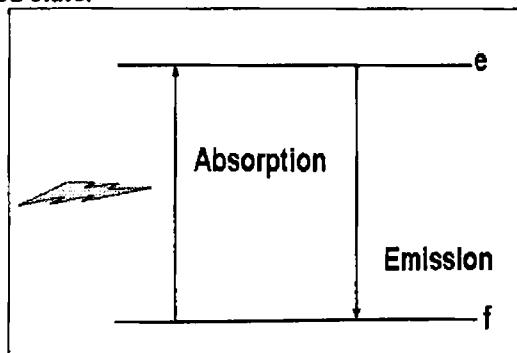


**Fig. 1.3:** Schematic representation of fluorescence.

Figure 1.3 describes direct recombination, where light equivalent to the difference in energy of the final and initial stage is given off. For steady state excitation, the recombination of EHP occurs at the same rate as the generation, and one photon is emitted for each photon absorbed. Direct recombination is a fast process where the mean lifetime  $\tau$  is typically of the order of  $10^{-8}$  s or less. Thus emission of photons stops within approximately  $10^{-8}$  s after the excitation is turned off. Such fast processes are called fluorescence. One of the criteria for an emission to be called fluorescence is that the system must remain in the excited state for a time  $\tau$ , large compared with the frequency of the emitted radiation.<sup>4</sup> In the previous system, if a meta-stable level  $m$  (trap or trapping state) is included then it could lead to emissions which continue for periods up to seconds or minutes after the excitation is removed. Such delayed emissions are called phosphorescence and the materials are called phosphors. Figure 1.4 describes this slow emission.

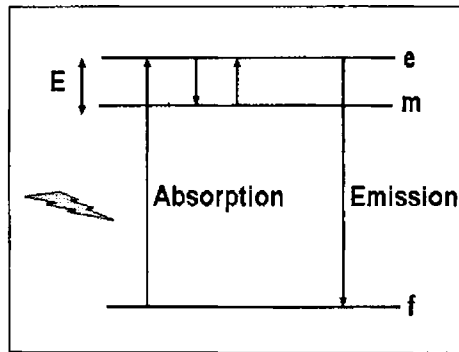


Fig. 1.4: Schematic representation of phosphorescence.

In Fig. 1.4 the system on excitation to the state “e” can make a transition to the state “m”, which by definition is meta-stable, will not allow further transition “m”  $\rightarrow$  “f”. Thus the system will not change from the state “m” unless it receives energy “E” lifting it again to the excited state “e”. Then phosphorescence occurs (if there is no return to the state “m” - recapture into the trap) identical in emission with fluorescence. The relative intensities of the various emission bands may be different and is delayed in time by an amount  $\tau_m$  equal to the time spent in the state “m”.

If the energy  $E$  (usually called the trap depth) is provided by thermal activation, then in general<sup>5</sup>

$$1/\tau_m = s \cdot \exp(-E/k_B T) \quad (1.5)$$

where  $\tau_m \gg \tau$ ,  $s$  is a constant,  $k_B$  is Boltzmann's constant and  $T$  is the absolute temperature. Thus a luminescence emission with a lifetime of about  $10^{-8}$  s can be defined as fluorescence, whereas if an emission persists for an order of 1 second, or a longer duration even after the excitation ends, it is called phosphorescence. In the intermediate time range say  $10^{-1}$  to  $10^{-5}$  s, it is difficult to distinguish between a long fluorescence (forbidden transition) and short phosphorescence (due to very shallow traps). The easiest method to distinguish between the two is to study the variation of luminescence decay with temperature. The decay of fluorescence is little dependent on the temperature while the decay of phosphorescence is strongly temperature dependent (determined by a Boltzmann function).

Operation of almost all opto-electronic devices is based on creation or annihilation of EHPs. In semiconductors, if an energetic particle can impart at least energy equal to the band gap energy, it will lead to creation of pairs.<sup>6</sup> Pair formation is equivalent to breaking a covalent bond, with respect to the bonding in the lattice. The electron from the VB is raised to the CB, leaving behind a hole in the VB. This process is called absorption.<sup>7</sup> The annihilation of the pair by giving up its excess energy is called recombination. There are two recombination paths that can be followed by the excess carriers generated: 1) a non-radiative recombination transition where excess energy due to recombination is given to phonons which get dissipated as heat and 2) a radiative recombination where the excess energy is dissipated as photons [which are the luminescent processes classified on the basis of the method by which EHPs are generated].

Hence no description of the luminescence process is complete without the corresponding absorption process. The reverse of all absorption processes can occur to produce radiation. An absorption process couples a broad energy range of filled and empty states which gives rise to broad absorption spectrum, while the emission process couples a narrow band of non-equilibrium filled states with a narrow band of empty states, to give a narrow emission spectrum. Usually shoulders in the absorption spectrum correspond to narrow emission peaks. The absorption and spontaneous emission processes are related by the principle of detailed balance. Absorption expressed in terms of absorption coefficient  $\alpha(h\nu)$ , defined as the relative rate of decrease in light intensity  $L(h\nu)$  along its propagation path can be written as<sup>8</sup>

$$\alpha = (1/L(h\nu)) * (d[L(h\nu)]/dx) \quad (1.6)$$

The absorption coefficient  $\alpha(h\nu)$  for a given photon energy  $h\nu$  is proportional to the probability  $P_{if}$  for transition from the initial state to the final state and to the density of electrons in the initial state  $n_i$ , and to the density of available (empty) final states  $n_f$ , and this process must be summed for all possible transitions between states separated by an energy difference equal to  $h\nu$  :

$$\alpha(h\nu) = A \sum P_{if} n_i n_f \quad (1.7)$$

where  $A$  is a constant given by <sup>8</sup>:

$$A \approx q^2 (2(m_h^* m_e^* / (m_h^* + m_e^*)))^{3/2} / n c h^2 m_e^* \quad (1.8)$$

where  $q$  is the electronic charge,  $m_e^*$  and  $m_h^*$  are the electron and hole effective mass,  $n$  the refractive index,  $c$  the velocity of light and  $h$  the Planck's constant.

Under the condition of thermodynamic equilibrium, the number of radiative recombination of electrons and holes in an interval  $d\nu$  is equal to that of the generation of electrons and holes by thermal radiation. At thermodynamic equilibrium, the rate of spontaneous photon emission  $R_{sp}(\nu)$  at a frequency  $\nu$  in an interval  $d\nu$  is given by

$$R_{sp}(\nu) d\nu = P_{abs}(\nu) \Phi(\nu) d\nu \quad (1.9)$$

where  $P_{abs}(\nu)$  is the probability of absorbing a photon of energy  $h\nu$  per unit time and  $\phi(\nu) d\nu$  is the radiation density of frequency  $\nu$  in an interval  $d\nu$ . This is obtained from Planck's radiation law as

$$\phi(\nu) d\nu = ((8\Pi\nu^3 n_r^3) / c^3) (1 / (\exp^{(h\nu / k_b T)} - 1)) d\nu \quad (1.10)$$

The absorption probability  $P_{abs}(\nu)$  is given as

$$P_{abs}(\nu) = \alpha(\nu) v_g \quad (1.11)$$

where  $v_g$  is the group velocity of photons expressed as

$$v_g = cd\nu / d(n\nu) \quad (1.12)$$

The mean lifetime of the photon is given by

$$\tau(\nu) = 1 / \alpha(\nu) v_g \quad (1.13)$$

and hence the absorption probability becomes

$$P_{abs}(\nu) = 1 / \tau(\nu) = \alpha(\nu) v_g = \alpha(\nu) (c / n) \quad (1.14)$$



Substituting equations (1.10) and (1.14) in equation (1.9) yields

$$R_{sp}(\nu)d\nu = (\alpha(\nu)8\pi\nu^3 n^2)/(c^2[\exp^{h\nu/k_B T} - 1])d\nu \quad (1.15)$$

which yields the desired relation between absorption and emission spectra. This equation (1.15) is called the van-Roosbroeck and Shockley relation. The total emission rate per unit volume is obtained by integrating equation (1.15) over all frequencies or energies as

$$R_{sp} = \{(8\pi^2(k_B T)^2)/c^2 h^4\} \int_0^\infty (\alpha(\nu)u^3/(e^u - 1))du \quad (1.16)$$

where  $u = h\nu/k_B T$ . This equation expresses the fundamental relation between absorption and emission spectra for any means of excitation. The formulation is valid for any transition between a higher energy and lower energy state.

As generation and recombination involve transition of carriers across the energy band gap, this must be different for direct and indirect band gap semiconductors.<sup>8</sup> In direct band gap semiconductors the VB maxima and CB minima occur at the zone center ( $\mathbf{k} = 0$ ) and an upward or downward transition of electron does not require a change in momentum or the involvement of a phonon. Thus, in direct band gap semiconductors, an electron raised to the CB by photon absorption remains in the CB for a very short duration of time and recombines with a VB hole to emit light of energy equal to the band gap. Thus the probability of radiative recombination is very high in direct band gap semiconductors.

In indirect band gap semiconductors the CB minima are not at  $\mathbf{k} = 0$ , because of which an upward absorption or a downward transition of carriers requires a change in momentum by either absorbing a phonon or emitting a phonon.<sup>9</sup> Here an electron in the CB minima at  $\mathbf{k} \neq 0$ , cannot recombine with a hole at  $\mathbf{k} = 0$  until a phonon with the right energy and momentum is available. In order for the right phonon collision to occur, the dwelling time of the electron in the CB increases. Most of the semiconductors have impurities and defects in the lattice that manifest themselves as traps and recombination centers. Thus most of the electrons and holes will recombine non-radiatively through such defect centers and the excess energy is dissipated into the lattice as heat. The competing non-radiative processes reduce the probability of radiative recombination in indirect band gap semiconductors, making them not suitable for realization of light sources such as light-emitting diodes and laser.

In a semiconductor at equilibrium (i.e., with no incident photons or injected electrons) the carrier densities can be calculated from an equilibrium Fermi level by using Fermi-Dirac or Boltzmann statistics.<sup>10</sup> When excess carriers are generated non-equilibrium conditions are generated and concept of a Fermi level is no longer valid. The non-equilibrium distribution function for electrons and holes can be defined as

$$f_n(\varepsilon) = 1/(1 + \exp\{\varepsilon - \varepsilon_{fn}\}/k_B T) \quad (1.17)$$

$$1 - f_p(\varepsilon) = 1/(1 + \exp\{\varepsilon_{fp} - \varepsilon\}/k_B T) \quad (1.18)$$

These distribution functions define  $\varepsilon_{fn}$  and  $\varepsilon_{fp}$ , the quasi-Fermi levels for electrons and holes respectively. When the excitation source creating excess carriers is removed,  $\varepsilon_{fn} = \varepsilon_{fp} = \varepsilon_f$ . The non-equilibrium carrier concentration can be written as

$$n = N_c \exp\{\{\varepsilon_{fn} - \varepsilon_c\}/k_B T\} \quad (1.19)$$

$$p = N_v \exp\{\{\varepsilon_v - \varepsilon_{fp}\}/k_B T\} \quad (1.20)$$

If we consider the case of an n-type semiconductor with an equilibrium electron density  $n_0$  uniformly irradiated with above band gap light, so as to produce  $\Delta n$  electron-hole pairs with a generation rate  $G$ , the electrons and holes are created and annihilated in pairs and depending upon  $G$ , a steady state excess density  $\Delta n = \Delta p$  is established. This equality is necessary for the maintenance of overall charge neutrality and when the excitation is removed the density of excess carriers returns to the equilibrium values  $n_0$  and  $p_0$ . The decay of the excess carriers follow an exponential law with respect to time  $\sim \exp(-t/\tau)$ , where  $\tau$  is defined as the 'lifetime of the excess carriers'. The lifetime is determined by a combination of extrinsic and intrinsic parameters and the performance characteristics of most opto-electronic devices depend upon it. Excess carriers decay by radiative or non-radiative recombination in which the excess energy is dissipated by photons and phonons. Radiative recombination is important for operation of luminescent devices. The total lifetime  $\tau$  of the excess carriers can be written as

$$1/\tau = 1/\tau_r + 1/\tau_{nr} \quad (1.21)$$

where  $\tau_r$  and  $\tau_{nr}$  are the radiative and non-radiative lifetimes, respectively. The internal quantum efficiency or radiative recombination efficiency is defined as

$$\eta_r = 1/(1 + \{\tau_r / \tau_{nr}\}) \quad (1.22)$$

To achieve high internal quantum efficiency, the ratio  $\tau_r / \tau_{nr}$  should be as small as possible or  $\tau_{nr}$  should be as large as possible. The value of  $\tau_{nr}$  is controlled by properties of defects, which produce levels in the band gap of the semiconductor. The excess energy of carriers recombining at these levels is dissipated by phonons. Under steady state conditions, the recombination rate must be equal to the generation rate i.e.

$$G = R \quad (1.23)$$

From which it follows that

$$\Delta n = G\tau_r \quad (1.24)$$

Thus it can be seen from relation (1.24) that the excess carrier concentration is determined by the radiative recombination lifetime  $\tau_r$ . PL which results from the radiative recombination of EHPs created by injection of photons can be divided into two major types in semiconductors namely intrinsic and extrinsic luminescence. The former is divided into three types: band-to-band luminescence, exciton luminescence and cross-luminescence. Extrinsic luminescence is divided into two: 1) Un-localized (DAP and iso-electronic traps) and 2) Localized types (allowed and forbidden transitions between ions) depending on whether excited carriers [electrons and holes] of the host lattice participate in luminescence process or whether the luminescence excitation and emission processes are confined to localized centers.

## ***1.2.2 Exciton photo-luminescence***

### ***1.2.2A Free excitons***

In very pure semiconductors, where the screening effect of free carriers is almost absent, electrons and holes formed by the absorption of a photon of near band gap energy pair up by Coulomb interaction. Each EHP is called an "exciton" because the electron orbits about the hole forming a Hydrogen-like atom and hence these are also named **free excitons**. The binding energy of the exciton  $\varepsilon_{ex}$  is calculated by analogy with the Bohr atom for an impurity center and is quantized. It is expressed as

$$\epsilon_{ex}^l = \{-m_r^* q^4 / (2\{4\pi\epsilon_r \epsilon_0 \hbar\}^2)\} (1/l^2); l = 1, 2, 3, \dots$$

$$= (-13.6/l^2)(m_r^*/m_0)(1/\epsilon_r)^2 \quad (1.25)$$

Here  $l$  is an integer and  $m_r^*$  is the reduced effective mass of the exciton given by

$$1/m_r^* = (1/m_e^*) + (1/m_h^*) \quad (1.26)$$

where  $m_e^*$  and  $m_h^*$  are the electron and hole effective masses respectively.

The exciton can wander through the crystal as the electron and hole are associated as a mobile pair. Because of their mobility they do not have a well defined potential in the semiconductor's energy diagram and hence are not spatially localized. Customarily the CB edge is used as a reference level and this edge is considered as the continuum state ( $l = \infty$ ). Such excitons are also known as *effective mass* or *Wannier excitons*.

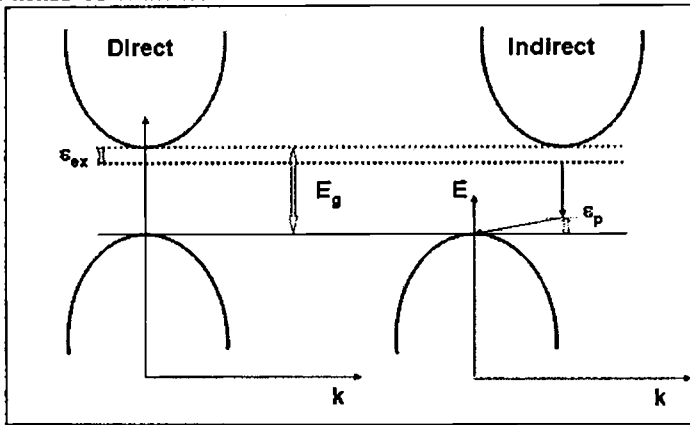


Fig. 1.5: Direct and Indirect exciton recombination.

When a free electron and free hole have the same momentum  $k$ , they move with different velocities:  $\hbar(dE_c/dk)$  for electron and  $\hbar(dE_v/dk)$  for the hole. Since the electron and hole have to move together in the crystal, their translation velocities must be identical. This places a restriction on the region in  $(E - k)$  space where excitons can be found, namely at “critical points”:

$$[dE/dk]_{electron} = [dE/dk]_{hole} \quad (1.27)$$

Since the effective mass of the hole is many orders smaller than that of the proton, the analogy to the Hydrogen atom has to be modified: the center of gravity of the exciton may be located many lattice spaces away from the hole. The moving exciton has a kinetic energy

$$K.E. = \hbar^2 k_{ex}^2 / 2(m_e^* + m_h^*) \quad (1.28)$$

The addition of kinetic energy means that exciton levels are slightly broadened into bands. The total energy of the exciton is hence given by

$$\varepsilon_{ex} = \{\hbar^2 k_{ex}^2 / 2(m_e^* + m_h^*)\} - \varepsilon_{ex}' \quad (1.29)$$

When the exciton dissociates it creates a free electron and a free hole. Recombination of the EHP results in emission of photons with energy

$$h\nu = E_g - \varepsilon_{ex} \quad (1.30)$$

where  $E_g$  is the band gap of the semiconductor and  $\varepsilon_{ex}$  is given by relation (1.29). Exciton luminescence peaks are very narrow in nature at very low temperatures. The high energy side of the exciton emission line is approximated by the Boltzmann factor. Hence as the temperature is raised their width increases and for  $k_B T > \varepsilon_{ex}$  the exciton dissociates and the luminescence emission merges with the band to band emission. Thus in very pure crystals emission lines corresponding to the ground state and higher-order may be seen. The intensity of higher order peaks decreases rapidly ( $\sim I^{-3}$ ) and is difficult to observe in the presence of other radiative processes.<sup>11</sup> In an indirect gap semiconductor, momentum conservation requires that a phonon be emitted to complete the transition. Then the energy of emitted photon is

$$h\nu = E_g - \varepsilon_{ex} - m\varepsilon_p \quad (1.31)$$

where  $\varepsilon_p$  is the energy of the phonon involved and  $m$  the number of optical phonons emitted per transition. The larger  $m$  is, lower is the transition probability and weaker the emission line. Although the transition with phonon emission is less probable than the direct recombination, the resulting photon has a greater chance of escape because it occurs at a lower photon energy than the direct recombination, i.e., in a region of the spectrum where the semiconductor is more transparent.

### 1.2.2B Bound excitons

In semiconductors with impurities- donors and/or acceptors, the free exciton couples with the impurity atoms to produce **bound excitons**. Here a free hole combines with a neutral donor to form a positively charged excitonic ion, and the electron bound to the donor travels in a wide orbit about the donor. The associated hole which moves in the electrostatic field of the fixed dipole also travels about the donor and for this reason this complex is called a bound

excitons. An electron associated with a neutral acceptor is also a bound exciton. Both of these types of bound excitons were first reported observed in Si.<sup>12</sup> Bound excitons produce sharp peaks at photon energies lower than that of free exciton. The line width of the bound exciton emission line is much smaller than that of the free exciton almost by a factor of 10. Often both free exciton and bound excitons emission are found from the same semiconductor, and are identified on the basis of its energy and line width.

The bound exciton is characterized by very large oscillator strengths, known as “giant oscillator strengths” so that the lifetime of the bound exciton is very short. The concentration of bound excitons decreases with increase in temperature because of which the intensity of the luminescence emission line also decreases. The temperature dependence of the emission intensity follows the relation:

$$L(T)/L(0) = 1/\{1 + CT^{3/2} \exp(-\varepsilon_i / k_B T)\} \quad (1.32)$$

where  $L(T)$  is the emission intensity at a temperature  $T$ ,  $L(0)$  is the emission intensity at absolute zero,  $C$  is a constant related to the capture cross-section of the defect and  $\varepsilon_i$  is the ionization energy for the bound exciton given by

$$\varepsilon_i = \varepsilon_{ex} + \varepsilon_b \quad (1.33)$$

where  $\varepsilon_b$  is the additional energy binding the free exciton to the defect center.

### 1.2.2C Excitonic molecules

Three or more particles combine to form ion-like or molecule like complexes.<sup>13</sup> An exciton molecule consists of two holes and two electrons.<sup>14, 15</sup> In this process as an EHP recombines, a photon is emitted with energy

$$h\nu = E_g - 2\varepsilon_{ex} - E_{x_1} - \varepsilon_{p_m} \quad (1.34)$$

where  $E_{x_1}$  is binding energy of two excitons and  $\varepsilon_{p_m}$  the energy of the a phonon of mode  $m$ . The remaining electron and hole of the quartet are either ejected into the conduction and valence bands and form a new exciton or remain as an exciton. The characteristic of an excitonic molecule emission line is that its intensity increases as the square of the intensity of the exciton line, proving that two excitons are needed to produce the molecular complex. If the exciton complex contains two electrons bound to one hole or two holes bound to one

electron, then its intensity would grow as the (3/2) power of the exciton emission line intensity.

Wannier excitons, created in high densities by high-intensity excitation, lead to rapid collision among them and can also lead to formation of excitonic molecules (or biexcitons). These are stable because of the attractive covalent interaction between two excitons, analogous to the formation of a hydrogen molecule. The energy of the excitonic molecule  $E_m$  is given by

$$E_m = 2h\nu - \varepsilon_m \quad (1.35)$$

where  $h\nu$  is the energy of the exciton, and  $\varepsilon_m$  is the binding energy of the molecule. The binding energy of the exciton complex  $\varepsilon_m$  should be within the limit  $0.055E_i < \varepsilon_m < 0.35E_i$ , where  $E_i$  is the binding energy of the impurity (Donor or acceptor). The lower limit corresponds to the removal of an electron from the Hydrogen like ion, while the upper limit corresponds to the dissociation of the hydrogen like molecule.<sup>16</sup> The luminescence of the excitonic molecule is the process in which a molecule emits a photon of energy  $h\nu - \varepsilon_m$ , leaving a single exciton.

The energies of an exciton and an exciton molecule as a function of  $k$  can be written as

$$h\nu_{ex}(k) = h\nu_{ex} + (\hbar^2 k^2 / 2M) \quad (1.36)$$

and

$$h\nu_m(k) = 2h\nu_{ex} - \varepsilon_m + (\hbar^2 k^2 / 4M) \quad (1.37)$$

where  $M$  is the effective mass of the excitonic molecule. Thus the photon energy of the M line is written as

$$h\nu_m = h\nu_m(k) - h\nu_{ex}(k) = h\nu_{ex} - \varepsilon_m - (\hbar^2 k^2 / 4M) \quad (1.38)$$

Since the third term in equation (1.38) has a negative sign, the low energy side of the M line (excitonic molecule emission line) spectral shapes is approximated by the Boltzmann factor contradictory to the case for the exciton line described in previous section. The high energy side of the M line-shape is broadened and is suggested to be due to the elastic collision between excitonic molecules and between the exciton molecule and a single exciton.

Exciton molecules can be formed directly by two-photon absorption with photon energy of  $h\nu - (\varepsilon_m / 2)$ . The probability of this two-photon absorption is high because of two positive effects: the first that the exciton state acts as an intermediate virtual state in the two-photon resonant condition and the second

that the transition from the exciton to the molecular state has giant oscillator strength.<sup>9</sup> The two-photon absorption line is very sharp and is hence useful for determination of the value of  $\epsilon_m$ .

### 1.2.3 Photo-luminescence due to band-to-band recombination

Excitons are formed easily only in purest materials and at low temperatures. A fraction of the excited electron-hole pairs remain as free carriers occupying band states at temperatures such that  $k_B T > \epsilon_{ex}$  and also in less pure or less perfect crystals.<sup>7</sup> When the temperature of the sample is high enough so that  $k_B T > \epsilon_g$  or if there are sufficient number of free carriers in the semiconductor which produce local fields to dissociate the exciton, then most photo-generated carriers exist as separate electrons and holes in the bands. The electrons recombine with the holes, conserving their momentum. Luminescence owing to the band-to-band transition, i.e. to the recombination of an electron in the CB with a hole in the VB can hence be observed in pure crystals at relatively high temperatures. This has been observed in Si, Ge<sup>6</sup> and some IIIb-VIb compounds like GaAs.<sup>6, 17</sup> Band to band luminescence is observed in only very pure materials. If there are impurity levels within the forbidden band gap, electrons and/or holes get trapped by these impurities. These carriers then recombine via the defect levels radiatively giving low energy luminescence emission different to band-to-band luminescence or non-radiatively emitting a large number of phonons.

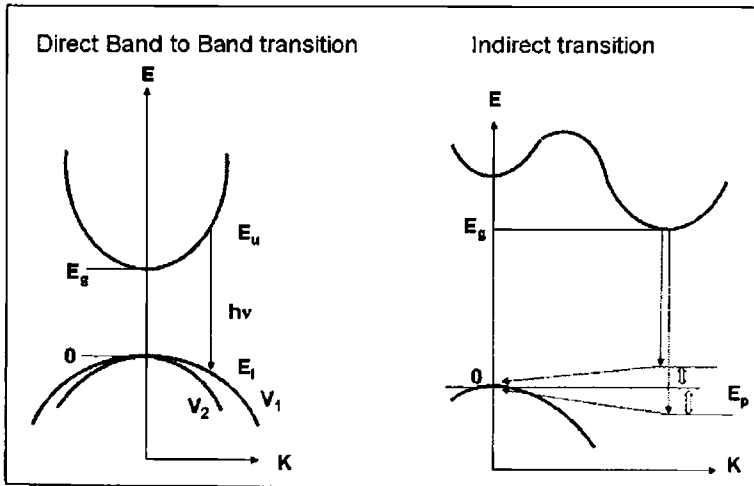


Fig. 1.6: Direct band-to-band radiative transition and radiative indirect transition.

The radiative recombination cross section  $\sigma$  is given by



$$\sigma = B / v \quad (1.39)$$

where  $B$  is a constant and  $v$  is the velocity of thermal motion of the electrons and holes and is obtained from  $(mv^2/2) = k_B T$ . Value of  $\sigma$  for direct transition type semiconductors such as GaAs and GaSb are  $(0.5-10) \times 10^{-17} \text{ cm}^2$ . Values of the capture cross section of impurities depend upon the nature of the impurities, i.e., if they are neutral, positively charged or negatively charged. The values are roughly given by the size of the atomic cross sections, i.e.  $10^{-15} \text{ cm}^2$ . Since this is nearly two orders larger than radiative recombination cross sections in direct transition type semiconductors this explains as to why band-to-band luminescence is seen only in very pure materials.

### 1.2.3A Direct transitions

In direct band gap semiconductors, momentum conserving recombination occur between electrons in the CB and holes in the VB. States having the same  $k$  value are connected by these transitions. The emission spectra can be mathematically represented as<sup>7</sup>

$$R(\nu) = A(\hbar\nu - E_g)^{1/2} \quad (1.40)$$

As the excitation intensity or the temperature is increased, states deeper in the band become filled, permitting emission at higher photon energies. Thus the recombination is characterized by a temperature dependent high energy tail, while the low energy edge is abruptly cut off at  $\hbar\nu = E_g$ . At low excitation intensity the full width at half maximum (FWHM) of the emission peak is approximately equal to  $0.7k_B T$ . The schematic for direct band-to-band luminescence is shown in Fig. 1.6. Band-to-band transition can also terminate on the light hole sub band. However since the transition probability is proportional to  $(m^*)^{3/2}$  for direct transitions, and since  $m_{h_2}^* < m_{h_1}^*$ , the transition probability to the light hole sub band is lower than a transition to the heavy hole states.

### 1.2.3B Indirect transitions

In indirect band gap semiconductors all the occupied upper states are connected to all of the unoccupied empty lower states. The transitions are mediated by an intermediate process of phonon emission which conserves momentum (Fig. 1.6). The emission of phonons by electrons which are in the high energy state is highly probable. Hence the optical transition assisted by phonon occurs at lower photon energy than the band gap energy. The minimum energy of the emitted photon in such transitions will be

$$h\nu_{\min} = E_g - E_p \quad (1.41)$$

In an indirect band gap material, as the excitation intensity increases, the quasi-fermi level moves deeper into the bands, causing the emission spectrum to comprise all the possible transitions between any pair of states separated by  $h\nu$ , regardless of the difference in crystal momentum between the initial and final states. Hence the emission spectrum can be described by

$$R(\nu) = A' (h\nu - E_g + E_p)^2 \quad (1.42)$$

where the transition probability coefficient  $A'$  is much smaller than that for the direct transition. The indirect transition rises much faster (quadratically) with the excess energy above a threshold for emission compared to the square-root dependence for direct transition as shown by relation (1.40).

### 1.2.3C Effect of doping

If a material is heavily doped, the Fermi level is somewhere inside the band (conduction band for n-type material, valence band for p-type material). In a p-type semiconductor, if we introduce some electrons in the CB, an emission spectrum with a lower energy threshold at  $E_g$  results and grows as  $(h\nu - E_g)^{1/2}$ .

Thus at 0 K the peak position will occur at

$$h\nu_{\text{peak}} = E_g + (1 + (m_e^*/m_h^*))\xi_n \quad (1.43)$$

where

$$\xi_n = (3\pi^2 n)^{2/3} (\hbar^2 / 2m_e^*) \quad (1.44)$$

The factor  $m_e^*/m_h^*$  expresses the restriction imposed by momentum conservation. If this restriction is relaxed by processes like electron-impurity scattering or electron-electron scattering, all the occupied states in the CB can make radiative transitions to empty states in the VB and the emission at 0 K are centered at

$$h\nu_{\text{peak}} = E_g + \xi_n + \xi_p \quad (1.45)$$

where

$$\xi_p = [3\pi^2 (p_0 + \Delta p)]^{2/3} (\hbar^2 / 2m_h^*) \quad (1.46)$$

and where  $p_0$  is the hole concentration due to doping before excitation and  $\Delta p$  the increase in hole concentration due to excitation. The spectral distribution is described by

$$R(\nu) = A(h\nu - \varepsilon_g)^2 \quad (1.47)$$

Since the emission spectrum is a convolution of all the upper and lower states that are connected by the same  $h\nu$ . Equations (1.43) and (1.47) hold true for indirect gap semiconductors also, where momentum conservation does not involve phonons.<sup>7</sup> The emission peak and high energy edge shift to higher energies as doping increases due to penetration of Fermi level into the band. The structures at lower photon energies arise due to transitions involving impurity bands and tail states.

### 1.2.3D Carrier interaction assisted emission<sup>18</sup>

It is possible, in semiconductors, to absorb photons of energy lower than the gap energy, the additional energy needed to satisfy energy conservation comes from simultaneously absorbed phonon. A photon of energy  $h\nu = E_g - \Delta E$  may not be absorbed (Fig. 1.7) because of the energy deficiency. But if the deficiency is small the photon can promote an electron from the valence band to a virtual state  $a$  where it receives the additional energy  $\Delta E$  and momentum  $\Delta k$  to complete the transition. The additional increment can be obtained from a phonon emitted by another hot electron in the conduction band.<sup>18</sup> The converse of this absorption process is the 'carrier interaction assisted emission'. The process can be illustrated as follows: an electron in the CB band makes a transition to a virtual state  $a$  at a potential  $\Delta E$  below the CB and excites an electron to a higher energy state inside the band causing the momentum to be changed. The first electron then completes the transition from the state  $a$  to the VB by emitting a photon of energy  $h\nu$ . In direct band gap semiconductors this process is difficult because an additional phonon may be needed as illustrated in Fig. 1.7, making the transition a three step process having a very low probability of occurrence.

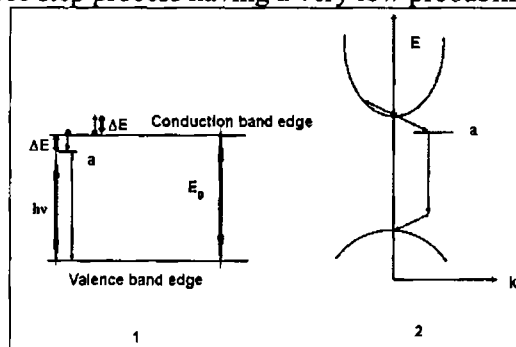


**Fig. 1.7:** (1) Emission of a photon with energy  $h\nu = E_g - \Delta E$  by heating another electron such that  $k_B T_e = \Delta E$  and (2) Three step recombination in direct band gap semiconductor.

In indirect band gap semiconductors, the recombination is a two step process. The interaction with the third carrier reduces the transition probability. The recombining electron heats up another electron in the conduction band and thus changes its energy by  $\Delta E$  and its momentum by  $\Delta k$ . To complete the transition to the valence band, the recombining electron emits a photon  $h\nu$  and a phonon  $E_p$ . Thus it leads to either the acoustic or optical phonon selected from the phonon dispersion curves. Hence the photon energy emitted is

$$h\nu = E_g - E_p - \Delta E \tag{1.48}$$

With the increase in temperature of the carriers a low energy tail is found which grows with the excitation intensity. But along with increase in injected carrier density, a shift of this emission edge occurs towards lower energy side due to shrinkage of energy gap arising from the Coulomb interaction between the carriers.

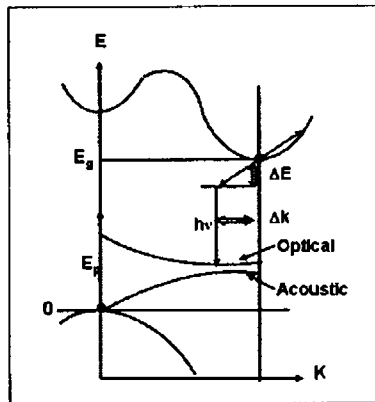


Fig. 1.8: Illustration of the indirect emission due to carrier interaction and phonons.

#### 1. 2.4 Photo-luminescence due to transitions between a band and impurity level

The transition between a neutral donor and the CB or between the VB and the neutral acceptor can occur by absorption of low energy photons. The photon energy for this must be at least equal to the ionization energy  $E_i$  of the impurity. This energy corresponds to the far Infrared region of the spectrum. The transition between the valence band and an ionized donor (the donor must be empty to allow this transition) or between an ionized acceptor and the conduction band occur at photon energy greater than the difference between the band gap energy  $E_g$  and ionization energy  $E_i$ . The transition between a band and an

impurity level involves the whole band of levels and hence this transition manifests itself as a shoulder in the optical absorption edge at a threshold lower than the energy gap by an amount  $E_i$ . In low energy transitions between the impurity level and the nearest band edge there is no problem with momentum conservation because the band edge is the excited state of the impurity. Phonon emission or absorption may be needed to complete the high energy transition from the VB to the ionized donor or from the ionized acceptor to the CB if the transitions are indirect or other scattering processes are absent. The luminescence arising from the reverse of the transitions described above are illustrated in Fig. 1.9.

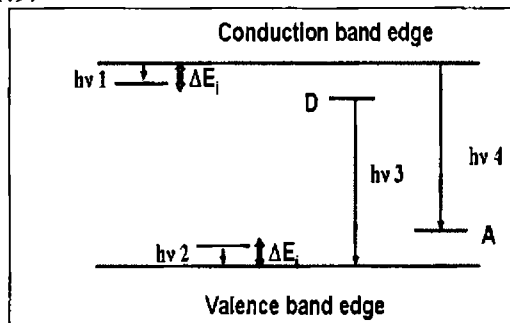


Fig. 1.9: Radiative transitions between a band and impurity level.

#### 1.2.4A Shallow transitions

Shallow transitions to neutralize ionized donors or acceptors usually cause emissions in the far Infrared (IR) region. The possibilities of such transitions were calculated based on the probabilities of transition by photon emission.<sup>19</sup> It was proved that phonon emission process is much more probable. The recombination process, considering a donor as an example, can be described as follows: at first, an electron gets trapped in the excited state of the donor; then the electron cascades to the lower lying states, emitting a phonon at each step. Thus the excess energy is dissipated as heat in the lattice.

#### 1.2.4B Deep transitions

This recombination process includes electron transition from neutral donor level to the valence band ( $D^0, h$ ) and/or transition from the conduction band to the neutral acceptor level ( $e, A^0$ ). Recombination through the transition from donor level to the valence band will emit photons of energy

$$E_{PLD} = E_g - E_D \quad (1.49)$$

where  $E_{PLD}$  is the PL peak energy of the  $(D^0, h)$  emission and  $E_D$  is the ionization energy of the donor impurity. The PL emission peak energy related to transitions between the conduction band and acceptor level is described by

$$E_{PLA} = E_g - E_A + (1/2)k_B T_e \quad (1.50)$$

where  $E_{PLA}$  is the PL peak energy of  $(e, A^0)$  emission,  $E_A$  is the ionization energy of acceptor impurities and  $T_e$  is the effective temperature of electrons in the conduction band. This effective temperature can be obtained from the high-energy side of the exponential tail of the emission band. The binding energies of various acceptor impurities can also be determined by analyzing the PL emission spectra, using equation (1.50). As the temperature increases, the  $(e, A^0)$  transition becomes more intense because of the thermal ionization of shallow donor states. The  $(e, A^0)$  emission exhibits a shift in the PL peak position towards the higher energy side, with an increase in excitation power and temperature due to band filling.<sup>20</sup> The shift in energy due to increasing temperature can be offset by the band gap-narrowing, with the increase of temperature. The line shape of  $(e, A^0)$  transition is given by

$$I(h\nu) = CE_{PLE} (E_{PLE} - E_g)^{1/2} \exp(-(E_{PLE} - E_g - E_A)/k_B T_e) \quad (1.51)$$

where  $C$  is approximately a constant. The FWHM of a transition of  $(e, A^0)$  kind is theoretically  $1.8k_B T$ .

These radiative transitions between impurity levels and band edges are limited to semiconductors with relatively low concentration of impurities. When the impurity concentration is large enough to form an impurity band, which merges with the nearest intrinsic band, the identification of the process becomes ambiguous. If there are electrons in the CB and in the donor states and holes in the VB and acceptor states, quantum mechanical calculations have showed that the band to band transition would be 4 times more probable than the transition between the impurity and the band.<sup>21</sup> If the radiative transition occurred from the CB to the acceptor states, the emission peak would shift to higher energy side, as the excitation is increased, driving the quasi-Fermi level for electrons deeper into the conduction band. As the quasi-Fermi level for holes moves deeper into the VB under increased excitation, the donor to valence band transition would produce an emission spectrum with a threshold at  $E_g - E_D$  and emission peak would shift to higher energy. Ultimately under increased excitation, this leads to a shifting band to band emission.<sup>9</sup>

### *1.2.4C Transitions to deep levels*

Deep levels in the forbidden energy gap of semiconductors act as carrier recombination or trapping centers that adversely affect device performance.<sup>6</sup> Radiative transitions between these states and the band edge cause emission at  $h\nu = E_g - E_i$ . Native defects in the lattice such as vacancies, interstitials or substitutional impurities or impurity-vacancy complexes, can give rise to deep levels in semiconductors. The excess energy of the carriers recombining at these levels is carried away by single or multiple phonons because of which, these are also called “killer centers”. A correlation has been found to exist between the depth of these centers and the Frank-Condon shift.<sup>22</sup> As the ionization energy of the impurity increases, the orbit of the electrons and holes becomes more localized. The increased localization of the carrier, trapped in the potential of the impurity, leads to a stronger interaction with the surrounding ions and therefore to a larger lattice relaxation. Thus the Frank-Condon shift of deep levels increases with increase in ionization energy. In the configuration diagram a larger Frank-Condon shift implies a stronger phonon interaction.

### *1.2.5 Luminescence due to donor-acceptor pair recombination*

#### *1.2.5A Spectral features*

Donors and acceptors can act as stationary molecules embedded in the host crystal by forming pairs. When the neutral donor and the neutral acceptor come close, the electrons of the donors become increasingly shared by the acceptor, making the donor and acceptor ionized. In the fully ionized state, the binding energy is zero and the corresponding level lies at the band edge. This lowering in binding energy is simply due to the Coulomb interaction between the electrons and holes at the donor and acceptor levels. Thus it becomes clear that the emission energy of the DAP luminescence depends on the spatial separation between the donor and acceptor in a pair as shown in Fig. 1.10. In the initial state from which the emission starts, an electron is located at the donor level with a hole located at the acceptor level. The energy of this state is given by

$$E_i = E_g - (E_D + E_A) \quad (1.52)$$

This is true if the origin of the energy scale is taken to be the position of the acceptor level. As the distance between the pair decreases, finally no electron is left with the donor level so that an effective charge of +1 remains with the

donor, while in the acceptor an effective charge of  $-1$  is left. As a result, the Coulomb attractive force works between the donor and acceptor, so that the energy of the final state is given by

$$E_f = -(e^2 / \epsilon r) \quad (1.53)$$

where  $\epsilon$  is the dielectric constant for the static field and  $r$  the intra-pair separation then the emission energy as a function of  $r$  (Fig. 1.10(b)) can be thus expressed as

$$E_n(r_n) = E_i - E_f \quad (1.54)$$

If we consider only the Coulomb and van der Waals interaction and designate the distance between the donor and acceptor of the  $n^{\text{th}}$  pair as  $r_n$ , the energy of the pair can be written as<sup>23</sup>

$$E_n(r_n) = E_g - (E_D + E_A) + (e^2 / \epsilon r_n) - (e^2 / \epsilon)(a / r_n)^6 \quad (1.55)$$

where  $a$  is the constant of van der Waals interaction. Since the quantities  $E_n(r_n)$  and  $r_n$  assume discrete values, the absorption and luminescence spectra of donor-acceptor pairs (DAP) in principle should consist of individual lines. The distance between the lines decreases as number of pairs  $n$  increases. The line structure of absorption and luminescence of DAPs are observed only on the short wavelength side of corresponding bands.<sup>26</sup> This is opposite to the exciton absorption and luminescence properties, whose fine structure appears on the long wavelength side of the band (section 1.2). Shallow DAP luminescence is characterized by the Poisson distribution. Here one pair is regarded as one localized center to which the 'Configuration-Coordinate (CC) model' is applied. The strongest peak is an assembly of numerous unresolved zero-phonon lines of DAPs, with different intra-pair separations. The low energy edge of the emission spectrum extends over a large range and consists of a series of phonon-emission replicas of the main band. The high energy side of the zero phonon peak contains numerous sharp lines, whose energy separation are well represented by equation (1.55).

From equation (1.55) it can be found that the peak position of the DAP luminescence will shift towards lower energies with increasing  $r_n$ . For distant pairs, the Coulomb and van der Waals interaction are very small and the lowest possible photon energy is emitted. Between impurities separated by distances more than the Bohr radius, the transitions are assisted by tunneling process. A transition between nearer pairs is more probable than between distant pairs;



hence the emission intensity increases as pair separation decreases. But simultaneously the number of possible pairing decreases as  $r$  decreases. Thus the emission intensity goes through a maximum as the separation  $r$  is varied. Because of this dependence on  $r$ , discrete line structures are obtained only for pair separation in the range 10 to 40 Å. At larger values of  $r$  ( $r > 40$  Å), the emission lines overlap forming a broad spectrum.

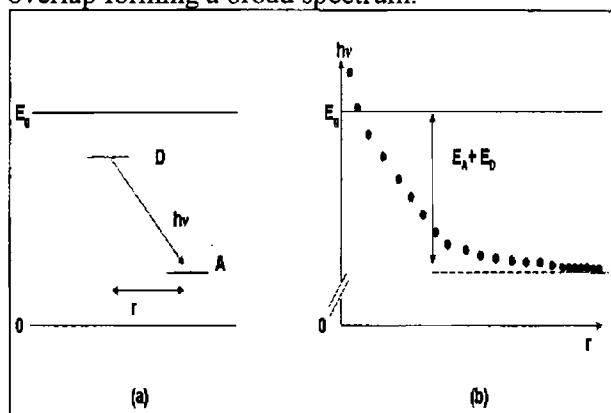


Fig. 1.10: (a) Donor-acceptor pair transition and (b) effect of Coulomb interaction on emission energy.

Different pairings occur depending upon the sites occupied by the impurities. If the donor and acceptor occupy similar substitutional sites, type I pairing occurs. If the donor and acceptor occupy opposite sites, type II pairing occurs. The number of possible pairings  $N$ , and the Coulomb interaction term can be calculated as a function of  $r$  for each type. The Coulomb interaction term for near pairs drives the donor and acceptor levels out of the energy gap. Recombination between donor and acceptor states located inside the intrinsic bands would compete with band-to-band transitions; since bands have very high density the donor-acceptor transitions would have to be extremely efficient to contribute to an emission line. The transition probability between donors and acceptors, neglecting the Coulomb interaction and the tunneling factor, has been calculated.<sup>28</sup> Assuming the donor and acceptors to be forming Gaussian band states with a characteristic distribution width  $E_0$ , the transition probability turned out to be proportional to  $1/E_0$ . For small  $E_0$  the donor-to-acceptor coupling is stronger than the band to band or band to impurity transitions. The transition probability of the DAP luminescence also depends on  $r$ . The probability is considered to be proportional to the square of the overlap of the donor and acceptor wave functions. Spread of the wave function of a donor is generally

much larger than that of the acceptor. The transition probability as a function of  $r$ , using the Bohr radius  $r_B$  of the donor, is given as

$$W(r) = W_0 \exp(-2r/r_B) \quad (1.56)$$

### 1.2.5B Emission energy dependence on time

The transition probability is expressed as the reciprocal of the pair lifetime. From equation (1.55), it is clear that, with decrease in the intra-pair separation  $r$ , the energy position shifts to higher energy and thus the resultant transition probability becomes larger i.e. the luminescence decay becomes more rapid. Hence the recombination at low photon energies will be slower than the high energy transition i.e., the more distant pairs live longer. The peak of a narrow emission band composed of many unresolved pair lines would shift towards lower energies during decay. The high-energy edge of the DAP luminescence spectrum decays much faster than the low-energy edge.

### 1.2.5C Emission energy dependence on excitation intensity

The peak position of the DAP radiative transition is independent of the position of the quasi-Fermi levels. For donor states close to the CB edge, the density of states overlaps with the tail of the CB. When the transition probability between the donors and acceptors is greater than the CB to acceptor transition probability, the dominant recombination will be from the donors to acceptors. At excitation rates sufficient to observe an emission, the quasi-Fermi level for electrons is above the donor states. The electrons will leak out of the CB through the donors and the quasi-Fermi level for electrons will not affect the emission spectrum. The variation of PL intensity  $I$  with excitation intensity can be fitted using the relation<sup>29</sup>

$$I = I_0 P^\gamma \quad (1.57)$$

where  $I_0$  and  $\gamma$  are constants and  $P$  is the excitation intensity per unit area. For excitation with photons of energy exceeding the band gap energy  $E_g$ , the coefficient  $\gamma$  is generally  $1 < \gamma < 2$  for the free- and bound exciton emission, and  $\lambda \leq 1$  for free-to-bound and DAP recombination. The dependence of PL peak energy  $\hbar\omega_p$  on the excitation intensity  $I$  for DAP emission can be fitted with the relation<sup>30</sup>

$$I = \{D(\hbar\omega_p - \hbar\omega_\infty)^3 \exp[-2E_b / (\hbar\omega_p - \hbar\omega_\infty)]\} / [E_b - 2(\hbar\omega_p - \hbar\omega_\infty)] \quad (1.58)$$

where  $D$  is a constant,

$$\hbar\omega_\infty = E_g - E_A - E_D \quad (1.59)$$

and

$$E_b = e^2 / \epsilon r_b = \hbar\omega_b - \hbar\omega_\infty \quad (1.60)$$

Equation (1.58) holds well in case of compensated semiconductors. The coefficient  $E_b - 2(\hbar\omega_p - \hbar\omega_\infty)$  depends on the compensation and becomes very small in non-compensated samples in which case no shift in emission peak will be observed.

### *1.2.5D Luminescence due to iso-electronic traps*<sup>9</sup>

In a semiconductor an atom of an element belonging to the same column of the periodic table as that of the constituent atom of that semiconductor can replace the constituent atom and attracts an electron or hole because of the difference in electron affinity. Such an atom is called an “iso-electronic trap”. If the electron (hole) affinity of the introduced atom is larger (smaller) than that of the constituent atom, that atom becomes an electron (hole) trap. If an electron (hole) is trapped then a hole (electron) is attracted through Coulomb interaction, resulting in formation of a bound exciton which can produce luminescence. Luminescence from iso-electronic traps is important in indirect-gap materials. Iso-electronic traps attract electrons or holes by short range force which is resultant of the difference in electron affinities. The wave function of the trapped electrons or holes is thus extremely localized in real space; but is widely spread out in  $k$ -space.

### *1.2.6 Intra-band luminescence*

At the zone center, the VB structure of most semiconductors consists of the light hole (LH), the heavy hole (HH) band and the split-off (SO) band. These three bands are separated by spin-orbit interaction. In a p- type semiconductor, the valence band is filled with holes and the occupancy of the different bands depends on the degree of doping and position of the Fermi level. Absorption of photons of right energy can lead to transition from LH to HH, SO to HH and SO to LH bands, depending on the temperature and doping of the sample. These transitions are seldom observed in n- type semiconductors. Radiative intra valence band transitions have been observed in Ge.<sup>31</sup> These transitions are also

called “emission by hot light holes” because an electric field is used to produce a non-equilibrium distribution between the light and heavy holes.<sup>4</sup> Radiative transition from the HH sub band to the LH sub band have been observed whose energy lies in the far Infrared region of the spectrum. The Peak position of this is in the region of the  $E(k)$  – space where the two sub bands become parallel.

### 1.3 Photo-conductivity

If the energy of the incident photon is greater than the energy difference between the lowest point of CB and highest point of VB, then each photon absorbed in the material has a high probability of producing an EHP i.e., a photon is absorbed by ionizing an electron originally in the VB. In this case, the electron in the CB and the hole in the VB contribute to the electrical conductivity of the material under an applied bias. The increase in the electrical conductivity of a material caused by irradiation is termed as **Photo-conductivity**.<sup>2</sup> The first paper on PC dates back to 1873, in which William Smith reported the change in resistance of Selenium under illumination. This was even before the knowledge of existence of bands in solids. Gudden and Pohl were the major contributors in this field. PC enjoys a pivotal position in the field of optical studies of semiconductors and is the basis for the branch termed “Opto-electronics”. It reaches both into semiconductors and insulators by giving the details of the internal electronic process in these materials. PC involves several basic processes like the generation, transportation and recombination of charge carriers. The phenomenon of PC vary tremendously with material, temperature, doping level, presence of donors, acceptors and traps and their concentration, capture cross section, mobility of charge carriers, types of electrical contacts and potential barriers created near them and unintentionally created defect states in the growth process. In the field of phosphors, the measurement of PC helps to identify the steady state Fermi level, the key parameter, needed to understand their complex recombination kinetics.

#### 1.3.1 Theoretical background<sup>2</sup>

In a semiconductor with free electrons and/or free holes the electrical conductivity in dark is given by

$$\sigma_0 = q(n_0\mu_{n0} + p_0\mu_{p0}) \quad (1.61)$$

where  $n_0, p_0$  are the equilibrium concentrations of electrons and holes respectively and  $\mu_{n0}, \mu_{p0}$  are the electron and hole mobilities respectively. When the semiconductor is illuminated with light, its conductivity is increased by the charge carriers generated due to illumination called PC, represented as  $\Delta\sigma$ ,

$$\sigma_{ill} = \sigma_0 + \Delta\sigma \quad (1.62)$$

Thus the conductivity under illumination can be given as

$$\sigma_0 + \Delta\sigma = (n_0 + \Delta n)q(\mu_{n0} + \Delta\mu_n) + (p_0 + \Delta p)q(\mu_{p0} + \Delta\mu_p) \quad (1.63)$$

which indicates that photo-excitation can change both the carrier density ( $\Delta n / \Delta p$ ) and the carrier mobility ( $\mu$ ). Then considering the case of one-carrier transport for simplicity

$$\Delta\sigma = q\mu_{n0}\Delta n + (n_0 + \Delta n)q\Delta\mu_n \quad (1.64)$$

Since carriers are being generated due to photo-excitation, it is generally true that

$$\Delta n = G\tau_n \quad (1.65)$$

where  $G$  is the photo-excitation rate ( $\text{m}^{-3}\text{s}^{-1}$ ) and  $\tau_n$  is the electron lifetime, so that

$$\Delta\sigma = q\mu_{n0}G\tau_n + nq\Delta\mu_n \quad (1.66)$$

This is the general expression for PC for a material with one-type of charge carrier. Photo-conductivity  $\Delta\sigma$  can be approximated to

$$\Delta\sigma \approx qG(\mu_{n0}\tau_n + \mu_{p0}\tau_p) \quad (1.67)$$

so that the “figure of merit” for a single-carrier photoconductor can be defined as

$$\Delta\sigma / qG = \mu\tau \quad (1.68)$$

Thus the lifetime-mobility product is a measure of the photoconductor’s sensitivity to photo-excitation.

### ***1.3.2 Measure of photosensitivity***

Two major definitions of ‘photosensitivity’ are found in literature. One of these simply describes photosensitivity by the magnitude of  $\Delta\sigma$ , where as the other is more device-oriented. That definition is in terms of the ratio  $\Delta\sigma / \sigma_0$ .

Some of the scientific definitions of parameters related to photosensitivity are the following

### Specific Sensitivity:

'Specific Sensitivity' is a measure of the material's actual sensitivity in terms of the  $\mu\tau$  product. It is cited for large signal PC ( $\Delta\sigma \gg \sigma_0$ ) in insulators as

$$S^* = \Delta I d^2 / \phi P \text{ m}^2 \Omega^{-1} \text{W}^{-1} \quad (1.69)$$

where  $\Delta I = \Delta\sigma A \phi / d$ ,  $d$  is distance between the two electrodes across which a bias  $\phi$  V is applied and  $A$  is the area of illumination.  $P$ , the input light power is given as  $P = Gh\nu dA$ . Using these two definitions eq. (1.69) can be rewritten as

$$S^* = (q / h\nu) \tau \mu \quad (1.70)$$

### Detectivity:

"Detectivity" is applied to small signal AC -  $\Delta\sigma$  situations where  $\Delta\sigma \leq \sigma_0$ . Most commonly this definition finds application in the case of an IR detector, where signal is to be detected in the presence of background noise

$$D^* = (A\Delta\nu)^{1/2} NEP \quad (1.71)$$

where  $A$  is the area of the detector,  $\Delta\nu$  is the bandwidth used for measurement of noise and  $NEP$  represents the radiation power needed to produce a signal equal to the noise.

### Photo-conductivity Gain:

The gain of a photo-detector can be defined as the number of charges collected in the external circuit for each photon absorbed. If  $F$  is the total number of photons absorbed, so that the photo-excitation rate  $G = F / Ad$  then the gain  $G^*$  can be expressed as

$$G^* = (\Delta I / q) / F = \tau \mu \phi / d^2 \quad (1.72)$$

where  $A$  is area of the detector and  $d$  the distance between the electrodes. This can be rewritten in the form  $G^* = \tau / (d^2 / \mu \phi)$  which represents the ratio of the carrier lifetime to the carrier transit time. If both electrons and holes contribute to PC, then

$$G^* = (\tau_n \mu_n + \tau_p \mu_p) \phi / d^2 = (h\nu / q)(\phi / d^2) S^* \quad (1.73)$$

PC gain can be physically pictured as following: photo-excitation creates free electrons and holes. If the lifetime of a carrier is greater than its transit time, it will make several effective transits through the material between the contacts, provided contacts are ohmic and are able to replenish carriers drawn off at the opposite contact.

### 1.3.3 Model of a photoconductor<sup>2,32</sup>

In the simplest model of a photoconductor, it is assumed that EHPs are produced uniformly throughout the volume of the material by irradiation with an external light source. Recombination of the EHP is postulated to occur by direct recombination. The rate of change of the electron concentration  $n$  is given by<sup>32</sup>

$$dn / dt = L - Anp = L - An^2 \quad (\text{by using } n = p) \quad (1.74)$$

where  $L$  is the number of photons absorbed per unit volume per unit time,  $A$  is the recombination coefficient;  $Anp$  gives a recombination rate proportional to the product of hole and electron concentrations. A similar expression for hole concentration can be written as

$$dp / dt = L - Anp \quad (1.75)$$

In the steady state, the concentrations are constants and we have the relation

$$n_0 = (L / A)^{1/2} \quad (1.76)$$

The associated PC can be written as

$$\sigma = n_0 e \mu = (L / A)^{1/2} e \mu \quad (1.77)$$

This relation predicts that the photocurrent will vary as the light intensity to the power,  $1/2$ . The exponent value is usually between 0.5 and 1.0. If the illumination is cut off suddenly, the decay of carriers is described by

$$dn / dt = -An^2 \quad (1.78)$$

which has the solution

$$n = n_0 / (1 + Atn_0) \quad (1.79)$$

where  $n_0$  is the concentration at time  $t = 0$  when the illumination is switched off. The carrier concentration would drop to  $(1/2)n_0$  in the time

$$t_0 = 1 / An_0 = n_0 / L \quad (1.80)$$

The above elementary theory predicts that, for a given illumination level  $L$ , the response time is proportional to the photoconductivity (Eq.1.80). Sensitive photoconductors would have longer response times. Sensitivity or Gain factor  $[G]$  can be defined as the ratio of the number of carriers crossing the specimen to the number of photons absorbed in the specimen. If the thickness of the specimen is  $d$  and the cross section area is unity, then the voltage  $V$  produces a particle current  $I = J$ , the current density, as the cross sectional area is unity.

$$J = I = \sigma E = ne\mu E \quad (1.81)$$

Or  $I/e = n_0\mu V/d$ , where we take the steady state value  $n = n_0$ . Thus

$$J = V\mu L d / (d^2 (AL)^{1/2}) \quad (1.82)$$

The gain can hence be expressed as

$$G = (V\mu) / (d^2 (AL)^{1/2}) \quad (1.83)$$

The transit time between the electrodes for a carrier is given by  $T_d = d / (V\mu / d)$ . If we take the lifetime of the electron equal to the response time (Eq.1.80),  $t_0 = T_0$  we have

$$G = T_0 / T_d \quad (1.84)$$

If  $T_0$  is taken as the observed response time, it is found that the gain thus calculated is very much larger than that observed experimentally. A study of the above phenomenon of direct recombination in terms of extrinsic materials results in modification of Eq. (1.74).<sup>33</sup> If  $n_0$  and  $p_0$  are the equilibrium concentrations of both electrons and holes at  $t = 0$ , the excess carrier concentration can be given as  $\delta n_0$  and  $\delta p_0$  and the instantaneous excess carrier concentrations can be given as  $\delta n(t)$  and  $\delta p(t)$  for any time  $t$ . Hence we have

$$d\delta n / dt = A_e n_0^2 - A_e (n_0 + \delta n)(p_0 + \delta p) \quad (1.85)$$

We assume that the excess carrier concentrations  $\delta n_0$ ,  $\delta p_0$  are both equal. If we consider the material to be  $p$ -type  $p_0 \gg n_0$  and neglect higher order terms of minority carriers the equation becomes

$$d\delta n / dt = -A_e p_0 \delta n(t) \quad (1.86)$$

whose solution is of the form

$$\delta n(t) = \delta n_0 \exp(-A_e p_0 t) \quad (1.87)$$



Excess electrons in a p- type semiconductor thus recombine with decay constant  $\tau = 1 / A_e p_0$ . This can also be called as the ‘minority carrier lifetime’ as it depends on electrons which are minority carriers in p- type materials or as the recombination lifetime. Similar is the case of excess holes in an n- type semiconductor, where the decay time becomes  $\tau = 1 / A_e n_0$ .

### 1.3.4 Effect of traps

If we consider a crystal with  $N$  electron trap levels per unit volume, the effect of traps modifies the Eq.(1.74) as <sup>34</sup>

$$dn / dt = L - An^2 - AnN + Bn, \quad (1.88)$$

where  $n$  is the electron concentration in the conduction band. The last term represents the rate of thermal evaporation of trapped electrons back to the conduction band. Here we consider this to be negligible as the temperature is sufficiently low. In the steady state

$$n_0(n_0 + N) = L / A \quad (1.89)$$

There are two limiting cases to be discussed. It is difficult to grow crystals with trap concentrations  $N$  less than  $10^{14} \text{ cm}^{-3}$  and secondly at low illumination level, the concentration of carriers  $n_0$  is very much less than this. If  $n_0 \ll N$  Eq. (1.89) changes to

$$n_0 = L / AN \quad (1.90)$$

so that photocurrent is now proportional to the illumination  $L$ . At high levels of illumination if  $n_0 \gg N$  the equation (1.90) becomes

$$n_0 = (L / A)^{1/2} \quad (1.91)$$

as found in Eq. (1.76) in the absence of traps. The three major effects of traps in a semiconductor can be summarized as (1) decrease in speed of response, (2) decrease in drift mobility, and (3) a decrease in the photosensitivity.

#### 1.3.4A Decrease in speed of response

The speed of response of a material is inversely proportional to the time constant associated with the increase of PC to its steady state value after turning on the photo-excitation (the rise time) and the time constant associated with the decrease of PC to its dark value after turning off the photo-excitation (the decay time). In the absence of traps in the material the free carrier lifetime in the

material determines the value of these time constants. However in the presence of traps, additional time dependent processes are involved with trap filling [during the rise] and trap emptying [during the decay]. This leads to an increase in the observed decay time of the photocurrent making it longer than the carrier lifetime. So the 'measured' lifetime, which we take as time for photocurrent to decay to  $1/e$  of initial value, cannot be less than the actual lifetime (without trap effects), but can be much larger. The speed of response is inversely proportional to the experimentally measured lifetime, so that, the speed of response decreases, as lifetime increases. Thus, the presence of traps leads to a decrease in the speed of response.<sup>2</sup> If the intensity of illumination is so high or the density of excess carriers is larger than density of traps, then the observed decay time will be equal to the carrier lifetime (Eq. 1.91).

### 1.3.4B Decrease in mobility

The drift mobility is determined by the time taken by the carriers at one point to travel to a distant point under an electric field. If there are no traps, the injected carriers are free and the drift mobility is same as the conductivity mobility  $\mu$ . If traps are present, the carriers spent some amount of time in the traps which increases their time of travel and hence a decrease in mobility.<sup>2</sup> We modify drift mobility as  $\mu_d = \gamma\mu$ , where  $\gamma$  is the average time spent by the carriers in the traps divided by the average time to escape from a trap and  $\mu$  the mobility in the absence of traps. Now the drift mobility can be written as<sup>2</sup>

$$\mu_d = [\nu \exp(-E_t / KT) / \nu S_t N_t] \mu \quad (1.92)$$

where  $\nu$  is the attempt-to-escape-frequency,  $\nu$  the thermal velocity,  $E_t$  is the energy difference between the lowest part of conduction band and the trap level,  $S_t$  is the capture cross section of the trap for electrons and  $N_t$ , the density of traps.

### 1.3.4C Decrease in photosensitivity

From Eq. (1.65) we can write<sup>2</sup>

$$G = n / \tau = n S_t \nu N_r \quad (1.93)$$

where  $N_r$  is the density of available empty recombination centers with cross section  $S_r$ . For every free electron there is a corresponding hole either in the valence band,  $p$  or in  $N_r$ , so that  $n = N_r + p$  and it is reasonable to assume that  $N_r \gg p$ . Hence from Eq. (1.93), the lifetime without traps can be written as

$$\tau_1 = 1 / n\nu S_t \quad (1.94)$$

In the presence of traps  $N_r = n + N_t \cong N_t$ , where  $N_t$  is the total density of trapped electrons and the lifetime is given by

$$\tau_2 = 1 / N_t \nu S_t \quad (1.95)$$

It is evident, by comparing the two equations, that the lifetime is reduced by the factor  $n / N_t$ . Thus in the presence of traps the photosensitivity of the materials gets reduced.

#### 1.3.4D Temperature dependence of photo-conductivity

In many photoconductors, the photocurrent is essentially independent of temperature. For an exponential trap distribution, the expected variation of photocurrent is rapid and photocurrent increases with temperature. The change in photocurrent with temperature can be used to predict the activation energy of levels involved in the PC. This is done with the help of the Arrhenius relation<sup>2</sup>

$$I_{ph}(T) = I_0 / (1 + c \exp(-E_a / KT)) \quad (1.96)$$

where  $I_{ph}(T)$  is the photocurrent at a temperature  $T$ ,  $I_0$  is the photocurrent at temperature 0 K,  $c$  is a constant related to the capture cross section of traps/defect levels and  $E_a$  is the activation energy of the respective traps/defect levels. The plot obtained for variation of photocurrent with temperature can be fitted with the above equation and the activation energy of the trap involved can be predicted.

#### 1.3.4E Effect of excitation intensity on photo-conductivity

Variation of the photocurrent with intensity gives the information regarding the recombination process existing in the material. In general, the photocurrent – excitation intensity relation is given by

$$I_{ph} \propto I_{ex}^\gamma \quad (1.97)$$

where  $I_{ph}$  is generated photocurrent,  $I_{ex}$  is the excitation intensity and  $\gamma$  a dimensionless constant. Evidently, the induced photocurrent depends on the value of  $\gamma$ . When  $\gamma = 0.5$  the emission is due to bimolecular recombination where the photocurrent varies as the square root of incident light intensity.<sup>2</sup> A model has also been developed stating that when  $\gamma = 0.5$ , the bimolecular recombination is at the surface and when  $\gamma = 1.0$  it represents monomolecular reaction in the bulk. In the model that does not deal with traps,  $\gamma = 1$  for low light intensities and

$\bar{\eta} = 0.5$  for high light intensities where surface recombination becomes important.

### 1.3.5 Fermi level in photoconductor<sup>2</sup>

The thermal equilibrium Fermi level is useful because knowledge of its location permits the description of the occupancy of all other levels in the semiconductor. Even under illumination, the concept of a Fermi level can be usefully retained. A solution of equations considering the trapping and recombination processes and optical excitation helps in determining the position of Fermi levels in dark and under excitation. The position of Fermi level in the dark and under excitation is shown in the Fig. 1.11. The steady state Fermi level describes the occupancy of those levels that are still in effective thermal equilibrium with the bands i.e. with those imperfections whose occupancy is determined by thermal exchange with the bands rather than by recombination. An alternate way of expressing this is to say that the steady state Fermi level continues to describe the occupancy of traps during illumination, but not of recombination centers.

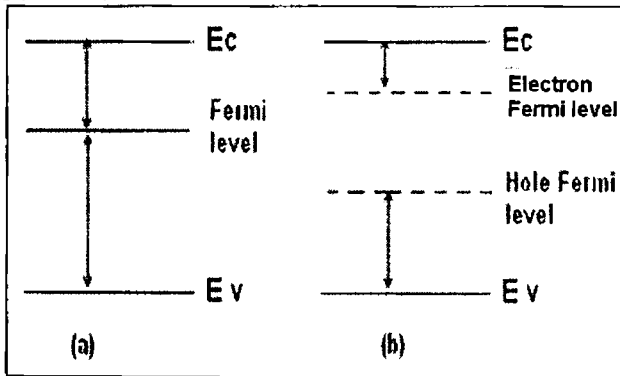


**Fig. 1.11:** Energy band diagram showing (a) the thermal equilibrium Fermi level and (b) the steady state electron and hole Fermi levels under optical excitation.

The position of the electron Fermi level from the CB is given by the equation<sup>32</sup>

$$E_f = KT \ln(N_c e \mu / \sigma) \quad (1.98)$$

where  $N_c$  the effective density of states in the CB,  $T$  the absolute temperature and  $\mu$  the mobility. Similar definition can be made for the 'hole Fermi level' too. It is also considered that the defect levels which are lying above the electron Fermi level or below the hole Fermi level can act as a trapping center and the

levels in between the Fermi levels can act as a recombination center. So a recombination center can act as a trap at another condition of light level and temperature as the Fermi level varies with light level and temperature. As evident from equation (1.98) as the temperature increases the electron Fermi level shifts down and the hole Fermi level moves up.

#### 1.4 PL in analysis of semiconductors<sup>35</sup>

PL measurement is a standard technique to observe defects and impurities in semiconductors. The study of luminescence processes can, not only show the content as well as the behavior of defects and impurities in semiconductors, but also improve the operational characteristics of semiconductor devices based on radiative recombination. The PL spectrum and its dependence on the irradiation intensity and device temperature can deliver important information for device characterization. In particular, PL spectra and their energy/intensity dependence can be used

- to determine the band gap energy and/or the wavelength of maximum gain
- to determine the composition of ternary or quaternary layers
- to determine impurity levels
- to investigate recombination mechanisms

If multiple excitation wavelengths are available, this property of PL can be used to distinguish surface and bulk contributions. Garcia-Garcia et al. have used such an approach to study the surface layer of chemically etched CdTe.<sup>36</sup> When the surface structure is poor, the PL spectrum changes with increasing excitation energy; the strength of defect-related lines increases relative to bulk features. Correlation of these changes with penetration depth indicates the location of near-surface defects. Furthermore, the authors found that the PL spectrum of a high-quality surface is independent of excitation energy. In an extension of this technique, Wang et al. used the widely divergent penetration of one and two photon absorption processes to distinguish surface and bulk effects.<sup>37</sup> In contrast to relatively slow recombination with two-photon excitation, a fast recombination mechanism dominated the one-photon excitation experiment. Their results indicated the presence of rapid recombination sites near the surface of the semiconductor, where the single-photon excitation is absorbed.

9 Dangling bonds on a semiconductor surface or interface give rise to electronic states within the band gap. These mid-gap states fill up to the Fermi level with electrons that originate in the bulk of the material. The accumulation of charge at the surface creates an electric field – a depletion region – that leads to bending of the valence and conduction band edges. According to a simple dead-layer model, EHPs that are generated in this region are swept apart by the electric field, prohibiting radiative recombination.<sup>38</sup> The phenomenon is described quantitatively by a depletion thickness that characterizes this “dead layer”. Although the dead-layer picture of carrier kinetics at the surface of a semiconductor overlooks the complicated role of surface states in the recombination process, it is useful when PL quenching has an electrostatic origin. Ryswyk and Ellis studied the effect of I<sub>2</sub> on n-GaAs using this model.<sup>39</sup> They used PL depth profiling with multiple excitation wavelengths to determine the depletion thickness in the I<sub>2</sub>-treated sample. Uosaki et al. have used a similar experimental approach to characterize p- GaAs/electrolyte interfaces.<sup>40</sup> Results were analyzed within the context of the more sophisticated model proposed by Mettler, which accounts for changes in charge separation and surface-state recombination.<sup>41</sup>

The intensity of the incident light controls a critical property of the PL experiment: the density of photo-excited electrons and holes. When the incident excitation intensity is low the generated carrier density is low, and the PL measurements are dominated by discrete defect and impurity sites at the interfaces and within the bulk of the material. Recombination at these energetically favored sites is frequently referred to as Shockley–Read–Hall (SRH) recombination. The SRH rate is proportional to the dominant carrier density  $n$ . In systems with high interface-to-volume ratio and active layers that are thin relative to the carrier diffusion length, interface effects dominate SRH recombination. In planar structures, the interface-to-volume dependence of SRH recombination can be separated from actual interface phenomena via the interface recombination velocity  $S$ . The interface recombination rate is defined as  $R_s = (S/d)*n$ , where  $d$  is the thickness of the optically active layer. When two interfaces are present, as in a double hetero-structure, the two interface contributions are combined:  $S$  is replaced by  $S_1$  and  $S_2$  (or  $2S$  for equivalent interfaces). Because  $S$  is independent of carrier density and layer thickness, it can be used to compare interface recombination in a variety of materials.  $S$  depends strongly on the nature of the interface. For example,  $S$  is of the order of  $10^7$  cm s<sup>-1</sup> at the interface of GaAs and air, whereas high-quality GaAs/GaInP

interfaces can have  $S < 10 \text{ cm s}^{-1}$ .<sup>42</sup> This reduction of the interface recombination velocity at the edge of a material is called surface passivation. Because the performance of many opto-electronic devices is limited by interface recombination, interface passivation has been studied extensively. Passivation techniques include epitaxial growth of lattice-matched semiconductor alloys and a variety of chemical surface treatments. Qualitative evaluation of these techniques is straightforward: an increase in the PL signal indicates a decrease in non-radiative interface recombination. Quantitative information on  $S$  requires more sophisticated techniques, many of which involve investigations of the excitation intensity dependence of PL.

Komiya et al. measured the excitation intensity dependent PL signal from a series of InGaAsP/InP double hetero structures.<sup>43</sup> Although the PL signal was usually linear with excitation power, some samples showed super-linear dependence under intermediate excitation, indicating a transition between non-radiative and radiative recombination regimes. The lack of such a transition in the other samples suggested that radiative recombination dominated at all excitation levels, which gave an upper limit for  $S$ . In a very different approach, Mullenborn and Haegel studied single AlGaAs/GaAs and GaInP/GaAs hetero-structures where the buried GaAs layer was excited indirectly via either carrier diffusion or recycling (i.e. re-absorption and emission) of photons.<sup>44</sup> The excitation intensity dependence of PL from both layers was used to distinguish between the two mechanisms for carrier generation in the buried layer. Saitoh et al. have argued that the simple picture of an excitation-independent surface recombination velocity is not sufficient to describe the excitation dependence of the PL signal.<sup>45</sup> In particular, when the excitation is intermediate between the SRH and radiative recombination dominated regimes, the quasi-Fermi levels for electrons and holes split away from the low-excitation pinned position and move towards their respective band edges. The quasi-Fermi levels determine the energy range of surface-states that contribute to recombination. Thus, the PL efficiency in this transition region is very sensitive to the density and energy distribution of surface-states. The authors developed an elaborate model of carrier behavior near the surface of the semiconductor that accounts for carrier transport, surface-state occupation, band bending, and recombination. Analysis of the excitation intensity dependent PL signal in the context of this model is referred to as Photo-luminescence Surface-State Spectroscopy (PLS).<sup>38</sup>

The shape of the radiative efficiency curve in the SRH and radiative recombination transition region, depends on the distribution of surface-states that

participate in recombination. If the distribution consists of a discrete set of states with similar energetic positions within the gap, complete saturation of the SRH recombination process will lead to a PL efficiency slope of unity. Efficiency curves with slopes less than unity indicate that the surface-state distribution is continuous. More over, an increasing number of surface-states are participating in recombination as the quasi-Fermi levels move through the band gap. Hence, variation in the slope of the efficiency curve with increasing excitation can be used to map the surface-state distribution within the gap. Since its development in 1991, PLS has been applied to a wide number of semiconductor systems.<sup>38</sup> Although some of these studies have uncovered surface-states with discrete energies, most have revealed that the surface-state distribution is U-shaped, with increasing density near the band edges.<sup>45</sup>

Excitation intensity dependent PL can also be used to study the properties of QWs. Ding et al. measured the excitation intensity  $I_{ex}$  dependence of the integrated PL signal from asymmetrically coupled QWs.<sup>46</sup> They noted that the PL intensity varied as  $I_{ex}^2$  when recombination is dominated by nearly-saturated-interface traps. But it was proportional to  $I_{ex}$  when radiative recombination was more prominent. They used the transition intensity to estimate the non-radiative decay time, which suggested that traps were located at the interface of the coupling barrier and the larger well. Excitation-dependent saturation of PL can also be used to determine the relative density of different radiative states. When splitting is observed in the PL from QWs, the lower energy peak often saturates with increasing excitation because of state filling. In this case, the saturation intensity can be used to estimate the size of interface islands in the QW, where the low energy PL is believed to originate.<sup>47</sup>

The third application of excitation intensity dependent PL is in the evaluation of interface band alignment. Vignaud et al. observed a dramatic excitation-dependent blue shift in the PL from InAlAs/InP hetero-structures. They attributed this blue shift to spatially indirect type II transitions across the interface.<sup>48</sup> They explained the blue shift as follows: when the conduction band minimum and valence band maximum occur on opposite sides of a semiconductor interface, electrons and holes are trapped in different regions of the hetero-structure. Because the electrons and holes are attracted to each other, narrow QWs are formed adjacent to the interface. As the excitation is increased, carriers accumulate in these wells, increasing the confinement energy of the wells and the dipole energy across the interface. Both of these mechanisms lead to substantial blue shifts in the PL. It is interesting to note that type II transitions,



which occur across the interface itself, are especially sensitive to interface quality.

Surfaces and interfaces usually contain a high concentration of impurity and defect states. As the physical termination of the sample, the surface represents a drastic interruption of the material itself. Dangling bonds often provide numerous mid-gap states that facilitate rapid non-radiative recombination. They also act as getters for ambient impurities. Dangling bonds can be accommodated by a variety of surface treatments and lattice-matching semiconductor epilayers. Even so, impurities accumulate on surfaces before treatment and during growth interruptions. In addition, interface defects due to slight lattice mismatch at semiconductor hetero-junctions are inevitable. In systems where the interfaces and bulk material contribute to the PL, the two components can be distinguished via depth profiling. Thewalt et al. combined PL with Spreading Resistance Analysis (SRA) depth profiling to identify the type and location of several impurities in ultrahigh-purity epitaxial silicon.<sup>49</sup> Destructive depth profiling can be accomplished by step-etching and measuring the PL vs. etch depth. Akimoto et al. used this approach to connect specific PL peaks with vacancy complexes at a GaAs/AlGaAs interface.<sup>50</sup> Some good examples of PL spectral analysis in the characterization of bare surfaces are in the field of semiconductor etching. Reactive Ion Etching (RIE), where etching is accomplished by bombarding the surface with energetic reactive ions, is an important procedure in the fabrication of opto-electronic devices with sub-micron features. However, RIE can produce various types of defects in the near-surface region. For optimal device performance, the damage and contamination caused by RIE should be minimized. PL analysis is very useful in identifying and controlling RIE-induced defects. Henry et al. used PL to study the effects of various plasmas on exposed surfaces of phosphorus- and boron doped Silicon.<sup>51</sup>

Broad and deep PL emission is a common characteristic of damaged semiconductors. Foad et al. investigated changes in the PL spectrum of ZnTe/GaAs epitaxial layers, after RIE and subsequent annealing.<sup>52</sup> RIE reduces the near-band edge emission by a factor of 100 and is accompanied by the appearance of new features, well below the gap. One of the low-energy peaks coincides with a specific defect found in bulk ZnTe, but the peak is much broader than the one observed previously. Upon annealing, near-band edge PL recovers by one order of magnitude and the deep emission shows more structures, revealing that the very broad, deep emission seen prior to annealing was actually composed of several phonon involved transitions (transitions

assisted by one or more phonons). The annealing results suggest that the strain around RIE induced defects is reduced.

Deep emission has also been attributed to dislocation networks at the interface of lattice-mismatched hetero-structures. The effects of strain and dislocations can be separated in InGaAs/GaAs hetero-structures, where accommodation of lattice mismatch depends on the InGaAs layer thickness. Joyce et al. observed broad, deep PL in the InGaAs/GaAs system and measured the spectrum as a function of InGaAs thickness.<sup>53</sup> They found that the intensity of the deep emission increased rapidly above the critical thickness, suggesting that interface dislocations were responsible for the broad, sub-band gap PL.

As with surface damage, relative changes in surface state and band edge emission can be used to evaluate surface passivation. Xu et al. used PL to study the properties of CuSe coatings on CdSe nanocrystals.<sup>54</sup> The uncoated CdSe nanocrystals produced broad, sub-band gap PL, which they attributed to recombination at deep surface traps. With increasing CuSe fraction on the CdSe cores, they observed a monotonic decrease in this emission accompanied by steadily increasing band edge PL. Normally, materials with larger band gaps are required for surface passivation so that carriers see potential barriers at the interface, shielding them from the surface. Because CuSe has a smaller band gap than CdSe, surface passivation with this material is unusual. The authors suggest that the CuSe coating is very thin so that the CuSe gap is enhanced by quantum confinement.

Spectral analysis of sub-band gap emission is useful for characterizing interfaces. The peak position of the band edge PL itself provides important information on atomic inter-diffusion and interface alloying. The band gap of a semiconductor alloy depends directly on alloy composition. When hetero-junctions are not abrupt, unintentional alloy layers are formed at the interface. Depending on composition, such layers can have band gaps larger, smaller, or intermediate between the adjoining materials. Guimaraes et al. observed an anomalous emission band, below the GaAs and GaInP gaps in GaInP/GaAs hetero-structures.<sup>55</sup> They postulated that this was due to recombination in GaInPAs intermediate layers, and confirmed their hypothesis by observing an enhancement of the band with an As-rich growth interruption at the interface.

The intensity of the PL signal has received the maximum attention as it can be utilized in the analysis of interfaces. This interest is due to the fact that, although several important mechanisms affect the PL response, it is generally found that large PL signals generally occur as a result of good interface

properties. A useful review of the dominant mechanism and the relationship between them has been provided by Chang et al.<sup>56</sup> In particular, they discuss the roles of surface recombination velocity  $S$  and band bending at the surface as seen through the PL measurement. Because surface recombination is usually non-radiative, and band bending can lead to the formation of a depletion region or “dead layer” [where PL is effectively quenched], both the phenomena tend to reduce the PL intensity. It is difficult to distinguish between the two effects and usually a supplementary measurement of the surface potential is required. All other parameters remaining constant, the surface recombination velocity is proportional to the density of surface states. However, changes in the surface-state density can affect the accumulation of charge at the surface, thereby altering the depletion thickness. Conversely, if the space-charge region is reduced by an increase in the density of surface states, the two mechanisms will have opposite effects on the PL signal and tend to cancel each other out.

In-situ PL has been used to assess InP surfaces during various cleaning, etching steps, oxidation, ambient gas flow, plasma exposure, and heating.<sup>56, 57</sup> In some cases, laser-induced interactions were found to alter etch rates, surface morphology, and surface contamination.<sup>57</sup> The results are explained by the availability of photo-excited electrons and holes that catalyze chemical reactions. In-situ PL has also been used to probe the passivation of GaAs with hetero-epitaxially deposited AlGaAs monolayer.<sup>58</sup> Timoshenko et al. extended the in-situ PL technique to evaluate electrochemical treatments of indirect semiconductor surfaces, where pulsed excitation is required to obtain a sufficient PL signal.<sup>59</sup>

PL intensity is an indicator of interface quality; measurement of the PL signal vs. position provides information on the spatial uniformity of interface properties. The non-destructive and environment-insensitive features of PL make this application particularly useful in the evaluation of substrate surfaces, where detection of electrically active features may help to control problems in epitaxial devices. Such features might be overlooked in mechanical investigations of surface morphology. Although the spatial resolution in a PL scanning application is ultimately dictated by surface area and scan time, the diffraction limit of approximately 1  $\mu\text{m}$  can be achieved in the best experimental arrangements. These high-resolution schemes must address carrier diffusion, which can smear images on a much larger scale. Spatially resolved PL measurements are usually accomplished by scanning the optical excitation spot relative to the sample surface and detecting the PL signal in the far field. One of the first

Demonstrations of this approach was made by Krawczyk et al. in an investigation of InP surface treatments.<sup>60</sup> By coupling the excitation into one end of an optical fiber and scanning the other end relative to a focusing objective, they achieved resolution of the order of a few microns. They observed wide variation in the PL signal on a microscopic scale.

Although spatially resolved PL usually focuses on the band edge or integrated PL signal, spectral selectivity can be incorporated to map the distribution of particular surface-states. Tajima used this approach to plot the deep-level distribution in the near-surface region of GaAs and Si wafers.<sup>61</sup> As these states tend to saturate at high excitation, he emphasized the importance of using a low laser power and stabilizing the system mechanically to accommodate long dwell times. He also pointed out that the surface finish must be controlled carefully to avoid surface-treatment-related phenomena like those discussed above. The spatial dependence of the PL spectrum itself can be used to evaluate uniformity of alloy composition, epilayer thickness, and a variety of other material properties that affect PL spectra. The PL spectrum has been recorded as a function of position, to look for signs of dislocations or residual stress in laterally overgrown InP on InP-coated Si substrates.<sup>62</sup> Dislocations are expected to reduce the PL signal while stress tends to shift and broaden PL peaks. Hence, the spatially resolved InP/Si PL was compared with that of lattice-matched InP layers grown homo-epitaxially on InP substrates. The measured PL peak was as strong and narrow as that of the homo-epitaxial InP with little shift in peak wavelength, suggesting that the overgrown layer was free from dislocation and stress. In addition, the PL spectrum was independent of position, indicating good uniformity in layer quality.

Fong et al. used confocal PL to study a GaAs/AlGaAs QW grown on a grooved substrate.<sup>63</sup> The improved spatial resolution permitted them to profile abrupt fluctuations (on a scale of 1  $\mu\text{m}$ ) in alloy composition and QW thickness. In the confocal measurement, if the detection aperture is translated laterally in the image plane, the corresponding detection spot can be maneuvered relative to the excitation spot. This technique can be used to monitor the diffusion process itself. Hubner et al. measured the diffusion length along semiconductor quantum wire structures.<sup>64</sup> A variation in carrier transport with wire width is explained by changes in side-wall recombination due to different surface-to-volume ratios.

A more popular technique, known as 'Near-Field Scanning Optical Microscopy' (NSOM) utilizes the tip of an extruded optical fiber to excite and/or collect the PL emission. NSOM probes are made of silica fibers designed for UV

transmission, by pulling and subsequent coating with Al to make 100 nm optical aperture. Tip height regulation is achieved by electrical shear-force detection.<sup>65</sup> The sample is excited through the tip with the 325 nm line of a He–Cd laser. The emitted light is collected on the other side of the sample with a high numerical aperture microscope objective. The microscopic optical property associated with the defect distribution of InGaN alloys, using NSOM has been very well-established.<sup>66-69</sup> Excitons in narrow quantum wells and wires tend to be localized by width fluctuations. This picture was put forth relatively early on the basis of observed inhomogeneous and homogeneous PL line widths.<sup>70</sup> This picture was affirmed using NSOM, where optical spectroscopy of individual excitons was carried out.<sup>71-77</sup> Based on these PL experiments, it is now clear that narrow quantum wells and wires are usually better described as an inhomogeneous distribution of zero-dimensional (0D) quantum dots.

In the characterization of discrete low-energy states, quantitative analysis of the decrease in PL intensity with temperature helps to measure the depth of the trap. Plotting the log of the PL intensity vs. the reciprocal of the temperature, the slope yields the activation energy for exciting carriers out of the traps. These graphs, often referred to as Arrhenius plots, have been used to study interface alloy formation in ZnSe/CdSe QWs.<sup>78</sup> Temperature is also an important parameter in carrier dynamics. At the lowest temperature, excitons dominate radiative transitions and thermal energy in this regime leads to difficulties in momentum conservation. Because photons have small momentum, only low-momentum excitons can directly recombine. Rising temperatures confound recombination by increasing the fraction of excitons with excessive momentum. Beyond this regime, the excitons themselves begin to dissociate and the oscillator strength of free carriers is usually much smaller than that for excitons. In this case, recombining carriers must have equal and opposite momentum, a condition that decreases in likelihood as the average energy increases. In contrast, non-radiative recombination processes tend to accelerate with increasing temperature. In particular, non-radiative interface recombination usually involves thermally activated multi-phonon events.<sup>79</sup>

Single photon above-gap excitation takes place very close to the surface, whereas two-photon excitation penetrates deep into the bulk. In the former experiments, the transient PL indicates short carrier lifetimes that diminish with increasing temperature, as expected for non-radiative surface recombination. In contrast, relatively long lifetimes are observed under two-photon excitation and the lifetime is extended at higher temperatures, indicating that radiative

transitions dominate in the bulk. A good example of this behavior is the single and two-photon excitation studies of ZnSe conducted by Wang et al.<sup>36</sup>

Polarization is another important parameter in optical measurements. In PL experiments, the emission polarization depends on the orientation of the dipole oscillators. Ordinarily, all orientations of electron-hole pair recombination events are equally probable, and hence the PL is not polarized. However, a variation in PL intensity with electric field orientation is sometimes observed. The maxima and minima in the polarization-angle-dependent PL signal usually occur for electric fields aligned with crystallographic axes. Polarization anisotropy in PL can be attributed to bond asymmetries, alloy composition modulation, and strain. Vignaud et al. observed large polarization anisotropy in the PL from InAlAs/InP hetero-structures.<sup>48</sup> They found that the polarization angle yielding the maximum PL signal depended on the specific interface structure. The polarization anisotropy was tentatively attributed to local interface bond asymmetry. Another system that has displayed marked PL polarization anisotropy is ZnCdSe/ZnSe QWs, grown on GaAs(110) surfaces.<sup>80</sup> The ratio of maximum to minimum polarized PL signals can be calculated using Luttinger parameters, which describe the valence band dispersion in the semiconductor. Assuming that the Luttinger parameters of ZnCdSe are similar to those of ZnSe, the calculated ratio is much smaller than that found experimentally. The enhanced polarization anisotropy in this system is attributed to compressive strain in the well layer. This interpretation was consistent with the observation of a very narrow PL line width in this sample.

### 1.5 PC in analysis of semiconductors

PC is really a complex field since it involves several basic processes such as generation, recombination and transport of charge carriers. In order to understand these, one requires knowledge of other parameters that are not easy to control as these vary tremendously with the material, temperature, doping level, presence of donors, acceptors and traps, their concentration, capture cross-section, mobility of the charge carriers, type of electrical contacts, potential barriers created near them and unintentionally introduced defect states in the growth process. Because of the presence of these parameters and complex relationships between them, PC technique alone is not enough and other complementary techniques such as Hall-effect and photo-Hall effect, optical

absorption, reflection and emission data are necessarily needed to interpret the results.

After the very first report on PC in bars of Se, rapid inroads were made in this branch of science.<sup>81</sup> The next significant publications came from Bube, in which many of the typical photoconducting properties of CdSe and CdS crystals were explained in terms of the presence and location of particular set of energy levels, probably associated with the characteristic crystal defects.<sup>32, 82, 83</sup> Super-linear PC [a phenomenon where the photocurrent increases according to a power of the excitation intensity greater than unity] was observed in CdSe.<sup>84</sup> The movement of Fermi level through the region of forbidden gap occupied by a class of levels located within the same range was identified to be the cause of the super-linear PC.<sup>85</sup> Other major contribution came from Moss who studied the basis of PC in PbS, PbTe and PbSe and their application in highly sensitive Infrared (IR) detectors.<sup>86</sup> His major conclusion was that potential barriers are not theoretically necessary to achieve very high sensitivities. Ge and Si, which were widely being used in transistors and diodes, were little probed for PC. Their intrinsic response extending throughout the entire visible region and even into the near IR, could be made very effective into the far IR portion of the spectrum also upon doping, as reported by Morton et al.<sup>87</sup> IR quenching and a slow S-shaped growth of photocurrent in CdS and CdSe were explained based on the shift of Fermi level across a defect band lying 0.8-0.6 eV below the conduction band in CdS and 0.6-0.3 eV below the CB in CdSe.<sup>32</sup>

Characteristic parameters of minority carriers in semiconductors [mainly the recombination constants and mobility of minority carriers] were worked by Ravich.<sup>88</sup> Conclusive results on electron and hole capture rate in Ni doped Ge using Photomagnetolectric (PME) and PC methods were reported.<sup>89</sup> The role of traps on the PME and PC were theoretically modeled by Zitter.<sup>90</sup> His important conclusion was that when carriers recombine through traps the excess concentrations of mobile electrons and holes were not characterized by a single lifetime  $\tau$ . Ryvkin et al. carried out transient PC studies to investigate the kinetics of impurity PC as a method to determine parameters of local levels.<sup>91</sup> A theoretical model of impurity centers, distributed below the conduction band, was proposed in their report. Recombination and trapping kinetics from the application point of view to analyze transient PC decay measurements in semiconductors was reviewed by Streetman.<sup>92</sup> The role of minority carrier trapping in transient measurement was discussed along with the effect of recombination in the trapping center. Methods for the calculation of trap density,

capture cross-section and level position from the transient measurements at a temperature were proposed.<sup>93, 94</sup>

Fourier transform of the relaxation curves obtained from the PC process was used to detect the presence of the delayed component and its parameter, uniquely in single crystals of CdTe.<sup>95</sup> Time of flight (TOF) type of transient PC measurements in studying the nature of charge transport in a-Si:H were reported in large volumes.<sup>96-99</sup> Interrupted transit time (ITT) TOF was successfully used in identifying two species of a trap and extracting the hole trapping and release times in a-Se layers.<sup>100</sup> Monte-carlo methods were used to study PC transients in GaAs.<sup>101</sup> Their results demonstrated that an appropriately designed experiment can be used to observe sub-pico second carrier transport transients.

PC in GaAs-GaAlAs super lattices, grown by molecular-beam-epitaxy, showed series of peaks of photon energies corresponding to transition between quantum states in the valence and conduction bands. They observed that the photocurrent exhibited negative differential conductance when the potential energy difference between two adjacent wells of the super lattice exceeded the band width of the quantum states.<sup>102</sup> High photoconductive gain in  $\text{Ge}_x\text{Si}_{1-x}/\text{Si}$  strained super lattice detectors grown by MBE was demonstrated and the gain mechanism was interpreted in terms of preferential hole trapping in the  $\text{Ge}_x\text{Si}_{1-x}$  wells.<sup>101</sup> TOF techniques were applied to study transport of electrons in the GaAs/AlGaAs hetero-structures.<sup>103</sup> By applying a constant background illumination, they were able to distinguish between lateral transport processes and effects of perpendicular transport processes across the GaAs/AlGaAs interface. It was shown that the initial part of the PC signal was due to lateral transport only. The in-plane PC response of quaternary InGaAsP/InP super lattice was studied by Helgesen et al.<sup>104</sup> They observed two transitions between the confined hole (electron) ground state in the well and the electron (hole) continuum. The transition energies gave direct determination of the band offset, both in the CB and in the VB. Temperature dependence of current due to photo-excited carriers in p-i-n single quantum well optical modulators was carried out to ascertain the transport processes.<sup>105</sup> Their model described temperature and field dependence of thermal emission, tunneling, mobility and the recombination rate.

Rakhshani measured the planar PC as a function of the incident photon energy at different temperatures for CdS.<sup>106</sup> From the fit of experimental results to the existing models, various opto-electronic parameters, including those related to the temperature dependence of band gap, the Urbach tail and the donor



concentration, were evaluated. In addition to the existing models, the PC model was extended to account for the effect of incident light in lowering the grain-boundary potential barrier. This allowed the measurement of both the grain-boundary potential barrier and the energy of the dominant defect level at grain boundaries.

The density of states map in the band gap of a-Si:H was determined by the measurement of the photo-transport properties of its majority and minority carriers.<sup>107</sup> Their comparison of the observed temperature dependence of the photo-transport properties of this material with model simulations suggested that, while the conduction-band tail has an exponential distribution of states, the valence band tail states have a Gaussian-like distribution. They suggested that this distribution is associated with the route through which the transport and photo-transport take place. Hence we could conclude that both the recombination and transport in undoped single-phase  $\mu$ -Si:H take place in the disordered layer that wraps the crystallites.

The local photo conductance in polycrystalline CdS films using Conductance Atomic Force Microscopy (CAFM) under illumination was studied. This revealed that PC along the grain boundaries was excited at photon energies significantly smaller than the CdS band gap,  $E_g$ , whereas photo-transport through the grains is detected only above  $E_g$ . In addition, they observed a rather strong persistent PC effect at both conduction channels.<sup>108</sup> Balberg et al., applied CAFM to measure the local current routes in ensembles of CdSe nanocrystallites of diameters in the range of 8–12 nm, and found that the electrical transport takes place through the crystallites themselves rather than along their grain boundaries.<sup>109</sup> Single grain boundaries in CuGaSe<sub>2</sub> were grown epitaxially by Siebentritt et al.<sup>110</sup> Their Hall measurements indicated a barrier of 30–40 meV to majority carrier transport. However, local surface potential measurements show the absence of space charge around the grain boundary; i.e., they were neutral.

Using near-field optical beam induced current, spatially resolved photocurrent in polycrystalline CdTe/CdS solar cells were observed and it was found that an increased photocurrent collection at grain boundaries (relative to the intra-grain volume) occurred. This observation supported previously reported hypothesis that grain boundaries present a hole-barrier, thereby assisting in charge separation at the grain boundaries in these devices. The results offer compelling evidence of the role of grain boundaries in explaining the surprisingly high performance of these highly defected devices.<sup>111</sup> Local probe

study in undoped hydrogenated microcrystalline Silicon [ $\mu\text{c-Si:H}$ ] clearly indicated that the dominant transport route in this material was in the disordered tissue that encapsulated the crystallites columns.<sup>112</sup> This conclusion seems to explain the fundamentals of the transport phenomena observed in this system and provides a general approach for the evaluation of electrical transport in other semiconductor composites.

## 1.6 Conclusions

PC complements PL and hence finds immense application in this new era of opto-electronics. The opto-electronics industry that drives investigations on layered structures, surfaces, interfaces their quality and performance is ultimately concerned with the optical and electronic properties. PL spectroscopy though an optical tool provides electrical characterization. Although a number of experimental techniques can provide detailed mechanical information about the samples they typically require more sophisticated excitation or detection schemes. PL signal is characterized by three essential features: energy, intensity, and polarization. Because PL is the result of optical transitions between electronic states, the PL spectrum gives precise information on the energy levels available in the material. The intensity of the PL signal depends on the rate of radiative and non-radiative events, which in turn, depends on the density of non-radiative interface states. PL measurements are not sensitive to the pressure in the sample chamber and can be performed at virtually any temperature. These features make PL an excellent in-situ probe of surface or interface modification. Variation of the PL signal with external parameters such as temperature and applied bias can provide additional information on the nature of interfaces. Temperature-dependent thermal activation of electronic states can be used to estimate their depth below the intrinsic bands. An applied bias shifts the bands at the surface, permitting evaluation of the zero-bias band bending. Applications of PL analysis range from simple spatial scans of epitaxial wafers to exhaustive investigations of excitation-intensity-dependent PL in novel materials. Furthermore, new PL techniques continue to emerge, expanding the arsenal of PL analysis. Interfaces are increasingly important in new opto-electronic materials where layered structures are becoming thinner and more complex. Although PL measurements have been useful for the characterization and refinement of such materials, they can be expected to play an even greater role in the future.

PL and PC serve as the ideal combination for the Photovoltaic industry. Tools which are fast and powerful in quantifying flaws in the wafers in the production line are sought after as it will lead to reduction in loss of material, energy and man power on defective wafers. Investigations on photonic devices have convincingly proved that there are dramatic changes in optical and electrical properties when the dimension of the system is changed from three to two to one (quantum wire). PL and PC have many applications in devices which are fine combination of art, science and technology. The next season of advances in PL and PC will be based on studying biological systems and micro-or nanostructures or a combination of both using these tools.

### 1.7 Reference

1. Charles Kittel, Introduction to Solid State Physics, 7<sup>th</sup> ed. John Wiley and Sons, Inc. (Asia) (1996).
2. Richard Bube, H., Photo electronic Properties of Semiconductors, Cambridge University Press, Cambridge (1992).
3. Richard Bube, H., Electronic Properties of Crystalline Solids, Academic Press, NY (1974).
4. Vavilov, S. I., J. Phys. U.S.S.R., **10**, 499 (1948).
5. Curie, D. and Garlick, G. F. J., Luminescence in Crystals, John Wiley and Sons Inc, NY (1963).
6. Pallab Bhattacharya, Semiconductor Opto-electronic Devices, 2<sup>nd</sup> ed. Pearson education, Singapore (2002).
7. Pankove, J. I., Optical Processes in Semiconductors, Dover Publication, Inc. NY (1971).
8. Bardeen, J., Blatt, F. J. and Hall L. H., Proc. of Atlantic city Photoconductivity Conference (1954), J. Wiley and Chapman and Hall, p. 146 (1956).
9. Vij, D. R., Luminescence of Solids, Plenum Press, NY (1998).
10. Keer, H. V., Principles of Solid State, Newage International (P) Ltd, New Delhi (2000).
11. Elliott, R. J., Phys. Rev. **108**, 1384 (1957).
12. Haynes, J. R., Phys. Rev. Lett. **4**, 361 (1960).
13. Lampert, M. A., Phys. Rev. Lett. **1**, 450 (1958).
14. Haynes, J. R., Phys. Rev. Lett. **17**, 860 (1966).

15. Benoit-a-la-Guillaume, C., Salvan F. and Voos, M., *Bull. Am. Phys. Soc.* **14**, 867 (1969).
16. Hopfield, J. J., *Proc. 7<sup>th</sup> Int. Conf. Phys. Semiconductors, Paris (Dunod)* p.725 (1964).
17. Pankove, J. I., *Proceedings of the International Conference on the Physics of Semiconductors, Kyoto (1966)*.
18. Ryvkin, M., *Phys. Stat. Sol.* **11**, 285 (1965).
19. Ascarelli, G. and Rodriguez, S., *Phys. Rev.* **124**, 1321 (1961).
20. Jayakrishnan, R., Deepa, K. G., Sudha, Kartha, C., Vijayakumar, K. P., *J. Appl. Phys.* **101**, 046104 (2006).
21. Dumke, W. P., *Phys. Rev.* **132**, 1998 (1963).
22. Williams, E. W. and Brit, J. *Appl. Phys.* **18**, 253 (1967).
23. Hopfield, J.J., *Phys. Semicond. Paris* p. 725 (1964).
24. Thomas, D. G., Gershenson, M. and Trumbore, F. A., *Phys. Rev. A*, **133**, 269 (1964).
25. Dean, P. J., *Progress in Solid State Chemistry (Pregamon, Oxford)*, vol 8, (1973).
26. Williams, F., *Phys. Stat. Sol.* **25**, 493 (1968).
27. Radomsky, L. Y., Yi G. J. and Neumark, G. F., *Appl. Phys. Lett.* **64**, 1027 (1994).
28. Callaway, J., *J. Phys. Chem. Solids* **24**, 1063 (1964).
29. Zott, S., Leo, K., Ruckh, M. and Schock, H. W., *Appl. Phys. Lett.* **68** (8), 1144 (1995).
30. Eliam Zacks, H. and Halperin, A., *Phys. Rev. B*, **6**, 3072 (1972).
31. Pankove, J. I., *J. Phys. Chem. Solids*, **6**, 100 (1958).
32. Richard Bube, H., *Phy. Rev.* **99**(4), 15 (1955).
33. Ben Streetman, G., *Solid State Electronic Devices 5<sup>th</sup> Ed. Prentice-Hall Inc*, (2000).
34. Thyagi, M.S., *Introduction to Semiconductor Material and Devices, John Wiley & Sons (1991)*.
35. Timothy Gfroerer, H., *Photoluminescence in Analysis of Surfaces and Interfaces, Encyclopedia of Analytical chemistry, John Wiely & Sons Ltd., Chichester*, p. 9209 (2000).
36. Garcia-Garcia, J., Gonzalez-Hernandez, J., Mendoza- Alvarez, J. G., Cruz, E.L. and Contreras-Puente, G., *J. Appl. Phys.* **67**, 3810 (1990).
37. Wang, H., Wong, K. S., Foreman, B. A., Yang, Z. Y. and Wong, G. K. L., *J. Appl. Phys.* **83**, 4773 (1998).

38. Hollingsworth, R. E. and Sites, J. R., *J. Appl. Phys.* **53**, 5357 (1982).
39. Van Ryswyk, H. and Arthur Ellis, B., *J. Am. Chem. Soc.* **108**, 2454 (1986).
40. Uosaki, K., Shigematsu, Y., Kaneko, S. and Kita, H., *J. Phys. Chem.* **93**, 6521 (1989).
41. Mettler, K. *Appl. Phys.* **12**, 75 (1977).
42. Olson, J. M., Ahrenkiel, R. K., Dunlavy, D. J., Keyes, B. and Kibbler, A. E., *Appl. Phys. Lett.* **55**, 1208 (1989).
43. Komiya, S., Yamaguchi, A. and Umebu, I., *Solid State Electron.* **29**, 235 (1986).
44. Mullenborn, M. and Haegel, N. M., *J. Appl. Phys.* **74**, 5748 (1993).
45. Yoshida, T., Hashizume, T. and Hasegawa, H., *Jpn. J. Appl. Phys.* **36**, 1453 (1997).
46. Ding, Y. J., Guo, C. L., Khurgin, J. B., Law K. K. and Merz, J. L., *Appl. Phys. Lett.* **60**, 2051 (1992).
47. Ding, Y. J., Reynolds, D. C., Lee, S. J., Khurgin, J. B., Rabinovich, W. S. and Katzer, D. S., *Phys. Lett.* **71**, 2581 (1997).
48. Vignaud, D., Wallart, X., Mollot, F. and Sermage, B., *J. Appl. Phys.* **84**, 2138 (1998).
49. Thewalt, M. L. W., Steele, A. G. and Huffman, J. E., *Appl. Phys. Lett.* **49**, 1444 (1986).
50. Akimoto, K., Tamamura, K., Ogawa, J., Mori, Y. and Kojima, C., *J. Appl. Phys.* **63**, 460 (1988).
51. Henry, A., Monemar, B., Lindstrom, J. L., Bestwick, T. D. and Oehrlein, G. S., *J. Appl. Phys.* **70**, 5597 (1991).
52. Foad, M. A., Watt, M., Smart, A. P., Sotomayor Torres, C. M., Wilkinson, C. D. W., Kuhn, W., Wagner, H. P., Bauer, S., Leiderer, H. and Gebhardt, W., *Semicond. Sci. Technol.* **6**, A115 (1991).
53. Joyce, M. J., Gal, M. and Tann, J., *J. Appl. Phys.* **65**, 1377 (1989).
54. Xu, L., Huang, X., Huang, H., Chen, H., Xu, J. and Chen, K., *Jpn. J. Appl. Phys.* **37**, 3491 (1998).
55. Guimaraes, F. E. G., Elsner, B., Westphalen, R., Spangenberg, B., Geelen, H. J., Balk, P. and Heime, K., *J. Cryst. Growth*, **124**, 199 (1992).
56. Chang, R. R., Iyer, R. and Lile, D. L., *J. Appl. Phys.* **61**, 1995 (1987).
57. Freneck, H. J., Kulisch, W. and Kassing, R., *Proc. SPIE*, **1144**, 250 (1989).
58. Sandroff, C. J., Turco-Sandroff, F. S., Florez, L. T. and Harbison, J. P., *J. Appl. Phys.* **70**, 3632 (1991).

59. Timoshenko, V. Yu., Rappich, J. and Dittrich, Th., *Appl. Surf. Sci.* **123/124**, 111 (1998).
60. Krawczyk, S. K., Garrigues, M. and Bouredoucen, H., *J. Appl. Phys.* **60**, 392 (1986).
61. Tajima, M., *J. Cryst. Growth*, **103**, 1 (1990).
62. Naritsuka, S. and Nishinaga, T., *J. Cryst. Growth*, **174**, 622 (1997).
63. Fong, Y. -C., Armour, E. A., Hersee, S. D. and Brueck, S. R. J., *J. Appl. Phys.* **75**, 3049 (1994).
64. Wolford, D. J., Gilliland, G. D., Kuech, T. F., Smith, L. M., Martinsen, J., Bradley, J. A., Tsang, C. F., Venkatasubramanian, R., Ghandi, S. K. and Hjalmarson, H. P., *J. Vac. Sci. Technol.* **B9**, 2369 (1991).
65. Brunner, R., Bietsch, A., Hollricher, O. and Marti, O., *Rev. Sci. Instrum.* **68**, 1769 (1997).
66. Liu, Perkins, J., Horton, N. R., Redwing, J. M., Tischler, M. A. and Kuech, T. F., *Appl. Phys. Lett.* **69**, 3519 (1996).
67. Crowell, P. A., Young, D. K., Keller, S., Hu, E. L. and Awschalom, D. D., *Appl. Phys. Lett.* **72**, 927 (1998).
68. Vertikov, A., Kuball, M., Nurmikko, A. V., Chen, Y. and Wang, S. Y., *Appl. Phys. Lett.* **72**, 2645 (1998).
69. Jeong, M. S., Kim, J. Y., Kim, Y. -W., White, J. O., Suh, E. -K., Hong, C. -H. and Lee, H., *J. Appl. Phys. Lett.* **79**, 976 (2001).
70. Hegarty, J., Sturge, M. D., Weisbuch, C., Gossard, A. C. and Wiegmann, W., *Phys. Rev. Lett.* **49**, 930 (1982).
71. Hess, H. F., Betzig, E., Harris, T. D., Pfeiffer, L. N. and West, K. W., *Science*, **264**, 1740 (1994).
72. Zrenner, A., Butov, L.V., Hagn, M., Abstreiter, G., Böhm, G. and Weimann, G., *Phys. Rev. Lett.* **72**, 3382 (1994).
73. Gammon, D., Shanabrook, B. V. and Katzer, D. S., *Appl. Phys. Lett.* **57**, 2710 (1990).
74. Gammon, D., Snow, E. S., Shanabrook, B. V., Katzer, D. S. and Park, D., *Phys. Rev. Lett.* **76**, 3005 (1996).
75. Ghaemi, H. F., Goldberg, B. B., Cates, C., Wang, P. D., Sotomayor Torres, C. M., Fritze, M. and Nurmikko, A., *Superlattices Microstruct.* **17**, 15 (1995).
76. Bonadeo, N. H., Gang Chen, Gammon, D., Katzer, D. S., Park, D. and Steel D. G., *Phys. Rev. Lett.* **81**, 2759 (1998).

77. Hasen, J., Loren Pfeiffer, N., Aron Pinczuk, Song He, Ken West, W. and Brian Dennis, S., *Nature (London)* **390**, 54 (1997).
78. Zhu, Z., Yoshihara, H., Takebayashi, K. and Yao, T., *J. Cryst. Growth*, **138**, 619 (1994).
79. Molenkamp, L. W. and van't Blik, H. F. J., *J. Appl. Phys.* **64**, 4253 (1988).
80. Ko, H. -C., Park, D. -C., Kawakami, Y. and Fujita, S., *Semicond. Sci. Technol.* **11**, 1873 (1996).
81. Willoughby Smith, *Nature* **7** (173), 303 (1873).
82. Richard Bube, H. and Thomsen, S.M., *J. Chem. Phys.* **23**, 15 (1955).
83. Richard Bube, H., *J. Chem. Phys.* **23**, 18 (1955).
84. Swith, R. W., *RCA Rev.* **12**, 350 (1951).
85. Richard Bube, H., *Photoconductivity Conference*, p. 575 (1954).
86. Moss, T. S., *Proceedings of the IRE*, **43** (12), 1869 (1955).
87. Schultz, M. L. and Morton, G. A., *Proceedings of the IRE*, **43**(12), 1819 (1955).
88. Ravich, Yu. I., *Soviet Physics-Solid State*, **3**(5), 1162 (1961).
89. Tseng, H. F. and Li, S. S., *Phys. Rev. B*, **6**(8), 3066 (1972).
90. Zitter, R. N., *Phys. Rev.* **112**(3), 852 (1958).
91. Ryvkin, S. M., Paritskii, L. G., Khansevaov, Yu. R., and Yaroshetskii, I. D., *Soviet Physics-Solid State*, **3**(1), 185 (1961).
92. Streetman, B. G., *J. Appl. Phys.* **37** (8), 3137 (1966).
93. Baicker, J. A., *Phys. Rev.* **129**, 1174 (1963).
94. Joshi, N. V. and Martin, J. M., *Phys. Lett.* **113A** (6), 318 (1985).
95. Marshall, J. M., Street, R. A. and Thompson, M. J., *J. Non-Cryst. Solids*, **66**, 175 (1984).
96. Spear, W. E., *J. Non-Cryst. Solids*, **59-60**, 1 (1987).
97. Street, R. A., *Appl. Phys. Lett.* **41**, 1060 (1982).
98. Tiedje, T., Abeles, B., Morel, D. L., Moustakas, T. D. and Wronski, C. R., *Appl. Phys. Lett.* **36**, 695 (1980).
99. Kasap, S. O., Thankur, R. S. P. and Dodds, D., *J. Phys. E: Sci. Instruments*, **21**, 1195 (1988).
100. Chamoun, S. N., Joshi, R., Arnold, E. N., Grondin, R. O., Meyer, K. E., Pessot, M., and Mourou, G. A., *J. Appl. Phys.* **66** (1), 236 (1989).
101. Tsu, R., Chang, L. L., Sai-Halasz, G. A. and Esaki, L., *Phys. Rev. Lett.* **34**(24), 1509 (1975).
102. Temkin, H., Bean, J. C., Pearsall, T. P., Olsson, N. A. and Lang, D. V., *Appl. Phys. Lett.* **49**(3), 155 (1986).

103. Zwaal, E. A. E., Gorissen, W. T., Haverkort, J. E. M., van Hall, P. J., and Wolter, J. H., *Solid-State Electronics*, **32**(12), 1109 (1989).
104. Zachau, M., Helgesen, P., Kux, A., Koch, F., Grutzmacher, D., Meyer, R., Jurgensen, H. and Balk, P., *Super-lattices and Microstructures*, **5**(1), 1921 (1989).
105. Vickers, A. J., Wicks, V. R., Rivers, A., Roberts, J. and Mistry, P., *J. Modern Optics*, **37**(4), 653 (1990).
106. Rakhshani, A. E., *J. Phys.:Condens. Mater.* **12**, 4391 (2000).
107. Balberg, I., Dover, Y., Naides, R., Conde, J. P. and Chu, V., *Phys. Rev. B*, **69**, 035203 (2004).
108. Azulay, D., Millo, O., Silbert, S., Balberg, I. and Naghavi, N., *Appl. Phys. Lett.* **86**, 212102 (2005).
109. Toker, D., Balberg, I., Zelaya-Angel, O., Savir, E. and Millo, E., *Phy. Rev. B*, **73**, 045317 (2006).
110. Susanne Siebentritt, Sascha Sadewasser, Mark Wimmer, Caspar Leendertz, Tobias Eisenbarth and Martha Ch. Lux-steiner, *Phy. Rev. Lett.* **97**, 146601 (2006).
111. Smith, S., Zhang, P., Gessert, T. and Mascarenhas, A., *Appl. Phys. Lett.* **85** (17), 3854 (2004).
112. Azulay, D., Balberg, I., Chu, V., Conde, J. P. and Millo, O., *Phy. Rev. B*, **71**, 113304 (2005).



## CHAPTER 2

### A System for Low Temperature Photo-luminescence and Photo-conductivity Studies

---

*Whole wafer processing for the fabrication of opto-electronic devices provides significant advantages in terms of ease of handling and increased potential yield. However it imposes a stringent demand on the development of non-destructive and spatially resolved analytical methods to characterize substrates, epitaxial layers and devices. In the present work, a photoluminescence (PL) system has been developed which allows quantitative study of semiconductor thin films through spectral information. This leads to the optimization of material quality related to electrical and/or optical properties and helps in standardizing conditions required for the deposition of higher quality and highly uniform thin films. This system with surface scanning facility has the capacity to quantitatively map films as large as  $1\text{cm}^2$  at 12 K and  $5\text{ cm} \times 5\text{ cm}$  at 300 K, with a minimum sampling grid size of  $0.225\ \mu\text{m}$ . PL signals in the wavelength range from 350 to 1730 nm can be measured with appropriate choice of spectrophotometer. Excitation energy can be selected by selecting the required laser source while the excitation intensity can be varied using neutral density filters. Sample temperature can be varied by keeping it on the cold head of a closed cycle liquid He- cryostat. Facilities for spatial measurement at a single wavelength (topography), spatial mapping of PL peak wavelength and excitation/intensity dependent studies are provided in the system. In addition to this, the system can also be used for the low temperature PC characterization. The details of the experimental set up are described in this chapter.*

## **2.1 Characterization using photo-luminescence mapping and photo-conductivity: An introduction**

Optical spectroscopy experiments require three basic elements: a light source, a light dispersing element and a light detector. Rapid development in spectroscopic instruments occurred in the 19<sup>th</sup> century, as a result of understanding the nature and properties of light.<sup>1</sup> Kirchhoff realized that each element shows a characteristic absorption and emission line and hence the technique could become a powerful tool in qualitative analysis of elements. The Sun was replaced by different arc sources, which could be used as light sources. Theory of diffraction inspired Fraunhofer to invent a new light dispersing element: the grating. Invention of photo-emissive cell with a number of electron multiplier steps, led to the development of the Photo Multiplier tubes (PMTs), which could be used as a sensor from ultraviolet (UV), to near IR regions. Success in optical spectroscopy grew with rapid technological development occurring on the three elements, mentioned earlier. The field of luminescence spectroscopy expanded after World War II, partly because of the wide application of luminescent materials in devices like fluorescent tubes, color television screens, night viewers, X-ray photography and scintillators.

The spatial dependence of optical properties of materials is often neglected which can result in two of the following ways. One is the case in which atomic composition or structure is not homogenous. (In this case the spatial variation can be analyzed using mapping<sup>2</sup>) In the other case, there exists a spatial correlation in solids. If there is a migration of energy or particles in solids, the spatial dependence can appear in macroscopic optical properties.<sup>3, 4</sup> Both optical (luminescence) and electrical (transport) properties are important in materials used for opto-electronic devices. PL has been used as a non-destructive tool for the evaluation of quality of semiconductor substrates and thin films.<sup>5-7</sup> PL spectroscopy is widely used to characterize impurities and defects in semiconductors. The PL measurement at low temperature makes the spectral line very sharp and strong. This is specifically important for the case of band edge PL, related to shallow impurities. PL characterization using band edge PL emission at low temperature has been standardized for impurity analysis in Si by 'American Standards for Testing and Materials'.<sup>8</sup> The band edge PL is detectable at room temperature under strong excitation condition. Mapping of the band edge PL has been shown to be useful to characterize the homogeneity of the crystalline quality of semiconductor wafers.<sup>9-11</sup> Deep level PL spectroscopy has been applied on GaAs and Si crystals and a direct correlation

Between deep level PL and micro-defects have been recognized.<sup>12, 13</sup> The thermal quenching and broadening effects are much smaller in deep-level PL than those for band edge PL; therefore, the former dominates the spectrum with the spectral shape similar to that at low temperature. This makes the radiative recombination process very simple, leading to semi-qualitative mapping of defects responsible for deep-level PL.<sup>14</sup>

Photoconductivity [PC] is a phenomenon usually observed in semiconductor materials. Its measurement permits one to obtain important information about the lifetime and diffusivity of radiatively excited carriers.<sup>15</sup> Since PC is observed in semiconductors, the measurement methods deal with high-resistivity samples (tens to hundreds of  $\Omega\text{cm}$ ).<sup>16</sup> PC decay experiments, in particular the decay of photocurrent from the steady state after an abrupt termination of illumination, allow calculation of drift mobility of minority carriers, which is an important parameter describing the opto-electronic quality of crystalline and amorphous semiconductors.<sup>17</sup> Measurement of PC at different incident photon energies and intensities at different temperatures provide valuable information on the opto-electronic properties of the material.<sup>18</sup> Opto-electronic properties are very sensitive to the presence of impurities. A significant concentration of undesired impurities and defects that give rise to recombination centers which control the minority carrier lifetime ( $\tau$ ) have decisive influence on the performance of devices based on these excess carriers. The minority carrier lifetime provides information on fast or slow nature of the recombination of the carriers, taking place in that semiconductor material. Since impurities present in the semiconductor lead to creation of recombination centre directly or by causing defects in the semiconductor, the value of ( $\tau$ ) is intimately related with the concentration of the impurities. Alternately, value of ( $\tau$ ) provides a direct assessment of the quality of the material for various device applications.<sup>19</sup>

PL mapping system has been developed by the Hewlett-Packard Opto-electronics Division, for the measurement of III-V semiconductor epitaxial layer uniformity in light-emitting diode (LED) device structures. It has been used as an aid in the development of new epitaxial growth processes and as a quality screening method for cost reduction in a 'high volume' production line.<sup>20</sup> The high production cost of the conventional Si solar cells makes it essential to search for cheaper methods and materials for solar energy conversion. Cheaper methods and materials must be complemented with cheaper and robust tools to characterize in-situ the production as well as to diagnose faults. This would cut short production cost by eliminating material and labor loss on faulty panels. PL technique has practical advantages of being non-destructive, capable of

delivering high spatial resolution and lacks the requirement of a special environment (low temperature, high vacuum etc.) for measurement. Correlating the operational characteristics of semiconductor devices, based on the radiative recombination and carrier lifetime ( $\tau$ ), will yield industry related processes an advanced characterization tool where quality analysis and testing of each wafer in a batch process can be done using PL and PC.

## **2.2 Requirements for the fabrication of a PL mapping and PC measurement system**

The PL system basically requires four elements: Excitation source, Light dispersing system, Signal collection system and Detection system. Characteristics of these fundamental elements have changed over the years, but the basic experimental principles have remained the same.

### ***A) Excitation System***

Excitation System used in optical spectroscopy has evolved over time. The Sun was originally used as the light source, which got replaced with different kinds of arc lamps and many of these are today replaced by laser systems.

***(A.1) White light source:*** White light source has broad optical bandwidth. There are two kinds of white light sources: incandescent and arc. The former one acts as black body radiator in which high temperature is achieved by using a Tungsten filament in combination with halogen in the bulb, to regenerate the slowly evaporating Tungsten wire. These lamps can be used as excitation sources in the visible and IR region. But these can not be used in the UV range where arc lamps have to be used. Arc lamps create radiation by discharging energy through ionized gases. In low pressure discharge lamps, the characteristic lines of atoms in the discharge are emitted. At high pressure and temperature, a continuous background is there owing to broadening of the spectral lines. The most widely used arc lamps are those of high pressure Xenon, Mercury and Deuterium.<sup>21</sup> Xe and Hg lamps give a continuous background between 220 to 2000 nm. On top of the background, the line spectrum is visible which is undesirable for a continuous excitation source. For Hg, the line spectra are more prominent and hence Xe lamps are more prominently used in spectrofluorimeters. Deuterium lamps produce a good continuous spectrum at short wavelengths and can be used for measurements below 240 nm.

**(A.2) Lasers:** Lasers are the perfect excitation sources which are highly monochromatic, having very high power density, small divergence, high coherence, and capable of emitting very short pulses. Different kinds of lasers find application in different areas of optical spectroscopy. Three kinds of laser systems are commonly known: (a) Gas lasers<sup>22, 23</sup> (b) Dye lasers<sup>24</sup> and (c) Solid state lasers.<sup>25</sup> In gas lasers, an electric current is discharged through a gas to produce light. The first gas laser constructed was Helium-Neon laser. Carbon dioxide laser, Argon ion laser etc. come under this category. A dye laser uses an organic dye as the 'lasing medium', usually as a liquid solution. Compared to gases and most solid state lasing media, a dye can usually be used for a much wider range of wavelengths. The wide bandwidth makes them particularly suitable for tunable lasers and pulsed lasers. A solid-state laser is the one that uses a solid gain medium. Generally, the active medium of a solid-state laser consists of a glass or crystalline host material to which a dopant is added such as Neodymium, Chromium, Erbium, etc. Many of the common dopants are rare earth elements, because the excited states of such ions are not strongly coupled with thermal vibrations of the crystalline lattice (phonons), and the lasing threshold can be reached at relatively low brightness of pump. Most common type is Neodymium doped Yttrium Aluminium Garnet (YAG).<sup>26</sup>

### ***B) Light Dispersing Elements:***

Light dispersing elements in luminescence spectroscopy are necessary due to the following requirements:

1. To produce monochromatic light from a continuous light source
2. To analyze the wavelength distribution in the emitted light.

The commonly used light dispersing elements are monochromators based on gratings or prisms and interferometers.<sup>27</sup> In luminescence spectroscopy, the most commonly used light-dispersing element is the grating monochromator.

**(B.1) Grating monochromator:** Among the monochromators with flat gratings (Ebert, Czerny-Turner, and Littrow) and with curved grating (Rowland, Passchen-Runge and Wadsworth), the most popular design is the Czerny-Turner (C-T) configuration as shown in Fig. 2.1. In C-T configuration, the broad band illumination is focused to the entrance slit. The amount of light energy available for the system depends on the intensity of illumination and the acceptance angle of the optical system. The slit is placed at the focal point of a curved mirror so that light reflected from the mirror is collimated (focused at infinity). The collimated light is made incident on the diffraction grating. Gratings are made by ruling or etching a series of lines onto a polished reflecting surface. The number

of lines varies from 300 to 3600 lines/mm. A diffraction grating is basically an optical component with surface covered by a regular pattern of parallel lines, typically the distance between the lines is comparable to the wavelength of light. The intensity distribution function is given by<sup>28</sup>

$$I = I_0 (\sin \beta / \beta)^2 (\sin N\gamma / N \sin \gamma)^2 \quad (2.1)$$

where  $\beta = (1/2)kh \sin \theta$  and  $\gamma = (1/2)kh \sin \phi$ , and  $N$  is the number of lines in the grating of width  $b$  and separation  $h$ . Principal maxima occur within the envelope at  $\gamma = n\pi$ ,  $n = 0, 1, 2, \dots$  that is,

$$n\lambda = h \sin \theta \quad (2.2)$$

which is the grating formula, giving the relation between wavelength and angle of diffraction. The integer 'n' is called the "order of diffraction". Also, resolving power of the grating is equal to the number of grooves/mm 'N' multiplied by the order number  $n$ . The diffracted light is then focused on to the exit slit with the help of another curved mirror. The dispersed beams appear on the exit slit, at a particular wavelength. The angle of incidence on the diffraction grating can be controlled from outside. Rotation of the dispersing element causes the band of colors to move relative to the exit slit. Thus light output at a particular wavelength can be adjusted by controlling the angle of incidence at the grating element.

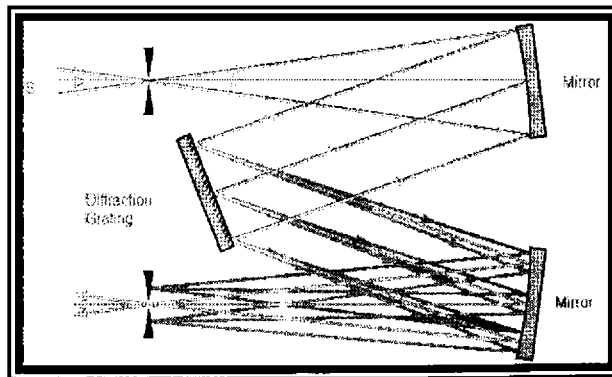


Fig. 2.1: Arrangement in a C-T Mounting.

The angular dispersion of a grating is an important parameter for its performance which is given as<sup>29</sup>

$$d\theta_d / d\lambda = n / (d \cos \theta_d) \quad [\text{rad/nm}] \quad (2.3)$$

In practice, the linear dispersion is more important, which represents the linear distance between two diffracted wavelengths at the exit slit. The linear dispersion depends on the focal length of the monochromator and is given by<sup>29</sup>

$$dx/d\lambda = nf/d \cos \theta_d \quad [\text{mm/mm}] \quad (2.4)$$

where  $dx/d\lambda$  is the linear dispersion at the exit slit and  $f$  is the focal length of the monochromator. In order to improve the efficiency of the light throughput in a monochromator, gratings are ruled at a specific angle with the grating surface,  $\theta_b$ , known as the 'blaze angle'. The intensity of the diffracted light is highest in the direction for which the grooves act as a mirror (angle of reflection from the grating surface). The blaze angle is related to the blaze wavelength by<sup>29</sup>

$$n\lambda_b = 2d \sin \theta_b \quad (2.5)$$

The efficiency remains high for several hundreds of nanometers around the 'blaze wavelength'. Another important aspect of the monochromator is its  $f$  number. The  $f$  number of a monochromator is defined as  $f/W$ , the focal length divided by diameter of the focusing optics in the monochromator. The highest collection efficiency and resolution are achieved if the  $f$  number of the light collecting optics (lens) matches with that of the monochromator. The  $f$  number of a lens is defined as the focal length divided by the diameter of the lens. If the  $f$  numbers of the lens and monochromator match, the light exactly fills the grating. If the  $f$  number of the focusing lens is too small then the light over fills the grating and causes lowering of efficiency by loss of light and if the  $f$  number is too large, the grating will only be partially filled and number of rulings used will be smaller and lead to lower resolution.

### ***C) Signal Collection System: Fiber optic collimator***

An **optical fiber** (or **fibre**) is a glass or plastic fiber, designed to guide light along its length, by confining as much light as possible along its axis. In fibers with large core diameter, the confinement is based on total internal reflection.<sup>28</sup> In core fibers with small diameter, (widely used for most communication links longer than 200 meters) the confinement relies on establishing a waveguide.<sup>29</sup> Light can be guided along the fibre if it enters at an angle, less than the critical angle. For step index fibre, light entering the fibre will be guided, if it falls within the acceptance cone of the fiber. The term 'optical fiber' covers a range of different designs including graded-index optical fibers, step-index optical fibers, bi-refrington polarization-maintaining fibers and more recently photonic crystal fibers. The fiber consists of a core surrounded by a cladding layer. To

confine the optical signal in the core, the refractive index of the core must be greater than that of the cladding. The boundary between the core and cladding may either be abrupt, [as in step-index fiber], or gradual, [as in graded-index fiber]. For step-index multimode fiber, the acceptance angle is determined only by the indices of refraction<sup>30</sup>

$$n \sin \theta_{\max} = \sqrt{n_1^2 - n_2^2} \quad (2.6)$$

where  $n_1$  is the refractive index of the fiber core,  $n_2$  is the refractive index of the cladding and half-angle of the acceptance cone is called the acceptance angle,  $\theta_{\max}$ . The same relation holds for the numerical aperture (NA) for any kind of fiber. For maximum signal collection, there has to be a match between the NA of the fiber and the lens or system of lenses used.

The angular acceptance of a lens is expressed by the  $f$  number ( $f/\#$ ), and for a thin lens, imaging an object at infinity, it is given by<sup>31</sup>

$$f/\# \approx 1/2NA \quad (2.7)$$

This approximation holds well when the numerical aperture is small. The  $f$ -number describes the light-gathering ability of the lens. In optical design, the finite distance between the object and the lens must often be considered. In these cases, the “working  $f$  number” is used instead. The working  $f$  number is defined by making the approximate relation above exact:

$$f/\#_w = 1/2NA \approx (1-m)(f/\#) \quad (2.8)$$

where  $f/\#_w$  is the working  $f$  number and ‘ $m$ ’ is the lens's magnification for an object a particular distance away.<sup>32</sup>

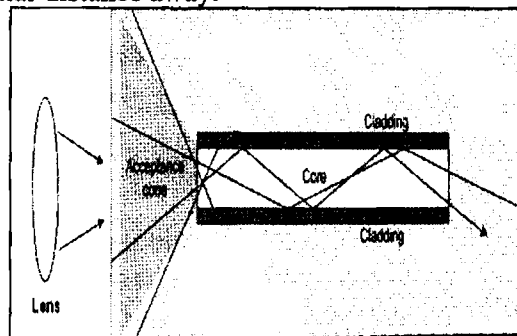


**Fig. 2.2:** Propagation of light through a multi-mode optical fibre.

PL signal is emitted maximum at an angle  $90^\circ$  to the incident beam where there is minimum scattering. The emitted radiation can be collected by using a



system of lens and optical fibers which constitute the signal collection system (Fig. 2.2). Emission signals are allowed to fall in the acceptance cone with the help of a lens or a combination of lenses. This combination of the lenses and optic fibre is called “fibre optic collimator”.

#### ***D) Detection System***

Success of the PL experiment depends on the ability to detect weak signals. The most commonly used detection systems are Photo Multiplier Tubes (PMT), Diode Detectors and Charge Coupled Devices (CCD). Of these, PMT is the most widely used one because of its high sensitivity and ability to do even single-photon counting. Progress in CCD technology has made it very sensitive today which competes with the conventional PMT in their signal-to-noise detection limit. Various detection techniques such as lock-in amplifier and boxcar averaging can be used to improve the signal-to-noise ratio.

**(D.1) Photo Multiplier Tube (PMT)**<sup>33</sup>: Photo multiplier tubes or PMTs are extremely sensitive detectors of light in the UV, visible and near IR region. These detectors multiply the signal produced by incident light by as much as  $10^8$ , from which single photons can be resolved. Incident photons strike the photocathode material, which is present as a thin deposit on the entry window of the device; this results in emission of electrons as a consequence of the photoelectric effect. These electrons are directed by the focusing electrode towards the electron multiplier, where electrons are multiplied by the process of secondary emission.

The electron multiplier consists of a number of electrodes, called ‘dynodes’. Each dynode is held at a more positive voltage than the previous one. The electrons leave the photocathode, having the energy of the incoming photon (minus the work function of the photocathode). As they move towards the first dynode they are accelerated by the electric field and arrive with much greater energy. On striking the first dynode, more low energy electrons are emitted and these, in turn, are accelerated towards the second dynode. The geometry of the dynode chain is such that a cascade occurs with an ever-increasing number of electrons being produced at each stage. Finally the anode is reached where the accumulation of charge results in a sharp current pulse, indicating the arrival of a photon at the photocathode.

**(D.2) Diode Detector or Photodiode**<sup>34</sup>: Beyond 900 nm, where the sensitivity of the PMT is poor, the photodiodes, which are photovoltaic detectors, are used. A photodiode is a semiconductor diode that functions as a photo-detector. Photodiodes are having either a window or optical fibre

connection, in order to let in the light to the sensitive part of the device. They may also be used without a window to detect vacuum UV or X-rays. A photodiode is a junction, having either p-n or p-i-n structure. When a photon of sufficient energy strikes the diode, it excites an electron thereby creating a mobile electron and a positively charged 'hole'. If the absorption occurs in the junction's depletion region, or one diffusion length away from it, these carriers are swept from the junction by the built-in field of the depletion region, producing a photocurrent.

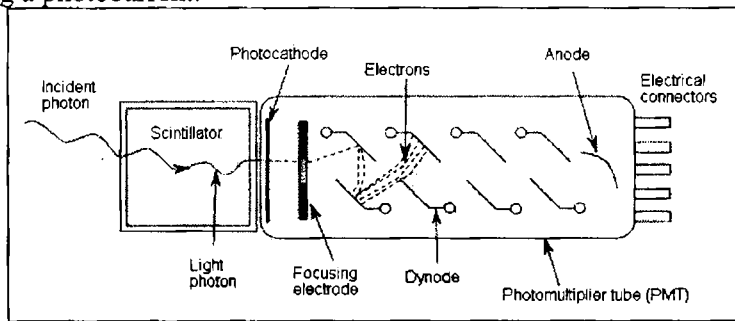


Fig. 2.3: Schematic of a working of a Photomultiplier tube.

The highest sensitivity is obtained when the signal from the photodiode is amplified with an operational amplifier. Photodiodes suffer from a relatively high noise. Photodiodes can be used under either zero bias (photovoltaic mode) or reverse bias (photoconductive mode). In the former case, light falling on the diode causes a current across the device, leading to forward bias which in turn induces "dark current" in the opposite direction to the photocurrent. Reverse bias induces only little current (known as 'saturation' or 'back current') along its direction. But a more important effect of reverse bias is widening of the depletion layer (hence expanding the reaction volume) and strengthening the photocurrent. Circuits based on this effect are more sensitive to light than the ones based on the photovoltaic effect and also tend to have lower capacitance, which improves the response speed. On the other hand, the photovoltaic mode tends to exhibit less electronic noise. Avalanche photodiodes have a similar structure, but these are operated with much higher reverse bias. This allows each photo-generated carrier to be multiplied by avalanche breakdown, resulting in internal gain within the photodiode, which increases the effective responsivity of the device.

**(D.3) Charge Coupled Device (CCD)** <sup>35</sup>: A charge-coupled device (CCD) is an image sensor, consisting of an integrated circuit, containing an array of linked or coupled, capacitors sensitive to light. The light-sensitive capacitors detect the

Intensity of light received and convert it into an electrical signal. Under the control of an external circuit, each capacitor can transfer its electric charge to one or the other of its neighbors. CCDs are used in digital photography and astronomy (particularly in photometry, optical and UV spectroscopy and high speed techniques such as lucky imaging). A CCD consists of an array of metal oxide semiconductor (MOS) capacitors which are made from p- type silicon or grown on insulating layer of  $\text{SiO}_2$ . On top of the  $\text{SiO}_2$  layer, a thin metal structure (called gate) is deposited. Electric contacts are made on the gates and the Si substrate. Illumination of MOS capacitor results in generation of free electrons and holes. When a positive voltage is applied to the gate, the holes are pushed away from it. The electrons are collected at the Si-SiO<sub>2</sub> interface under the gate as long as the potential is applied to the gate. The number of electrons trapped under the gate is proportional to the number of incident photons. Charge coupled devices can be used as a form of memory or for delaying analog, sampled signals.

The charge is moved through arrays to the horizontal array and from there to the detector. Here the number of stored electrons from every pixel is measured. The number of electrons, which is proportional to the incident light intensity at every point on the CCD plate, is known after a readout procedure and the image is made available on a screen which can be processed with a computer. The sensitivity of CCD is very high; but thermal electrons are the main source of noise. By cooling the CCD, the noise can be reduced. The resolution of a CCD depends on the number of pixels. But for large number of pixels, a large read out time is needed leading to problems. The spectral response of CCD is determined by the light absorption in the Si substrate and this is similar to that of the Si photodiode (200-1100 nm). The CCD array can measure the entire spectrum simultaneously, avoiding the scanning process, using a monochromator. This is a great advantage when the intensity of signal is expected to change during the time required to scan.

### **2.3 Schematic of the low temperature photo-luminescence scanning and photo-conductivity set up**

In order to fabricate a system to measure PL and PC of semiconductor thin films, the requirements are: (a) stable monochromatic light source (b) optics to focus light on the sample (c) sample holder (d) collection optics (e) monochromator (f) detector (h) voltage source (i) chopper and (j) oscilloscope.

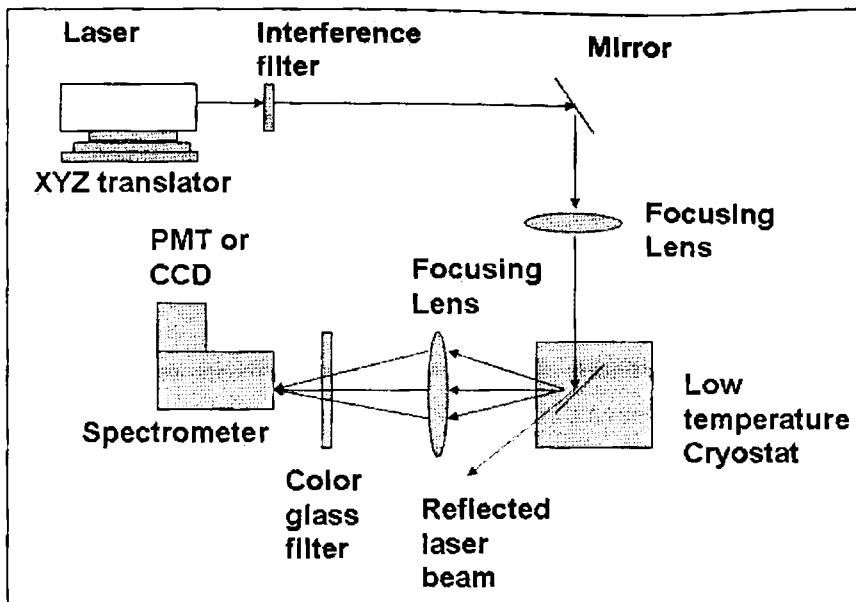


Fig. 2.4: Schematic for the PL scanning system.

A typical PL mapping system should contain a variable excitation source, a variable temperature cryostat with sample holder assembly, a translation system to move the excitation beam over the surface area of the sample or move the sample keeping the excitation beam fixed, a high resolution scanning spectrometer and a detection system. The schematic of the required set up is shown in Fig. 2.4. The excitation source for most I-III-VI<sub>2</sub>, II-VI and III<sub>2</sub>-VI<sub>3</sub> semiconductors can be a He-Cd laser, capable of delivering 0-20 mW of power at 325 nm. A narrow band interference filter can be used between the laser and the sample to avoid radiation from the plasma. The laser beam can be typically focused to a spot of 100-500 μm diameter on the sample surface. By varying the intensity using neutral density filter, it is possible to change the power density on the sample in the range 10-10<sup>3</sup> W/cm<sup>2</sup>. To obtain maximum information on radiative process, it is necessary to avoid thermal relaxation/ excitation processes. For this, the sample is cooled to cryogenic temperatures where non-radiative processes are minimal. This is done by mounting the sample on a Copper cold finger of a liquid He cryostat equipped with optical windows using thermally conducting grease. The luminescence from the sample is collected by using suitable lens and is focused on the slit of a high resolution spectrometer. The laser beam is incident at an angle on the sample so that the reflected beam does not fall on the collection lens. A long pass glass filter is placed between the spectrometer and the sample to avoid any of the laser excitation from reaching

the detector. Keeping these points as our basic requirements, a PL mapping system was fabricated.

In the existing PL scanning system, to carry out PC studies, it had to be integrated additionally with a white light source, a monochromator, an electronic shutter [to deliver light pulses], a detection system to monitor the current in the sample as a function of the incident light intensity and wavelength and a voltage source to bias the sample. It was further required that the cryostat be provided with provision for making electrical contacts from the sample without breaking the vacuum and maintaining the low temperature in the cryostat. The basic design of a PC set up is show in Fig. 2.5 below.

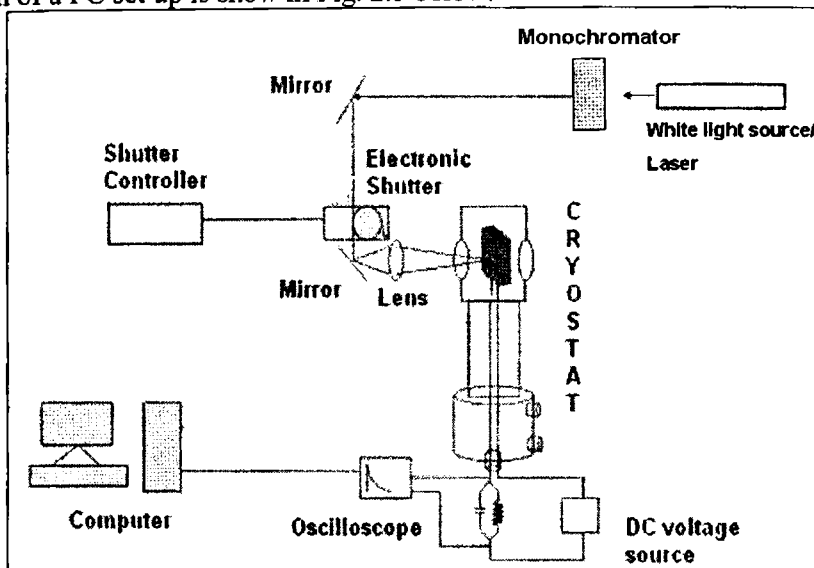


Fig. 2.5: Schematic of the PC system.

A Xe arc lamp (of power 1 KW) was used as the white light excitation source for wavelength dependent PC studies. A water bath had to be used to avoid heating of the sample and other optical accessories while operating the light source. Two detection systems were used for the PC experiment. A Source Measuring Unit (SMU: Keithley 236) which could act as both a voltage source and as a current measuring unit simultaneously was the main detection unit. The voltage and current range of the instrument used was  $\pm 100 \mu\text{V}$  to 110 V and  $\pm 10 \text{ fA}$  to 100 mA respectively. Measurements made with the instrument were controlled using computer interface. The data was logged into the computer which was later used for plotting graphs. An Oscilloscope (Tektronix TDS 210) was also used to measure the rise and decay of photocurrent under excitation with the laser pulses. The oscilloscope was interfaced with a computer so that

data recorded in the oscilloscope could be transferred directly to the computer and used for further processing. Rise and decay time, lifetime, photosensitivity and intensity dependence of photocurrent for the thin films were measured using the data collected using the oscilloscope.

## 2.4 On the assembled opto-electronic characterization unit

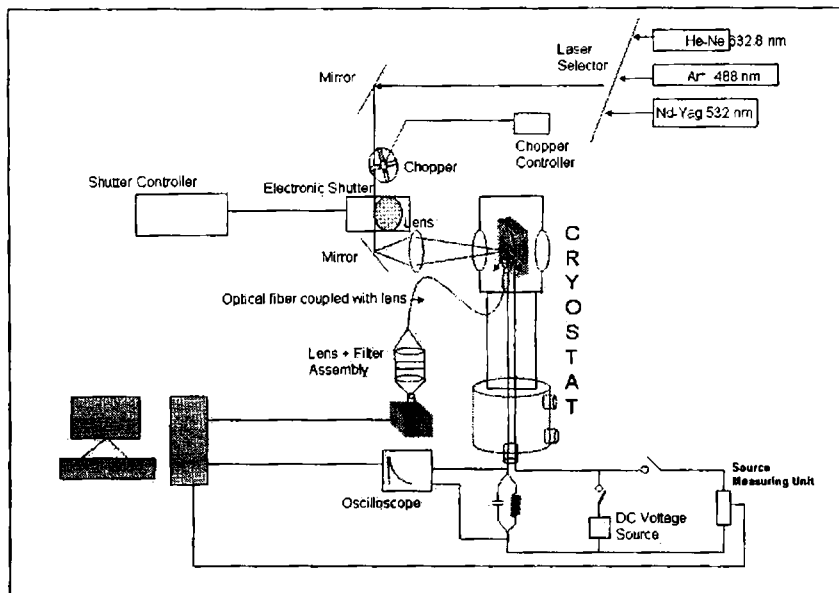


Fig. 2.6: Schematic of the low temperature PL and PC system.

Figure 2.6 represents the schematic of the PL and PC systems fabricated for the present work, by assembling the various fundamental spectroscopic elements necessary for the experimental set up. The system was successfully assembled and was tested on several I-III-VI<sub>2</sub>, II-VI, III<sub>2</sub>-VI<sub>3</sub> semi-conducting thin films (polymers and dye molecules not part of this thesis). The system can be used for PL studies in the wavelength region from 350-1730 nm. Also the temperature can be varied from 10-300 K in the system which allows carrying out several characterization studies by reducing thermal noise. This helps one to understand temperature dependence of luminescence phenomenon. The excitation energy can also be varied from 3.82 eV to 1.96 eV by choosing the appropriate laser. The lowest resolution that could be achieved in the system is 4 meV (Please see chapter 3 for more details). PL from different ionized states of the same defect was also resolved at 10 meV resolution.<sup>36</sup>

## **2.4.1 Excitation sources**

### **2.4.1A He-Cd laser**

He-Cd laser (Kimmon Koha Ltd) was used for PL and PC studies of the samples. Some of the basic features of this laser system are:

- This system works at 325 nm with an o/p power of 20 mW and at 442 nm with an o/p power of 80 mW.
- Beam diameter of the unfocussed beam was  $1 \pm 5\%$  mm, with a divergence of  $0.3 \pm 5\%$  mm.
- Samples with band gap up to 3.83 eV could be studied using this laser.

### **2.4.1B Ar ion laser**

An Argon ion laser (Melles Griote) was used for PL and PC studies of the samples. Some of the basic features of this laser system are:

- The 488 nm line in the TEM<sub>00</sub> mode, having a maximum power of 150 mW was used.
- Beam diameter of the unfocussed beam was  $0.68 \pm 5\%$  mm, with a divergence of  $1.1 \pm 5\%$  mm.
- The noise level in the <100 kHz range was 4% while that in the < 1 MHz range was 6%.
- The laser beam was focused onto the sample using lenses. The  $1/e^2$  diameter of the final spot on the sample was  $0.5 \pm 5\%$  mm.
- Samples with band gap up to 2.54 eV could be studied using this laser.

### **2.4.1C Solid state diode pumped green laser**

A solid state diode pumped green laser (Coherent Inc) was used for PL and PC studies of the samples. Some of the basic features of this laser system are:

- The 532 nm line in the TEM<sub>00</sub> mode, having a maximum power of 20 mW was used.
- Beam diameter of the unfocused beam was  $0.32 \pm 10\%$  mm, with a divergence of  $0.5 \pm 5\%$  mm.
- Samples with band gap up to 2.33 eV could be studied using this laser.

### **2.4.1D He-Ne laser**

He-Ne laser (Melles Griote) was used for PC studies of the samples. Some of the basic features of this laser system are:

- The 632.8 nm line in the TEM<sub>00</sub> mode, having a maximum power of 15 mW was used.

- Beam diameter of the unfocused beam was  $0.62 \pm 5\%$  mm, with a divergence of  $0.5 \pm 5\%$  mm.
- Samples with band gap up to 1.96 eV could be studied using this laser.

#### 2.4.1E Xenon arc lamp

The experimental set up used for determining the intensity profile of the Xenon arc lamp was as shown in Fig. 2.7. Light from the lamp was focused on to the monochromator entrance slit with the help of a lens.

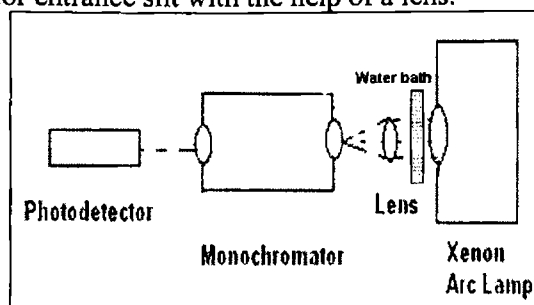


Fig. 2.7: Experimental set up for determining Xenon arc profile.

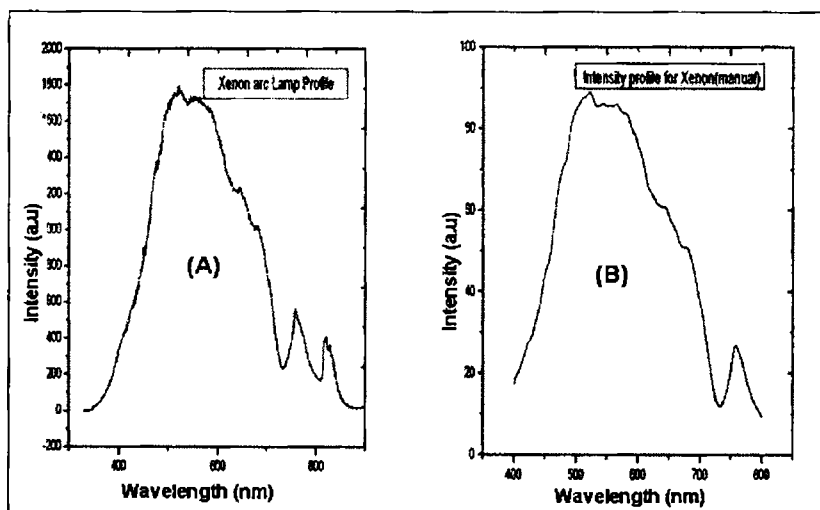


Fig. 2.8: Profile of the Xenon arc lamp recorded using (a) Spectrophotometer (USB2000) and (b) Assembled set up containing Monochromator and detector.

Output light from the monochromator was made to fall on a calibrated photo detector which measured the power of the incident wavelength (Fig. 2.8(a)). The profile of the arc lamp was also studied with the help of a computer interfaced spectrophotometer (USB2000). The light from the arc lamp was coupled with the help of an optical fiber into the entrance slit of the spectrophotometer. The software OOI Base 32 was used to control the spectrophotometer and the arc



lamp profile was obtained on the computer using this interface (Fig. 2.8(b)). The Xenon Arc Lamp showed high emission intensity in the green region (520 nm) and low intensity emission towards UV and IR regions.

#### **2.4.2 Detection system**

A minimal detection system consists of lens and sensor. A more complex system could consist of transmission, recording, analysis, and display systems. The current system consists of most of these entities which were incorporated in user friendly manner.

##### **2.4.2A Spectrophotometer for UV-VIS-IR region**

A spectrophotometer is a photometer (a device for measuring light intensity) that can measure intensity as a function of the color, or more specifically, the wavelength of light. It does this by dispersing the light beam into a spectrum of wavelengths, detecting the intensities with a CCD, and displaying the results as a graph. The output of a spectrophotometer is usually a graph of light intensity versus wavelength. In the 'Ocean Optics Spectrophotometer' light enters the spectrophotometer through a slit and is reflected to a grating with the help of a concave mirror. The dispersion grating [which is reflecting type] reflects the light after dispersion, towards the second concave mirror. This mirror focuses the light onto the detector.

At the end of the light path, there is a detector (CCD). Each pixel on the CCD measures the intensity of a specific wavelength of light; hence the more photons absorbed, the more electrical signal generated. Therefore, the electrical signal output from each pixel is proportional to the light intensity of the corresponding wavelength. The PL system used in the present work has two spectrophotometers. The first spectrometer (USB 2000, Ocean Optics) has a slit width of 25  $\mu\text{m}$  with a grating of 600 lines/mm and is attached to a 2048 pixel, linear array detector (Sony ILX511) charge coupled device (CCD) detector having an average sensitivity of 0.7 in the 330-1000 nm. The pixel size is 14  $\mu\text{m}$  X 200  $\mu\text{m}$  with a well depth of 62,500 electrons. The signal-to-noise ratio at full signal is 250:1 with A/D resolution of 12 bits. The  $f/\#$  number of the spectrometer is  $f/4$  with a focal length of 40 mm. It consists of a grating blazed at 500 nm so as to achieve peak efficiency in the 400-700 nm range. The integration time can be varied from 3 ms to 65 s. Technical specification of the slit width, number of line on the grating and the grating blaze angle were custom made as per our specifications.

The second spectrometer (NIR 512, Ocean Optics) consists of a grating with 1200 lines/ mm with a slit width of 50  $\mu\text{m}$ . This spectrometer is attached to a thermoelectrically cooled 512 element, InGaAs array detector (Hamamatsu G9204-512). The array has an average sensitivity of 0.7 in the wavelength range 900-1700 nm. The  $f/\#$  number of this spectrometer is  $f/4$  with a focal length of 40 mm. The pixel size is 25  $\mu\text{m}$  X 500  $\mu\text{m}$  and the pixel well depth is 188 million electrons. The signal to noise ratio is 4000:1 with A/D resolution of 16 bits. The integration time can be varied from 1 ms to 5 s for this spectrometer.

**Optical resolution** is the ability of a system to distinguish, detect, and/or record physical details by electromagnetic means. The system may be imaging (e.g., a camera) or non-imaging (e.g. a quad-cell laser detector). The electromagnetic spectrum ranges from Gamma rays to the Radio waves spectrum. A minimal optical system consists of a lens and a sensor. The optical resolution (OR) in nm of the opto-electronic system here can be defined as

$$OR = (Grating\ Spectral\ Range * Pixel\ Resolution) / \{Number\ of\ Detector\ Elements\} \quad (2.9)$$

For the detector in the 350-900 nm range, this was calculated to be 1.67 nm while for the detector in the 900-1700 nm it was calculated to be 2.34 nm.

#### 2.4.2B Optical fibers

A Reflection fiber probe [with 5 illumination fibers and 1 read fiber, each with a core diameter of 400  $\mu\text{m}$ ], was used for signal collection in the backscattering mode. The fiber had a flexible metal sheathing with “sub miniature version A (SMA) termination” that could be fastened to the spectrophotometer. The total length of the fiber was 2 m which allowed flexibility in making the experimental arrangement. Bifurcated fiber cable with a core diameter of 400  $\mu\text{m}$  and length 2 m with SMA termination is used when both of the spectrophotometers are to be used simultaneously so as to scan the wavelength range 330-1700 nm. An in-line-filter holder with SMA termination is attached to the spectrophotometer so as to avoid the excitation wavelength from getting picked up by the detector. The fiber probes with the lens and filter constituted the transmission system in this unit.

#### 2.4.2C Software package

Analysis and display system consists of a computer with the custom made software to control the spectrophotometers. The software has provision to provide electronic shutter which can be used to control the signal collection

timing. There is also option to average the total number of reading to be taken. Thus a spectrum could be plotted as the average of [maximum] 100 number of collection trails by the detector. A boxcar averaging program was used to improve the signal-to-noise ratio. The program was used to average the results obtained on each pixel of the CCD detector. The software could be used to command all of the pixels to monitor a single wavelength. This provision allowed to do time dependent decay of the signal. There was provision to monitor 7 wavelength channels at a time i.e. the time dependent variations of seven wavelengths could be monitored simultaneously.

#### *2.4.3 Closed cycle liquid He cryostat-A cooling system*

The cooling system consisted of a closed cycle (CCR) liquid He (Model CCS-100/202) optical cryostat, from Janis Research Inc. The temperature range for the loaded cryostat was  $\sim 10$ -325 K with a cooling power of  $\sim 2.5$  W at 20 K. The cryostat had a 'two stage cold head' with a cold finger of 3.81 cm diameter Cu- sample mount and a 25 ohm control heater. Temperature sensor (a Si diode) was fitted on the cold head which was interfaced with a Lakeshore (Model 321) temperature controller having an accuracy of  $\pm 1$  K. Initial cool down time was  $\sim 90$  minutes to reach 10 K for the CCR with the optical sample holder alone.

#### *2.4.3A Modifications for signal collection*

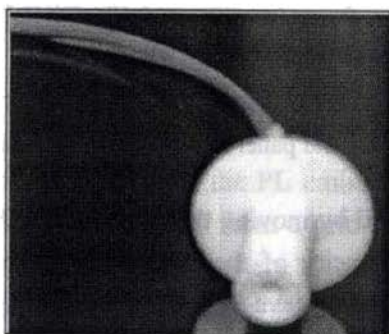


**Fig. 2.9:** Teflon mounting for insertion into the cryostat.

One of the optical windows was removed and steel mounting was fabricated which had an ordinary glass window at one end and was open at the other end. A Teflon mounting was fabricated with a small hole through which the optical fibre could be inserted. This piece could be inserted into the steel mounting and fixed to the cryostat so that the optical fibre could be placed at a distance of  $< 1$  cm from the sample, without breaking the vacuum. Also, since the fibre position

could be adjusted from the outside, it could be varied to select the ideal position from where maximum signal could be collected.

#### 2.4.4 Mechanical translator system

A positioning apparatus for performing coarse and fine positioning of samples for scanning is termed as 'XYZ translator'. The least count of the xyz translator used is 0.225  $\mu\text{m}$ . Experiments were carried out with larger step sizes because of limitation imposed by the excitation spot size. At the end of the rod, a sample could be mounted such that the translation mechanism could move the rod in different directions so that the sample could be scanned. Stepper Motor Control was used to control the motion of the XYZ translator. With the help of a system interface, the scanning process could be carried out automatically over the sample.

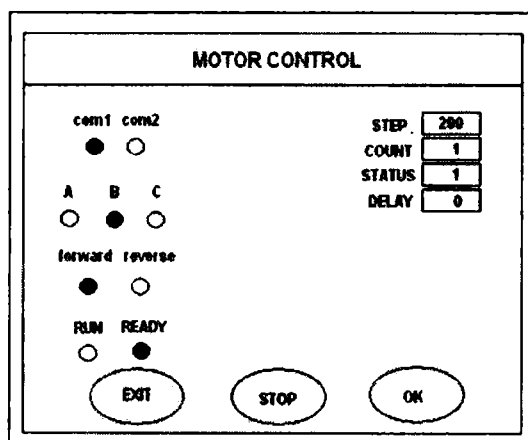


Fig. 2.10: Schematic of the front end panel of software used for stepper motor control.

An image was generated by moving the sample in a (X-Y) mode and storing the digitized values of intensity of the spectrum at each point. Moving the sample while the probe beam stays stationary in space has the advantage of fixing the probe beam shape and power density. These parameters remain constant throughout the measurement, allowing a quantitative comparison of data on a point by point basis, without generation of image artifacts due to spatial variations in the probe beam and the non-linear response of PL due to power density. The front panel of the Motor Control is as shown in Fig. 2.10.

The low-temperature PL scanning set-up is shown in Fig. 2.11. Here imaging is done with the sample mounted on the cold head of the closed cycle liquid He cryostat. Instead of the sample translation, here the beam spot is scanned over the sample surface by mounting the laser on the mechanical system. The beam was focused on to the sample through one of the optical windows of the cryostat [with the diameter of 0.5 mm]. Another optical window, at 90° to this, was modified with the Steel coupling unit which allowed the insertion of the optical fibre into the cryostat without breaking the vacuum, as explained earlier. The fibre was mounted with a lens into this unit and was brought to a distance <5 mm from the sample mounted on the cold head, which enabled the collection of the PL signal from the far field.

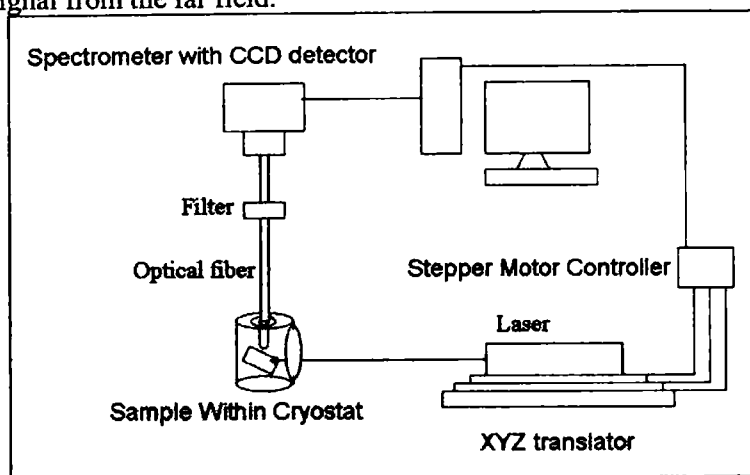


Fig. 2.11: Schematic of the low temperature PL scanning system.

To make a spectroscopic image of the PL emission intensity, we recorded the PL emission at a single wavelength from a grid of points, yielding a three dimensional matrix of data,  $M(x, y, I)$ , where  $x$  and  $y$  are position coordinates and  $I$  the intensity. By moving the translation stage, signal intensity at each point of the sample was collected. This was converted into a false color image, where the color was coded as a function of the signal intensity. The color palette followed the spectrum (blue, green, yellow, orange, red) with the minimum and maximum of the intensity of the signal, represented by the blue and red colors respectively. In single wavelength (topography) measurements, the decrease in signal strength may be due to a shift in the peak wavelength, rather than due to the decrease in absolute intensity. To avoid this artifact, peak wavelength, as a function of spatial position, was also recorded and the data was processed to

produce contour map of peak wavelength. A spectroscopic image of the PL peak wavelength was developed from a three dimensional matrix of data,  $H(x, y, W)$ , where  $x$  and  $y$  were position coordinates and  $W$  was the PL peak wavelength.

Figure 2.12 shows the results of a PL scan at 12 K of  $\text{CuInSe}_2$  thin films over an area of 8 mm X 6 mm, grown using Physical Vapor Deposition (PVD) technique. The step size for the X-Y translation was 1 mm and the stop size was 0.5 mm for this experiment. The spatial variation in emission intensity of the 1278 nm emission is plotted. Peak position of PL emission is known to be very sensitive to fluctuations of composition of ternary and quaternary semiconductors.<sup>37</sup> A direct correlation between deep level PL and micro-defect has been recognized in GaAs and Si crystals.<sup>38, 39</sup> Since thermal broadening and quenching effects are smaller in deep level PL, the radiative recombination process is simple, leading to the semi-quantitative mapping of the defects responsible for the PL.

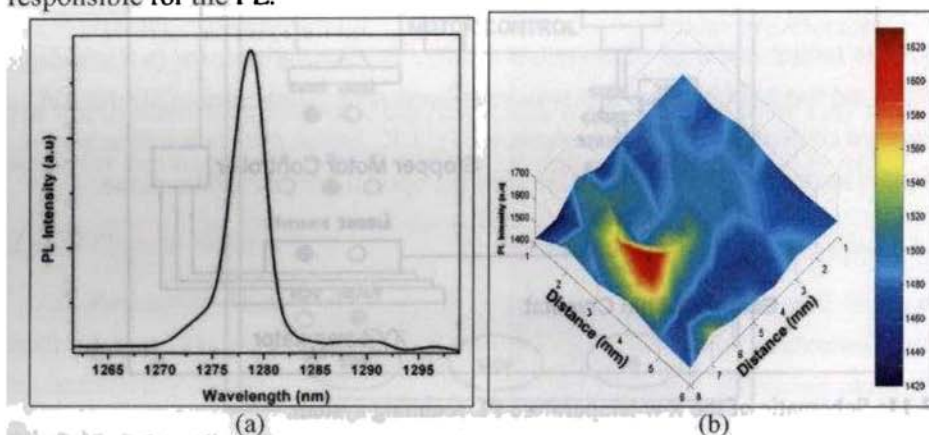


Fig. 2.12: PL emission at 1278 nm at 12 K for a  $\text{CuInSe}_2$  sample grown using Physical vapor deposition (a) PL spectra at a singular point and (b) Spatial PL intensity map.

The intensity of a deep level transition ( $I_{DL}$ ) is given by<sup>40</sup>

$$I_{DL} \propto n_{ex} \tau N_D \quad (2.10)$$

where  $n_{ex}$  is the concentration of the excited carriers,  $\tau$  is the carrier lifetime and  $N_D$  is the concentration of the deep levels. Relation (2.10) shows that the intensity  $I_{DL}$  is proportional to  $\tau N_D$ . Thus, if the variation of  $\tau$  on a film is small, the variation of  $I_{DL}$  will reflect the distribution of deep levels. Damages in the near-surface layer, due to non-uniform film growth, can result in the increase of non-radiative recombination rate causing the integrated PL intensity to vary from point to point in the sample. Intensity of the band edge transition  $I_B$  is proportional to the carrier lifetime  $\tau$  or is inversely proportional

to the concentration of the killer centers.<sup>14</sup> In general, the band edge recombination intensity is given by relation<sup>10, 40</sup>

$$I_B \propto n_{ex}^2 h \tau \quad (2.11)$$

where  $h$  is the Planck's constant and  $n_{ex}$  the number of excited carriers.

PL line width and peak position of the scanned region showed a variation within the expected 5 % variation due to the variation in laser spot, during translation. Hence it was concluded that the film was of uniform composition in the scanned region. An area of 1 mm<sup>2</sup> showed larger luminescence intensity compared to rest of the scanned region. But it did not show any variation in PL peak position. Hence it was concluded that this non-uniformity could be due to increase in  $n_{ex}$  resulting from variation in thickness. Had there been a variation in  $\tau$ , it would have resulted in variation in peak position. The emission at 1278 nm was identified to be the 'bound exciton emission', arising from the exciton bound to the V<sub>Cu</sub> acceptor.<sup>41</sup> Based on this result and using the relation (2.10), it could be concluded that the intensity variation map of the PL emission at 1278 nm, shown in Fig. 2.12, reflected the in-homogeneity in the spatial distribution of the V<sub>Cu</sub> defect level over the film.

The schematic for backscattering mode of PL at room temperature is shown in Fig. 2.13. The laser beam was focused onto a split fibre bundle, by using a lens and SMA assembly coupled to the fibre bundle. The 1/e<sup>2</sup> diameter of the final spot on the sample was 0.5 mm. The split fibre had five collection and one illumination channels. Laser light was brought in by the illumination channel. The collection channel, with the in-line-filter holder, was fed into the spectrophotometer. The optical fibre bundle was brought to an optimal distance from the sample from where the maximum signal strength of the backscattered luminescence signal could be detected. Position of the fibre bundle was then fixed with no further disturbance. The signal intensity collected by the fibre at 90° to the incident excitation beam was larger than that collected in the back scattering mode.<sup>42</sup> This improvement in signal collection was in direct agreement with earlier reports made on the use of tip illumination/far field collection for PL measurements.<sup>43</sup> The limited throughput of collection lead to the decrease in collected PL signal in the back scattering mode. Increase in numerical aperture of collection optics lead to high collection efficiency, which could be one reason as to why improvement in signal collection occurs in the former technique. Using the above set up, the laser backscattered image for Cu- rich and In-rich CuInSe<sub>2</sub> thin films was obtained. There existed a correlation between the Atomic Force Microscopy (AFM) image and the image constructed using back-scattered

laser light.<sup>44</sup> The Cu- rich sample contained triangular surface features for the grains, as seen from AFM image. Such features on the surface of absorber layer, in photovoltaic technology, are of immense use, as it reduces reflection loss and enhanced light trapping in solar cells.<sup>45</sup>

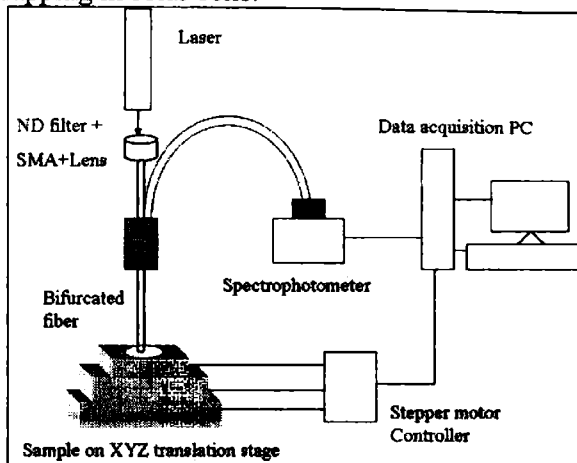


Fig. 2.13: Schematic of the room temperature PL scanning system in the back scattering mode.

## 2.5 Integration of Photo-conductivity Experiments

PC studies involve I-V measurements conducted under dark (reference) and under illumination (with intensity of light and its wavelength as parameters). A low temperature PC set up should consist of the following parts:

- A. Excitation Source
- B. Light Dispersing element
- C. Chopper to deliver light pulses
- D. Detection system, and a
- E. Cryostat

For PL system since parts A, B and E had already been assembled only parts C and D were further required to extend the capacity of the system to perform PC experiments.

### 2.5.1 DC photo-conductivity

A constant DC voltage source (Aplab) was used to provide DC bias voltage up to 30 V. Silver electrodes of area 5 mm<sup>2</sup> were deposited over the films with a separation of 5 mm between them. A resistor was connected in series to the sample. An oscilloscope was used to measure the decay of photo-voltage across this resistor, as a result of the illumination pulse on the sample. A capacitor was



used for some samples parallel to this load resistor to improve the signal to noise ratio. The time constant of the resultant RC network and the illumination pulse width used were smaller than the lifetime of the carriers in the material.

### 2.5.2 AC- photo-conductivity

The kinetics of the ac-PC was studied from its frequency dependence ( $\Delta\sigma_{ac}(F)/\Delta\sigma_{st}$ ): where  $\Delta\sigma_{ac}$  is the ac-component of the ac-PC,  $\Delta\sigma_{st}$  is the steady state conductivity and F the chopping frequency. AC-photo-conductivity (AC-PC) measurements were carried out to measure the lifetime ( $\tau$ ). The lifetime of the charge carriers can be determined for each temperature, applied voltage and light intensity using the relation <sup>46</sup>

$$\Delta\sigma_{ac}(F)/\Delta\sigma_{st} = \tanh(1/4F\tau) \quad (2.12)$$

The lifetime is calculated by drawing a straight line parallel to the frequency axis at a height of 0.76 from the maximum (where  $\tanh 1 = 0.76$ ) and a normal drops from the point of intersection on the frequency axis to cut off a segment equal to  $1/4 \tau$  from the frequency axis.

An Optical chopper (SR 450) (Stanford Research Inc.) was used to deliver symmetric pulses of the excitation beam. Photo current generated in the sample was passed through a load resistance ( $\sim 10$  ohm) and the variation of voltage developed across the load resistance, due to modulated PC, was measured using the oscilloscope [Tektronix TDS210]. The data was collected by a computer through an interface.

## 2.6 Conclusions

Photovoltaic requires a robust tool which can non-destructively evaluate the quality of each layer of the cell at each stage of production. PL is an ideal tool for this purpose because of its versatility. The strength of PL lies in its ability to analyze the surface and interface. An instrument for measuring the PL and PC was fabricated and was optimized for measurements on semiconducting thin films. Because the absorption of most materials depends on energy, penetration depth of the incident light will depend on the excitation wavelength. Hence, different excitation energies probe different regions of the sample. Different lasers were used as excitation sources in PL and PC. Photovoltaic devices have a wide band gap window material, a mid band gap buffer layer and a small band gap absorber layer. Hence optical analysis of the cell structure requires a wide wavelength range. The system was developed to work in the 350–1730 nm

wavelength range, which makes this useful for analysis of almost all of the semi-conducting compounds currently being used in our opto-electronic industry. One of the major criteria in any industrial fabrication process is in quality testing and checking uniformity over large area of the wafer. As an initial step, in the present work, a system was fabricated, which can be used for spatial mapping at room temperature and low temperature. This was used for scanning over an area of 8 mm X 6 mm at 12 K while at room temperature. The system is designed to work in the 10-300 K temperature range. Intensity or wavelength dependent experiments described in this thesis have been done using this set up. The system has a resolution of 4 meV (chapter 3). From the details presented here and from the works described in the following chapters, one can conclude that system is versatile. This is capable of performing spatial studies at low temperature, which is normally absent in many systems. Since PC studies can also be done along with the PL study in this system, the system itself is a complete unit for optical and electrical measurements.

## 2.7 Reference

1. Baly, E. C. C., Spectroscopy, Longmans, Green, London, (1912).
2. Proc. 3<sup>rd</sup> Inter. Symp. On Defect Recognition and Image Processing in III-V compounds (DRIP III), Tokyo, (1989) Ed. Ogawa, T., J. Crystal Growth, **103** (1990).
3. Nishimura, H., J. Lumin. **36**, 75 (1986).
4. Kawai, T., Arai, I. and Karasawa, T., J. Phys. Soc. Japan, **58**, 969 (1989).
5. Leverenz, H. W., An Introduction to the Luminescence of solids. New York: Dover, (1968).
6. Lumb, M. D., Luminescence Spectroscopy, Academic, NY (1978).
7. Dean, P.J., "Photoluminescence as a diagnostic of semiconductors", Progress in Crystal Growth and Characterization, vol. 5. p. 89 (1982).
8. Annual Book of ASTM standards (American Society for Testing and Materials, Philadelphia) F1 Proposal P213 (1989).
9. Nakashima, H. and Shiraki, Y., Appl. Phys. Lett. **33**, 257 (1978).
10. Hovel, H. J. and Guidotti, D., IEEE Trans. Electron Devices ED-**32**, 2331 (1985).
11. Wettling, W. and Windsheif, J. Appl. Phys. **A40**, 191 (1986).
12. Tajima, M., Semi-Insulating III-V Materials, Malmö, (1988) Eds. Grossmann, G. and Ledebø, L., Hilger, Bristol, p. 119 (1988).
13. Minaev, N. S. and Mudryi, A. V., Phys. Stat. Solidi (a), **68**, 561 (1981).

14. Michio Tajima, *J. Cryst. Growth*, **103**, 1 (1990).
15. Bube, R. H., *Photoelectronic Properties of Semiconductors*, Cambridge University Press, Cambridge (1992).
16. Orton, J. W. and Blood, P., *The Electrical Characterization of Semiconductors: Measurement of Minority Carrier Properties*, Academic, London (1990).
17. Pisarkiewicz, T. and Kuta, S., *Meas. Sci. Technol.* **9**, 1007 (1998).
18. Rakhshani, A. E., *J. Phys: Condens. Matter*, **12**, 4391 (2000).
19. Singh, S. N., Gandotra, R., Singh, P. K. and Chakravarty, B. C., *Bull. Mater. Sci.* **28**, 317 (2005).
20. William R. Imler, *IEEE Journal of selected topics in quantum electronics*, **1**, No. 4, 987 (1995).
21. Kruithof, A. A., *Modern Light Sources*, in *Advanced Optical Techniques*, A. C. S. van Heel, Ed, North Holland, Amsterdam (1967).
22. Seigman, A. E., *Lasers*, University Science Books, Mill Valley Calif. (1986).
23. Wright, J. C., *Lecture notes on Experimental Spectroscopy*, University of Wisconsin, Madison (1990).
24. Schäfer, F. P., *Dye Lasers*, Springer-Verlag, Berlin, vol. I (1977).
25. Maiman, T., *Nature*, **187**, 493 (1960).
26. Hendrson, B. and Imbusch, G. F., *Optical Spectroscopy of Inorganic Solids*, Clarendon, Oxford, ch. 11 (1989).
27. Moore, J. H., Davis C. C. and Coplan, M. A., *Building Scientific Apparatus*, Addison-Wesely, Menlo Park, Calif. (1989).
28. Ajoy Ghatak and Thyagarajan, K., *Optical Electronics*, Cambridge University Press, New Delhi (1991).
29. Vij, D. R., *Luminescence in Solids*, Plenum Press, NY (1998).
30. Adams, M. J., *An Introduction to Optical Waveguides*, John Wiley and Sons, Chichester (1981).
31. Michael Bass (ed), *Hand book of Optics. Devices, Measurements, & Properties*, Vol II, second edition, McGraw Hill, NY (1998).
32. Greivenkamp, John E., *Field Guide to Geometrical Optics*, SPIE Field Guides vol. FG01, p. 29 (2004).
33. Engstrom, Ralph W., *Photomultiplier Handbook*, RCA (1980).
34. Jacob Mllman and Christos C. Halkias, *Electronic Devices and Circuits*, Tata McGraw-Hill, New Delhi (1991).
35. Louis Lenert, H. *Semiconductor Physics, Devices and Circuits*, Charles E. Merrill publishing company, Ohio (1968).

36. Jayakrishnan, R., Deepa, K. G., Sudha Kartha, C. and Vijayakumar, K. P., *J. Appl. Phys.* **100**, 046104 (2006).
37. Pritchard, R. E., Collis, N. C., Hamilton, B., Thompson, J., Carr N. and Wood, A. K., *Semi. Con. Sci. Technol.* **8**, 1162 (1993).
38. Mooradian, A. and Fan, H. Y., *Phys. Rev.* **13**, 873 (1966).
39. Slichter, C. P., *Principles of Magnetic Resonance*, Springer, Berlin (1978).
40. Leo, K., Rühle, W. W., Nordberg, P. and Fujii, T., *J. Appl. Phys.* **66**, 1800 (1989).
41. Deepa, K. G., Jayakrishnan, R., Vijayakumar, K. P., Sudha Kartha, C., Ganesan, V., Phase, D. M., Kashiwaba, Y. and Abe, T., To be Communicated
42. Jayakrishnan, R., Tina Sebastian, Sudha Kartha, C. and Vijayakumar K. P., *J. Phys.: Conference Series* **28**, 62 (2006).
43. Safvi, S. A., Liu, J. and Kuech, T. F., *J. Appl. Phys.* **82**(11), 5352 (1997).
44. Jayakrishnan, R., Ratheesh Kumar, P. M., Sudha Kartha, C. and Vijayakumar, K. P., *Meas. Sci. Technol.* **17**, 3301 (2006).
45. Patric Campbell and Martin Green, A., *J. Appl. Phys.* **62**(1), 243 (1987).
46. Ryvkin, S. M., *Photoelectric Phenomenon in semiconductors*, NY, p. 40 (1964).

## CHAPTER 3

### Photo-luminescence in Analysis of $\text{CuInS}_2$ Thin Films

---

*Thin films of  $\text{CuInS}_2$  were prepared using Chemical Spray Pyrolysis technique, and the variation in photo-luminescence emission due to deviations in atomic ratio of the elements / stoichiometry is presented in this chapter. Variations in 'near band edge' (exciton) emissions from samples having different compositions were investigated as a function of temperature and excitation intensity. These studies revealed the ionization energy of the exciton to be 20 meV in these thin film samples. Recombination of the free exciton, belonging to the deep lying  $\Gamma_7$  valence band, was also observed. A correlation between the free exciton "A" ( $\text{FE}_A$ ) emission and the composition of the films could be identified. Position of the  $\text{FE}_A$  emission for stoichiometric, In-excess and Cu-excess films were identified. The possibility of using spatial mapping of  $\text{FE}_A$  emission for quality analysis of the films has been demonstrated with due importance. Based on the position of the  $\text{FE}_A$  emission, the substrate temperature and concentration of the precursor solution for depositing good quality samples was also optimized. Position of the intrinsic defects like vacancies of Sulphur, Indium and Copper has been identified using photo-luminescence studies on samples of different stoichiometry.*

#### 3.1 Introduction

In recent years, ternary compounds, with chalcopyrite (Ch-) type crystal structure, has received great attention of different research groups, as suitable candidates for next generation opto-electronic devices.<sup>1</sup> The  $A^I B^{III} X_2^{VI}$  Ch- crystal structure resembles the Zincblende structure where each of the two cations  $A$  and  $B$  are coordinated tetrahedrally by four anions  $X$ ; but the anion is coordinated by

$2A+2B$ , with generally dissimilar nearest neighbor bond lengths  $R_{AX} \neq R_{BX}$ . The unit cell is thus tetragonal.<sup>2</sup> Each ternary Ch- has a “binary II-VI chemical analogue” derived by taking the “average cation” of  $A+B$ . Thus,  $ZnX$  is the binary analogue  $CuGaX_2$  ( $X= S, Se$  and  $Te$ ) and  $Zn_{0.5}Cd_{0.5}X$  is the binary analogue of  $CuInX_2$ , etc. Studies have shown that electronic energy band structure of the I-III-VI<sub>2</sub> chalcopyrite is anomalous in several ways.<sup>3, 4</sup> The principal questions were ‘why the energy band gap of the ternary compounds were as much as 1.6 eV less than the energy gap of the respective binary analogs’ and again ‘why the spin-orbit splitting  $\Delta_{S.O.}$  observed in the ternary compounds are considerably smaller than the corresponding values obtained in the binary analogues’. It was suggested that these anomalies were resulting from a hybridization of the p- like valence bands with the noble-metal  $d$  levels.

The uppermost valence bands of Ch-compounds are lifted due to simultaneous influences of spin-orbit and crystal-field interactions, caused by the uniaxial tetragonal distortion of the crystal lattice ( $c/a$ ) and the displacement of group VI anions, from the ideal position  $[(1/4, 1/4, 1/8)]$  of the Ch-structure]. The  $3d$  or  $4d$  electrons of the noble metal hybridize with the p- like valence band ( $p-d$  hybridization) due to the proximity of their levels and causes the band gap energy of the Ch-compounds to become smaller than the corresponding II-VI analog compounds.<sup>5</sup> The above two effects along with lower crystal symmetry make the effective masses of Ch-compounds larger than those of II-VI compounds having comparable band gap energies, thus causing the absorption coefficient of Ch-compounds to become very large.<sup>6</sup> The  $CuInS_2$  chalcopyrite structure is shown in Fig. 3.1. It possesses the tetragonal  $E1$ , structure –type space group  $I\bar{4}2d$ , with four formula units per cell.

$CuInS_2$  is a prototype of the I-III-VI<sub>2</sub> chalcopyrite family of compound semiconductors.<sup>2, 3</sup> Polycrystalline  $CuInS_2$  thin films can be prepared by a variety of deposition techniques, such as Chemical Vapor Transport (CVT), Co-evaporation, Reactive Magnetron Sputtering, Chemical Bath Deposition (CBD), sulphurization of Cu-In precursors, Aerosol-assisted Chemical Vapor Deposition or Chemical Spray Pyrolysis (CSP).<sup>7-14</sup> Whichever is the technique employed, problems with stoichiometry may be anticipated and the film properties are critically influenced by deviations from stoichiometric composition and defect chemistry.<sup>15</sup>

Compositional relations in the ternary phase diagram of Cu, In, S can be expressed by the quantities, ‘molecularity deviation’ [ $\Delta m$ ] and ‘stoichiometry deviation’ [ $\Delta s$ ], which is also referred to as the valency<sup>16</sup>

$$\Delta m = \{[Cu]/[In]\} - 1$$

$$\Delta s = \{2[S]/([Cu] + 3[In])\} - 1$$

(3.1)

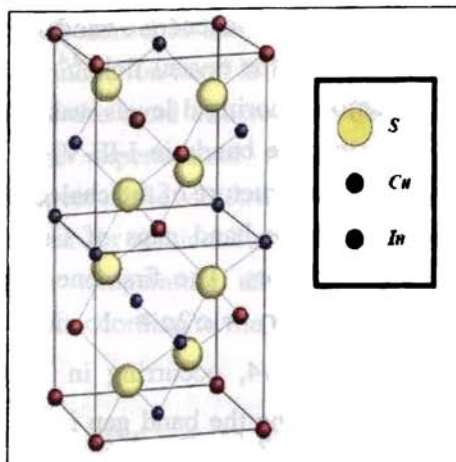


Fig. 3.1: The crystal structure of  $\text{CuInS}_2$ .

The meaning of deviations from molecularity and stoichiometry can be described as follows:

1.  $\Delta m > 0$  Cu-rich films (possibly secondary phase  $\text{Cu}_{2-x}\text{S}$ )  
 $\Delta m < 0$  In-rich films (possibly secondary phase  $\text{In}_2\text{S}_3$ )
2.  $\Delta s > 0$  Excess of Sulphur  
 $\Delta s < 0$  Sulphur deficiency

The band structure of this compound is a bit complicated. The Cu 3d bands are expected to contribute to the highest valence band. The d-band mixing is probably responsible for the large downshift in the energy gap of this compound, with respect to its II-VI analogues.<sup>17</sup> It is further reported that the highest valence band was a doublet with admixture of Cu 3d wave functions. Negative spin-orbit splitting of about 20 meV and crystal-field splitting below 5 meV were also reported in this system.<sup>18, 19</sup> Neumann et al. worked on flash evaporated  $\text{CuInS}_2$  thin films and identified the ground state energy of the free exciton to be about 8 meV.<sup>20</sup>

Also an indirect transition at  $1.565 \pm 0.005$  eV was observed and ascribed to an optical transition from the valence band maxima at the boundary of the Brillouin zone to the lowest CB minimum at the zone centre. Three further optical transitions, well above the fundamental edge, were observed; but their origin was speculated to be due to Copper d-states in the VB. Raman and

luminescence studies revealed that the VB of the CuInS<sub>2</sub> crystals is split into an upper non-degenerate valence band (A-band) and lower double degenerate bands (B- and C- bands).<sup>21-24</sup> This splitting of 19 meV was identified to be due to spin-orbit interaction and the double-degenerate bands were identified to be due to vanishing of the splitting due to the crystal-field.<sup>2,4</sup> Shay and Kasper showed that the energy band calculation ignoring d levels was unable to account for the structure of the upper-most valence bands in I-III-VI<sub>2</sub> compounds.<sup>25</sup> The work established the split valence band structure of the chalcopyrite compounds.

It has been concluded that the band gaps of Cu-III-VI<sub>2</sub> chalcopyrite are controlled essentially by two factors. The first one is pure structural factor, caused by the tetragonal distortion,  $\eta = c/2a \neq 1$ , and anion displacement from the ideal tetrahedral site,  $u \neq 1/4$ , occurring in the Ch- structure. These parameters, particularly  $u$ , determine the band gap in the system. Even a small increase of  $u$  from its ideal Zinblende value results in a substantial ionic polarization of the bonds and consequently in a remarkable increase of the band gap. The second one is an electronic factor. There was a great influence of the Cu 3*d*-states on the valence band of Cu-III-VI<sub>2</sub> chalcopyrite. These states hybridize with the *p*-states of the group VI components. As the *d*-states are found in the upper half of the valence band, they are responsible, in part, for the reduction of the band gap.

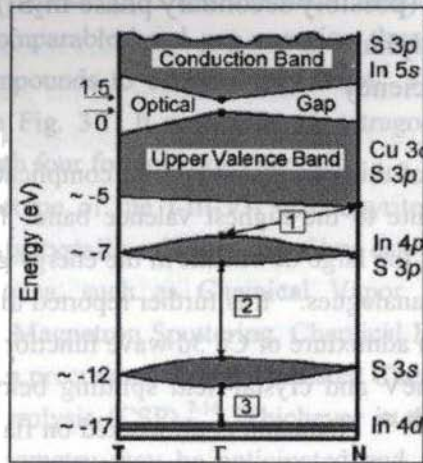


**Fig. 3.2:** Schematic band structure of CuInS<sub>2</sub>, with the indication of contributions of the atomic orbital and the corresponding energy levels. Shaded areas denote the major sub bands, and the boxed numbers mark the three internal gaps.<sup>26</sup>

Schematic band structure of CuInS<sub>2</sub> is shown in Fig. 3.2, with notation of the contributions of the atomic orbital. The valence band is separated into two parts,



with the upper part reaching 5 eV and the lower one located around 7 eV. The Cu 3*d* and S 3*p* orbital from the Cu-S bond contribute to the upper valence band whereas the S 3*p* and In 4*p* from the In-S bond form the lower valence band. At around 12 eV a band is built from S 3*s* states and a narrow band is set up near 17 eV by In 4*d* orbital. The conduction band is formed by S 3*p* and In 5*s* orbitals.<sup>26</sup> Theoretical calculations of the band structure of CuInS<sub>2</sub> were found to be in good agreement with the experimental results from X-ray Photoelectron Spectroscopy (XPS) in respect of the VB structure.<sup>27, 28</sup>

As is normally expected for semiconductors, the band gap of CuInS<sub>2</sub> films decreases with increasing temperature and can be characterized over the temperature range 300-77 K according to the relation<sup>29</sup>

$$E_g(T) = E_{g0} - \{\beta T^2 / \alpha + T\} \quad (3.2)$$

With the initial band gap of  $E_{g0} = 1.62$  eV, two constants  $\alpha = 231.54$  K and  $\beta = 4.3 \times 10^{-4}$  eV/K were determined.<sup>30</sup> Near the fundamental absorption edge, CuInS<sub>2</sub> has an absorption coefficient between  $10^4$  to  $10^5$  cm<sup>-1</sup>; because of which the incident light with photon energies higher than the band gap are absorbed within a few microns.

The historic development of the ternary chalcopyrite CuInS<sub>2</sub> into an efficient thin film solar cell absorber material was well reviewed by Lewerenz.<sup>31</sup> Today's situation is that we have an efficient CuInS<sub>2</sub> thin film solar cell with very little decisive information about the properties leading to good opto-electronic performance. CSP has been tried by several authors to deposit good quality CuInS<sub>2</sub> thin films. The variation in lattice constants and band gap of sprayed I-III-VI<sub>2</sub> chalcopyrite thin films were studied by Pamplin et al.<sup>32</sup> Gorska et al. used Cu<sub>2</sub>Cl<sub>2</sub>, InCl<sub>3</sub> and CS(NH<sub>2</sub>)<sub>2</sub> as the precursor solution for preparing CuInS<sub>2</sub> thin films.<sup>33</sup> Nitrogen was used as the carrier gas. Few drops of HCl were added to the solution to increase the stability of Cu<sub>2</sub>Cl<sub>2</sub>. The spray solution was maintained at 100 °C. Films were p-type and properties were found to be dependent on the substrate temperature. Spray pyrolysis conditions required to prepare single phase CuInS<sub>2</sub> films, were optimized by Tiwari et al. using Copper (II) acetate, InCl<sub>3</sub> and CS(NH<sub>2</sub>)<sub>2</sub> as the precursor solutions.<sup>34</sup> They observed that the properties of the films could be controlled by varying the Cu/In ratio in the spray solution. Sphalerite structure of the 'as deposited' films transformed to chalcopyrite on annealing. Bihri et al. deposited single phase CuInS<sub>2</sub> [Ch-structure], by spraying CuCl<sub>2</sub>, InCl<sub>3</sub> and CS(NH<sub>2</sub>)<sub>2</sub> in the ratio 1:1:3.<sup>35</sup> It had been observed that concentration of residues originated from the precursors and was

mainly controlled by the growth temperature. The content of impurity was less depending on the Cu/In ratio in the spray solution as the use of Cu-rich solutions lead to larger crystallites and lower impurity concentration. Improvement in stoichiometry of these films was achieved by increasing the Sulphur content in the spray solution. Single phase films with preferential orientation along (112) plane having chalcopyrite characteristic peak (103) was obtained by increasing the Sulphur content.<sup>36</sup>

Physico-chemical characterization of CuInS<sub>2</sub> thin films deposited using CSP technique showed that good quality films could be obtained on SnO<sub>2</sub> (F) coated glass substrates.<sup>37</sup> Their XPS study revealed the presence of Oxygen, bound to cations. Band gap was found to be closer to that of the single crystals as the substrate temperature was increased. Etching in KCN solution and thermal treatment in vacuum and Hydrogen were applied to 'as deposited' films by Krunk et al.<sup>38</sup> They observed that etching resulted in removal of conductive Copper Sulphide phase from the surface of Cu-rich films, but had no effect on the matrix composition. Vacuum annealing resulted in n-type films due to the formation of In<sub>2</sub>O<sub>3</sub> phase. Treatment in Hydrogen resulted in p-type CuInS<sub>2</sub> films. Marsillac et al. studied properties of films deposited at 650 K and the effect of Sulphur treatment at the same temperature on the properties of these films.<sup>39</sup> They observed improvement in crystallinity after heat treatment. They also reported that heat treatment lead to lower conductivity and higher activation energy. Changes in electrical properties were attributed to the replacement of Oxygen present at the grain boundaries.

Mellikov et al. studied the effect of the composition of starting solutions on the phase, chemical composition and the structure of the sprayed CuInS<sub>2</sub> thin films.<sup>40</sup> Cu/In ratio in the films was found to be higher than that in the solution for all the samples. In-rich and S-rich solutions lead to the multiphase films with poor crystallinity. Belgacem et al. reported that a substrate temperature  $T_s \geq 590$  K with ratio of [Cu]/[In]=1.1 in the pulverized solution permitted well crystallized thin films with the preferential orientation along the (112) direction.<sup>37</sup> For their best films, only 3–8 at.% of Oxygen was present, which was very promising for such a simple growth technique. Krunk et al. reported that the content of Cl, O, C and N impurities in sprayed CuInS<sub>2</sub> films were impurities from precursors which were mainly controlled by the growth temperature and in less extent, by the Cu/In ratio in spray solution.<sup>39</sup> The growth temperature of 260–280 °C resulted in Cl, C, N content of 8 mass% and the impurity phases contained SCN, CN, NH, SO<sub>4</sub> groups. The increase in the growth temperature up to 380 °C decreased the concentration of Cl, C, N to 1–2 mass%, concurrently

leading to oxidation of inorganic and organic phases resulting in O content of 16.7 at.%. Thermal treatments in reducing atmospheres at 450 °C improved the crystallinity of the films while annealing in flowing H<sub>2</sub> effectively reduced the percentage of Cl and O impurities.

López et al. studied the structural, electrical and optical properties of Na-doped CuInS<sub>2</sub> thin films grown by spray pyrolysis.<sup>41</sup> They observed that the films crystallized in the ‘Sphalerite’ structure of CuInS<sub>2</sub>, and contained traces of Indium Sulfide and CuIn<sub>5</sub>S<sub>8</sub> as impurity phases. Conductivity of the film was strongly affected by Na-doping, which decreased from 10<sup>-2</sup> to 10<sup>-5</sup> S/cm by increasing the [Na]/[Cu] ratio from 0.005 to 0.03 in the spray solution. Band gap increased, from 1.4 to 1.45 eV, with increase in the [Na]/[Cu] ratio. Aksay and Alt deposited polycrystalline CuInS<sub>2</sub> films using CSP technique at different substrate temperatures.<sup>42</sup> They reported that the direct band gap value varied between 1.51-1.80 eV, depending on the substrate temperatures.

### 3.2 Photo-luminescence of CuInS<sub>2</sub>

The PL of CuInS<sub>2</sub> single crystals in the ‘near band edge’ regions and in the regions away from the band edge have been investigated by Binsma et al.<sup>43</sup> A series of five sharp lines in the region 1.50–1.55 eV were reported which were related to the excitonic emissions. The near-edge (exciton) emissions were investigated for various material compositions, as a function of temperature. From their investigations, the exciton ionization energy (20 meV) and the temperature dependence of the energy gap were determined. For the first time, recombination of the free exciton, belonging to the deeper lying  $\Gamma_7$  valence bands, was reported. Moreover, six different ‘bound exciton emission’ lines and another one corresponding to ‘donor-to-VB transition’ were detected. These emissions could be assigned in terms of the defect chemical model. The study of PL emission as a function of the exact composition in terms of deviations from molecularity and stoichiometry by means of temperature dependent (4.2–220 K) and excitation intensity dependent measurements were also carried out.<sup>44</sup> In In-rich material, an acceptor level, located at 0.1 eV above the valence band was identified. This acceptor level was ascribed to vacancy of Copper (V<sub>Cu</sub>). In Cu-rich CuInS<sub>2</sub> the acceptor level was located at 0.15 eV above the valence band, which was attributed to either vacancy of Indium (V<sub>In</sub>), or to the Copper on Indium antisite (Cu<sub>In</sub>). Two donor levels were identified, with ionization energies of about 35 and 72 meV. These donors were present in both In- and Cu-rich

samples and were speculated to be due to either **intrinsic defects** or **impurities** (Fe).

Tell et al. reported that the free exciton energies at 1.537 eV and 1.556 eV, respectively were due to A-band and C-bands in  $\text{CuInS}_2$  crystals.<sup>4</sup> Single crystals grown using 'Traveling Heater Method (THM)' by Wakita et al. exhibited sharp peaks at 1.531 eV and 1.525 eV. They assigned these to the free exciton ( $\text{Ex}_1$  and  $\text{Ex}_2$  emission) lines.<sup>45</sup> A third line at 1.52 eV was assigned to 'donor-valence band transition' which was hidden in the low energy tail of the  $\text{Ex}_2$  emission. Broad emission bands at 1.435 eV and 1.410 eV were also identified. Ueng and Hwang reported the same emission lines in THM grown crystals at 1.529, 1.526, 1.520, 1.447 and 1.410 eV.<sup>46</sup> They argued that the peaks at 1.529, 1.526 and 1.520 eV correspond to exciton, bound to a neutral acceptor (vacancy of Cu ( $\text{V}_{\text{Cu}}$ )), exciton bound to a neutral donor (vacancy of Sulphur ( $\text{V}_{\text{S}}$ )), and a donor ( $\text{V}_{\text{S}}$ ) to VB transition respectively. Verheijen, who carried out measurements at 4.2 K, reported one additional exciton emission line at 1.509 eV in  $\text{CuInS}_2$  crystals but did not observe the 1.517 eV line reported by Tell et al.<sup>4</sup>

Burns et al. reported the PL studies of  $\text{CuInS}_2$  thin films and solar cells, as a function of post deposition treatments, for different temperatures and excitation intensities. They observed that annealing in Hydrogen atmosphere caused an increase of PL intensity at 1.445 eV by more than a factor of 100, while subsequent annealing in Oxygen or air reduced this transition. This was ascribed to a DAP recombination between Sulphur vacancy and Copper vacancy. A defect mechanism was suggested, that assumed the passivation of Sulphur vacancies by Oxygen in grain surfaces which could be activated by Hydrogen annealing.<sup>47</sup>

Electrical and PL measurements were carried out on CVT grown  $\text{CuInS}_2$  single crystals in order to determine intrinsic defect levels in this material by Schön and Bucher.<sup>48</sup> Post-growth treatments [like annealing in vacuum, air, Cu-, In, and S atmospheres] were used to identify the electronic defect levels. Using these data, along with the formation energy of the intrinsic point defects and the stoichiometry of the samples, a band diagram, showing the defect levels in CVT grown  $\text{CuInS}_2$  single crystals, was proposed. Activation energy of the acceptor and donor defect states in Ch- compounds was calculated by using a model based on the effective-mass theory for the case of single-, double- and triple-point defect centers by Rincon and Marquez.<sup>49</sup> They found that the values of the energies of shallow and moderate deep levels were in reasonable agreement with those obtained from experimental data. From the analysis of their results, most of the levels, due to the presence of cation and anion vacancies, interstitials, cation-cation and cation-anion antisite disorders, had been identified.

Low temperature PL emission due to deep donor–deep acceptor (DD–DA) pair recombination and close DA pairs in CuInS<sub>2</sub> at  $h\nu = 0.62$  eV revealed two well resolved lattice vibrational modes of energy 40.5 meV and 8 meV.<sup>50</sup> The recombination emission had an additional fine structure of  $\Delta E = 2$  meV. They interpreted this fine structure as due to a small difference in the DA separation between two otherwise equivalent interstitial donor sites. This was due to the tetragonal lattice distortion in the CuInS<sub>2</sub> structure. The effects of annealing on PL spectra in CuInS<sub>2</sub> crystals, grown by THM, were investigated by Wakita et al.<sup>51</sup> They reported that, after the CuInS<sub>2</sub> crystals were annealed in vacuum at 400 °C, a bound exciton emission at 1.525 eV (Ex<sub>2</sub>) was completely quenched and a new bound exciton peak (Ex<sub>3</sub>) appeared at 1.520 eV. On the other hand, after annealing in contact with In<sub>2</sub>S<sub>3</sub> powder, PL spectra of exciton emission did not exhibit significant changes. Wakita et al. latter reported on the defect-related donor-acceptor pair emissions from the crystals.<sup>52</sup> The donor energy levels were deduced to be 36 meV and 63-69 meV. Acceptors were estimated to lie much deeper with energy levels at 113, 150, 180 and 220 meV.

Very recently, Ch- type CuInS<sub>2</sub>-based alloyed fluorescent nanocrystals (NCs), which contained no regulated heavy metal ions, were synthesized by heating an organo-metallic solution to demonstrate optical property tunability.<sup>53</sup> Introduction of Zn into the CuInS<sub>2</sub> system enhanced the PL intensity. The resultant particles were 3-6 nm; which varied with experimental conditions and were discrete and colloidally stable. The band gap energy and PL wavelength of Zn-Cu-In-S (ZCIS) NC's varied with Zn content and particle size. Their PL was controllable within 570-800 nm by altering the band gap energy. Furthermore, Indium substitution with Gallium changed the band gap energy towards ~ 3.1 eV. In addition, ZnS coating of this NC could approximately double the PL strength.

### **3.3 Sprayed CuInS<sub>2</sub> thin films for photovoltaic application**

Photovoltaic devices are most suited for the production of convenient and low-cost energy. But the major problem is in developing easily available and eco-friendly absorbers that can give reasonably high-efficiency cells. Recently, chalcopyrite semiconductors have been successfully used as absorber layers in polycrystalline thin-film solar cells.<sup>54-56</sup> Among them, the ternary compound CuInS<sub>2</sub> (CIS) has the potential to reach high conversion efficiencies due to its large absorption coefficient and direct band gap of 1.5 eV, which matches well with the solar spectrum. First photovoltaic device, based on this material, was

reported by Kazmerski et al.<sup>57</sup> They fabricated CIS based homo-junction solar cells with 3.62% efficiency. Recently CIS based solar cell, with an efficiency of 12.5%, was fabricated by Klaer et al.<sup>58</sup> The technology was based on sequential process, using DC-magnetron sputtering of the metals and sulfurisation. Siemer et al. obtained efficiency of 11.4% by using rapid thermal process for the preparation of CIS absorbers.<sup>59</sup> Cells having Copper rich CIS phase, prepared using thermal evaporation method, could achieve efficiency of 10.2%.<sup>60</sup>

This ternary chalcopyrite semiconductor is well established as a future material for photovoltaic applications. However not much of literature is available on PL analysis of sprayed CIS thin films. Also a correlation between the opto-electronic properties and the quality of the films has not been worked upon. The aim of this work was hence to first characterize the sprayed CIS thin films based on the PL signal. Experiments were carried out by varying the stoichiometry to identify the defects which could be identified using PL. Information has been obtained on the defects which are inherently formed during spraying. Dependence of PL peak energy position on the stoichiometry of the films has also been identified. PL has also been used as a tool to map spatial uniformity in sprayed films. One of the major results was the observation of a critical substrate temperature at which the film quality improved which was reflected by the absence of defect related emissions and presence of only excitonic PL emissions. It was also observed that temperature controlled the stoichiometry of the deposited films irrespective of the precursor solution.

### ***3.3.1 Preparation of CuInS<sub>2</sub> thin films using Chemical Spray***

#### ***Pyrolysis***

CIS thin films were deposited on ordinary micro glass substrates. These slides were cleaned using soap solution (Dextran) and were then placed on a base plate (Mild Steel) which was supported by a heater rod assembly, facilitating the heating of the substrate. Substrate temperature was maintained with the help of a feed back circuit that controlled the heater supply. Temperature of the substrate could be varied from room temperature to 723 K. When the solution was being sprayed, temperature of the substrate was maintained to an accuracy of  $\pm 5$  K. Both the spray head and the heater with substrate were kept inside a chamber, provided with an exhaust fan for removing gaseous by products and vapors of the solvents used. Aqueous solution containing CuCl<sub>2</sub>, InCl<sub>3</sub> and Thiourea (CS (NH<sub>2</sub>)<sub>2</sub>) in the required proportion was

sprayed onto the substrate, using compressed air as the carrier gas. The carrier gas and the solution were fed into the spray nozzle at pre-determined pressure and flow rate. Uniform coverage of large area substrate was possible by scanning the spray head by employing two stepper motors with 'gear and belt' mechanism. The spray head could scan an area of 15 cm x 15 cm. The X movement was at a speed of 100 mm/sec while movement in Y direction was in steps of 50 mm/sec. The microcontroller of the device communicated with the PC through serial port. The data of each spray could be stored in the PC. This spray system had been indigenously fabricated in our lab to facilitate deposition of films over a large area, with better uniformity and repeatability in results.

The spray rate was 1ml/min and volume of spray solution used for each spray was 40 ml. The distance between spray head and substrate was maintained at 20 cm. Thickness as well as roughness of the thin film samples were measured using Dektak 6M profiler. Crystallinity of the samples was analyzed using Rigaku (D. Max. C) X-ray diffractometer, employing Cu-K  $\alpha$  line ( $\lambda=1.5405 \text{ \AA}$ ) and Ni filter operated at 30 KV and 20 mA. Chemical composition of the films was determined with the help of Energy Dispersive X-ray analysis (EDAX) technique (JEOL JSM-5600). Depth profile [i.e., the variation of atomic ratio along the sample thickness] of the samples was obtained using X-ray Photoelectron Spectroscopy (XPS), (ULVAC-PHI unit, Model ESCA5600 CIM) employing Argon ion sputtering. Optical properties were studied using UV-VIS-NIR spectrophotometer (Jasco V-570 model).

For PL measurement, the sample was mounted on the cold finger of a liquid Helium cryostat (Janis Research Inc) and cooled to 11 K. The temperature was controlled to an accuracy of  $\pm 1$  K using a Lakeshore temperature controller (321 Auto tuning). The 632.8 nm line of a He-Ne laser (15 mW) was used as the excitation source. The beam was focused on to the sample so as to get a spot of radius 0.5 mm. A 632.8 nm filter was placed in front of the window, from where the emission signal was collected. An optical fiber was kept behind the filter at  $90^\circ$  to the incident beam, outside the cryostat. The emission signal, was collected by a split fiber bundle, and was focused into the USB2000 and NIR512 spectrophotometers.

A battery of  $\text{CuInS}_2$  thin films were prepared with varied stoichiometry. The band gap of the samples was calculated from optical absorption studies at room temperature and was found to vary depending on their stoichiometry. In-rich films were having the largest band gap whereas Cu-rich films possessed the lowest. Stoichiometric films were found to have an intermediate band gap between the In-rich and Cu-rich films. For gaining information on the nature of

the exciton emissions from the CuInS<sub>2</sub> thin films, the PL properties of the films were studied by dividing the samples into three groups. In the first group of samples the Cu/In ratio in the film was always >1 so that Cu-rich stoichiometry could be claimed. The ideal sample selected for the PL study was named CIS155 where the Cu/In ratio in the spray precursor solution was fixed at 1.5 and the S/Cu ratio was fixed at 5. In the next group the Cu/In ratio in the film was between 0.9 and 1 so that films could be classified as nearly stoichiometric. The ideal sample selected for PL study from this group was named CIS15 where the Cu/In ratio in the spray precursor solution was fixed at 1 and the S/Cu ratio was fixed at 5. In the third group the Cu/In ratio in the film was <0.8 so that films could be called In-rich. The ideal sample selected for PL study from this group was named CIS55 where the Cu/In ratio in the spray precursor solution was fixed at 0.5 and the S/Cu ratio was fixed at 5. In all these specimens the S/Cu ratio was kept a constant. These variations in the atomic ratio were made by changing the atomic ratio in the spray solution. EDAX measurements were used to verify the composition of the deposited films and these results are presented later in this chapter.

### ***3.3.2 Structural, optical and chemical analysis of CuInS<sub>2</sub> thin films***

Detailed studies on the structural properties using XRD and its compositional dependence have been well established and reported earlier.<sup>63</sup> The samples showed orientation along the (112) plane at  $2\theta = 27.91^\circ$ . The  $d$  value was found to be 3.192 Å which coincided with that of CuInS<sub>2</sub> in the standard JCPDS data card 270159. The samples which were Cu-rich showed good crystallinity and orientation along the (112) plane. As the Cu-content was increased, the intensity of the peak corresponding to the (112) and (220) plane increased. Figure 3.3 shows the XRD pattern of the films CIS55, CIS15 and CIS155. The grain size of the film was calculated from the peak at  $2\theta = 27.91^\circ$  using the Debye–Scherer formula

$$D = 0.9\lambda / \beta \cos \theta \quad (3.3)$$

where  $D$  is the diameter of the crystallites forming the film,  $\lambda$  is the wavelength of the Cu-K $\alpha$  line,  $\beta$  the FWHM in radians and  $\theta$  is the Bragg angle. The grain size was found to vary from 5.8 nm [for the In-rich films] to 21.2 nm [for the Cu-rich films].



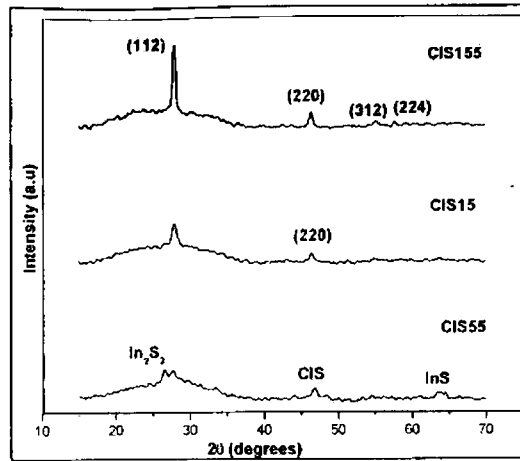


**Fig. 3.3:** XRD pattern of the  $\text{CuInS}_2$  thin films grown using Chemical Spray Pyrolysis. Precursor solution ratio for sample CIS55 was  $\text{Cu/In}=0.5$  &  $\text{S/Cu}=5$ , for sample CIS15 it was  $\text{Cu/In}=1$  &  $\text{S/Cu}=5$  and for sample CIS155 it was  $\text{Cu/In} = 1.5$  &  $\text{S/Cu} = 5$ .

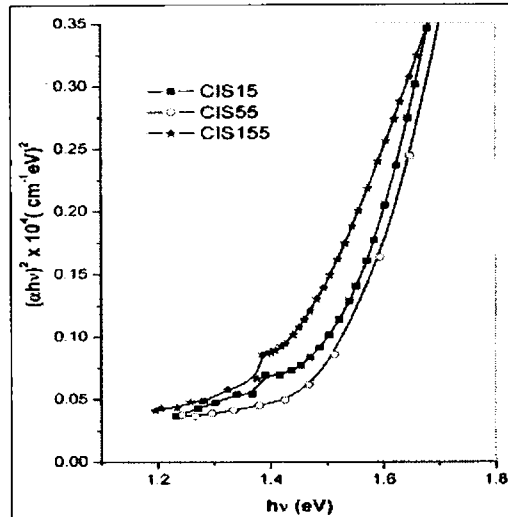


**Fig. 3.4:** Plot of  $(\alpha h\nu)^2$  versus  $h\nu$ , for samples CIS55, CIS15 and CIS155.

Figure 3.4 depicts the plot of  $(\alpha h\nu)^2$  versus  $h\nu$  for the samples with different stoichiometry. Optical absorption studies were carried out at room temperature. The band gap was found to decrease from 1.53 eV [for In-excess film] to 1.45 eV [for Cu-excess films]. The optical absorption also showed the presence of an optical absorption band at  $\sim 1.4$  eV for the Cu-excess and stoichiometric samples. This was absent in the In-rich films and hence was assumed to be due to defect related optical absorption, possibly due to the vacancies of Indium.

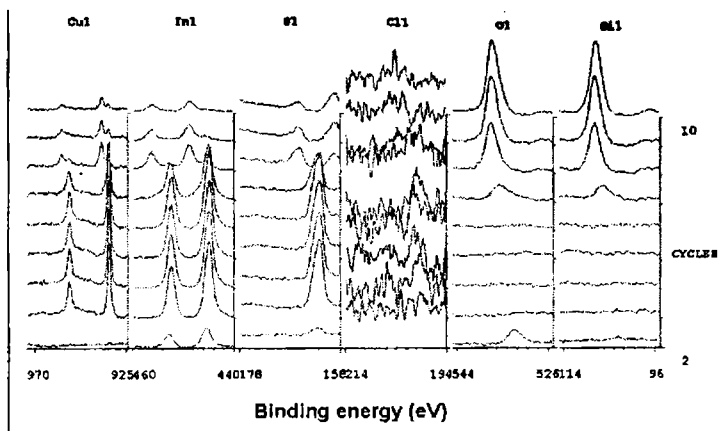


Fig. 3.5: XPS spectra for sample CIS55 on a glass substrate grown using Cu/In=0.5 and S/Cu=5 in the precursor solution.

Element	Binding Energy (eV)
Cu <sub>2p3/2</sub>	932.5
Cu <sub>2p1/2</sub>	952.5
In <sub>3d5/2</sub>	444.7
In <sub>3d3/2</sub>	452.7
S <sub>2p</sub>	162.0

**Table 3.1:** Binding energy value for the elements Cu, In and S from the CuInS<sub>2</sub> thin film.

Results of XPS analysis carried out on the samples to confirm the chemical nature of film are depicted in Fig. 3.5. All the elements diffused slightly into the glass substrate, due to the high temperature at which spray pyrolysis was carried out. But interestingly, Oxygen was present only at the surface of these samples in the form of an oxide contamination. It is worth mentioning here that this was in spite of using air as the carrier gas for the spray. The binding energy (BE) value of surface Oxygen was found to be 532 eV, which was due to surface contamination. Table 3.1 shows the binding energies of the elements obtained from the XPS studies. BE values of Cu, In and S indicated formation of CuInS<sub>2</sub>.

### 3.4 On the exciton emissions in CuInS<sub>2</sub> thin films

Emissions near the band edge in the 1.50-1.56 eV were observed at low temperature in the samples which were optimized, based on their stoichiometry and X-ray diffraction intensity. A total number of 12 samples were used for this study. More over the band edge emissions were always of lower intensity compared to the defect related emissions.

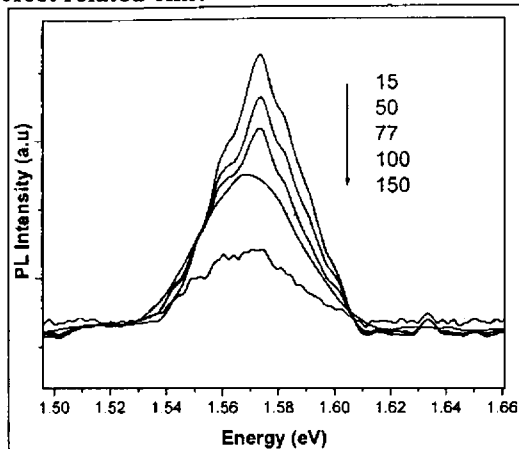


Fig. 3.6: Temperature dependence of PL for sample CIS55 from 15 K to 150 K.

Figure 3.6 shows the temperature dependence of band edge emission from sample CIS55 with Cu/In = 0.49 [From EDAX measurement]. The sample stoichiometry indicated the film to be In-rich and had a band gap of 1.53 eV at room temperature. The highest energy PL emission in the spectra was at 1.634 eV, as indicated in Fig. 3.6 and was due to secondary phase impurities of In<sub>2</sub>S<sub>3</sub> found in In-rich CuInS<sub>2</sub>. XRD pattern also proved the presence of In<sub>2</sub>S<sub>3</sub> phase and hence the result was well supported. There were other prominent emissions centered around 1.574 eV with a shoulder on the low energy side [ $\sim$  1.563 eV]. As the temperature was increased from 12 K, the PL emission intensity decreased. Again the low energy shoulder lost its significance with rise in temperature and merged indistinguishably with the main peak. Multiple fitting was used to resolve the peaks in the recorded spectra as shown in Fig. 3.7.

In spite of the numerous resolved peaks, analysis was concentrated on the temperature dependence of peak position and FWHM of the two resolved peaks at 1.574 eV and 1.563 eV. From the fitting, it could be seen that, at low temperature, the emission at 1.563 eV was more prominent than the emission at 1.574 eV. As temperature was increased, the relative intensity of the emission at

1.563 eV decreased faster than the emission at 1.574 eV. This was an evidence for the free exciton nature of these emission lines.

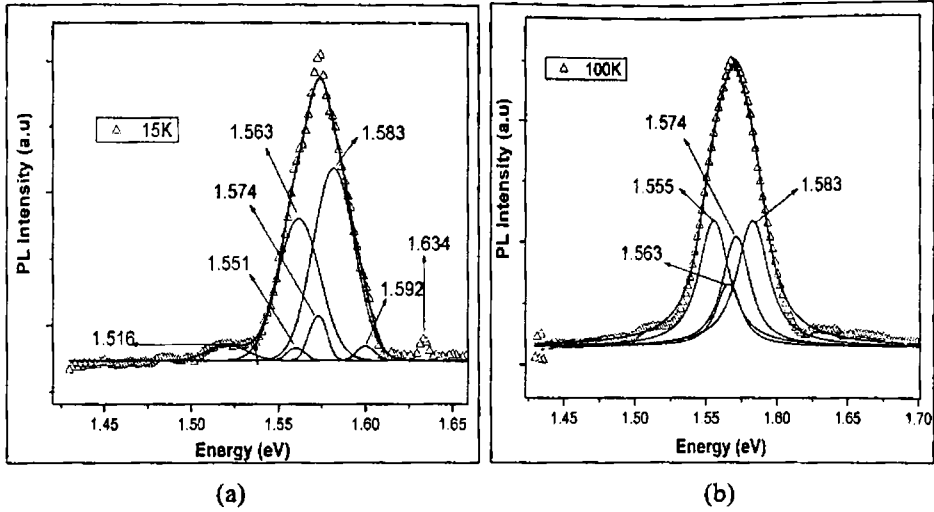


Fig. 3.7: Multiple curve fitting carried out to resolve the near band edge emission peaks at (a) 15 K and (b) 100 K.

The enhancement of relative intensity of the emission ( $I_1$ ) at 1.574 eV with increasing temperature was in accordance with the relation<sup>43</sup>

$$I_1 / I_2 = \exp(-\Delta E / kT) \tag{3.4}$$

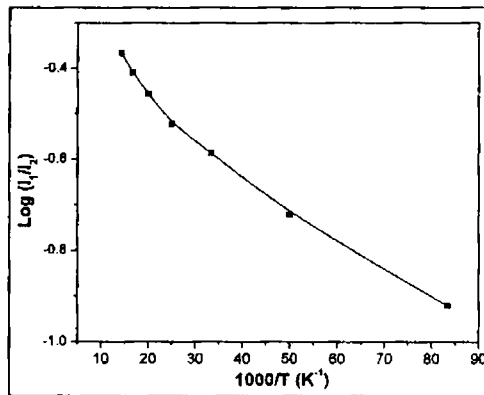


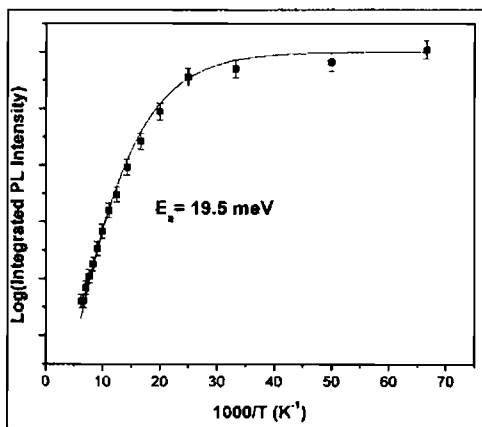
Fig. 3.8: Ratio of the intensities of the 1.574 eV and 1.563 eV emissions, ( $I_1 / I_2$ ) as a function of temperature.

Figure 3.8 shows the plot of the ratio of the intensities of the 1.574 eV and 1.563 eV emissions, as a function of temperature. The value of thermal activation energy  $\Delta E$  from this fitting (as per relation (3.4)) was obtained to be 10 meV. It was earlier reported that the level of free exciton, belonging to the double degenerate  $\Gamma_7$  valence band, lying near  $k=0$ , was about 10 meV below the

$\Gamma_6$  valence band. This was reported earlier for n-type  $\text{CuInS}_2$ .<sup>1</sup> From the agreement in  $\Delta E$ , the sample stoichiometry and the nature of increase in relative emission intensity with temperature, this emission at 1.574 eV was assigned to the “B” free exciton. Interpretation of this emission line in terms of the “A” free exciton or as a conduction band to the valence band transition could be excluded, because these emissions are to be present in both n- and p-type material. The absence of this emission in other samples also supported the assignment.

The emission line at 1.563 eV was attributed to the recombination of free exciton ( $\text{FE}_A$ ). For a relatively small band gap semiconductor, the excitons are Wannier type.<sup>16</sup> The photon energy  $h\nu$  of the radiative recombination of a free exciton is given by equation (1.30) (section 1.2.2A). The assignment of the free exciton ( $\text{FE}_A$ ) line was based on the following observations: Bound excitons have large binding energies and hence emit photons of lower energy. Hence based on relation (1.30) FE lines corresponding to states with  $l=1,2,3..$  can be expected. However, the energy separation and the relative intensities should be proportional to  $l^3$ .

Also the temperature dependence of the intensity does not allow the assignment of this emission to a bound exciton. Further evidence of the free exciton nature of the FE line was provided by the fact that the positions (peak energy) of the emission lines do not change with rise in temperature.



**Fig. 3.9:** Plot of  $1000/T$  vs.  $\text{Log}(\text{Integrated PL intensity})$  for the 1.563 eV emission fitted using relation (3.5).

The temperature dependence of PL intensity for the emission at 1.563 eV was fitted using relation<sup>62</sup>

$$I(T) = I(0) / (1 + C \exp(-\Delta E / k_B T)) \quad (3.5)$$

where  $I(T)$  represents the intensity at temperature  $T$ ,  $C$  a constant which is a measure of the capture cross-section and  $\Delta E$  represents the activation energy of the non-radiative recombination. For  $\Delta E$ , a value of 19.5 meV was obtained from the fitting as shown in Fig. 3.9. As the quenching of the free exciton line takes place when the exciton dissociates forming free charge carriers,  $\Delta E$  should be equal to the exciton binding energy ' $\epsilon_x$ ' as given by relation (1.30). The "A" free exciton binding energy in  $\text{CuInS}_2$  has been calculated to be 20 meV earlier.<sup>2</sup> The agreement of the obtained value with earlier reported value validated the assignment of this emission to the free exciton emission. Thus this emission at 1.563 eV in sample CIS55 could be assigned to the "A" free exciton emission  $\text{FE}_A$ .

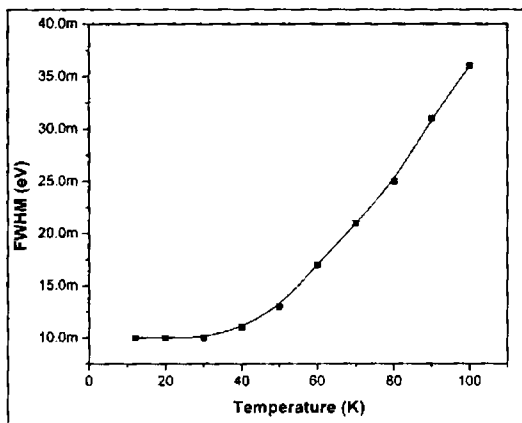


Fig. 3.10: Line width of the emission at 1.563 eV as a function of temperature.

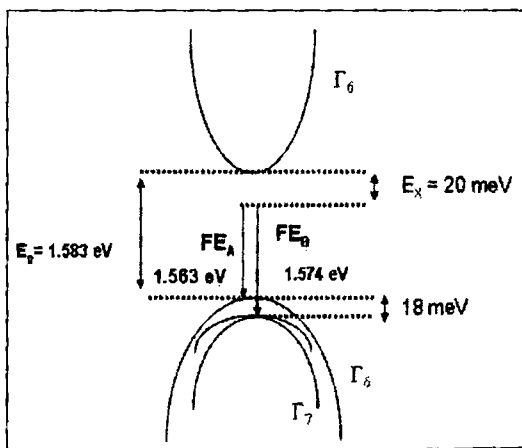
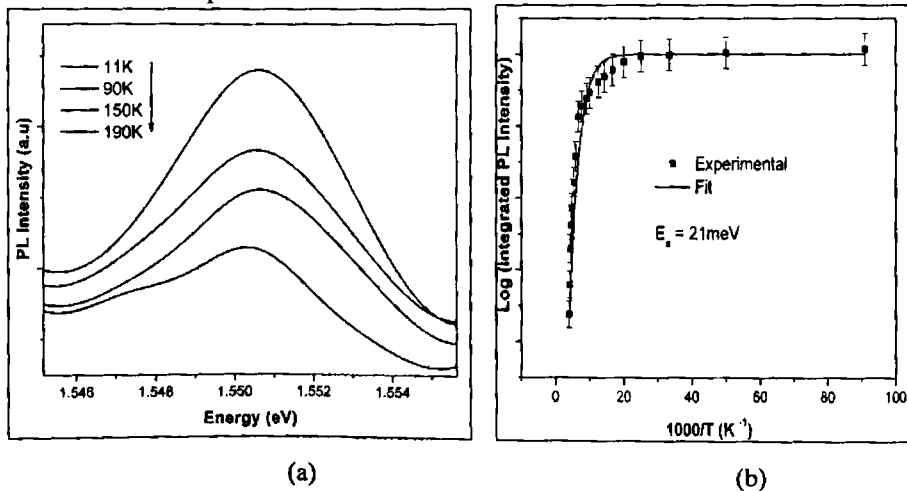


Fig. 3.11: Band diagram for sample CIS55 at 15 K.

In Fig. 3.10, temperature dependence of the line width of the free exciton emission  $\text{FE}_A$  has been plotted in the range 12–120 K. Up to 60 K, the line width

increases very gradually to around 18 meV, and at higher temperature, the width increases up to  $\sim 35$  meV at 120 K. The temperature broadening can be explained on the basis of decrease in lifetime of the  $k = 0$  state because, as the temperature increases, states with higher  $k$  become more populated.<sup>17</sup> Thus the number of occupants at the lowest state [ $k = 0$  state] is reduced which empty rapidly by the radiative decay while the higher states follow non-radiative transitions. Schematic band diagram of  $\text{CuInS}_2$  near  $k = 0$  with the free exciton transitions  $\text{FE}_A$  and  $\text{FE}_B$  is shown in Fig. 3.11.

When the stoichiometry is changed from an ‘n-type, In-rich  $\text{CuInS}_2$  thin film’ to a ‘stoichiometric  $\text{CuInS}_2$  thin film’ with no excess of ‘Cu’ or ‘In’ in the film, there is a change in position of the  $\Gamma$  valleys and hence in the band gap of the material. To identify these changes, a stoichiometric film was prepared. These samples (CIS15) were deposited with  $\text{Cu/In} = 0.94$  (based on EDAX) and could be called ‘nearly stoichiometric’. The PL line with the highest photon energy was located at 1.550 eV. There were no additional band edge emissions from the samples with this stoichiometry. Temperature dependence of the PL emission in this sample is depicted in Fig. 3.12. This band edge emission was not detected above 150 K. The temperature dependence of the emission intensity was fitted using relation (3.5) and  $\Delta E$  was found to be 21 meV. Hence this emission was assigned to the ‘A’ free exciton in this sample. There were no shoulders or splitting in this high energy emission. The ‘B’ exciton emission has been rarely observed in stoichiometric and Cu-rich samples. Thus it could be conclusively assumed that the emission at 1.550 eV was the  $\text{FE}_A$  emission for the stoichiometric samples.



**Fig. 3.12:** (a) Temperature dependence of PL in sample CIS15 from 15 K to 190 K and (b) Plot of  $1000/T$  vs.  $\text{Log (Integrated PL intensity)}$  for the PL emission fitted using

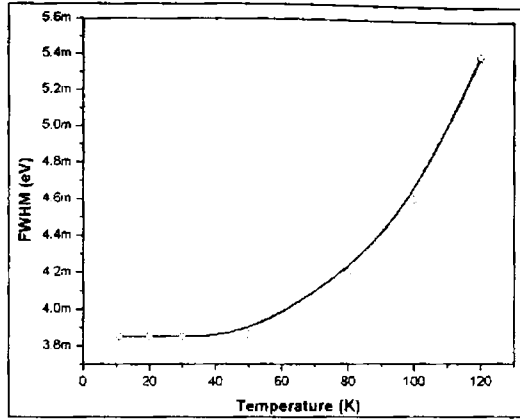


Fig. 3.13: Line width of the emission at 1.550 eV as a function of temperature.

Another strong proof to the assignment was the line width of the emission at 1.55 eV. The line width was only  $\sim 3.8$  meV at 12 K and was nearly independent of the temperature up to 50 K, beyond which it increased exponentially as shown in Fig. 3.13.

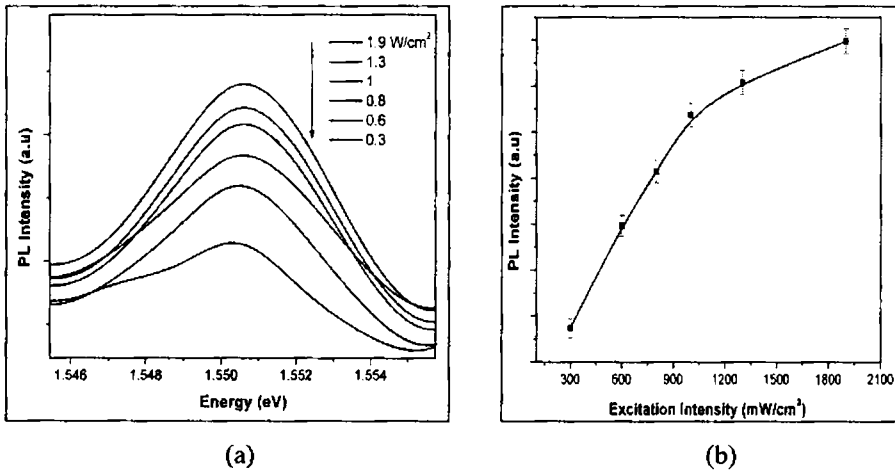


Fig. 3.14: (a) Excitation intensity dependence of 1.55 eV emission line at 15 K and (b) Plot of excitation intensity vs. PL intensity fitted using relation (1.57).

Figure 3.14 depicts the dependence of PL spectra on excitation intensity in this sample. As the excitation intensity was increased, there was a small shift of the peak position towards the higher energy side as evident from Fig. 3.14(a). But this shift was beyond the measurable limit of the detection system. Variation in intensity of emission with excitation intensity at 15 K was fitted using the relation (1.57) (section 1.2.5C). The value of  $\gamma$  was obtained to be 1.3 from the



fit (Fig. 3.14(b)) which was another proof, supporting the assignment of this emission to the exciton emission.<sup>63</sup>

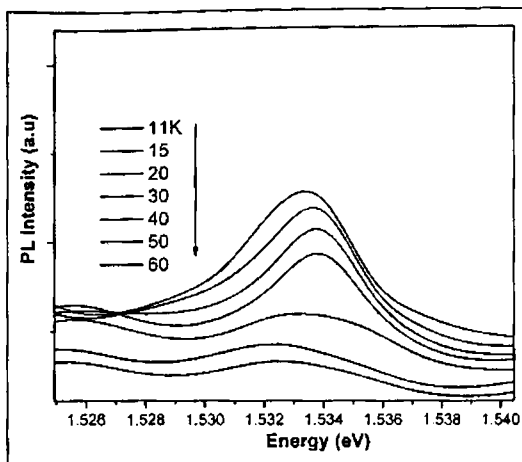


Fig. 3.15: Temperature dependence of PL emission in sample CIS155 from 11 K to 60 K.

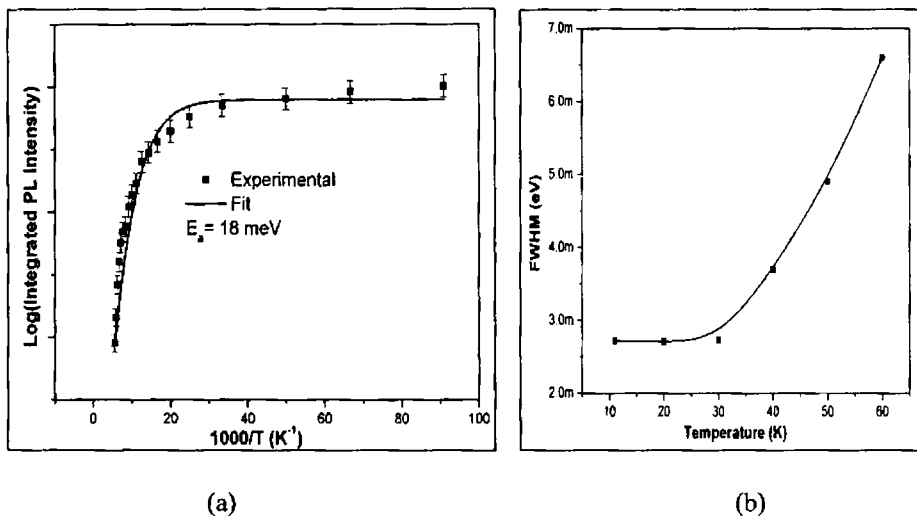


Fig. 3.16: (a) Plot of  $1000/T$  vs Log (Integrated PL intensity) for the 1.533 eV emission fitted using relation (3.5) and (b) Temperature dependence of FWHM for the emission.

Cu-rich samples (CIS155) with  $\text{Cu/In} = 1.24$  (based on EDAX) were analyzed next, for their band edge emissions. The highest energy of the PL emission was at 1.533 eV. The emission was not detected above 60 K from this sample. Most of the Cu-rich films exhibited band edge PL spectra like the one given in Fig. 3.15. The peak position shifted to lower energy as the temperature increased (as evident in Fig. 3.15). At 11 K, the peak position was at  $\sim 1.533$  eV and at 60 K it was shifted to  $\sim 1.532$  eV. The temperature dependence of the emission intensity was fitted using relation (3.5) as shown in Fig. 3.16(a) and

$\Delta E$  was found to be 18 meV. This was close to the free exciton binding energy in  $\text{CuInS}_2$ . The “A” free exciton in Cu-rich  $\text{CuInS}_2$  was identified to be responsible for the 1.535 eV by Binsma et al.<sup>44</sup> Hence we assigned this emission to be the “A” free exciton emission in Cu-rich samples like sample CIS115.

The FWHM at 11 K was found to be 2.7 meV and remained nearly constant up to 30 K, beyond which it increased exponentially, as temperature was raised as shown in Fig. 3.16(b). It could be observed that thin films with this composition (Cu-rich) showed the smallest FWHM.

For sample CIS110, where the Cu/In ratio was taken to be 1 and S/Cu ratio was taken to be 10 in spray precursor solution, “S” concentration was the highest compared to all other samples from EDAX analysis. The observed PL emission was centered at 1.492 eV and 1.488 eV and was the **highest resolution** with which a spectrum could be recorded using the PL system designed for this work. The temperature dependence of PL emission from this sample is shown in Fig. 3.17(a). The 1.492 eV emission lost prominence and the emission at 1.488 eV gained significance as the temperature was raised. However the emission was quenched above 80 K. Activation energy of the emission, calculated from the temperature dependence of PL intensity using relation (3.5), gave a value of 10 meV (Fig. 3.17(b)). Hence it could be concluded that the emission at 1.492 eV was the  $\text{FE}_A$  emission line in this sample. The emission at 1.488 eV could be assigned to the  $\text{FE}_B$  exciton in this sample, which originated from excitons bound to defects or impurities.

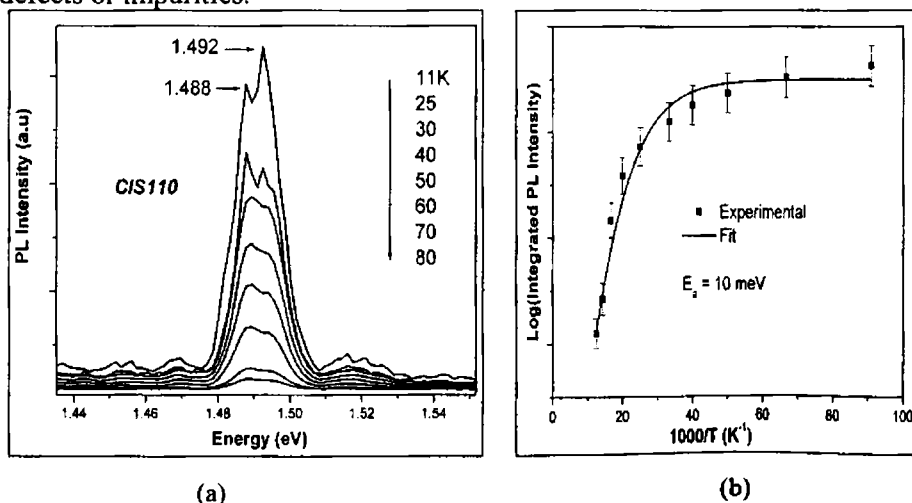
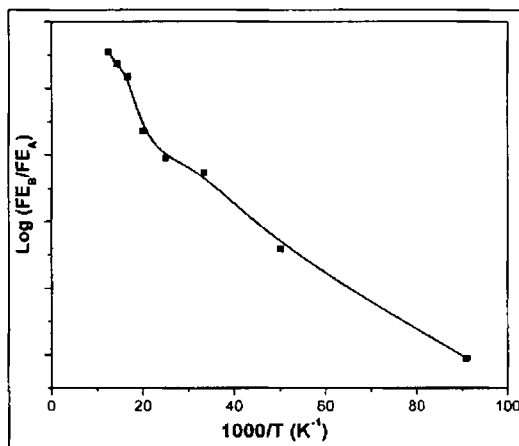


Fig. 3.17: (a) Temperature dependence of PL emission of sample CIS110 and (b) Plot of  $1000/T$  vs Log (Integrated PL intensity) of the 1.488 eV emission fitted using relation (3.5).

A proof of the exciton nature of these emission lines was evident in the temperature dependence of these lines. It is well established that the  $FE_B$  emission gains prominence compared to  $FE_A$ , as temperature is increased. The same was observed when temperature of the sample CIS110 was raised from 11 K to 25 K, causing the intensity of the emission at 1.488 eV to become more intense than the  $FE_A$  line. Figure 3.18 represents the plot of the relative intensity ( $FE_B/FE_A$ ) versus  $1000/T$ . The intensity of the  $FE_B$  line increased relative to the  $FE_A$  line according to the relation <sup>43</sup>

$$I_{FB} / I_{FA} = \exp(-\Delta E / kT) \quad (3.6)$$

From the fitting,  $\Delta E$  was found to be 10 meV which was in good agreement with the activation energy obtained from the temperature dependence of PL quenching. Thus it could be concluded that the emission at 1.488 eV was due to recombination of exciton belonging to the double degenerate  $\Gamma_7$  valence band.



**Fig. 3.18:** Ratio of the intensities of the emission at 1.488 eV to the 1.492 eV, as a function of temperature.

Thus it was observed that the position of the “A” free exciton varied with sample stoichiometry. Figure 3.19 gives the comparison of PL spectra at 12 K for a set of samples with different stoichiometry. Table 3.2 shows the observed position of the “A” exciton emission, their FWHM and the film stoichiometry for the same set of samples. From Fig. 3.19, it is evident that in these films the  $FE_A$  emission is very weak compared to other defect related emissions. Nevertheless, they provide a method of identifying the best films and their composition. Intensity of the emission is determined by the quality of the films. Comparison of the XRD pattern (Fig. 3.3) and the PL spectra (Fig. 3.19) showed that the intensity of the exciton emission was highest for the most crystalline

sample. Thus the film quality could be quantified in a batch of samples by comparing the intensity of the exciton emission in them. All samples do not show the  $FE_A$  lines but the films with emission lines at these specific positions are more crystalline and low resistive, compared to films with no  $FE_A$  emission line or lines at position different to that represented in Table 3.2.

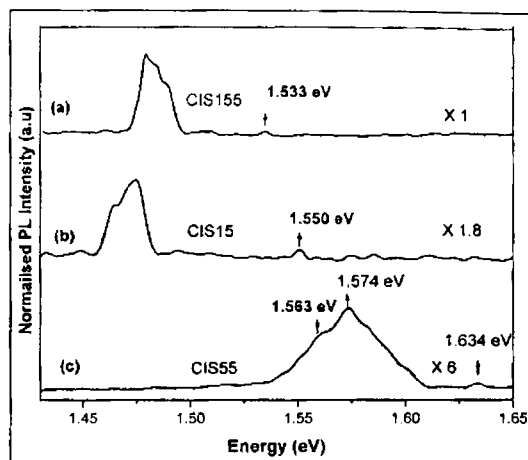


Fig. 3.19: PL spectra at 12 K for (a) sample CIS 155 with Cu/In = 1.24 (b) sample CIS15 with Cu/In =0.94 (c) sample CIS55 with Cu/In =0.49.

Sample Stoichiometry	"A" Exciton emission energy (eV)	FWHM at 11K (meV)	$\Delta m = [Cu / In] - 1$	No: of samples tested
In-rich	$1.563 \pm 0.003$	$10 \pm 2$	$-0.51 \pm 0.18$	4
Stoichiometric	$1.550 \pm 0.002$	$3.4 \pm 2$	$-0.06 \pm 0.08$	3
Cu-rich	$1.533 \pm 0.002$	$2.7 \pm 2$	$0.24 \pm 0.12$	5

Table 3.2: Peak position for the free exciton emission identified.

Sample CIS110 [which shows  $FE_A$  lines at 1.492 eV] is more resistive than CIS155 [which has  $FE_A$  line at 1.533 eV]. Though both films were Cu-rich in stoichiometry, CIS155 was more crystalline than CIS110. XRD analysis made it clear that grain size was the smallest for In-rich film and largest for the Cu-rich film which was the cause for band gap variation with stoichiometry. PL spectra suggested that the Cu-rich films possessed the lowest FWHM for the  $FE_A$  line while the In-rich had the largest FWHM. But the distinction limit is too small and hence could not be used as a quantifying tool. It is more established in

compounds grown using Metal-Organic Chemical Vapor Deposition (MOVCD) and MBE that the use of FWHM rather than the peak energy results in an accurate determination of composition.<sup>64, 65</sup>

In the case of sample CIS15, the relative exciton emission intensity (compared to the PL intensity due to defect related recombination) as well as temperature sustenance of the exciton emission was the highest. Thus it could be understood that, as the stoichiometry improved, the temperature sustenance and relative intensity of the band edge emission could be improved. Hence it was concluded that verification of the stoichiometry of the samples was possible from band edge emissions. Based on the above experiments it is concluded that the exciton emissions can be used to identify the composition of the CuInS<sub>2</sub> films. Out of a set of 12 samples put to random test, composition of 9 samples could be identified based on the position of the FE<sub>A</sub> emission line. Hence the success rate of this tool in establishing the composition of the films was found to be 75%.

### 3.5 Spatially resolved PL mapping

Growth techniques like MBE and MOVCD are used to develop device quality materials.<sup>66, 67</sup> This is essential to achieve good performance and better yield from the optical device. But one cannot use costly techniques like MBE or CVD for the preparation of devices like solar cells, where large area junctions are required. Hence cost effective and simple deposition techniques are essential. However large area samples prepared using simple techniques need strict characterization to know the uniformity in all respects. Performance of a solar cell can vary at different points due to the non-uniformity in the film, arising from different experimental artifacts like non-uniform film thickness, random defect distribution or deviation from stoichiometric growth due to extrinsic impurities. A simple technique to check these parameters becomes critical for large area cell fabrication.

For solar cells prepared using CSP technique, it was observed that the efficiency varied over different regions of the cell. In order to understand the reason for this spatial variation, PL surface-mapping study of the absorber layer of the cell was carried out. Experimental results based on “far field illumination” and “far field collection” for optical imaging is presented here. The results of PL surface scan, carried out at low temperature, on CuInS<sub>2</sub> thin films are presented in this section. Since it was established earlier that the FE<sub>A</sub> emission line

correlates to the chemical composition of the films and hence the intensity of this emission line was monitored spatially. Figure 3.20 represents a 3D plot of the spatial distribution of the  $FE_{\Lambda}$  emission line in the samples at 12 K. Samples of area 1 cm X 1 cm were scanned with a step size of 1 mm. The beam was focused to a spot of radius 0.5 mm.

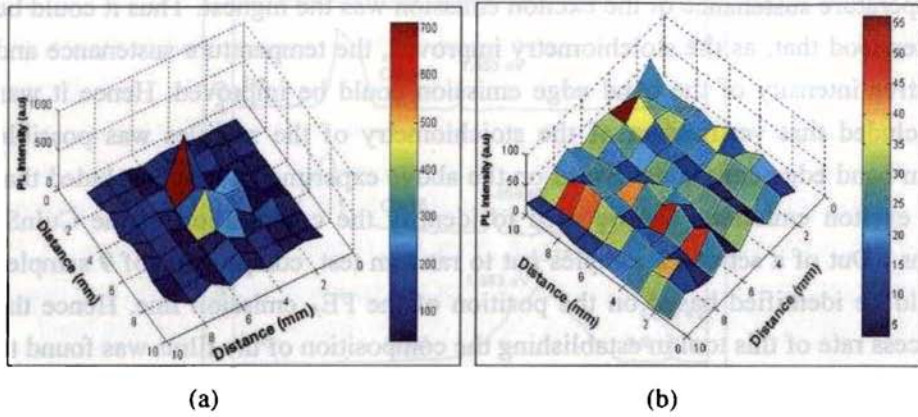


**Fig. 3.20:** Spatial distribution of intensity of (a) the emission at 1.42 eV in sample C1 [Cu/In=1.5; S/Cu=3] and (b) the emission at 1.53 in sample C2 [Cu/In=1.5 and S/Cu = 5].

To make a qualitative analysis using the obtained data we first defined a parameter “ $I(x, y)$ ” representing the intensity, whose correlation is being measured. Here the first index ‘x’ represents the intensity at a point and ‘y’ represents the number of points having the same intensity ‘x’. To measure the correlation between the two points [  $p, q$  ] we defined a correlation coefficient

$$\rho_{p,q} = \frac{\sum_{x,y} I^{(p)}(x, y) I^{(q)}(x, y)}{\sqrt{\sum_{x,y} [I^{(p)}(x, y)]^2 \sum_{x,y} [I^{(q)}(x, y)]^2}} \quad (3.7)$$

where  $I^p(x, y)$  and  $I^q(x, y)$  represent the quantity whose similarity is examined. The correlation coefficient  $\rho_{p,q}$  would be 1 for the highest correlation between two points  $p$  &  $q$ . Now  $\rho_{p,q} = 1$ , would mean that the quantities  $I^p(x, y)$  and  $I^q(x, y)$  are equal and as the value of  $\rho_{p,q}$  decreases from 1, the correlation between any of the two compared points decreases. Table 3.3 shows the average correlation coefficients in five different samples for the data taken from 72 different points on each sample. These coefficients clearly indicated that sample C1 possessed highest spatial homogeneity (correlation) among the set of samples put to test because for this sample  $\rho_{p,q} = 0.9$ , which indicated the least variation in intensity of the  $FE_{\Lambda}$  emission from point to point over the scanned area. This

was evident in the PL surface map developed as shown in Fig. 3.20(a), where most of the region was of the same color in sample C1.

For sample C2, the correlation coefficient was the least and the corresponding image supported this, as the variation in PL intensity over the scanned area (Fig. 3.20(b)) was minimal. It has been established that the intensity of the band edge transition ( $I_B$ ) in general is proportional to the carrier lifetime ( $\tau$ ) or is inversely proportional to the concentration of the killer centers.<sup>65</sup>

In general, the intensity of radiative band edge recombination emission is given by relation<sup>68, 69</sup>

$$I_B \propto n_{ex}^2 h \nu \quad (3.8)$$

where  $h$  is the Planck's constant and  $n_{ex}$  the number of excited carriers. This clearly indicated that the 'intensity variation map' of the exciton emission, shown in Fig. 3.20, reflected the in-homogeneity in the crystalline quality and /or composition of the film.

Sample	[Cu/In] ratio in precursor	[S/Cu] ratio precursor	FE <sub>A</sub> position	No: of points scanned	$\rho$ Correlation Co-efficient
C1	1.5	3	1.42	72	0.90
C2	1.5	5	1.53	72	0.44
C3	1.5	8	1.51	72	0.51
C4	1.5	10	1.48	72	0.56
A2	1	5	1.56	72	0.66
B2	1.2	5	1.53	72	0.45

**Table 3.3:** PL intensity correlation co-efficient for samples prepared with different precursor solution.

Based on this experiment, it could be concluded that sample C1 was the most homogenous among the specimens tested. This experiment also demonstrated the application of PL as a quality testing tool where a benchmark could be set with the correlation coefficient  $\rho$ . Specimen classification based on value of  $\rho$  in a

batch could be used in quality control in large scale production lines. When quality analysis in a batch of films is to be checked the average value of  $\rho$  in each sample can be set as a benchmark based on which faulty samples, low quality samples or good quality samples can be distinguished. For example in the above batch of samples C1 is the best quality sample while C2 and B2 are the samples of poor quality. Quality here refers to the spatial uniformity in the  $FE_A$  emission which is associated with good crystalline quality of the material and to its chemical composition.

### 3.6 Broad band defect related PL emissions in $CuInS_2$ thin films

For gaining information on the defects/impurities in the films, the PL properties of the films were studied by dividing the samples into two groups. In the first group, Cu/In ratio was varied keeping the S/Cu ratio constant. In the second group of samples, S/Cu ratio was varied by maintaining the Cu/In ratio constant. These variations in the atomic ratio were made by changing the ratio in the spray solution.

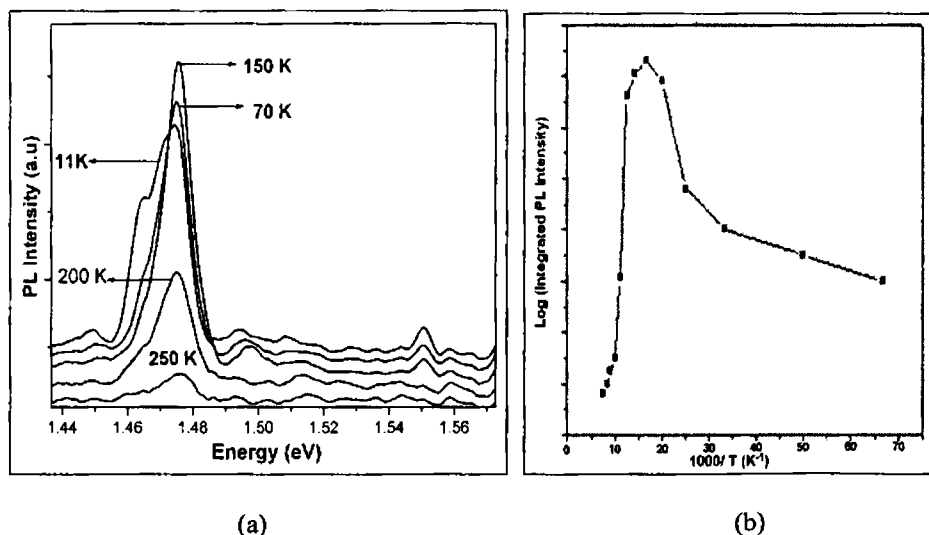


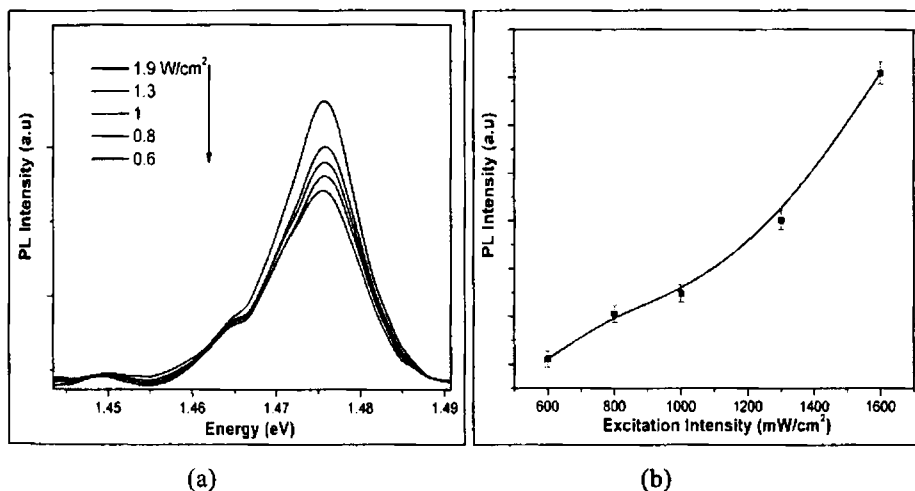
Fig. 3.21: (a) Temperature dependence of PL intensity of sample CIS15 and (b) Plot of  $1000/T$  vs. logarithmic (Integrated PL intensity).

Figure 3.21(a) shows the temperature dependence of PL emission in sample CIS15 which was identified to be stoichiometric in composition, based on the observation of the  $FE_A$  emission at 1.55 eV. Apart from the  $FE_A$  emission, a low energy emission centered at 1.475 eV with a shoulder at 1.464 eV was observed



in this sample. An interesting observation for the temperature dependence of the PL emission in this energy range was that as the temperature was raised from 11 K the PL intensity increased reaching a maximum at 150 K. Then it decreased, and was quenched beyond 250 K as shown in Fig. 3.21(a).

The thermal quenching energy for the emission at 1.475 eV was found to be 31 meV by fitting the  $1000/T$  vs.  $\log$  (Integrated PL intensity) plot using relation (3.5) in the higher temperature side of the plot (Fig. 3.21(b)). The activation energy agreed with the ionization energy for the  $V_s$  donor level in stoichiometric  $\text{CuInS}_2$ .<sup>31, 46, 70, 71</sup> The Sulphur vacancy could act as a double ionized donor and can be the reason for the double PL peak in the emission at 1.475 eV. The shoulder at 1.464 eV was quenched beyond 30 K. Peak energy of the emission at 1.475 eV shifted to higher energy with the increase in excitation intensity. This shift, though visible in the spectra, was very small to be quantified with the present resolution of the detection system. The peak shift to higher energy side due to the increase in excitation intensity is a characteristic of the Donor–Acceptor pair recombination. Figure 3.22(a) shows the excitation intensity dependence for this emission and the theoretical fit is shown in Fig. 3.22(b).



**Fig. 3.22:** (a) Excitation intensity dependence of emission line at 1.475 eV and (b) Plot of excitation intensity vs. PL intensity, fitted using relation (1.57).

The theoretical fit using relation (1.57) yielded  $\gamma = 0.73$  and hence this emission was assigned to be due to the donor acceptor pair (DAP) recombination. For DAP transitions, the emission energy is given by relation (1.55) (section 1.2.5A) using which the activation energy of the second defect level responsible for the PL emission can be obtained. Neglecting the Coulomb and van der Waal term in the relation (1.55) and using  $E_g = 1.575$  eV ( $\text{FE}_{A+}$

exciton binding energy) this value was found to be 69 meV, which agreed with the activation energy for the  $V_{Cu}$  acceptor level in stoichiometric  $CuInS_2$ .<sup>50, 70, 72, 73</sup> Hence the emission was assigned to the  $V_S - V_{Cu}$  DAP recombination.

The variations of the PL intensity (initial increase followed by a decrease) with temperature, could be explained by considering a ‘competition’ between two shallow acceptor levels. As was evident in the optical absorption for the Cu-rich films, the presence of an absorption peak just below the band edge absorption became clear. The PL peak was absent in In-rich films and its significance increased as the Cu-content in the films was increased. The optical absorption could be assigned to transition from the  $V_{In}$  acceptor level (located 0.1 eV above the  $V_B$ ) to the CB. Since its presence could be observed in room temperature optical absorption it could be assumed that this level was filled with electrons even at room temperature. The presence of two shallow acceptors  $V_{Cu}$  and  $V_{In}$  and the competition between the two can lead to the anomalous temperature dependence of PL. A model for the anomalous temperature dependence of PL has been proposed in chapter 4 based on the presence of two shallow donors in the  $CuInSe_2$  system. In the  $CuInS_2$  system, conclusive evidence was absent for the proposition of such a model.

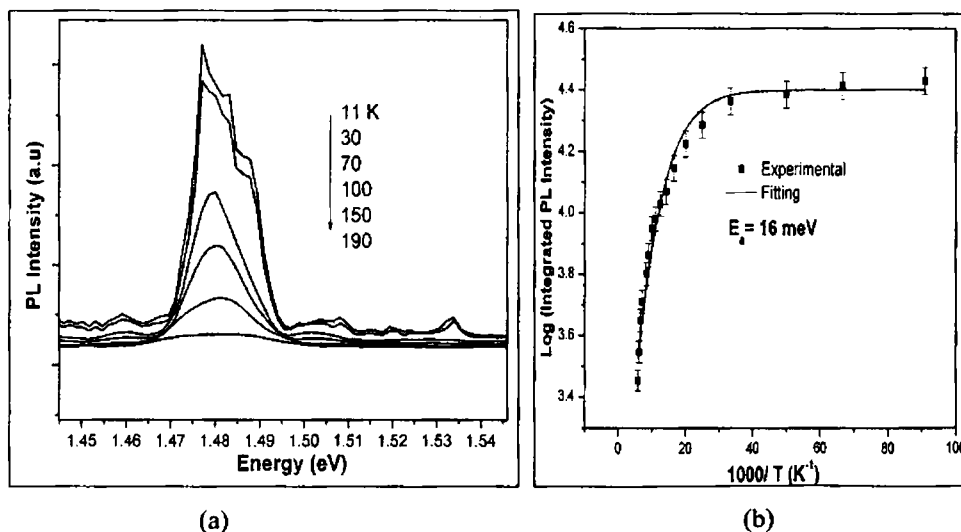


**Fig. 3.23:** (a) Temperature dependence of emission at 1.484 eV in sample CIS155 and (b) Plot of  $1000/T$  vs. logarithmic (Integrated PL intensity) for the emission at 1.484 eV fitted using relation (3.5).

In sample CIS155, which was Cu-rich, PL emission away from the band edge was centred at 1.484 eV (Fig. 3.23(a)). A high energy shoulder [at 1.489 eV] and a low energy shoulder (at 1.479 eV) was also recorded. These shoulders were quenched above 50 K and the PL peak at 1.484 eV gained significance

beyond this temperature. The temperature dependence of PL emission in this sample is shown in Fig. 3.23(a). The emission was quenched at 190 K.

Since the emission was much lower than the band edge emission, it could be assumed that the emission was due to a DAP recombination. The temperature dependence of PL intensity of the emission at 1.484 eV was fitted using relation (3.5) and the activation energy of the thermal quenching was obtained to be 16 meV as shown in Fig. 3.23(b). This value agreed with the activation energy of  $V_{In}$  acceptor level.<sup>50</sup> As the film was highly Cu-rich, the stoichiometry of the sample also supported this hypothesis that the defect responsible for this emission could be the  $V_{In}$  acceptor level. Activation energy of the second defect level, responsible for the PL emission was found to be 55 meV using relation (1.55) (where we used  $E_g = 1.555$  eV ( $FE_A +$  exciton binding energy)). This agreed with the activation energy of the  $V_S$  donor level.<sup>72, 73</sup> Thus this PL emission was assigned to the  $V_S-V_{In}$  DAP recombination.

SAMPLE	TYPE	ACCEPTOR	DONOR	Cu/In	S/Cu+In
CIS55	n	-----	-----	0.49	1.06
CIS15	p	$V_{Cu}$ (69meV)	$V_S$ (31 meV)	0.94	0.84
CIS155	p	$V_{In}$ (16 meV)	$V_S$ (55 meV)	1.24	0.95

**Table 3.4:** Activation energy of the defects identified using PL in the samples.

Thus we could conclude that when the film was made Cu-rich, (Sample CIS155), the  $V_{Cu}$  defect level could be eliminated. In sample CIS55, which was Sulphur rich and In-rich, none of the defect related emissions could be detected. This supported the argument that  $V_S$  defect was essential for the PL emissions to be observed. Also no side lobes were observed for films which were In-rich which strengthened this hypothesis. The position of the donor  $V_S$  was identified in our samples consistently. Table 3.4 represents the position of the various defect levels observed in samples where the Cu/In ratio was varied keeping the S/Cu ratio fixed in the precursor spray solution.

In order to further verify the position of these defect levels, we fixed the Cu/In ratio in the precursor as in CIS15 and varied the S/Cu ratio in the precursor spray solution. In the case of samples for which the S/Cu ratio was varied, it was found that the concentration of Sulphur increased in the samples as per the increase in the precursor spray solution. For sample CIS12, where the

S/Cu =2 in the precursor solution [ $S/(\text{Cu} + \text{In}) = 0.71$  from EDAX], deep PL emission at 0.978 eV was observed. Band edge emission relating to the exciton was not observed, which indicated a degraded quality of the films compared to the earlier set of samples.

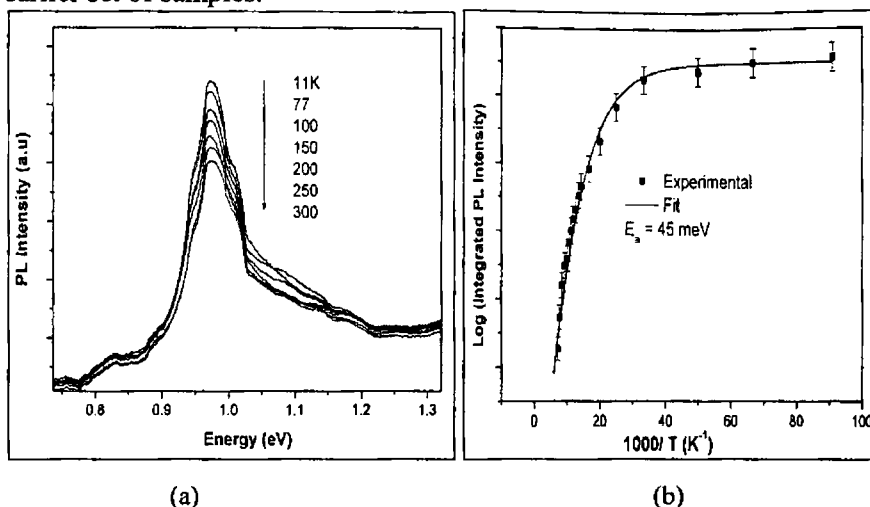


Fig. 3.24: (a) Temperature dependence of PL emission for sample CIS12 with  $S/(\text{Cu} + \text{In}) = 0.71$  and (b) Plot of  $1000/T$  vs logarithmic (Integrated PL intensity) fitted using relation (3.5).

Figure 3.24(a) shows the temperature dependence of this emission at 0.978 eV. Interestingly, this emission could be observed even at room temperature. Deep emissions in this energy range were reported to be because of deep donor- acceptor pairs in  $\text{CuInS}_2$ .<sup>48</sup> The activation energy corresponding to thermal quenching of this emission was found to be 45 meV, which could be assigned to the  $V_S$  donor level from our previous study. Sample stoichiometry also supported this. Using relation (1.55), the activation energy of the other level responsible for this emission was found to be 357 meV and could be naturally located above the valence band. Such deep acceptors are formed by  $\text{Cu}_{\text{In}}/\text{Cu}_S$ .<sup>48</sup> The sample stoichiometry was found to be highly Cu-rich, and supported this assignment.

When the Sulphur content was raised [ $S/\text{Cu}=5$ ] in sample CIS15, the Sulphur content increased but still the deviation from stoichiometry indicated a Sulphur deficient film. A low energy emission centered at 1.475 eV with a shoulder at 1.464 eV was observed in this sample. The details of this emission are described in the earlier section and it was identified that in this sample defect related emission was because of the  $V_S$  to  $V_{\text{Cu}}$  [i.e. DAP] transition. When the Sulphur content was further raised by increasing  $S/\text{Cu}=10$  in sample CIS110,

emissions from deep defects were not observed. One of reasons for this could be the absence of the  $V_S$  defect levels because of the improved Sulphur content in the film. Thus in this samples  $V_S$  related PL emissions were absent.

Thus the presence of defects like  $Cu_i$  and  $Cu_S$  were identified using samples whose Sulphur content was varied. Table 3.5 compares the defects identified using PL in samples where Cu/In was kept a constant and the S/Cu content was varied.

SAMPLE	TYPE	ACCEPTOR	DONOR	Cu/In	S/Cu+In
CIS12	p	$Cu_i/ Cu_S$ (357 meV)	$V_S$ (45 meV)	2.18	0.71
CIS15	p	$V_{Cu}$ (69 meV)	$V_S$ (31 meV)	0.94	0.84
CIS110	p	----	----	1.10	0.95

**Table 3.5:** Activation energy for the defects identified using PL in Sulphur content varied samples.

When the broad band emissions in the films prepared using CSP were studied as a function of their composition, intrinsic defects were found to play an important role in the shape and position of the PL emission. Deviation from stoichiometry (In-rich or Cu-rich) determined the type of broad band emission. Cu-excess films showed the maximum number of emission lines. The lines were broad and some of the defect-related emissions were observed even up to room temperature. On the other hand In-rich films showed defect related emissions close to the band gap. Thus it could be concluded that prominent defects that are formed during the spray pyrolysis of  $CuInS_2$  are  $V_S$ ,  $V_{Cu}$  and  $V_{In}$ . Defects like  $Cu_i/ Cu_S$  were formed as a result of deviation from molecularity in the precursor solution.

### 3.7 Effect of substrate temperature on the PL emissions in $CuInS_2$ thin films

Significance of substrate temperature in controlling the properties of CSP samples is well known. PL properties of sprayed  $CuInS_2$ , deposited at different substrate temperatures, were analyzed in the present study to standardize the substrate temperature. Sample properties exhibited progressive behavior with temperature.<sup>76, 77</sup> Samples with Cu/In ratio equal to 1 and S/Cu ratio equal to 5 in the precursor solution were sprayed on to substrates maintained at temperatures

of 573 K, 623 K and 673 K, keeping all other parameters constant. The spray rate was 1 ml/min and volume of the solution used for each spray was 40 ml. Thickness of the films decreased progressively from 460 nm to 270 nm, as the substrate temperature increased from 573 K to 673 K. Figure 3.25 compares the PL spectra for this set of samples. Samples prepared at 573 K (300 °C) showed prominent defect-related emissions centered on 1.46 eV and a weak exciton emission at 1.55 eV. The defect related emission was identified to the  $V_S$  and  $V_{Cu}$  donor-acceptor pair recombination.

When the substrate temperature was raised to 623 K (350 °C) band edge emission at 1.552 eV dominated and this was observed from 12 K up to 200 K (Fig. 3.25). The peak at 1.552 eV had a shoulder at 1.536 eV, which persisted up to room temperature. The difference in their peak energies was 16 meV, which agreed well with the exciton binding energy in  $CuInS_2$ . The persistence of band edge PL emission up to room temperature in samples prepared at 623 K clearly indicated better crystallinity, device quality and absence of non-radiative losses in this sample. This accounted for the improved properties of this sample. Also there was passivation of the donor acceptor transitions in samples prepared at this temperature.

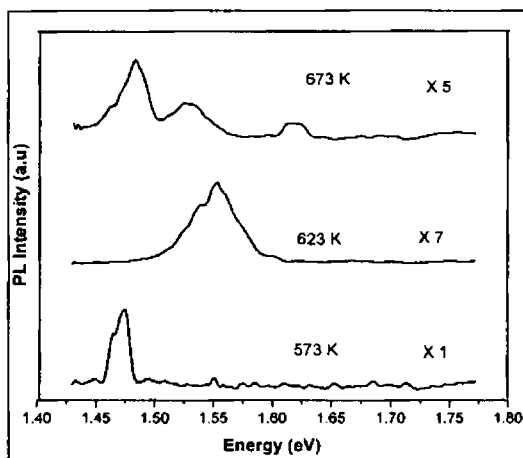


**Fig. 3.25:** PL spectra of samples at 12 K, prepared with different substrate temperatures, using same precursor solution.

Temperature dependence of the emission at 1.552 eV, in this sample, is shown in Fig. 3.26(a) and the data was fitted using relation<sup>74, 75</sup>

$$I(T)/I(0) = 1/[1 + C_1 \exp(-\Delta E_1/kT) + C_2 \exp(-\Delta E_2/kT)] \quad (3.9)$$

where the presence of a further non-radiative path with activation energy  $\Delta E_2$  is assumed. The fitting based on this assumption is shown in Fig. 3.26(b).

The activation energy related to the thermal quenching ( $\Delta E_2$ ) of this emission was found to be 81 meV. It could be concluded that the emission at 1.552 eV was the  $FE_A$  emission in this sample. The emission at 1.532 eV could be due to the defects at 81 meV. The peak position of the emission shifted to lower energy as temperature was raised. Thus we could assume that this emission at 1.532 eV in sample prepared at 623 K was a bound exciton emission.

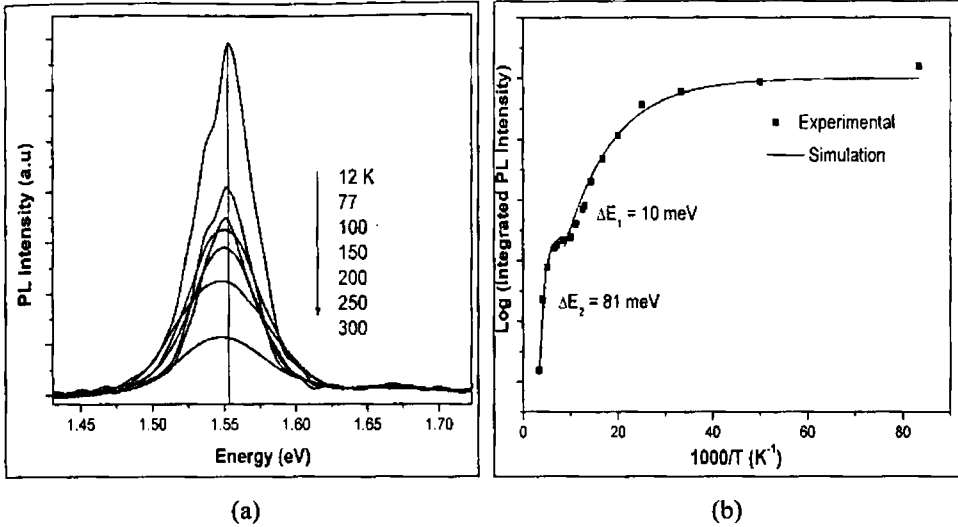


**Fig. 3.26:** (a) Temperature dependence of PL in sample prepared with substrate at 623 K and (b) Plot of  $1000/T$  vs. Logarithmic [Integrated PL intensity] of the PL emission fitted using relation (3.9).

Since most semi-conducting materials contain significant amounts of impurities and/or defects which can trap excitons, the identification of the bound exciton states provided an important characterization of impurities, which controlled the electro-optic properties of semiconductors. Bound excitons give rise to PL emission at lower energy than that of free excitons. Excitons bound to ionized donors ( $D^+$ , X), to neutral donors ( $D^0$ , X), to ionized acceptors ( $A^+$ , X), and to neutral acceptors ( $A^0$ , X) are the various types found in many semiconductor systems. The ( $D^+$ , X) complex consists of a donor ion, an electron and a hole. Similarly the ( $A^+$ , X) complex consists of an acceptor ion, an electron and a hole. The ( $D^0$ , X) bound exciton consists of a donor ion, two electrons, and a hole. The ( $A^0$ , X) bound exciton consists of an acceptor ion, an electron, and two holes. The observation of ( $D^+$ , X) emission or ( $A^+$ , X) PL emission bands in a particular material will depend on the ratio of electron and hole effective masses  $m_e$  and  $m_h$ . An exciton can be bound to an ionized donor if  $m_h/m_e > 1.4$ . Similarly, an exciton can be bound to an ionized acceptor if  $m_e/m_h > 1.4$ .

Donor bound excitons follow

$$\varepsilon_{DB} / \varepsilon_D = 0.2 \quad (3.10)$$

and acceptor-bound excitons follow

$$\varepsilon_{AB} / \varepsilon_A = 0.1 \quad (3.11)$$

where  $\varepsilon_{DB}$  and  $\varepsilon_{AB}$  are the binding energies of donor- and acceptor-bound excitons, respectively;  $\varepsilon_D$  and  $\varepsilon_A$  are the ionization energies of donor and acceptor impurities. Ratio of the exciton binding energy (16 meV) to the impurity ionization energy (81 meV) was obtained to be  $\sim 0.2$  which proved the emission at 1.532 eV to be a 'donor bound exciton' emission. Singly ionized defects of Indium (Indium interstitials ( $\text{In}_i$ ) or Indium at Copper anti sites ( $\text{In}_{\text{Cu}}$ ) occupy shallow states  $\sim 75$  meV below the conduction band.<sup>76, 77</sup> Thus it could be concluded that this emission was the ( $\text{D}^+$ , X) emission. The assignment was also supported by the film stoichiometry.

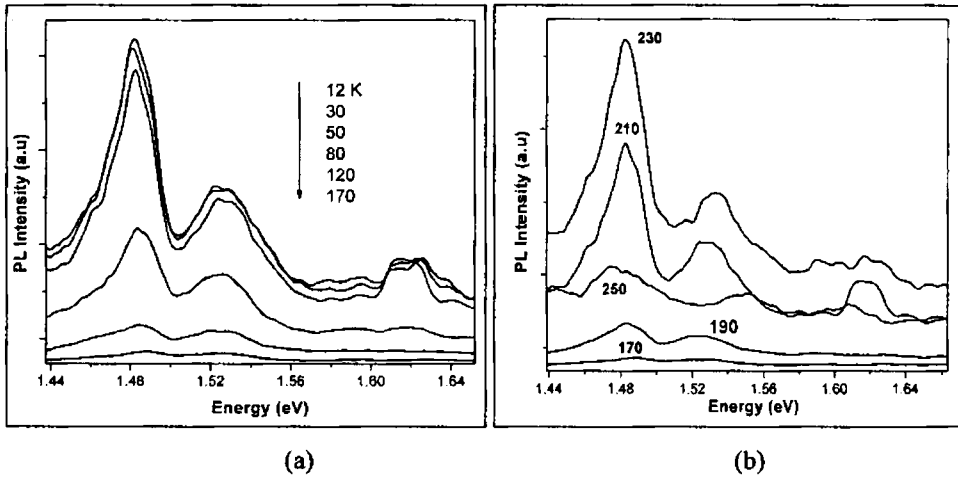


**Fig. 3.27:** Temperature dependence of PL emission intensity in sample prepared at 673 K (a) Temperature 12-170 K and (b) Temperature 170-230 K.

For samples prepared at 673 K, the band edge emissions were broadened. Broad emissions at 1.527 eV, 1.482 eV as well as at 1.634 eV exhibited negative temperature quenching as shown in Fig. 3.27. This indicated the presence of large number of competitive radiative defects and secondary phase impurities for samples prepared at this temperature.

Based on the PL results, it could be concluded that the ideal substrate temperature for the deposition of  $\text{CuInS}_2$  thin films using CSP was 623 K. Also as temperature was increased, it was observed that the composition of the film changed in spite of using the same concentration of precursor solution for preparation of all the three samples. Thus it could be concluded that the



stoichiometry of the deposited films could be controlled by changing the substrate temperature alone. This was an important and useful result from the device fabrication point of view. For example, in the case of solar cells where Cu-rich interface at the junction exists, the efficiency has been reported to be as high as 12% due to the improved collection of minority carriers across the junction where as an In-rich bulk is needed to increase the absorption coefficient. This work proved that by varying the substrate temperature alone, one can get films with different composition using the same precursor solution.

### 3.8 Conclusions

PL studies on  $\text{CuInS}_2$  thin films were carried out with the aim of identifying critical parameters like precursor solution concentration and substrate temperature for the deposition of device quality films for solar cell application. It was also aimed at non-destructively identifying the intrinsic defects formed during deposition in these ternary compound thin films. The most important aim was to establish a robust tool which could be used to identify the composition of the films non-destructively. The use of PL as a tool to establish the composition of the films has been demonstrated with success in this chapter. It is established that the free exciton [ $\text{FE}_A$ ] emission, which is the highest band edge emission energy, can be used to identify the composition of the film. Stoichiometric  $\text{CuInS}_2$  thin films yield  $\text{FE}_A$  emission at 1.55 eV whereas the In-excess films show  $\text{FE}_A$  emission at 1.56 eV. The Cu-excess films yield  $\text{FE}_A$  emission at 1.53 eV. Excitons bound to defects also yield PL emission; but they cannot be used to predict the composition accurately. The FWHM of the band edge emission varied as the composition varied.

The In-rich films showed maximum FWHM for the  $\text{FE}_A$  emission while the Cu-rich films showed the sharpest  $\text{FE}_A$  emissions. The stoichiometric films showed  $\text{FE}_A$  emissions of FWHM intermediate to the Cu-rich and In-rich films. Alternative to PL peak position, PL FWHM can also be used as a tool for composition analysis. Sharper PL emissions in general reflect improved crystallinity and decrease in defect density. Thus monitoring of FWHM can also be used for quality analysis of the films. Position of the PL emission lines observed, and their identified origin is shown in Table 3.6. Based on the data, it could be proposed that film composition could be identified based on the band edge emission lines. Position of the deep DAP recombination lines were too close to be used as a mark of stoichiometry.

Emission line (eV)	Film Parameter	PL origin
1.574	In-rich S-excess	FE <sub>B</sub>
1.563± 0.003	In-rich S-excess	FE <sub>A</sub>
1.475	In-rich S-deficient	V <sub>S</sub> - V <sub>Cu</sub>
1.550± 0.002	Stoichiometric	FE <sub>A</sub>
1.532± 0.004	Stoichiometric	BX:D( In <sub>Cu</sub> <sup>+</sup> )
1.533± 0.003	Cu-rich S-deficient	FE <sub>A</sub>
1.484	Cu-rich S-deficient	V <sub>S</sub> - V <sub>In</sub>
0.978	Cu-rich S-deficient	V <sub>S</sub> - Cu <sub>In</sub> /Cu <sub>S</sub>

**Table 3.6:** Emission lines assigned based on the stoichiometry of the sprayed CuInS<sub>2</sub> thin films.

The spatial variation in FE<sub>A</sub> emission can be used to monitor sample quality and uniformity. The presence of FE<sub>A</sub> emission from a film itself is an indication of good crystallinity and ordering in the film. Spatial fluctuation in intensity of the FE<sub>A</sub> emission was used to study in-homogeneity in the films due to problems in the growth process or the deposition technique. It was observed that a change in precursor solution itself was sufficient to create spatial distribution in FE<sub>A</sub> emission intensity. Spatial uniformity of composition for some of the films was tested using PL and it could be used to predict uniformity of films deposited. The drawback of PL technique remains in the collection optics and in the quality of the films deposited. Unless a film shows PL emission, its homogeneity cannot be verified by this technique.

Position of some of the intrinsic defects like vacancy of Sulphur [V<sub>S</sub>], vacancy of Indium [V<sub>In</sub>], vacancy of Copper [V<sub>Cu</sub>], Copper interstitials [Cu<sub>i</sub>] and Copper in Sulphur anti-site [Cu<sub>S</sub>] could also be identified as shown in Table 3.7. Compensation of some of these defects was observed when the concentration of the precursor solution was changed or when the substrate temperature was changed.

In conclusion, precursor solution having Cu to In ratio of 1, S to Cu ratio of 5, and substrate temperature of 623 K was found to be the best/optimum parameters to obtain good CuInS<sub>2</sub> thin films in laboratory scale which could be used for the preparation of solar cells using CSP technique.

Impurity	Acceptor (A) / Donor (D)	Activation Energy (meV)
V <sub>S</sub>	D	42± 3
V <sub>Cu</sub>	A	31
V <sub>In</sub>	A	16
In <sup>+</sup> <sub>Cu</sub>	D	81
Cu <sub>i</sub> /Cu <sub>s</sub>	A	357

**Table 3.7:** Point defects and their activation energy identified using PL in sprayed CuInS<sub>2</sub> thin films.

### 3.9 Reference

1. Katsuaki Sato, Mikio Isawa, Nobumitsu Takahashi and Hiroshi Tsunoda, Jap. J. Appl. Phys. **27**, 1359 (1988).
2. Zhang, S. B., Su-Huai Wei and Alex Zunger, Phys. Rev. B, **57**, 9642 (1998).
3. Tell, B., Shay, J. L. and Kasper, H. M., Phys. Rev. **44**, 2643 (1971).
4. Shay, J. L., Tell, B., Kasper, H. M. and Schiavone, L. M., Phys. Rev. B, **5**, 5003 (1972).
5. Shay, J. L. and Wernick, J. H., Ternary Chalcopyrite Semiconductors: Growth, Electronic Properties and Applications, Pergamon, Oxford, New York (1975).
6. Jaffee, J. E. and Zunger, A., Phys. Rev. B, **29**, 1882 (1984).
7. Krustok, J., Raudoja, J., Schön, J. H., Yakushev, M., and Collan, H., Thin Solid films, **361**, 406 (2000).
8. Scheer, R., Luck, I., Kanis, M., Kurps, R. and Krüger, D., Thin Solid Films, **361**, 408 (2000).
9. Gossila, M., Metzner, H. and Mahnke, H. E., Thin Solid Films, **413**, 92 (2002).
10. Ellmer, K., Hinze, J. and Klaer, J., Thin Solid films, **413**, 92 (2002).
11. Guha, P., Das, D., Maity, A.B., Ganguli, D. and Chaudhuri, S., Sol. Energy Mat. Sol. Cells, **80**, 115 (2003).
12. Bandyopdhaya, S., Chaudhuri, S. and Pal, A. K., Sol. Energy Mat. Sol. Cells, **60**, 323 (2000).

13. Michael Jin, H., Kulinder Banger, K., Jerry Harris, D. and Aloysius Hepp, F. 3<sup>rd</sup> world conference on Photovoltaic Energy Conversion, 2P-A8-21, 1 (2003).
14. Teny Theresa John, Wilson, K. C., Ratheesh Kumar, P. M., Sudha Kartha, C., Vijayakumar, K. P., Kashiwaba, Y., Abe, T. and Yashuiro, Y., Phys. Stat. Sol (a), **1**, 79 (2005).
15. Zahng, S. B., Su-Huai Wei and Alex Zhunger, Phys. Rev. B, **57**(16), 9642 (1998).
16. Scheer, R., Diesner, K. and Lewerenz, H. -J., Thin Solid Films, **268**, 130 (1995).
17. Tell, B. and Shay, J. L., Phys. Rev. B, **44**, 2463 (1971).
18. Tell, B., Shay, J. L., Kasper, H. M. and Barns, R. L., Phys. Rev. B, **10**, 1748 (1974).
19. Shay, J. L. and Tell, B., Surf. Sci. **31**, 748 (1973).
20. Neumann, H., Hörig, W., Savelev, V., Lagzdonis, J., Schumann, B. and Kühn, G., Thin solid films, **79**, 167 (1981).
21. Yamamoto, N., Kitakuni, M. and Susaki, M., Jpn. J. Appl. Phys. Part 1, **34**, 3019 (1995).
22. Susaki, M., Yamamoto, N., Prevot, B. and Schwab, C., Jpn. J. Appl. Phys. Part 1, **35**, 1652 (1996).
23. Yamamoto, N., Susaki, M., Huang, W. Z. and Wakita, K., Cryst. Res. Technol. **31**, S369 (1996).
24. Wakita, K., Sakai, Y., Yamamoto, N., and Susaki, M., Cryst. Res. Technol. **31**, S385 (1996).
25. Shay, J. L., and Kasper, H. M., Phys. Rev. Lett. **29**, 1162 (1972).
26. Jaffe, J. E. and Zunger, A., Phys. Rev. B, **28**, 5822 (1983).
27. Kono, S. and Okusawa, M., J. Phys. Soc. Jpn. **37**, 1301 (1974).
28. Braun, W., Goldmann, A. and Cardona, M., Phys. Rev. B, **10**, 5069 (1974).
29. Varshni, Y. P., Physica, **34**, 149 (1967).
30. Kazmerski, L. L. and Shieh, C. C., Thin Solid Films, **41**, 35 (1977).
31. Lewerenz, H. J. Sol. Energy Mater. Sol. Cells, **83**, 395 (2004).
32. Pamplin, B. and Feigelson, R. S., Thin Solid Films, **60**, 141 (1971).
33. Gorska, M., Beaulieu, R., Loferski, J. J. and Rossler, B., Sol. Energy Mater. **1**, 313 (1979).
34. Tiwari, A. N., Pandya, D. K. and Chopra, K. L., Thin Solid Films, **130**, 217 (1980).
35. Bihri, H., Messaoudi, C., Sayah, D., Boyer, A., Mzerd, A. and Abd-Lefdil, M., Phys. Stat. Sol. (a), **129**, 193 (1992).

36. Bihri, H. and Abd-Lefdil, M., *Thin Solid Films*, **354**, 5 (1994).
37. Zouaghi, M.C., Nasrallah, T.B., Marsillac, S., Bernede, J.C. and Belgacem, S., *Thin Solid Films*, **382**, 39 (2001).
38. Krunks, M., Bijakina, O., Mikli, V., Rebane, H., Varema, T., Altosaar, M. and Mellikov, E., *Sol. Energy Mater. Sol. Cells*, **69**, 93 (2001).
39. Krunks, M., Kijatkina, O., Rebane, H., Oja, I., Mikli, V. and Mere, A., *Thin Solid Films*, **403-404**, 71 (2002).
40. Krunks, M., Mikli, V., Bijakina, O., Rebane, H., Mere, A., Varema, T. and Mellikov, E., *Thin Solid Films*, **361-362**, 61 (2000).
41. Peza-Tapia, J. M., Sánchez-Reséndiz, V. M., Albor-Aguilera, M. L., Cayente-Romero, J. J., De León-Gutiérrez, L. R. and Ortega-López M., *Thin Solid Films*, **490(2)**, 142 (2005).
42. Aksay, S. and Alt okka B., *Phys. Stat. Sol. (c)*, **4(2)**, 585 (2007).
43. Binsma, J. J. M., Giling, L. J. and Bolem, J., *J. Lumin.* **27**, 55 (1982).
44. Binsma, J. J. M., Giling, L. J. and Bolem, J., *J. Lumin.* **27**, 35 (1982).
45. Wakita, K., Hiroyuki, H., Shusaku, Y., Futoshi, F. and Nobuyuki, Y., *J. Appl. Phys.* **83(1)**, 443 (1998).
46. Ueng, H. Y. and Hwang, H. L., *J. Phys. Chem. Solids*, **50**, 1297 (1989).
47. Töpfer, K., Bruns, J. Scheer, R. Weber, M. Weidinger, A. and Bräunig, D., *Appl. Phys. Lett.* **71(4)**, 482 (1997).
48. Schön, J. H. and Bucher, E., *Phys. Stat. Sol. (a)*, **171**, 511 (1999).
49. Márquez, R. and Rincón, C., *Mater. Lett.* **40**, 66 (1999).
50. Krustok, J., Raudoja, J. and Collan, H., *Thin Solid Films*, **387(1-2)**, 195 (2001).
51. Wakita, K., Matsuo, M., Hu, G., Iwai, M. and Yamamoto, N., E-MRS Spring Meeting, Symposium B: Thin film Chalcogenide Photovoltaic Materials, Strasbourg, France, vol. **431-32**, p. 184 (2003)
52. Onishi, Abe, T., Miyoshi, K., Iwai, Y. and Wakita, K., *Jpn. J. Appl. Phys. Part 1*, **44(1) B**, 722 (2005).
53. Hiroyuki Nakamura, Wataru Kato, Masato Uehara, Katsuhiko Nose, Takahisa Omata, Shinya Otsuka-Yao-Matsuo, Masaya Miyazaki, and Hideaki Maeda, *Chem. Mater.* **18 (14)**, 3330 (2006).
54. Contreras, M. A., Egaas, B., Ramanathan, K., Hiltner, J., Swartzlander, A., Hasoon, F. and Noufi, R., *Prog. Photovolt. Res. Appl.* **7**, 311 (1999).
55. AbuShama, J. A. M., Johnston, S., Moriarty, T., Teeter, G., Ramanathan, K. and Noufi, R., *Prog. Photovolt. Res. Appl.* **12**, 39 (2004).
56. Goto, H., Hashimoto, Y. and Ito, K., *Thin Solid Films*, **451-452**, 552 (2004).
57. Kazmerski, L. L. and Sanborn, G. A., *J. Appl. Phys.* **48**, 3178 (1977).

58. Klaer, J., Bruns, J., Henninger, R., Siemer, K., Klenk, R. Ellmer, K. and Bräunig, D., *Semicond. Sci. Technol.* **13**, 1456 (1998).
59. Siemer, K., Klaer, J., Luck, I., Bruns, J., Klenk, R. and Bräunig, D., *Sol. Energy Mat. Sol. Cells*, **67**, 159 (2001).
60. Scheer, R., Walter, T., Schock, H. W., Fearheiley, M. L. and Lewerenz, H. J., *Appl. Phys. Lett.* **63**, 3294 (1993).
61. Teny Theresa John, PhD thesis, Cochin University of Science and Technology (2004).
62. Dean, J. P., *Phys. Rev.* **157**, 655 (1967).
63. Igalson, M. and Schock, H. W., *J. Appl. Phys.* **80**, 5765 (1996).
64. Moore, C. J. L. and Miner, C. J., *J. Cryst. Growth*, **103**, 21 (1990).
65. Michio Tajima, *J. Cryst. Growth*, **103**, 1 (1990).
66. Smith, E. P. G., Venzor, G. M., Newton, M. D. and Liguori, M. V., *J. Elect. Mater.* **34**, 746 (2005).
67. Giorgio Biasiol, Frank Reinhardt, Anders Gustafsson, Eli kapon, *J. Elect. Mater.* **26**, 1194 (1997).
68. Hovel, H. J., and Guidotti, D., *IEEE Trans. Electron Devices* ED-32, 2331 (1985).
69. Leo, K., Rühle, W. W., Nordberg, P. and Fujii, T., *J. Appl. Phys.* **66**, 1800 (1989).
70. Massé, G., Lahlou, N. and Butti, C., *J. Phys. Chem. Solids*, **42**, 449 (1981).
71. Watanabe, T. and Yamamoto, T., *Jpn. J. Appl. Phys.* **39**, L1280 (2000).
72. Mauricio Ortega-López, Arturo Morales-Acevedo, *Thin Solid Films*, **330**, 96 (1998).
73. Zouaghi, M. C., Ben Narsrallah, T., Marsillac, S., Bernede, J. C., Belgacem, S., *Thin Solid Films*, **382**, 39 (2001).
74. Leroux, M., Grandjean, N., Beaumont, B., Nataf, G., Semond, F., Massies, J. and Gibart, P., *J. Appl. Phys.* **86**, 3721 (1999).
75. Goldys, E. M., Godlewski, M., Langer, R., Barski, A., Bergman, P. and Monemar, B., *Phys. Rev. B*, **60**, 5464 (1990).
76. Kroger, F. A., *The Chemistry of Imperfect Crystals*, 2nd Ed, Vol. 2. Amsterdam: North- Holland (1974).
77. Hwang, H. L., Liu, L. M., Yang, M. H., Chen, J. S., Chen, J. R. and Sun, C. Y., *Solar Energy Mater.* **7**, 225 (1982).

## CHAPTER 4

### Photo-luminescence studies on CuInSe<sub>2</sub> thin films

---

*PL studies were carried out on CuInSe<sub>2</sub> thin films deposited using three different techniques. It was aimed at standardizing a simple eco-friendly route to deposit CuInSe<sub>2</sub> which finds wide application in photovoltaics as a good absorber layer. It is established that device quality films could not be deposited using a combination of the Chemical Bath Deposition (CBD) and Sequential Elemental Layer (SEL) deposition techniques. In the present work, PL has been used mainly to identify the intrinsic defects due to deviation in stoichiometry of this important compound semiconductor. The near band edge (exciton) emissions were investigated for various film-compositions as a function of temperature. From these investigations, the exciton ionization energy (~5 meV) was determined. Positions of intrinsic defects, like vacancies of Copper ( $V_{Cu}$ ), Indium ( $V_{In}$ ) and Selenium ( $V_{Se}$ ); point defects like Indium in Copper ( $In_{Cu}$ ) and Copper interstitials ( $Cu_i$ ); and antisite like Copper in Indium ( $Cu_{In}$ ), were determined using PL. Emission lines belonging to the class of excitonic, 'free-to-bound' and 'donor-acceptor pair' transitions were recorded and analyzed through their temperature and excitation intensity dependence. In the present work, it is also shown that tuning of PL emission intensity from a CuInSe<sub>2</sub>/ ITO hetero-structure is possible. PL peak position for the emission from the hetero-structure was observed to be at 1550 nm, which is a wavelength sought after in fibre optic communication.*

#### 4.1 Introduction

CuInSe<sub>2</sub> is a member of the family of I-III-VI<sub>2</sub> chalcopyrite semiconductors.<sup>1</sup> The  $ABX_2$  Ch- crystal structure resembles the Zincblende structure, with two of the cations  $A$  and  $B$  being coordinated tetrahedrally by four of the anions ' $X$ ' but the

anion is coordinated by  $2A + 2B$ , with generally dissimilar nearest-neighbor bond lengths  $R_{AX} \neq R_{BX}$ .  $\text{CuInSe}_2$  is a ternary analog of the binary semiconductors like  $\text{CdSe}$  and  $\text{ZnSe}$ . It crystallizes in the Ch- structure which is an ordered superstructure of Zincblende. The electrical properties of I-III-VI<sub>2</sub> compounds are dominated by the presence of intrinsic defects such as Cu, In and Se vacancies and interstitials. Stable crystal structure of  $\text{CuInSe}_2$  is a subset of the ‘adamantine class’ and is named after the mineral chalcopyrite,  $\text{CuFeS}_2$ . The characteristic feature of the adamantine structure is a tetragonal arrangement of atoms in which each atom has four nearest neighbors. In general, crystal structure of various compounds is derived from the basic diamond close-packed structure. It has a sub lattice of anion in cubic close packing (as in the Zincblende (Sphalerite) structure) or in hexagonal close packing (as in the Wurtzite structure). In chalcopyrite compounds ( $\gamma$  phase), a slight shift of the anion sites results in the tetragonal symmetry with c-axis nearly twice the original axis (Zincblende structure).  $\text{CuInSe}_2$  crystallizes in this form at room temperature and reverts to the Sphalerite structure ( $\delta$  phase) above 1073 K. Devices based on this system may find application in optical communication systems when (and if) losses in the optical fibers are reduced below the present 1.3  $\mu\text{m}$  wavelength region.<sup>2</sup>

The defect physics of  $\text{CuInSe}_2$  shows three unusual effects with respect to the binary II-VI analogues: (a) Tolerance to large off-stoichiometry: Unlike its binary analogue it supports a large range of anion-to-cation off stoichiometry i.e. Cu-rich and In-rich films having variation by few percentages, are stable.<sup>3-4</sup> The extreme limit of “off stoichiometry” is manifested by the existence of a series of compounds with different Cu/In/Se ratios ( $\text{CuIn}_5\text{Se}_8$ ,  $\text{CuIn}_3\text{Se}_5$ ,  $\text{Cu}_3\text{In}_5\text{Se}_9$ , etc.).<sup>5-8</sup> (b) Ability to dope it to p-or n-type:  $\text{CuInSe}_2$  can be doped n- or p- type to a low-resistivity level merely by introducing native defects, without extrinsic impurities. Tell, Shay, and Kasper noted that either p- or n-type  $\text{CuInSe}_2$  crystals could be grown from the melt via stoichiometry control.<sup>9</sup> Migliorato et al. and Noufi et al. further investigated this effect, noting that p-type samples can be created by making the sample Cu poor or by annealing in Se atmosphere (high pressure), while n-type samples can be made by making the sample Cu-rich, or through annealing in low pressure Se atmosphere.<sup>10, 11</sup>

The ability to make p- and n-type  $\text{CuInSe}_2$  leads to the formation of a p-n homo-junction, and eventually to the fabrication of photovoltaic solar cells.<sup>12, 13</sup> (c) The electrically benign nature of the structural defects: In Si and in ordinary III-V semiconductors, polycrystallinity leads to a high concentration of



electrically active (grain-boundary) defects that have very detrimental effect on the performance of opto-electronic devices. Polycrystalline CuInSe<sub>2</sub> solar cells have reached efficiencies of ~ 17% outperforming their single crystal counterparts having efficiency of ~ 13%.<sup>14-16</sup> Significant gain in both scale and reliability of production methods, however, will be required before commercial production of CuInSe<sub>2</sub> becomes profitable for bulk power generation applications.

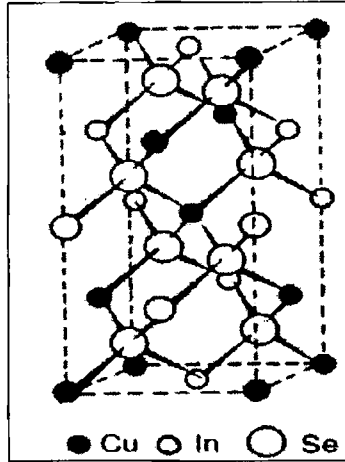


Fig. 4.1: Chalcopyrite structure of CuInSe<sub>2</sub>.

Formation energies of the leading point defects were estimated from the generalization of the ‘cavity model’ proposed by Van Vechten, using empirical atomic radii and bond energies as the inputs.<sup>17-20</sup> In accordance with the fact that the bond energy of chalcopyrite is larger than that of its binary analogue, energy for the formation of vacancy in chalcopyrite, relative to II-V compounds, was found to be larger.<sup>21, 22</sup> Zunger et al. used first-principles self-consistent electronic structure theory to calculate the formation energies and electrical transition levels of point defects, defect pairs and arrays in CuInSe<sub>2</sub> (CISe).<sup>23</sup> The order of formation energies excluding  $V_{Se}$  were reported as

$$\begin{array}{ll}
 V_{Cu} < Cu_{In} < V_{In} < Cu_i < In_{Cu} & \text{(Cu rich; In rich; } n \text{ type)} \\
 V_{Cu} < Cu_{In} < In_{Cu} < Cu_i < V_{In} & \text{(Cu rich; In rich; } p \text{ type)} \\
 V_{Cu} < V_{In} < In_{Cu} < Cu_{In} < Cu_i & \text{(Cu poor; In rich; } n \text{ type)} \\
 V_{Cu} < In_{Cu} < V_{In} < Cu_{In} < Cu_i & \text{(Cu poor; In rich; } p \text{ type)} \\
 Cu_{In} < V_{In} < V_{Cu} < Cu_i < In_{Cu} & \text{(Cu rich; In poor; } n \text{ type)} \\
 Cu_{In} < V_{Cu} < V_{In} < Cu_i < In_{Cu} & \text{(Cu rich; In poor; } p \text{ type)}
 \end{array}$$

Composition of CISe films, used as absorbers in thin film solar cells, is a topic of importance since many cell properties are influenced by the deviations

from stoichiometry. Based on the defect chemistry model of ternary compounds proposed by Groenik and Janse, the deviations from stoichiometric composition can be described by two parameters  $\Delta m$  and  $\Delta s$  which determine the deviation from 'molecularity' and 'stoichiometry' respectively.<sup>24</sup>

$$\Delta m = \left\{ \frac{[Cu]}{[In]} \right\} - 1 \quad (4.1)$$

$$\Delta s = \left\{ \frac{2[S]}{[Cu] + 3[In]} \right\} - 1 \quad (4.2)$$

where  $[Cu]$ ,  $[In]$  and  $[Se]$  are the total concentrations of Cu, In and Se atoms respectively in the crystal.

Meaning of the deviations from molecularity and stoichiometry was described as follows:

1.  $\Delta m > 0$  Cu-rich films (possibly secondary phase  $Cu_{2-x}Se$ )  
 $\Delta m < 0$  In-rich films (possibly secondary phase  $In_2Se_3$ )
2.  $\Delta s > 0$  Excess of Selenium  
 $\Delta s < 0$  Deficiency of Selenium

CISE has been deposited using a number of techniques, including those which have been demonstrated to be scalable to mass production. A brief review on some of the important techniques is as follows: One promising approach, based on data disclosed by ARCO Solar (now Siemens Solar) in a European patent application, consists of sputtering Cu and In layers followed by selenization in  $H_2Se$  gas to yield CISE.<sup>25</sup> Neumann et al. reported successful preparation of CISE epitaxial layers by single-source evaporation.<sup>26</sup> Neelkanth et al. reported preparation of CISE films using co evaporation of constituent elements.<sup>27</sup> Trykozko et al. reported preparation of these films using flash evaporation and beam evaporation.<sup>28</sup> Isomura et al. reported preparation of CISE by D.C. sputtering and vacuum evaporation from synthesized bulk materials.<sup>29</sup> Mikihiro et al. prepared CISE by co-evaporation of the elements under ultrahigh vacuum by molecular-beam deposition technique. The process was found to be suitable for the fabrication of stoichiometric or slightly In-rich films.<sup>30</sup> Adurodija et al. reported solid-liquid reaction mechanisms leading to the formation of high quality CISE by the Stacked Elemental Layer (SEL) technique.<sup>31</sup>

Parretta et al. reported the growth of thin chalcopyrite CISE films using selenization of Cu-In alloys in a box.<sup>32</sup> Firoz Hasan et al. studied charge carrier transport mechanism in  $CuInSe_2$  films prepared using SEL technique in vacuum.<sup>33</sup> Zeenath et al. studied the trap levels of p-type  $CuInSe_2$  samples grown using the SEL technique. As prepared samples had two trap levels of activation

energies 70.72 meV and 40.5 meV and were identified as defect levels of vacancy of Selenium ( $V_{Se}$ ) and vacancy of Copper ( $V_{Cu}$ ). In air annealed samples, activation energy of  $V_{Cu}$  was identified to be 103 meV.<sup>34</sup> CISE films having chalcopyrite structure were successfully prepared by SEL technique where the Selenium film was grown using Chemical Bath Deposition, while the In-Cu layers were deposited by Physical Vapor Deposition. Studies on dependence of growth of the film with annealing temperature and composition were analyzed.<sup>35</sup> Deepa et al. reported that samples prepared using thermal diffusion of Cu into  $In_2Se_3$  were better than the ones prepared using SEL technique for the preparation of CISE. Cu-rich, In-rich and nearly stoichiometric samples could be prepared by thermal diffusion of Cu into  $In_2Se_3$ .<sup>36</sup>

## 4.2 PL of $CuInSe_2$

Kasper et al. observed a sharp band-to-band emission at 1.04 eV in the PL spectrum at 77 K.<sup>1</sup> The features of the PL spectra were explained in terms of a model suggesting the presence of an acceptor level ( $E_A=40$  meV) and a donor level ( $E_D=70$  meV). Both of the levels were proposed to have an intrinsic origin.<sup>37</sup> The PL spectrum of melt-grown n- $CuInSe_2$  single crystal at 7 K, were studied by Rincón et al.<sup>38</sup> They observed three peaks, at approximately 0.980 eV, 0.990 eV and 1.013 eV. Based on the probabilities of recombination processes, DAP and the corresponding free-to-bound transitions were assigned to these emissions. From the data of the absorption edge at  $1.023 \pm 0.003$  eV, a donor state at  $10 \pm 2$  meV, and an acceptor state at  $33 \pm 2$  meV had also been determined by them. The results of PL and PC measurements on stoichiometric and well-defined off-stoichiometric CISE were reported by Lange et al.<sup>39</sup> The energy gap at 10 K was found to be  $1.050 \pm 0.005$  eV and the free-exciton emission was observed at  $1.030 \pm 0.005$  eV in the PL spectra of stoichiometric and nominally un-doped CISE. They observed that for Cu:In and metal: Selenium ratios  $>1$ , recombination between Se-vacancy donors (70 meV below the conduction band edge) and In-vacancy acceptors (80 meV above the valence band edge) dominated the PL spectra. Excitation from two acceptor states ( $Cu_{In}$  antisite acceptors (40 meV) and  $V_{In}$ ), contributed to the PC spectra with complementary temperature dependence. (Normally photocurrent decreases with increase in temperature; but in the above case they observed the reverse). Lange et al. reported that CISE is dominated by free exciton emission at 1.03 eV [FWHM  $\sim 9$  meV]. PL emissions at 0.90 eV, 0.94 eV and 0.97 eV were observed and were attributed to the transitions involving residual native defect states.<sup>40</sup>

Rincon and Bellabarba reported results of optical absorption studies near the band gap of *n*-type CISE at 7 K.<sup>20</sup> Binding energy of the exciton and the ionization energy of acceptors and donors were determined to be 18, 54, and 26 ( $\pm 5$ ) meV, respectively by them. They suggested that  $\text{In}_{\text{Cu}}$  antisite donors and  $V_{\text{Cu}}$  acceptors form the predominant active intrinsic defects in “In-rich” CISE. Masayuki et al. studied PL of CISE films prepared using selenization technique with solid or vapor-phase Selenium.<sup>41</sup> PL spectra obtained from the samples could be explained by assuming the following levels: donor level of Se vacancy ( $V_{\text{Se}}$ ), 70 meV below conduction band, acceptor levels of copper vacancy ( $V_{\text{Cu}}$ ), 40 meV and 85 meV above valence band, In-vacancy ( $V_{\text{In}}$ ) 40 meV above the valence band and Copper on Indium ( $\text{Cu}_{\text{In}}$ ) antisite at 40 meV above valence band. Optical properties of CISE films, grown on (001) GaAs using MBE, were investigated by means of low temperature PL spectroscopy by Niki et al.<sup>42</sup> Distinct emission lines, including the band edge emission, were observed reproducibly from Cu-rich films, indicating high crystalline quality. Such well-defined PL spectra helped the extensive characterization of radiative recombination processes through the intrinsic defects in this material. Some of the emission lines were attributed to phonon replicas with phonon energy of 28-29 meV for the first time. PL spectra were found to be very sensitive to the MBE growth parameters such as substrate temperature, suggesting that dominant defects in CISE epitaxial films could be controlled by varying the growth conditions.

CISE epitaxial films grown on (001)-oriented GaAs substrates using MBE technique were characterized using low temperature PL spectroscopy at  $T = 2\text{--}102$  K by Niki et al. in 1995.<sup>43</sup> The emission at 1.0386 eV ( $E_{\text{X1}}$ ) became broader with increasing temperature, and remained up to  $T=102$  K. They observed a distinct, sharp emission at 1.0311 eV ( $I_{\text{X1}}$ ) which disappeared at a significantly lower temperature, compared to other weak donor-related emissions. They attributed such emissions to the ground-state free exciton [ $\text{FE}_{n-1}$ ] and exciton bound to neutral acceptor [ $A^0, X$ ], respectively. The band gap of CISE epitaxial films was also determined to be  $E_g = 1.046$  eV at 2 K using the reported exciton binding energy of  $E_{\text{ex}} = 7$  meV. Rincon et al. analyzed the donor-acceptor recombination band in the PL spectra of CISE.<sup>44</sup> Broad bands were observed in the PL spectra due to D-A pair recombination at 77 K and were analyzed using an empirical model.

Band edge luminescence of CISE single crystals was studied in the temperature region between 2 and 300 K by Schon and Bucher.<sup>45</sup> Sharp emission

lines were attributed to the decay of free and bound excitons and their phonon replica. Binding energy of the free exciton and the band gap at 2 K were reported to be 4.4 meV and 1.044 eV, respectively by them. Free-exciton series with  $n=1, 2$  in highly perfect CISE single crystals were observed in PL by Mudryi et al.<sup>46</sup> Binding energy of the exciton and direct energy gap were estimated as 5.1 meV and 1.0459 eV at 4.2 K. Mudryi et al. in 2000 studied CISE single crystals employing PL, Optical Reflection (OR), Optical Absorption (OA) and Wavelength Derivative Reflection (WDR) techniques in the temperature range from 4.2 to 300 K.<sup>47</sup> Exciton-related peaks were observed in the near-band edge region of the PL spectra: There were several narrow lines, with FWHM of about 0.3 meV, and two wider peaks (FWHM about 0.7 meV) at 1.0414 (peak A) and 1.0449 eV (peak B). Peaks A and B were also observed in the OR and OA spectra and identified as 'A and B free excitonic states'. The narrow lines were attributed to bound exciton recombination on intrinsic defects. The third exciton resonance (peak C) was observed in the WDR spectra at 1.2779 eV. Crystal-field and spin-orbit splittings were derived to be 5.3 and 234.7 meV, respectively.

Yakushev et al. studied CISE single crystals, grown using the vertical Bridgman method, employing PL and OR techniques, at temperatures 4.2 and 78 K.<sup>48</sup> In a number of samples, A and B free exciton peaks were well resolved in both the PL and OR spectra measured at low temperatures. The energy, spectral separation, and the width of the excitonic lines varied considerably for samples with different elemental compositions. They observed that closer the stoichiometry was to that of the ideal crystal, higher the energies and smaller the A-B separation became. High-quality CISE single crystals were grown by the vertical Bridgman method and studied using PL and OR techniques.<sup>49</sup> The Cu/In ratio of the crystals varied from 0.8 to 1.2. At 4.2 K free-exciton peaks A and B as well as a number of bound-exciton peaks were observed and well resolved in the PL spectra. Deviations from Cu/In = 1 resulted in shifts of the free-exciton peaks to lower energy and an increase in their FWHM. The A-B separation energy was found to be strongly influenced by the Cu/In ratio and temperature, suggesting that the valence band B is less sensitive to the tetragonal distortion in the lattice than the uppermost valence band A. Martin et al. reported PL measurements in the temperature range from 4.2 to 300 K carried out on CISE thin films, synthesized on soda-lime glass substrates by a two-stage selenisation process.<sup>50</sup> For near stoichiometric films, intense band-to-band recombination at room temperature generated PL peak at 1.028 eV with FWHM of [approximately] 50 meV. At 78 K, the A and B free exciton peaks merged into a band at approximately 1.044 eV. The A and B excitonic peaks shifted to 1.0409

eV (A) and 1.0444 eV (B) and were well resolved, with their FWHM reduced to 2.5 meV.

Defect spectra of CISE epitaxial thin films grown on GaAs (0 0 1) wafers using metal organic vapor phase epitaxy was reported by Rega et al.<sup>51</sup> The PL spectra of p-type Cu-rich ([Cu]/[In]>1.05) samples were dominated by donor acceptor pair transition at 0.972 eV. For slightly Cu-poor and stoichiometric samples, a free-to-bound transition at 0.992 eV was observed. Also an exciton emission could be detected at  $E_{FX} = 1.032$  eV, indicating a band gap of  $E_G = 1.038$  eV at 10 K. These results could be combined to yield a defect model for CISE containing two acceptors states with 40 and 60 meV and a compensating 6 meV donor state. PL and time-resolved PL were recorded for bulk CISE single crystals grown by a traveling heater method by Sho and Hideto.<sup>52</sup> PL exhibited an exciton peak at 1.036 eV at 8 K. Other PL peaks at 0.99 eV and 1.01 eV were quenched at 40 K and 100 K, respectively. They observed that in the 50-200 K temperature range, exciton PL exhibited thermal quenching with activation energy ( $\Delta E$ ) of 16 meV. Further increase in temperature ( $200 \text{ K} < T < 300 \text{ K}$ ) lead to broadening of the PL, PL energy decrease, and a negative thermal quenching ( $\Delta E = -89$  meV).

With increase in temperature, the PL lifetime decreased in the temperature range  $80 \text{ K} < T < 160 \text{ K}$ , while it increased in the range  $180 \text{ K} < T < 300 \text{ K}$ . Their results suggested a change of the recombination mechanism at about 200 K. Micro-structural and radiative properties of CISE films, prepared using three-source evaporation were investigated to identify the energy levels associated with various defects.<sup>53</sup> PL measurements were carried out on as-deposited and annealed polycrystalline CISE thin films deposited onto (100)-oriented Si wafers doped with Boron. PL spectra of the films, before and after annealing in Argon atmosphere at  $400^\circ\text{C}$ , showed emission peaks ranging from 0.88 to 1 eV. They observed that annealing strongly increased PL signal at 0.958 eV.

### **4.3 Sequential layer deposition of CuInSe<sub>2</sub> thin films for photovoltaic applications**

In recent years, I-III-VI<sub>2</sub> binary semiconductor compounds, which crystallize in the tetragonal Ch- structure, have received considerable attention because of their possible application in electro-optical devices. Of these compounds, CISE either in the form of single crystals or as polycrystalline thin films, has emerged as an ideal candidate for solar energy conversion, because it possesses the

following useful properties: (a) it has direct band gap of about 1 eV at room temperature which is in the range for optimum solar conversion; (b) it has the highest optical absorption coefficient value among all the semiconductors reported so far in literature (c) it can be made either n- or p- type, which permits the formation of homo-junctions and several types of hetero-junctions; (d) p-type CISE materials with low resistivity ( $\rho \sim 0.5 \Omega\text{cm}$ ) and high mobility of minority carriers ( $\mu_e > 550 \text{ cm}^2\text{v}^{-1}\text{s}^{-1}$ ), required for efficient hetero-junctions, are easily prepared by introducing an excess of Se into the material.<sup>20</sup>

#### *4.3.1 Preparation of CuInSe<sub>2</sub> thin films*

Micro glass slides were cleaned with chromic acid initially and then rinsed with water. The slides were then cleaned with basic soap solution (Dextran) and were then dried in a Petri dish. These slides were used as the substrates for film deposition. The substrates were dipped horizontally in a beaker containing 0.0125 Molar Na<sub>2</sub>SeSO<sub>3</sub> solution. The pH of the solution was adjusted to be  $\sim 4.5$  by adding 50% diluted acetic acid to the solution. The dipping time was increased gradually from 1 hr to 3 hr and it was found that uniform films could be deposited for a dipping time of three hours. The Se films thus prepared were used for the conversion into CISE films. These Se films were then divided into two batches to prepare CISE. One batch of Se films was converted to CISE by following the SEL technique of film deposition while for the other batch, thermal diffusion of the constituent elements followed by vacuum annealing was carried out. In the first process (i.e. SEL technique) Indium and Copper were sequentially deposited on to the Se layer using vacuum evaporation and then the samples were annealed in vacuum at 400 °C for one hour to obtain polycrystalline CISE thin films. This method of preparation is named “**Technique A**” here after in this thesis. In the second method, first In was deposited over the Se layer using vacuum evaporation and this bilayer was annealed in vacuum at 100 °C for one hour to form In<sub>2</sub>Se<sub>3</sub>. In the next stage, Cu was deposited over the In<sub>2</sub>Se<sub>3</sub> thin films by vacuum evaporation and this bilayer Cu/ In<sub>2</sub>Se<sub>3</sub> was annealed in vacuum at 400 °C for one hour to get CISE. This method of preparation is named “**Technique B**” in this thesis.

In order to standardize a route to the preparation of stoichiometric CuInSe<sub>2</sub> thin films, concentrations of Cu- and In- were varied, keeping the thickness of Se- layer constant (0.25  $\mu\text{m}$ ) for both the preparation techniques, **A** & **B**. Samples were prepared by varying the concentration of In, keeping the mass of Cu fixed at 20 mg in both of the deposition techniques. Indium was varied from

following basis: A sample was named as CIS22- when Cu 20 mg and In 20 mg was evaporated on to the Se film. Similarly for sample CIS24- Cu 20 mg and In 40 mg; for sample CIS26- Cu 20 mg and In 60 mg; for sample CIS28- Cu 20 mg and In 80 mg and for sample CIS210- Cu 20 mg and In 100 mg were used respectively for film preparation. In the next step, In was fixed at 80 mg and Cu was varied from 30 to 50 mg in steps of 10 mg. Samples in this set were named as CIS38, CIS48 and CIS58 following the same nomenclature rule as for the In varied set of samples.

Another deposition technique was the Physical Vapor Deposition of the constituent elements on to the glass substrate. In this method, Se was first evaporated onto the glass substrate and then In and Cu were evaporated sequentially. The stacked multi-layer was then annealed at 400 °C to obtain CISE thin films. This method of preparation of CISE is named “**Technique- C**” in this thesis.

The use of a combination of SEL and CBD for the deposition of CISE films was carried out by Zeenath et al. and Bindu et al.<sup>34, 35</sup> The use of the same technique for production of device quality CISE films was carried out by Deepa et al.<sup>36</sup> The PL analysis of CISE films prepared using these techniques was not reported previous to this work. PL as a standard nondestructive technique for diagnosis as well as quality control, in semiconductor R&D and industrial environments is well established. It was aimed at characterizing the PL emission of these films as a function of composition. Experiments were carried out in such a manner as to identify PL emission peaks which could be used as the signature of film composition.

#### ***4.3.2 Structural and optical studies***

Structural characterization using XRD showed the presence of three prominent peaks corresponding to the planes (112) at  $2\theta = 26.6^\circ$ , (220) / (204) at  $44.1^\circ$  and (116) / (312) at  $52.3^\circ$  respectively (Fig. 4.2). Peaks (204) / (220) and (116) / (312) could not be resolved in the XRD pattern. It was seen that the crystallinity increased with increase in In and Cu concentration but reached a maximum and showed degradation beyond a certain limit. Maximum grain size of 240 Å was obtained for the samples prepared using SEL technique while for the samples prepared by **Technique B** it was 180 Å for the same composition. Using **Technique C** the grain size could be improved to 600 Å.



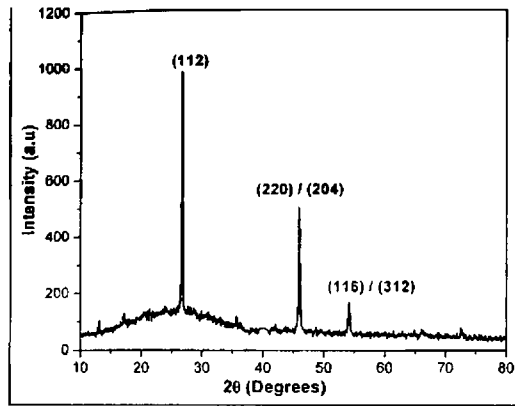


Fig. 4.2: XRD spectrum for SEL deposited  $\text{CuInSe}_2$  thin film sample CIS48.

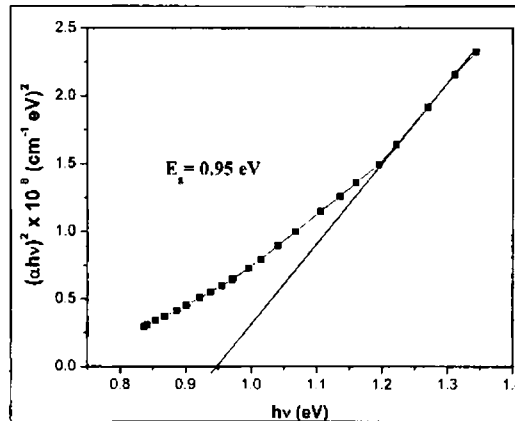


Fig. 4.3: Plot of  $(\alpha hv)^2$  versus  $hv$ , at room temperature for SEL deposited  $\text{CuInSe}_2$  thin film sample.

Sample	Cu	In	Se	Type	$\Delta m$	$\Delta s$
CIS38	19.44	31.91	48.66	p	-0.39	-0.15
CIS48	20.73	24.65	54.65	p	-0.16	-0.15
CIS111	23.63	26.07	50.3	p	-0.09	-0.01
C1	24.92	24.98	50.10	p	-0.01	0.00
CIS115	26.9	26.09	47.01	n	0.03	-0.11
CIS50	23.89	21.44	54.67	p	0.11	0.24
CIS80	27.15	21.71	51.14	p	0.25	0.11
CIS40	20.67	23.38	56.05	n	-0.12	0.23

Table 4.1: Results of the EDAX measurements and majority carrier type of the stoichiometry varied samples.

Optical absorption studies were carried out at room temperature on all the samples in the wavelength range 500–1500 nm. Band gap  $E_g$  was obtained by extrapolating the linear portion of the  $(\alpha hv)^2$  versus  $hv$  graph to  $hv$  axis as

shown in Fig. 4.3. Variation in band gap was observed with the changes in Cu/In ratio for the samples. It was observed that as the films became Cu-rich in composition the band gap  $E_g$  decreased. In order to establish a relation between the PL emission and film stoichiometry, a battery of samples were prepared. Table 4.1 presents the results of the Energy Dispersive Analysis using X-rays (EDAX) measurements carried out on the best samples which were selected based on results of the XRD and PL analysis of the samples.

#### 4.4 PL from SEL deposited CuInSe<sub>2</sub> thin films

When semiconductor materials are irradiated with photons of energy greater than their band gap, photo-excitation of carriers takes place. These carriers recombine through different processes, emitting optical photons of specific energy and spectral distribution. For direct band gap materials at room temperature, the PL spectra are broad with the peak corresponding to energy close to that of the band gap. Low temperature PL spectra consist of narrow band edge peaks related to excitons, along with peaks on longer wavelength region related to specific dopants or impurities. The PL spectra thus give characteristic information, which can be used to characterize the films and/or the defects in it. The PL spectra can thus be divided into two groups a) Band edge emissions and b) Deep emissions. The band edge emissions are prominent at low temperature and are characterized by very small line widths. The deep emissions are due to impurities and are dominant even at room temperature and possess large line widths.

##### 4.4.1 CuInSe<sub>2</sub> thin films grown using Se layer deposited employing CBD

CuInSe thin film samples were prepared by annealing a stack layer, having structure Se/In/Cu using “**Technique –A**”. As described earlier, samples of CuInSe with a wide range of stoichiometry were prepared with the composition varying from Copper rich, to near stoichiometric, to Indium rich. Figure 4.4 represents the PL of the sample CIS38 prepared using “**Technique-A**”: Of the numerous samples prepared, only one sample yielded PL emission, which was quenched when temperature was raised above 40 K.

The PL spectra had three peaks centered at 1.038 eV, 0.985 eV and 0.957 eV at 12 K, as shown in Fig. 4.4. The emission at 1.038 eV could be assigned to the free exciton emission (FE) because of its proximity to the fundamental band-edge of 1.04 eV.<sup>54</sup> Free exciton emission at this energy in CuInSe single crystals was reported by Niki et al. and Leo et al.<sup>43, 55</sup> High energy side of the emission at

1.038 eV possessed a long tail, going up to 1.15 eV. De-convolution of the spectrum yielded additional emission at 1.073 eV at 15 and 20 K, which was absent in the de-convoluted spectra obtained at higher temperatures. The de-convoluted emission at 1.073 eV was 35 meV above the free exciton emission energy, and this difference was in good agreement with the theoretical value of the crystal-field splitting of valence band in CISE reported by Shay et al. and Neumann.<sup>56, 54</sup> Presence of non-radiative paths might be causing the rapid quenching of this emission, as this emission peak was not detected above 20 K.

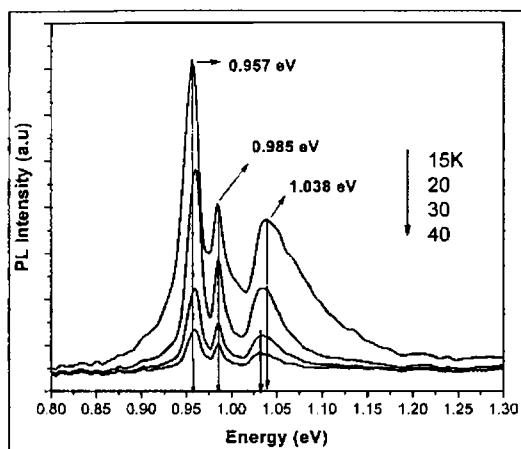


Fig. 4.4: Temperature dependence of PL emission from sample CIS38.

When the temperature was raised, the peak position of the FE emission shifted gradually to lower energy side with a gradual increase in its FWHM, which was reported by Niki et al.<sup>43</sup> Shift in the peak energy position was found to be  $2.8 \times 10^{-4}$  eV/K and was reasonable to assume that this was due to the increase in band gap of CISE with temperature, in line with the calculations reported by Kazmerski and Shieh using Varshani's equation.<sup>57, 58</sup> For all temperatures the line width of the 0.984 eV emission ( $I_A$ ) was the smallest while it was the largest for the 0.957 eV emission ( $I_B$ ).

Figure 4.5 represents the plot of log of ratio of the intensities of the emission at 1.037 eV to the emission at 0.984 eV versus  $1000/T$ , fitted using the relation (3.6) (section 3.4) from which, for  $\Delta E$  a value of  $\sim 5$  meV was obtained which agreed with the exciton binding energy in CISE.<sup>45, 46, 43</sup> Hence it was concluded that the 1.037 eV emission was the FE emission in this sample. Takahashi et al. had observed an emission at 0.984 eV and assigned it to the transition from CB to neutral acceptor level (vacancy of Indium ( $V_{In}$ )) ( $e, A^0$ ) in single crystals.<sup>41</sup> Leo et al. observed a line at 0.987 eV, in thin films grown by multi-source PVD. However they left it unassigned.<sup>59</sup> Mickelsen et al. observed sharp narrow band

emission near 0.98 eV in In-rich samples only. <sup>60</sup> CIS38 was In-rich by stoichiometry and was in line with the observations of Mickelsen et al.

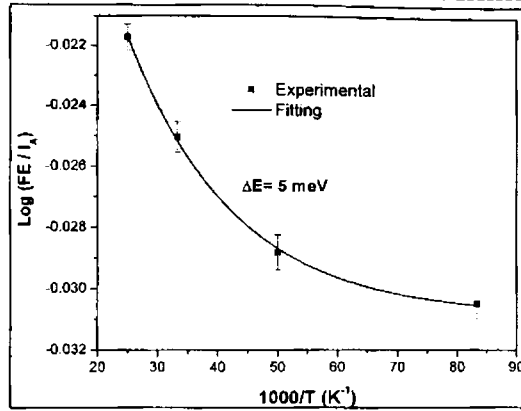


Fig. 4.5: Ratio of the intensities of FE emission to  $I_A$ , as a function of temperature fitted using relation (3.6).

From Fig. 4.5 it could also be realized that the intensity of the  $I_A$  emission increased relative to that of the FE emission - a characteristic nature of the free-to-bound transition. Thermal energy causes a shift of  $4.1 \times 10^{-5}$  eV/K for a free-to-bound ( $e, A^0$ ) transition based on the ( $\frac{1}{2} k_B T$ ) contribution and this was beyond the resolution limit of the equipment. Since there was no detectable shift in the PL peak position of this emission, it was assigned to the ( $D^0, h$ ) transition which follows the mathematical relation (1.49) (section 1.2.4A). Using relation (1.49), the activation energy of the impurity  $E_D$  was found to be 59 meV, which was same as that of the ionized  $V_{Se}$  donor level.<sup>61</sup> Film stoichiometry also supported this assignment. Vacancy of Se could be in one of the three charge states  $V_{Se}, V_{Se}^-$  or  $V_{Se}^{--}$ . As the concentration of Selenium vacancies grow with the deviation from the valence stoichiometry, the  $V_{Se}$  charge state drives from neutral to the charged states (-1 or -2), and the donor level gets embedded deeper into the band gap from  $E_D = 55-80$  meV.<sup>20, 59, 62, 63</sup> Thus the emission at 0.985 eV could be assigned to the transition from the ionized donor  $V_{Se}$  to the VB.

Saoussen et al. earlier observed the emission at 0.958 eV in CISE thin films grown on Si-wafers doped with Boron. They also observed that the intensity of the emission increased as a result of annealing in Argon atmosphere.<sup>53</sup> Rincón et al. also reported that the emission at 0.958 eV was due to transition between the ionized donor  $V_{Se}$  and the valence band.<sup>20</sup> Niki et al. observed emission at 0.959 eV in MBE grown films and had assigned it to a transition arising from the  $V_{Se} - V_{Cu}$  DAP recombination.<sup>64</sup>

In sample CIS38, the emission at 0.957 eV was separated from the  $(D^0, h)$  emission at 0.985 eV by 28 meV. This energy separation lies close to the longitudinal optical phonon modes of 28-29 meV in CISE as reported by Neumann et al and Tanino.<sup>65, 66</sup> However temperature dependence of this PL emission did not show characteristics of a LO phonon replica whose intensity increases as temperature increases. The plot of the ratio of intensities  $(FE/I_B)$  versus  $1000/T$  followed the relation (3.6), and for  $\Delta E$ , a value of  $\sim 6$  meV was obtained. This agreed with the exciton binding energy in CISE. Thus it was concluded that the emission at 0.957 eV was due to “bound-to-free transition”. The peak position of this emission shifted to higher energy side with increase in temperature which was again a characteristic of the  $(e, A^0)$  free-to-bound transition.

In general, for a PL emission occurring due to the transitions between the conduction band and acceptor impurity, the peak energy of emission can be described by the relation (1.50) (section 1.2.4B). The binding energies of various acceptor impurities can be determined from analysis of PL emission spectra using this relation. Ionization energy of the acceptor impurity  $E_A$  was found to be  $\sim 86$  meV from equation (1.50) using sample temperature  $T = T_e$  and  $E_g = 1.043$  eV. This energy closely agreed with the activation energy of the ionized  $V_{In}$  acceptor.<sup>44, 67</sup> Thus it could now be concluded that this emission was due to  $(e, A^0)$  transition between the conduction band and an acceptor impurity  $\sim 86$  meV above the valence band. Dagan et al had also reported 86 meV as the ionization energy for the ionized acceptor  $V_{In}$ .<sup>67</sup>

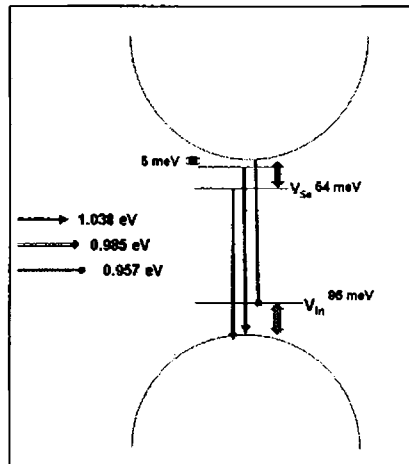


Fig. 4.6: Band diagram for sample CIS38.

Among a set of six samples prepared by this technique, only CIS38 yielded PL emission. Figure 4.6 shows the defect band diagram for this film. The repeatability of this sample was poor. Hence it was concluded that an alternate technique had to be developed for film deposition on a regular basis which could exhibit repeatable properties.

#### 4.4.2 $\text{CuInSe}_2$ thin films grown by diffusing Cu into $\text{In}_2\text{Se}_3$

In this process, films were prepared using “Technique -B” as described earlier. Wide ranges of samples of  $\text{CuInSe}_2$  were prepared with the composition varying from ‘Copper rich’ to ‘near stoichiometric’ to ‘Indium rich’ as in “Technique A”.

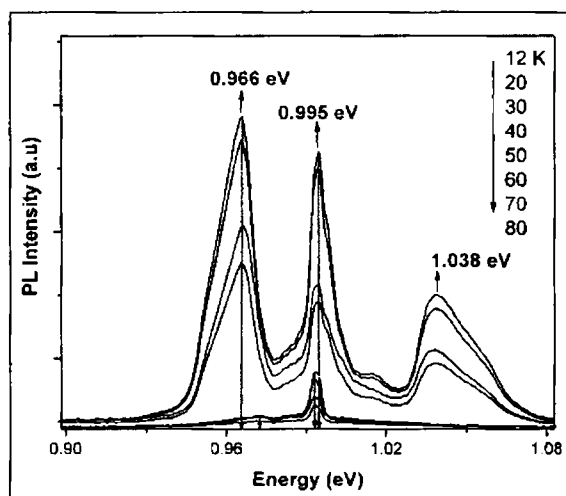
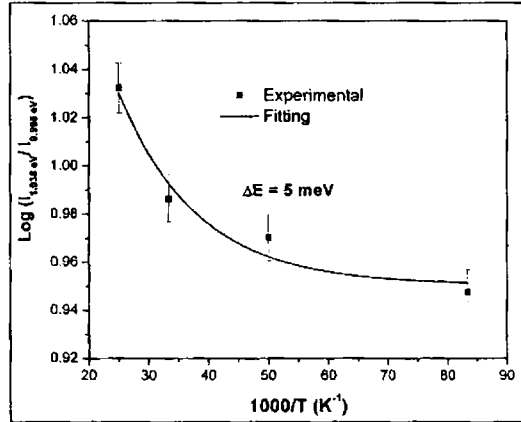


Fig. 4.7: Temperature dependence of PL emission in sample CIS48.

Figure 4.7 shows the temperature dependent PL spectra of sample CIS48. Three distinct PL emissions could be obtained from the films centered at 1.037 eV, 0.995 eV and 0.966 eV. These emissions were sharper compared to those obtained from sample CIS38. Also the peak position of the emissions on the low energy side of the emission at 1.037 eV was shifted to higher energy side compared to the position in sample CIS38. There was also strong indication of the better crystalline quality of these films in comparison with CIS38 from the XRD studies. The highest PL emission was at 1.038 eV and it possessed a high energy tail, going up to 1.076 eV. The FWHM of this emission was lower by an order, compared to that of sample CIS38. This was an indication of the improved

crystallinity of this sample compared to CIS38. The emission at 1.038 eV and its high energy tail were quenched above 40 K.

Figure 4.8 represents the plot of log of ratio of the intensity of emission at 1.038 eV to the intensity of the emission at 0.995 eV versus  $1000/T$  fitted using the relation (3.6). For  $\Delta E$ , a value of  $\sim 5$  meV was obtained which agreed with the exciton binding energy in CISe.<sup>43, 45, 46</sup> Hence it was concluded that the 1.038 eV emission was the FE emission in this sample. De-convolution of the spectrum yielded additional emission at 1.045 eV at 15, 20, 30 and 40 K. The de-convoluted emission at 1.045 eV was 7 meV above the emission at 1.038 eV and hence could be assigned to the band-to-band transition taking place in these films.



**Fig. 4.8:** Ratio of intensity of the emissions at 1.038 eV and 0.995 eV as a function of  $1000/T$  fitted using relation (3.6).

PL emission at 0.995 eV was observed by Tseng et al. in MBE grown films and they ascribed it to the LB-A ( $Cu_{In}$ ) transition.<sup>68</sup> Matsushita et al. in 1995 assigned emissions in the range 0.99-1.0 eV to the DAP transitions from the  $V_{Se}-Cu_{In}$  pair.<sup>69</sup> Rincón et al. had assigned the emission at 0.996 eV to the LB- $Cu_{In}$  transition.<sup>44</sup> Alberts et al. had assigned the emission at 0.992 eV to the VB-D ( $In_{Cu}/Cu_i$ ) transition.<sup>70</sup>

Sample CIS48 was In-rich with  $\Delta m = -0.16$ . Hence it could be assumed that defects like  $V_{Cu}/Cu_{In}/In_{Cu}$ , with the lowest formation energy, would have the highest probability of occurrence. The emission at 0.995 eV was persistent up to 80 K in this sample. As the temperature was raised, there was a shift in the energy of the position of the peak towards lower energy as evident from the temperature dependence of this emission (Fig. 4.7). This is one of the characteristic natures of the donor-acceptor pair (DAP) transition. The emission

energy of a DAP pair at a distance 'r' is given by relation (1.55) (section 1.2.5A).<sup>62</sup> Assuming that the Coulomb and van der Waal term in this relation are negligible, the binding energy of the DAP causing the emission at 0.995 eV was determined to be 47 meV.

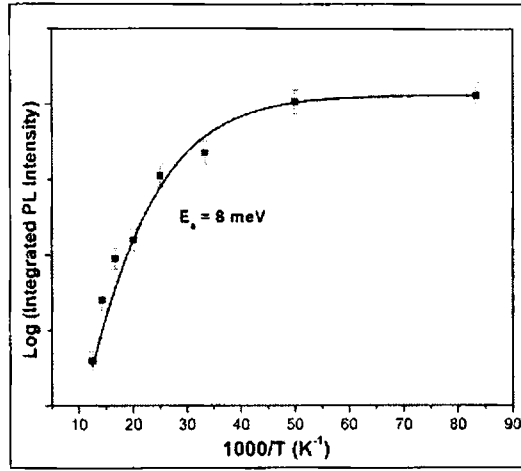


Fig. 4.9: Plot of 1000/T versus logarithmic (Integrated PL intensity) fitted using expression (3.5) for the emission at 0.995 eV.

Dirnstorfer et al. had also observed a DAP transition in this energy scale and had assigned it to a donor at 10 meV and the ionized acceptor complex [Cu<sub>n</sub>-Cu<sub>i</sub>] at 40 meV.<sup>71</sup> The sustenance of this emission to high temperature in sample CIS48 was another proof to the DAP dynamics. The activation energy of the shallower center among the DAP can be calculated by fitting the plot of log (Integrated PL intensity) vs. 1000/T, as shown in Fig. 4.9. Using the relation (3.5), describing the thermal quenching of PL in semiconductors  $\Delta E$  the activation energy of the capture center can be determined.<sup>72</sup> The activation energy of the shallow center was found to be 8 meV which agreed with the reported activation energy of the singly ionized  $In_{Cu}$  donor level.<sup>56</sup> Using  $E_D = 8$  meV,  $h\nu = 0.995$  eV,  $E_g = 1.042$  eV and neglecting the Coulomb and van der Waal term in relation (1.55) the activation energy of the acceptor  $E_A$  was found to be 39 meV. This agreed with the activation energy of the singly ionized  $V_{Cu}$  acceptor level reported by Dagan et al. and Masse et al.<sup>68, 73</sup>

The acceptor level due to vacancy of Copper  $V_{Cu}$  can be formed by the vacancy being in one of the three states  $V_{Cu}^0; V_{Cu}^-; V_{Cu}^{--}$ . The difference in the  $E_D$  value can be explained by changing the charge state of the main acceptor  $V_{Cu}$ . Sample stoichiometry indicated that CIS48 was less Cu-deficient. As the concentration of Copper vacancies grow with the deviation from the



valence stoichiometry, the  $V_{Cu}$  charge state drives from neutral into one of charged states (-1 or -2), and the acceptor level gets embedded deeper in the band gap. The same physics can be applied to the donor  $In_{Cu}$  which can also be ionized in three states. Thus it could be concluded that the PL emission at 0.995 eV in this sample was from the  $In_{Cu} - V_{Cu}$  DAP recombination. The sample stoichiometry was also supportive of this assigned as the film was Cu-deficient. Dagan et al. had reported the transitions between 0.96-0.97 eV due to the  $In_{Cu} - Cu_{In}$  DAP recombination.<sup>67</sup> Rincòn et al. had reported that the origin of the emission at 0.967 eV to be due to the LB- $V_{In}$  transition.<sup>44</sup> Albert et al. had on the other hand, reported the 0.969-0.975 eV emission to the LB- $Cu_{In}$  transition.<sup>70</sup> Dirnstorfer et al reported that the transitions between 0.86-0.97 eV were due to DAP transitions, but did not assign the pair.<sup>71</sup> The emission at 0.966 eV in our sample was quenched above 60 K. Also the peak position of this emission varied gradually when the temperature was raised from 12 to 40 K. Beyond this temperature, the position of the impurity shifted rapidly towards the high energy side. Figure 4.10(a) shows the peak position of this emission as temperature is raised and Fig. 4.10(b) shows the relative shift in peak position with respect to the band gap ( $E_g$ ).

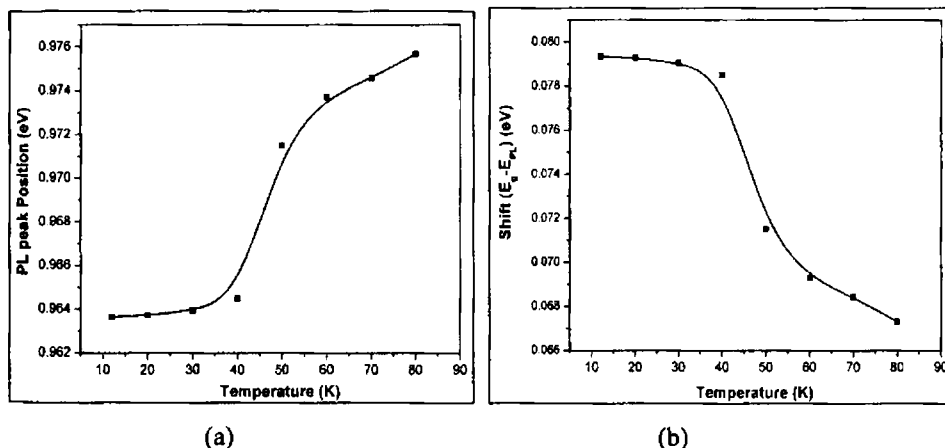


Fig. 4.10: (a) Plot of PL peak position of the emission with increase in temperature and (b) plot of the relative shift of this emission with respect to the band gap  $E_g$ .

The average shift in peak position of this emission was found to be  $1.76 \times 10^{-4}$  eV/K, which was of the same order as that for the  $\beta$  coefficient for CISE in this temperature range, representing the average temperature coefficient of band gap.<sup>46</sup> The peak energy of the PL emission shifted towards higher energy as temperature was raised. This gave conclusive evidence to the  $(e, A^0)$  free-to-bound nature of this transition. Using relation (1.50) the activation of the

acceptor impurity for this transition was obtained to be 77 meV which agreed closely to the activation energy of the ionized acceptor  $V_{In}$  level reported by Rincón et al. and Dagan et al.<sup>44, 67</sup> Thus it was concluded that the emission at 0.966 eV in this sample was due to the CB-  $V_{In}$  ( $e, A^0$ ) transition.

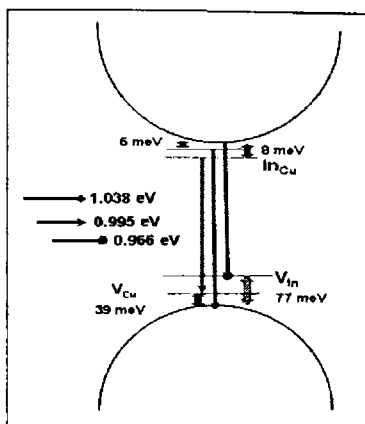


Fig. 4.11: Band diagram for sample CIS48.

Among samples prepared using this technique, only for this specific stoichiometry band edge emissions were observed. Other defect-related emissions obtained from films grown using “**Technique B**” are described as a separate section in this work. The repeatability of the samples was low because of the inability to control the Se-layer thickness and its properties using CBD technique. Hence the technique of CISE deposition had to be changed to improve the repeatability and quality. Figure 4.11 represents the schematic band diagram for CIS48 film prepared using **Technique B**.

#### 4.4.3 $CuInSe_2$ thin films grown by vacuum evaporation

To improve the optical quality and repeatability of the deposited CISE thin films, the deposition technique named “**Technique- C**” described in section (4.3.1). Figure 4.12 shows the temperature dependence of PL spectrum of sample CIS50. The PL was quenched above 20 K. There were 3 prominent peaks, centered at 1.027 eV, 0.987 eV and 0.951 eV. The highest energy PL emission line was centered at 1.027 eV and could be assigned to the FE line of this sample. This was shifted to lower energy side compared to that of the In-rich samples like CIS38 and CIS48. CIS50 was Cu-rich in stoichiometry and it has been reported that Cu-rich films have smaller band gap.<sup>36</sup> The shift in FE line to lower energy could be, hence, correlated to the decrease in band gap of Cu-rich films. The emission at 0.987 eV was ~ 45 meV below the band edge of 1.032 eV

(obtained by adding exciton binding energy to the FE energy). Peak position of this emission did not change when the temperature was raised. Hence this emission could be assigned to the free-to-bound ( $D^0, h$ ) transition, with the neutral  $Cu_i$  donor level located  $\sim 45$  meV below the CB.<sup>74</sup> Film stoichiometry supported this assignment as the films were Cu-rich in composition.

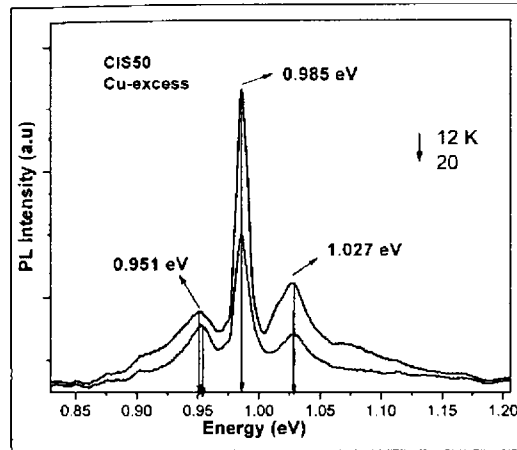


Fig. 4.12: Temperature dependence of PL emission in sample CIS50 (Cu/In = 1.11).

The emission at 0.951 eV shifted towards higher energy as temperature was raised in sample CIS50 and this is a characteristic of the free-to-bound ( $e, A$ ) transition. Using relation (1.50) (section 1.2.4B), the activation energy of the acceptor impurity was found to be 81 meV, which agreed with the activation energy of the ionized  $V_{In}$  acceptor level. The film stoichiometry also supported this assignment as the films were In-deficient. Thus it could be concluded that the emission at 0.951 eV in this sample was the ‘free-to-bound’ transition from the CB to the ionized  $V_{In}$  acceptor.

To further verify these assignments, an In-rich sample [CIS111] was prepared using the same technique by increasing the mass of In used for film deposition. When the films are made In-rich,  $V_{In}$  defect should be compensated and hence the emission CB- $V_{In}$  should be absent in such films. Figure 4.13 shows the PL spectrum for sample CIS111 which was prepared with a deficiency of Cu and excess of In. As can be seen in Fig. 4.13, the sample had no emission in the  $\sim 0.95$  eV region. This proved that the emission at  $\sim 0.951$  eV in Cu-rich films were due to the free-to-bound ( $e, A$ ) transition from the CB to the  $V_{In}$  acceptor. The highest PL peak energy in sample CIS111 was obtained to be 1.023 eV. This could be assigned to the FE line, based on the fitting of the plot of log of ratio of the intensities of the emissions at 1.023 eV and 0.988 eV versus  $1000/T$  using

the relation (3.6). This yielded the  $\Delta E = 5$  meV, agreeing with the exciton binding energy. Position of the FE line was supportive of the general observation that Cu-rich CISE have lower band gap compared to the In-rich counterparts. The emission at 0.988 eV was the most prominent in this sample and did not show any peak shift with increase in temperature. Using relation (1.49) energy position of the impurity was found to be 40 meV, which agreed with the activation energy of the donor  $Cu_i$ .<sup>74</sup> Hence this emission could be assigned to the  $Cu_i$  - VB free-to-bound ( $D^0, h$ ) transition.

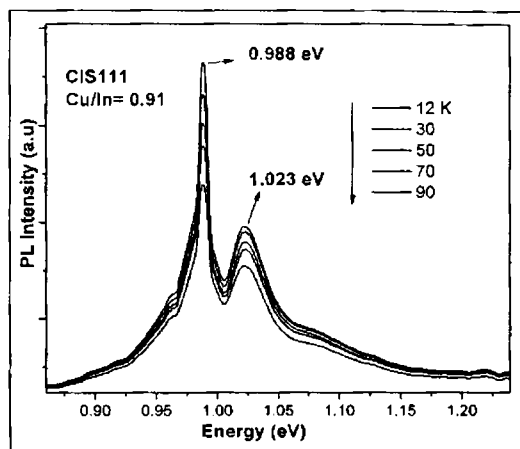


Fig. 4.13: Temperature dependent PL spectra for sample CIS111 (Cu/In =0.91).

Thus it was observed that the emission due to  $Cu_i$  - VB free-to-bound ( $D^0, h$ ) transition was present in both Cu-rich and In-rich samples. Hence it was essential to nail the origin of this emission. One method of verifying this assignment was studying the PL of a Cu-and In-rich CISE film, where the formation energy of the  $Cu_i$  donor level is very high. Also on a strictly stoichiometric sample such an emission would be absent.

To verify this idea, a critically stoichiometric sample (C1) and a sample with excess of both Cu- and In- were prepared. For both samples the amount of Selenium used was identical and only the content of In- and Cu- in the initial boat were varied. The film with excess of Cu- and In- was named as 'CIS115'. This sample could also be called 'stoichiometric' by the definition  $\Delta m = (Cu / In) - 1$  which turned out to be 0.03.

Figure 4.14 shows the PL spectrum for sample CIS115, taken at 12 K. From the figure it was very evident that there was no emission, which could be assigned to the  $Cu_i$  - VB free-to-bound ( $D^0, h$ ) transition. The highest PL peak energy was at 1.019 eV which could be the FE line in this sample. This emission had a shoulder at 0.974 eV. Thus our earlier assumption that the emission at

$0.985 \pm 5$  eV in CISe thin films was because of the  $Cu_i$  - VB free-to-bound ( $D^0, h$ ) transition could be verified. It could also be proposed that that the emission would be absent in a strictly stoichiometric sample.

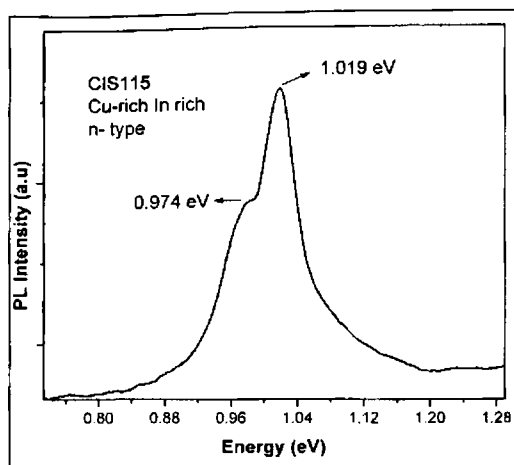
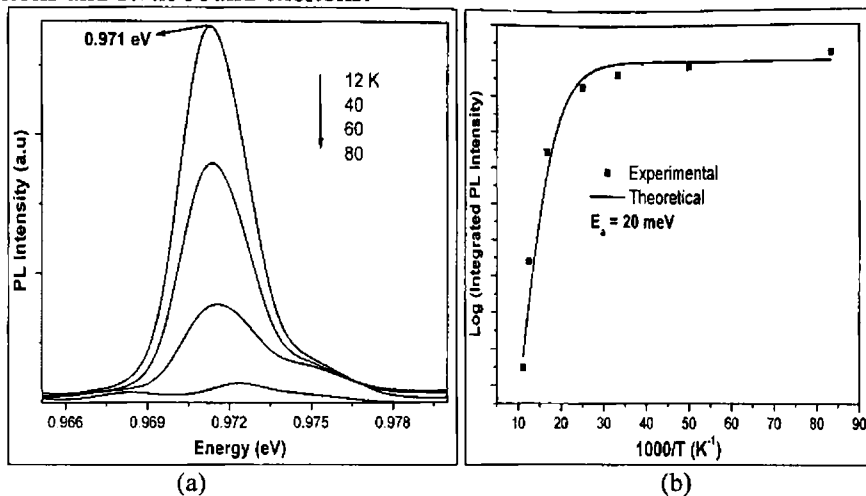


Fig. 4.14: PL spectra for sample CIS115 at 12 K.

Figure 4.15 shows the temperature dependence of PL of sample C1 which could be called strictly stoichiometric because of the definition of stoichiometry as per relation (4.1) and (4.2). This condition was well satisfied in this sample (Table 4.1). In sample C1 also the emission around 0.988 eV was absent which proved the correctness of the earlier assignment. The PL emission was centered at 0.971 eV, with a high energy shoulder at 0.976 eV. The FWHM of the emission at 0.971 eV [ $\sim 2$  meV] was the smallest among the samples studied in this work. The emission at 0.971 eV shifted to higher energy as the temperature was raised at the rate of  $1.1 \times 10^{-5}$  eV/K which was much smaller than the shift of  $4 \times 10^{-5}$  eV/K expected for a ( $e, A^0$ ) free-to-bound transition. Hence this was classified as a 'bound exciton emission'. When excitons are near defects, the defects can either increase or decrease the binding energy of the exciton. When the defects reduce the total system energy of the exciton, excitons will be trapped in the defects, which lead to the formation of bound excitons. Bound excitons give rise to PL emission at lower energy than that of free excitons. This could be the reason as to why the FE line was not observed in this sample. Bound exciton emission lines exhibit narrower line widths than free exciton emissions due to increased localization. This supported our observation as to why the emission at 0.971 eV exhibited very low FWHM. Since most semi-conducting materials contain significant quantity of impurities and/or defects which can trap excitons, the identification of the bound exciton states provides

an important characterization of impurities, which control the electro-optic properties of semiconductors. Neutral and ionized donors and acceptors can trap excitons and form bound excitons.



**Fig. 4.15:** (a) Temperature dependent PL spectra of sample C1 and (b) Plot of  $1000/T$  vs.  $\log$  (Integrated PL intensity) fitted using relation (3.5).

The bound exciton emission from the sample was quenched above 80 K. In order to calculate the PL quenching energy, a plot between logarithmic value of integrated PL intensity versus  $1000/T$  was fitted (Fig. 4.15(b)) using the relation (3.5). The activation energy ( $\Delta E$ ) of the impurity was obtained to be 20 meV. This was in good agreement with the reported activation energy of the doubly ionized  $In_{Cu}^{++}$  donor level.<sup>75, 76</sup> As temperature was raised, the localization decreased due to the thermal ionization of the defect center. This caused the bound exciton to become free, resulting in increase of FWHM and PL peak energy. Thus it could be concluded that this was the  $In_{Cu}^{++}$  donor bound exciton (BX:D2 ( $In_{Cu}$ )) emission in this sample. Figure 4.16(a) shows the PL spectra of sample CIS80 which was Cu-rich by composition. The film stoichiometry indicated this film to be highly Cu-rich. In CIS80 the highest PL peak position was at 1.032 eV. This emission was very weak compared to the other emissions in the sample. Also it was not observed above 12 K. Thus it could be assigned to be the FE line in this sample. Figure 4.16(b) depicts the temperature dependent PL in this sample. As the temperature was increased, the PL spectra broadened with the peak position shifting to 0.979 eV. Multiple fitting of the spectra at higher temperatures showed that the broad spectra contained emissions at 0.983 eV and 0.972 eV (Fig. 4.17(a) & (b)). Thus it could be concluded that merger of the line widths of the two emissions resulted in spectral broadening as well as

the shift in peak position of the PL emission. In the de-convoluted spectrum, since there was no change in peak position of the emission at 0.983 eV, it was realized that this was the  $Cu_i - VB$  free-to-bound ( $D^0, h$ ) transition observed in Cu-rich samples.

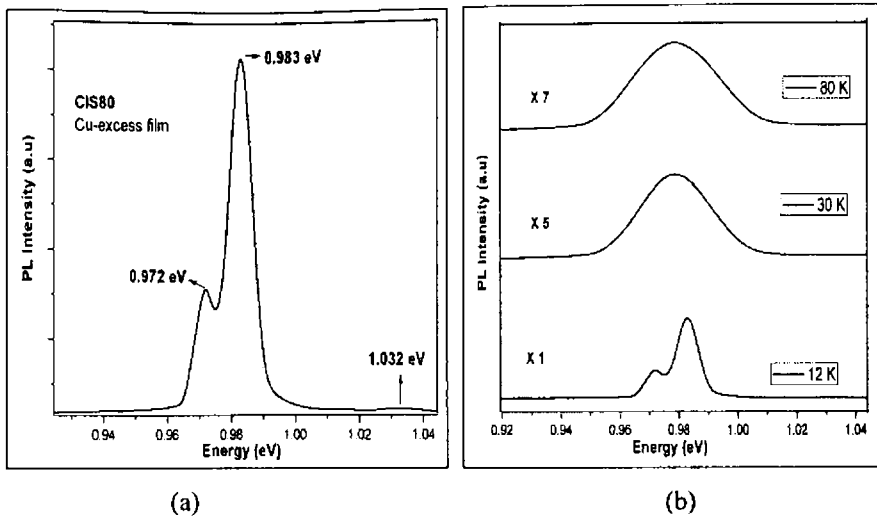


Fig. 4.16: (a) PL emission from sample CIS80 at 12 K and (b) Temperature dependence of PL emission in the sample.

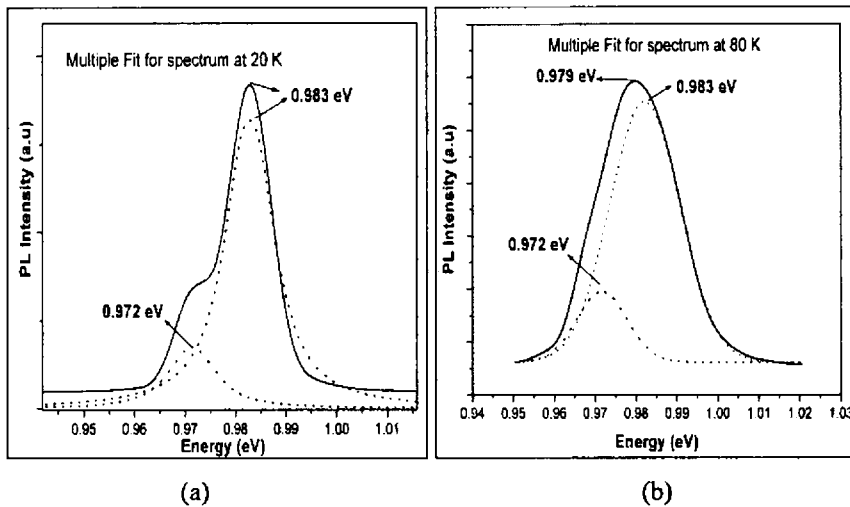


Fig. 4.17: 'Multiple curve fitting' of PL spectra for sample CIS80 at (a) 20 K and (b) 80 K.

Figure 4.18 represents the plot of ratio of the intensities ( $Cu_i - VB$  ( $D^0, h$ ) to 0.972 eV transitions) versus  $1000/T$  fitted using the relation (3.6). It could be realized that the intensity of the emission at 0.983 eV increased relative to the emission at 0.972 eV. A value of  $\sim 5$  meV was obtained for  $\Delta E$ , which agreed with the exciton binding energy in CISe.<sup>43, 45, 55</sup> Hence it was concluded that the emission at 0.972 eV was the 'bound exciton emission' in this sample. Rincon et

al. had observed lines at 0.973 eV and had speculated it to be the exciton bound to the acceptor  $Cu_{In}$  (BX2:  $Cu_{In}$ ).<sup>44</sup> Presently it can be only speculated that it may be the same BX2 emission, as the film stoichiometry supports the assignment. The absence of this emission line in In-rich samples also supported the hypothesis.

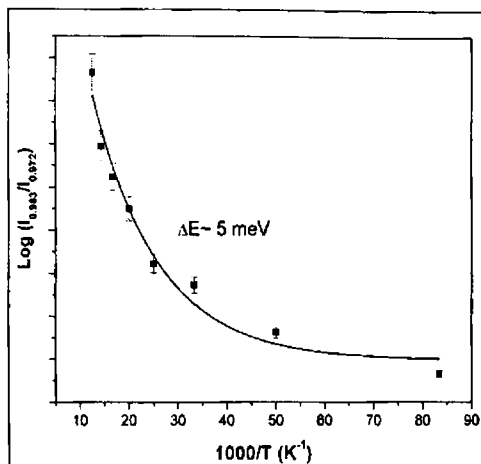


Fig. 4.18: Ratio of the intensities of the emission ( $I(0.983 \text{ eV}) : I(0.972 \text{ eV})$ ) as a function of temperature fitted using relation (3.6).

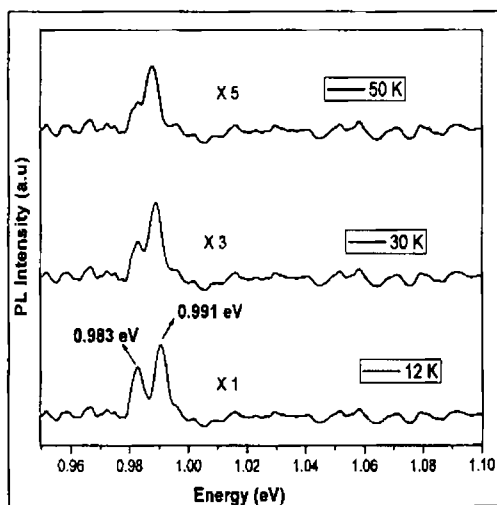


Fig. 4.19: Temperature dependence of PL spectra for sample CIS40.

The bound exciton emission BX2:  $Cu_{In}$  should be absent in a Cu-deficient film, if our earlier results were correct. To verify this, Cu-deficient film [CIS40] was prepared. Figure 4.19 shows the temperature dependence of PL of this sample. The signal was very noisy as seen in the figure. As expected, the 0.973



eV line due to the BX2:  $Cu_{in}$  was absent in this sample. The highest PL emission in this sample was centered at 0.991 eV at 12 K. This emission shifted to lower energy side as temperature was raised, and was not detected above 50 K. This shift proved that the transition was due to DAP recombination.

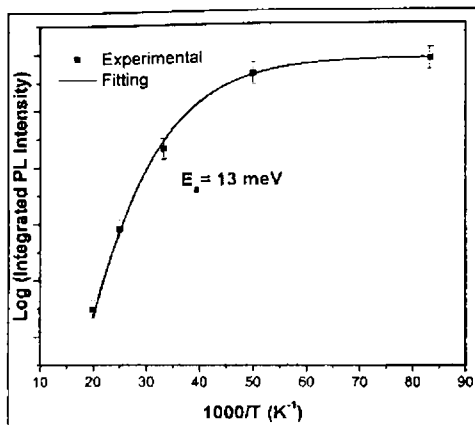


Fig. 4.20: Plot of  $1000/T$  vs.  $\log$  (Integrated PL intensity) fitted using relation (3.5).

The activation energy of the shallower center amongst the DAP was calculated by fitting the plot of logarithmic PL intensity vs.  $1000/T$ , as shown in Fig. 4.20 using the relation (3.5). The activation energy was obtained to be 13 meV which agreed with the activation energy of the  $In_{Cu}^+$  donor level. Neglecting the Coulomb and van der Waal terms and using  $E_D = 13$  meV and  $E_g = 1.042$  eV in relation (1.55),  $E_A$  was obtained as 38 meV which agreed with the activation energy of the  $V_{Cu}$  acceptor level. Hence this emission could be assigned to the  $In_{Cu}^+ - V_{Cu}$  DAP recombination. This supported our earlier assignment of the 0.995 eV emission to the same pair in sample CIS48 which was also In-rich by composition.

The 0.991 eV DAP line had a spike on the lower energy side, centered at 0.983 eV, whose position did not change with increase in temperature. But it was quenched at a much faster rate, compared to the DAP transition. Hence this emission could be assigned to the  $(D^0, h)$  transition. From our previous work, it was well established that the line at 0.983 eV is due to  $Cu_i - VB$  transition. For verification, we used relation (1.49) (section 1.2.4B) and obtained  $E_D = 59$  meV which agreed with the activation energy of ionized  $Cu_i$  donor level.<sup>74</sup> This result further strengthened our observation on the origin of the emission at 0.983 eV in CISe.

When the film stoichiometry was changed and PL analysis was carried out, emission lines with the same peak position were observed in Cu-rich and In-rich

films. The carrier recombination mechanisms identified were also identical for the emission lines at the same position. For example if we look at the emission at 0.985 eV, it follows the  $(D^0, h)$  recombination mechanism in both Cu-rich and In-rich samples. Our experiments indicated that to make use of PL as a tool to analyze the stoichiometry of CISE DAP recombination has to be monitored consistently. The  $0.995 \pm 0.005$  eV DAP transition was observed only in In-rich films and hence it could be used as the signature of In-excess composition. However the present results did not yield a PL emission line which could be specifically used to identify a stoichiometric or a Cu-rich film.

#### 4.4.4 Radiative Donor-Acceptor pair recombination in $\text{CuInSe}_2$ thin films

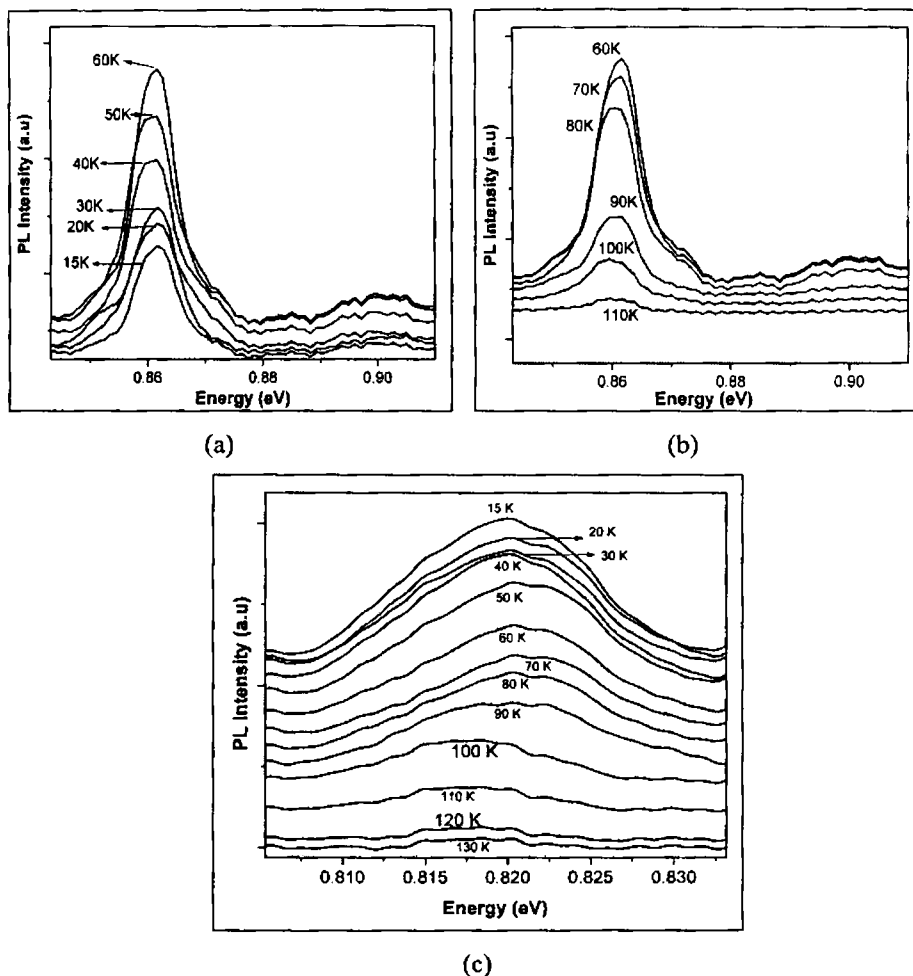


**Fig. 4.21:** Temperature dependence of PL intensity for sample CIS52: (a) Variation of emission at 0.86 eV from 15 to 60 K (b) Variation of the emission at 0.86 eV from 60 to 130 K (c) Variation of the emission at 0.82 eV from 15 to 130 K.

Cu-rich sample (CIS52) was investigated to study the DAP recombination, as the presence of this kind of emission in In-rich films was singular and could be used to identify the sample stoichiometry. The film stoichiometry was  $\Delta m = 1.53$  and  $\Delta s = -0.06$  and could be hence called a Cu-rich film. The temperature dependent PL spectra of sample CIS52 is shown in Fig. 4.21.

Two deep PL emissions, centered at 0.86 eV and 0.82 eV, could be recorded from the sample. Because of the position of the deep emission, it was natural to identify them to be related to impurities. The temperature dependence of the emission at 0.86 eV [named “A-band” hereafter], showed an anomalous behavior. The PL intensity increased as temperature was raised from 15 to 60 K (Fig. 4.21(a)). After this temperature, the intensity decreased and the emission was completely quenched beyond 110 K (Fig. 4.21(b)). It is normally expected that the PL emission intensity, for any kind of recombination, decreases as the temperature is increased. The second emission at 0.82 eV [named “B-band” hereafter] showed the normal decrease in PL intensity with increase in temperature (Fig. 4.21(c)).

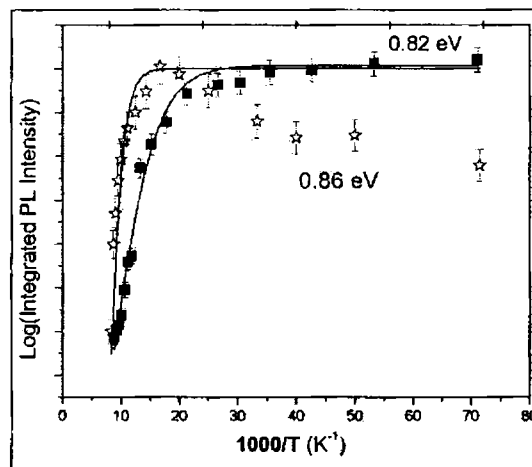


Fig. 4.22: Plot of log (Integrated PL intensity) versus  $1000/T$ , fitted using relation (3.5).

Activation energy of the shallower of the impurities associated with the two emissions were calculated by fitting the plot of logarithmic integrated PL intensity vs.  $1000/T$ , (Fig. 4.22), using the relation (3.5). The fit did not agree with the experimental results in the low temperature region for A-band. This disagreement was because of the unexpected increase in PL intensity with increase in temperature in the low temperature range ( $<60$  K). The activation energy was determined from the slope of the straight-line portion in higher

temperature region, where the fit agreed well and the activation energy was found to be 37 meV for the A-band. This agreed with the activation energy of 40 meV, reported for the  $\text{Cu}_{\text{In}}$  antisite acceptor, measured using PL and other techniques.<sup>13, 77</sup> Hence it was concluded that this emission was due to the  $\text{Cu}_{\text{In}}$  acceptor level. The film stoichiometry also supported this assignment.

Identification of the transition mechanism was done by analyzing the variation in PL intensity due to the changes in the excitation intensity. The plot depicting this dependence of variation in A-band as a function of excitation intensity is shown in Fig. 4.23(a). The experimental data was fitted using the relation (1.57) (section 1.2.5C). This equation depicts the PL intensity dependence on excitation intensity for semiconductors in general.<sup>61</sup>

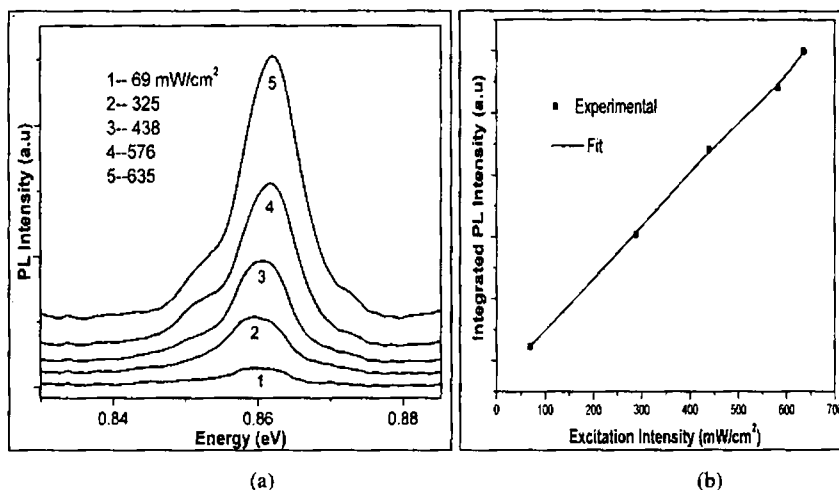


Fig. 4.23: (a) Variation in PL intensity with excitation power and (b) theoretical fit to the PL intensity dependence on excitation power dependence for the A-band.

From the fitting, the following parameters were obtained:  $\gamma=0.86$  and  $I_0=2500$  for A-band, as shown in Fig. 4.23(b). It is well known that for excitation with photons of energy exceeding the band gap energy  $E_g$ , the coefficient  $\gamma$  is generally  $<1$  for free-to-bound and donor-acceptor pair recombination.<sup>64</sup> The peak position of A-band was shifted by 21 meV to higher energy side, upon increasing the excitation intensity from 69 mW/cm<sup>2</sup> to 636 mW/cm<sup>2</sup>. This shift to higher energy is a characteristic nature of a donor-acceptor pair (DAP) recombination.<sup>13</sup> Based on these observations, it was concluded that the A-band emission was due to DAP recombination, with the  $\text{Cu}_{\text{In}}$  defect playing the role of the acceptor.

Binding energy of the acceptor of the A-band could be obtained from the minimum peak energy at low excitation power (Fig. 4.23(a)). Assuming that the

Coulomb and van der Waal terms in equation (1.55) are negligible and using  $E_g = 1.04$  eV, the donor energy was obtained to be 143 meV. This agreed with the activation energy of 120-160 meV reported for the ionized donor  $V_{Se}^+$ .<sup>61</sup> Thus it was concluded that the A-band emission was due to the  $V_{Se}^+ - Cu_{In}$  DAP transition. Wagner et al. had also observed a DAP transition at 0.90 eV in Cu-rich films, originating between a donor level at 10 meV and an acceptor level at 140 meV. However they had left the DAP unassigned.

For the B-band, logarithmic plot of integrated PL intensity vs.  $1000/T$  was fitted using the relation (3.5) as shown in Fig. 4.22. The activation energy of B-band was found to be 8 meV based on the fit. This agreed with the ionization energy of the ionized donor  $In_{Cu}^+$  reported and identified earlier. Hence it was concluded that this emission was associated with the  $In_{Cu}^+$  donor level.

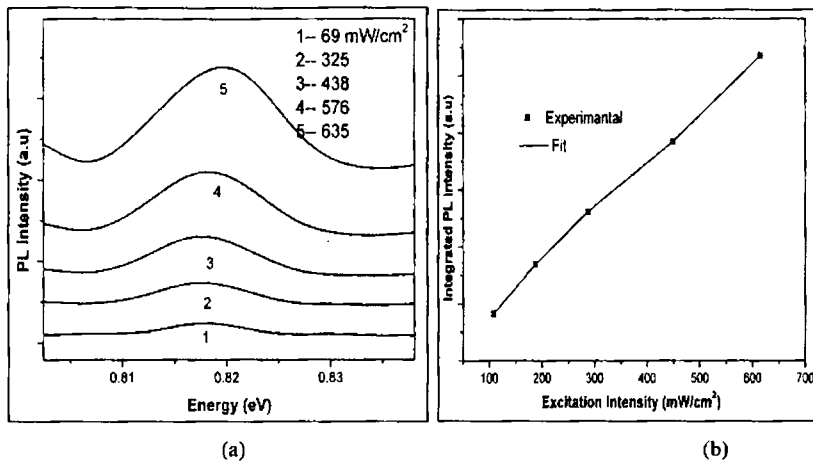


Fig. 4.24: (a) Variation in PL intensity with excitation power and (b) theoretical fit to the PL intensity dependence on excitation power dependence for the B-band.

The variation in PL intensity with excitation intensity in the case of B-band is shown in Fig. 4.24(a). Curve fitting was done, using equation (1.57) and this yielded  $I_0 = 12000$  and  $\gamma = 0.95$ , as depicted in Fig. 4.24(b). The PL peak position was shifted by 16 meV to the higher energy side on increasing the excitation intensity from 69 to 636 mW/cm<sup>2</sup>. The value of  $\gamma$  and blue shift of the PL peak proved the B-band to be due to DAP recombination. The acceptor activation energy was calculated from equation (1.55) neglecting the Coulomb and van der Waal terms, and was found to be 212 meV. This was in agreement with the expected value of  $250 \pm 60$  meV for the double acceptor  $V_{In}^-$  reported by Rincón et al.<sup>78</sup>

For the A-band emission (Fig. 4.21 (a & b)), instead of the expected decrease in PL intensity with increasing temperature, an anomalous increase of the PL

intensity with temperature was observed up to about 60 K, after which the intensity decreased. The emission was not detected above 120 K. Efficient non-radiative recombination mechanism above 60 K might have caused the decrease in PL intensity. The presence of two donor levels [ $V_{Se}$  and  $In_{Cu}$ ] could be used to explain the anomalous behavior shown by the A-band.

It can be assumed that electrons were released by the  $In_{Cu}^+$  donor level, to the conduction band, due to thermal activation. Subsequently, these electrons were trapped by the  $V_{Se}$  donor. As more and more electrons are trapped by the  $V_{Se}$  level, naturally there will be an increase in the PL intensity of the A-band. But the intensity of B-band was found to decrease in the temperature range where intensity of A-band was increasing. This happened as the electrons from  $In_{Cu}^+$  level were excited to the conduction band, which naturally decreased the intensity of B-band. Another point supporting this argument is that the temperature 60 K, (above which the intensity of A- band started decreasing) corresponds to a thermal energy of  $\sim 5$  meV which was matching well with (within the experimental error of our calculation for the  $In_{Cu}^+$ ) activation energy of 8 meV. Once the thermal excitation of the  $In_{Cu}^+$  defect level was complete, no further increase in trapping of electrons by  $V_{Se}^+$  would occur and hence the A – band intensity would decrease beyond this temperature.

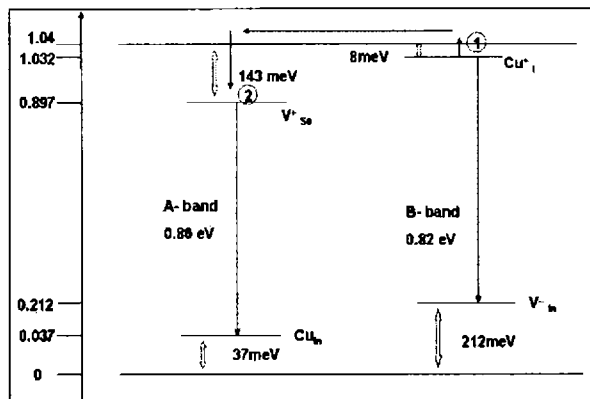
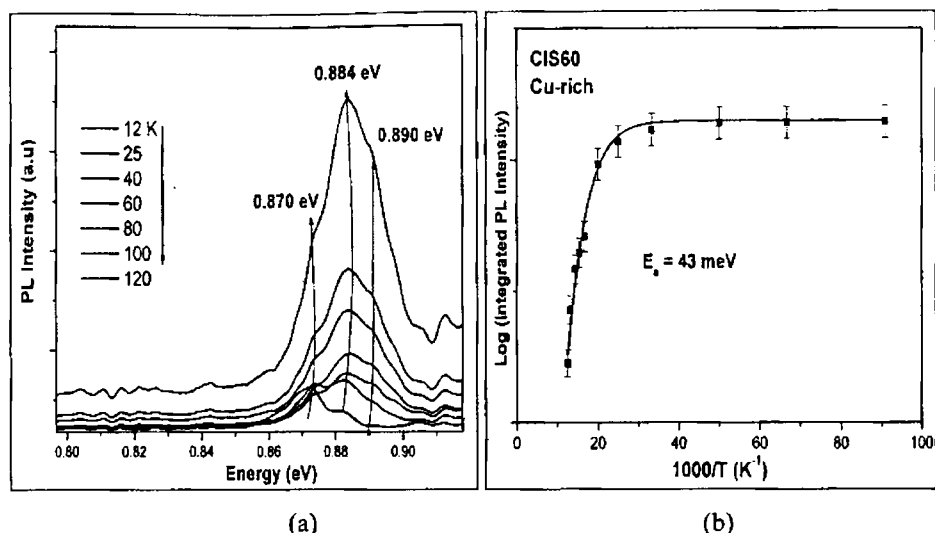


Fig. 4.25: Band diagram for Cu-rich CISE thin film at 15 K.

Based on this model, the band structure was proposed as shown in Fig. 4.25 for CIS52. As long as process 1 and process 2 are continuing, the increase in PL intensity with increase in temperature would take place. Once  $In_{Cu}^+$  defect level is completely exhausted, process 1 is terminated and process 2 does not occur. Hence the PL intensity starts decreasing with increase in temperature. A strong proof to this assignment was obtained when we carried out the PL analysis of In-

rich films for DAP transitions. It could be well assumed that when film stoichiometry is changed from Cu-rich to In-rich, point defects like  $Cu_{In}$  and  $V_{In}^{--}$  should be absent. None of our In-rich films like CIS38, CIS48, CIS111, C1 or C40 showed these DAP recombination.

With  $\Delta m = 1.53$  in sample CIS52, we were unsure why  $In_{Cu}^+$  defect level was present as the stoichiometry was against such an assignment. To verify this, PL analysis of other Cu-rich films were carried out.



**Fig. 4.26:** (a) Temperature dependence of PL emission in sample CIS60 and (b) Plot of logarithmic PL intensity versus  $1000/T$  of the emission at 0.884 eV, fitted using expression (3.5).

Figure 4.26(a) shows the temperature dependent PL spectra for CIS60 with  $\Delta m = 0.41$  where again the deep transition at 0.88 eV was observed. In this sample, the emission around 0.82 eV was absent. In sample CIS60, the 0.884 eV had a shoulder on the lower energy side centered at 0.870 eV and a high energy shoulder at 0.890 eV. When the temperature was raised, the intensity of the 0.884 eV emission decreased along with a shift in the peak position towards the lower energy side: a characteristic of the DAP recombination. The temperature dependence of the 0.884 eV emission was fitted using relation (3.5) as shown in Fig. 4.26(b) and the activation energy of the shallower of the two impurity levels involved in the DAP transition was obtained as 43 meV. This was in agreement with the activation energy of the  $Cu_{In}$  acceptor level.

Using relation (1.55) the activation energy of the donor level involved in this transition was obtained to be 113 meV in agreement with the activation energy of the  $V_{Se}^+$  donor level. Hence in this sample the  $V_{Se}^+ - Cu_{In}$  DAP recombination

was identified at 0.884 eV. However compared to sample CIS52, the anomalous behavior of the temperature dependence of PL intensity was not observed. This again proved that the competition between  $In_{Cu}^+$  and  $V_{Se}^+$  donor levels was responsible for the anomalous behavior. Since in CIS60, the defect  $In_{Cu}^+$  was not present, the anomalous behavior was not observed. The relative prominence of the 0.870 eV shoulder increased with the quenching of the shoulder at 0.890 eV. Again as temperature was raised, this emission at 0.870 eV gained prominence, which is a characteristic of the longitudinal optical phonon. This emission was not observed after the quenching of the 0.884 eV DAP emission. Hence it was assumed that this emission at 0.870 eV was the LO emission line of the  $V_{Se}^+$  -  $Cu_{In}$  DAP transition. However this assignment is speculative. The PL analysis of CISe for donor acceptor pair transitions identified the presence of defects like  $Cu_{In}$ ,  $V_{Se}^+$ ,  $In_{Cu}^+$  and  $V_{In}^+$ . Thus it was observed that the Cu-rich CISe films were rich with defect centers. The In-rich films possessed band edge emission which could be used as a signature of their composition.

#### 4.5 Donor-Acceptor and free-to-bound transitions in $CuInSe_2$ /ITO hetero-structure

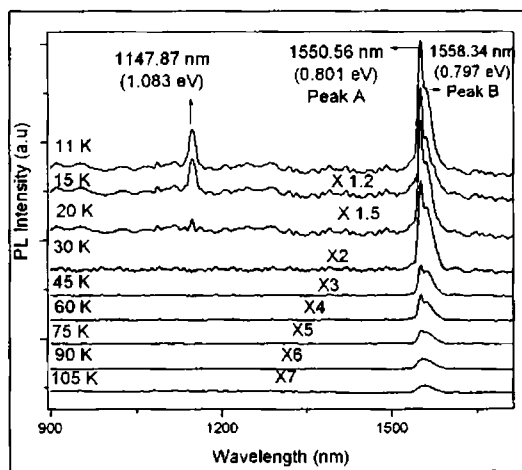


Fig. 4.27: Temperature dependence of PL spectra for the  $CuInSe_2$ /ITO hetero-structure.

PL spectra obtained from the  $CuInSe_2$ /ITO hetero-structure sample in the temperature range of 15 to 105 K is shown in Fig. 4.27. The highest energy peak was at 1147 nm (1.082 eV) with a FWHM of 10 meV whereas the most intense peak was split into two, namely peak A- at 1550 nm (0.801 eV) and peak B- at 1564 nm (0.794 eV). The emission peak at 1147 nm was 40 meV above the



fundamental band gap, 1.04 eV and this difference was in good agreement with the theoretical value of the crystal-field splitting of valence band in ClSe.<sup>54</sup> The presence of non-radiative paths might be causing the rapid quenching of this emission as this emission peak was not detected above 20 K.

From the temperature dependent PL studies (Fig. 4.27), it was observed that intensity of peak A- (1550 nm) rapidly decreased with increase in temperature. But the decrease in intensity of peak B (1564 nm) was gradual. Also peak A- was quenched at 90 K while peak B- persisted up to 105 K. The Arrhenius plots of logarithmic integrated PL intensity vs. 1000/T (Fig. 4.28), for peak A- and B- were fitted using the relation (3.5) describing the thermal quenching of the emission line. Activation energy/ thermal quenching energy for the PL emission was found to be 26 meV for peak A-, while for peak B- it was found to be 10 meV.

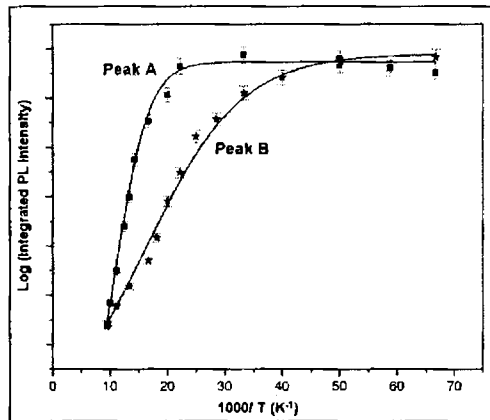


Fig. 4.28: Plot of logarithmic (Integrated PL intensity) versus 1000/T for Peak A- and Peak B-. The line represents the data fitted using equation (3.5).

Activation energy of the doubly ionized Indium in Copper ( $In_{Cu}^{++}$ ) antisite was reported to be  $21 \pm 5$  meV and for the singly ionized Indium in Copper ( $In_{Cu}^+$ ) antisite was reported to be in the  $9 \pm 2$  meV.<sup>20, 71</sup> The sample was n-type and the stoichiometry analysis showed that  $\Delta m = -0.16$ . This proved the film to be slightly In-rich, and from the agreement between the obtained activation energies with earlier reported values, peak A- was assigned to be due to the transition from the doubly ionized  $In_{Cu}^{++}$  donor, whereas peak B- was assigned to the transition from singly ionized  $In_{Cu}^+$  donor. The activation energy of the acceptor level involved in these two transitions was identified using relation (1.55). The acceptor level was identified to be the native hole band lying 0.25-0.28 eV above

the valence band. The existence of this band was reported to be universal in thin films and single crystals of CISE.<sup>80, 81</sup>

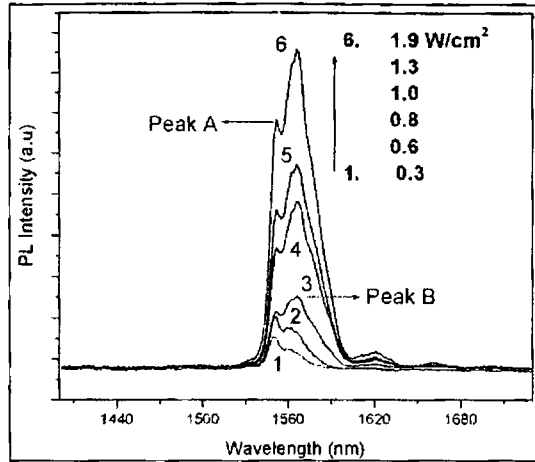


Fig. 4.29: Dependence of PL emission on various excitation intensities at 15 K.

In Fig. 4.29, the dependence of PL spectra on excitation intensity for this hetero-structure is depicted. It was observed that for low excitation intensities, the peak A was dominant. But on increasing excitation intensity, peak B- became very prominent. Variation in intensity of peak A- with excitation intensity at 15 K was fitted using the relation (1.57) [Fig. 4.30]. The raw data for this was obtained by fitting the PL spectra using peak fitting program. The value of  $\gamma$  was obtained to be 0.9 for peak A- (Fig. 4.30), which clearly indicated that this emission was associated with a DAP recombination.<sup>61</sup>

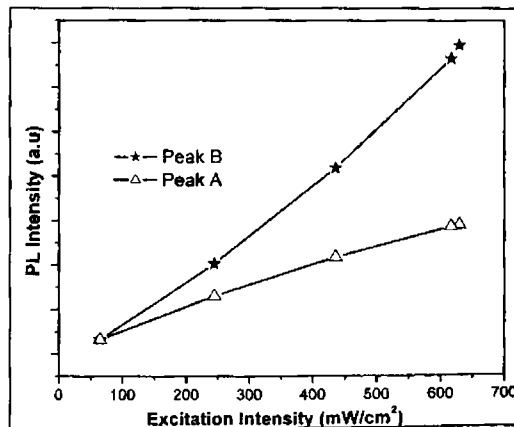


Fig. 4.30: PL intensity dependence on excitation intensity fitted using relation (1.57) for Peak A- at 15 K and for Peak B- at 90 K.

The fitting was also carried out for data obtained at 90 K where there was only peak B- was present. A good fit (Fig. 4.30) using relation (1.57) to the curve describing variation of PL intensity with excitation intensity gave  $\gamma = 1.1$ . This value was in good agreement with the predicted value of  $\gamma = 1$  for transition from a free state to a localized state.<sup>59</sup> Based on this observation, it was concluded that the intensity of peak B could be selectively tuned by increasing either the temperature of the sample (Fig. 4.27) (so that peak A- lost its prominence and only peak B- remained) or the excitation intensity at low temperature (Fig. 4.29). We concluded that the peak A- was due to DAP recombination and peak B- was due to 'conduction band-acceptor' ( $e, A$ ) transitions. This conclusion was supported by the nature of variation of PL emission intensity with excitation intensity. Selective occupation of the band- edge or the impurity level could lead to emission due to DAP recombination or impurity-band transitions. Selective occupation could be achieved by altering the temperature of the sample or by changing the excitation intensity as per theoretical models.<sup>82</sup>

We model the observed luminescence in this structure as follows: Both, donor ( $E_a = 26$  &  $10$  meV) and acceptor levels ( $0.25$ - $0.28$  eV) existed in the material. At low temperature, both the donor and acceptor levels were occupied with electrons and holes respectively, and hence the DA recombination (peak A) was prominent in the luminescence spectra. When the temperature was raised above 90 K the electrons from the donor levels were raised to the conduction band. Specifically here the  $In_{Cu}^+$  donor was completely ionized which has  $E_a = 10$  meV. Thus the peak in the luminescence corresponding to the band-acceptor transition gained prominence. As temperature was raised, the band-acceptor transition became prominent and the DA transition was quenched because of band edge filling. The energy separation between the two peaks was corresponding to the donor ionization energy, which further supported this model. Selective occupation of the donor levels and the conduction band edge was achieved at 15 K, by varying the excitation intensity. At low excitation levels, the DA transition (peak A) was prominent. As excitation intensity was increased, because of the band edge filling, the band-acceptor (peak B) transition became prominent.

We conclude that selective tuning of the donor acceptor pair transition or the conduction band to acceptor transition could be demonstrated by varying either of the two parameters- excitation intensity or temperature. The emission at 1550 nm was significant at low temperature and became weak as temperature was raised. The PL emission wavelength (1550 nm) is technologically critical

due to its applications in optical communication. Optical fiber communication is today mainly carried out at 0.6-0.8  $\mu\text{m}$ , whereas with the present optical fibers, it is desirable to have lasers emitting in the wavelength region 1.1 to 1.6  $\mu\text{m}$ . Optical fibers have their lowest loss and dispersion in the wavelength range 1.3 to 1.6  $\mu\text{m}$ . In particular, single-mode silica fibers have their lowest loss at 1.55  $\mu\text{m}$ . At this wavelength, the dispersion is not a minimum and hence, different frequency components will be transmitted at different speeds within the fiber. An alternative is to work at 1.33  $\mu\text{m}$ , where the fiber dispersion is minimal, but the losses are higher than the 1.55  $\mu\text{m}$ .<sup>82</sup> Therefore, the need of alternate hetero-structure systems, emitting these wavelengths useful for optical-fiber communication, is very evident and this is a widely researched area. Transparent-conducting-oxide (TCO)-based junctions like Indium Tin oxide (ITO)/Si, ITO/GaAs and ITO/InP have a wide variety of applications, in optoelectronic device fabrication.<sup>83-85</sup> Very few works on CuInSe<sub>2</sub>/ITO junction have been published previous to our work.<sup>86, 87, 76</sup> The PL emission at 1550 nm (0.801 eV) of this heterostructure can find application in the field of fiber-optic communication with some more R&D in this direction.

#### 4.6 Conclusions

Although various techniques have been performed to produce CISE thin films the efficiencies of solar cells based on CISE films have been limited to around 15% to date [at modular level], primarily due to the relatively low quality of the CISE absorber layers. In principle, CBD has the advantage of easy control of the film stoichiometry over a large scale at relatively low cost. It has already been utilized in industry for the production of a wide range of functional materials. Therefore, in this study, we have chosen the combination of the CBD technique and the SEL technique to deposit CISE thin films, and characterized the films in terms of its PL properties, to optimize and establish a process suitable for the production of CISE films for photovoltaic applications. This work primarily deals with two aspects: characterizing the PL emission from CISE films grown using diffusion of Cu- and In- into Se films [Here the Se layer was deposited using CBD] and secondly the PL characterization of CISE films grown through PVD of the elements and annealing the stacked layers. The other aspect was to possibly establish the use of PL as a stoichiometry identification tool.

- PL analysis of CISE thin films grown using a combination of the SEL and CBD showed that the repeatability of obtaining device quality films was very small. The films grown using “Technique A and B” were, in general, of poor device quality as they failed to give any PL signal. Only a very small percent of the samples deposited were good enough to yield any PL signal. The best of the films obtained showed free exciton emissions at 1.038 eV along with some free-to-bound  $((e, A^0)$  and  $(D^0, h))$  and donor acceptor pair transitions. The  $((e, A^0)$  and  $(D^0, h))$  transitions were very prominent and sustained to  $\sim 80$  K.

Impurity	Acceptor (A)/ Donor (D)	Activation Energy (meV)
$V_{In}$	A	$86 \pm 10$
$V_{In}^-$	A	212
$V_{Cu}$	A	39
$In_{Cu}^+$	D	8
$In_{Cu}^{++}$	D	20
$V_{Se}$	D	54
$V_{Se}^+$	D	143
$Cu_i$	D	45
$Cu_{In}$	A	37

**Table 4.3:** Point defects and their activation energy identified using PL.

- PL analysis of CISE samples with different compositions could identify shallow point defects and their thermal activation energy as tabulated in Table 4.3. The position of point defects like  $V_{In}, V_{In}^-, V_{Cu}, In_{Cu}^+, In_{Cu}^{++}, V_{Se}, V_{Se}^+, Cu_i$  and  $Cu_{In}$  were identified using PL.
- Various emission lines and their origin were identified in the course of this work. The peak positions, the film stoichiometry and their origin are summarized in Table 4.4.
- PL analysis of samples prepared using **Technique C** showed that the films were more consistent and repeatable in nature. The films possessed bound exciton emissions which are the characteristic of good quality films. The FE line was found to be very weak in samples prepared by

this technique. The  $((e, A^0)$  and  $(D^0, h)$ ) transition lines were the most dominant; but their temperature sustenance was lower compared to samples prepared by **Technique A** and **B**. The line widths of the emission were smaller which again indicated improvement of crystallinity of the films.

- Cu-rich films were having strong DAP recombination transitions which could be used to identify them. The In-rich films possessed relatively greater number of band edge emission compared to Cu-rich films. The DAP transitions in In-rich films had lower FWHM as compared to films of other stoichiometry. It could be concluded that Cu-rich films possessed DAP emissions in the 0.88-0.82 eV energy range which were absent for the In-rich films. Thus the DAP transitions could be used to distinguish Cu-rich and In-rich films. It has been possible to distinguish all films with  $Cu/In > 1$  from the films with  $Cu/In < 1$  based on the DAP recombination in the 0.88-0.82 eV range.

<b>Emission line (eV)</b>	<b>Film Parameters</b>	<b>PL origin</b>
$1.032 \pm 0.013$	Cu-rich/In-rich p/n type	FE
$0.995 \pm 0.005$	In-rich p/n type	$In_{Cu} - V_{Cu}$
$0.985 \pm 0.005$ 0.985	Cu-rich p type In-rich p type	$D(Cu_i) : VB$ $D(V_{Se}) : VB$
$0.972 \pm 0.002$ 0.971	Cu-rich p type Stoichiometric	$BX : A(Cu_{In})$ $BX : D2(In_{Cu})$
0.966 $0.955 \pm 0.003$	In-rich p type Cu-rich/ In-rich p type	$CB : A1(V_{In})$ $CB : V_{In}$
0.88-0.86	Cu-rich p type	$V_{Se}^+ - Cu_{In}$
0.82	Cu-rich p type	$In_{Cu}^+ - V_{In}^-$

**Table 4.4:** Various band edge emission lines with their origins assigned.

In the present work, characterization of PL emission from CISE samples grown using a combination of the SEL and CBD technique has been carried out. The characterization has enabled in establishing that CBD growth process leads to films with larger defect concentrations and hence making them unsuitable for device applications. This work also indicated an attractive perspective for the SEL grown CISE films. A *p*-type CISE absorber can be combined with *n*-type ZnO and/or ZnO:Al layers, which are normally prepared by the sputter

technique, to form a heterojunction solar cell, suggesting a continuous vacuum process for solar cell production. A hetero-structure of CISE on ITO has shown tunability in its luminescence at 1550 nm which is a wavelength region, critical in optical communication. Thus the work can be considered as the starting point to the development of opto-electronic devices using CuInSe<sub>2</sub> thin films.

#### 4.7 Reference

1. Shay, J. L. and Wernick, J. H., Ternary Chalcopyrite Semiconductors, Pergamon, Oxford, (1975).
2. Keck, D. B., Maurer, R. D. and Schultz, P. C., Appl. Phys. Lett. **22**, 307 (1973)
3. Fearheiley, M. L., Sol. Cells, **16**, 91 (1986).
4. Bachmann, K. J., Fearheiley, M., Shing, Y. H. and Tan, N., Appl. Phys. Lett. **44**, 407 (1989).
5. Zunger, A., Appl. Phys. Lett. **50**, 164 (1987).
6. Wei, S. -H., Ferreira, L. G. and Zunger, A., Phys. Rev. B, **45**, 2533 (1992).
7. Osorio, R., Lu, Z. W., Wei, S. -H. and Zunger, A., Phys. Rev. B, **47**, 9985 (1993).
8. Wei, S. -H. and Zunger, A., J. Appl. Phys. **78**, 3846 (1995).
9. Tell, B., Shay, J. L. and Kasper, H. M., J. Appl. Phys. **43**, 2469 (1972).
10. Migliorato, P., Shay, J. L., Kasper, H. M. and Wagner, S., J. Appl. Phys. **46**, 1777 (1975).
11. Noufi, R., Axton, R., Herrington, C. and Deb, S. K., Appl. Phys. Lett. **45**, 668 (1984).
12. Parkes, J., Thomlinson, R. D. and Hampshire, M. J., Solid-State Electron. **16**, 773 (1973).
13. Rockett, A. and Birkmire, E. W., J. Appl. Phys. **70**, R81 (1991).
14. Hedstrom, J., Olsen, H. J., Bodegard, M., Kylner, A., Stolt, L., Hariskos, D., Ruckh, M. and Schock, H. W., The Conference Record of the Twenty-third IEEE Photovoltaic Specialists Conference, IEEE, New York, p. 364 (1993).
15. Gabor, A. M., Tuttle, J. R., Albin, D. S., Contreras, M. A., Noufi, R. and Hermann, A. M., Appl. Phys. Lett. **65**, 198 (1994).
16. Champness, C. H., Proceedings of the 29th IEEE Conference, IEEE, Piscataway, NY, p. 732 (2002).

17. Neumann, H., Van Nam, N., Hobler, H. and Kuhn, G., *Solid State Commun.* **25**, 899 (1978).
18. Neumann, H., Nowak, E. and Kuhn, G., *Cryst. Res. Technol.* **16**, 1369 (1981).
19. Neumann, H., Tomlinson, R. D., Avgerinos, N. and Nowak, E., *Phys. Stat. Sol. (a)*, **75**, K199 (1983).
20. Rincòn, C. and Bellabarba, C., *Phys. Rev. B*, **33**, 7160 (1986).
21. Cahen, D. and Noufi, R., *J. Phys. Chem. Solids*, **53**, 991 (1992).
22. Madelung, O., Schulz, M. and Weiss, H., *Semiconductors: Physics of II-VI and I-VII Compounds, New Series, Group III, Vol. 17*, Springer, Berlin, (1982).
23. Zhang, S. B., Su-Huai Wei, Alex Zunger and Katayama-Yoshida, H., *Phys. Rev. B*, **57**, 9642 (1998).
24. Groenink, J. A. and Janse, P. H., *J. Phys. Chem.* **110**, 17 (1978).
25. Ermer, J. H. and Love, R. B., "Method for Forming CuInSe<sub>2</sub> Films," European patent application, filed July 10, 1986, application No. 86305324.5.
26. Neumann, H., Nowak, E., Schumann, B. and Kuhn, G., *Thin Solid Films*, **74**, 197 (1980).
27. Neelkanth Dhere, G., Cristina Lorenzo, M., Ramesh Dhere, G. and Lawrence Kazmerski, L., *Sol. Cells*, **13**, 59(1984).
28. Trykozko, R., Bacewicz, R., Filipowicz, J., *Sol. Cells*, **16**, 351 (1986).
29. Isomura, S., Nagamatsu, A., Shinohara, K. and Aono, T., *Sol. Cells*, **16**, 143 (1986).
30. Mikihiro Nishitani, Takayuki Negami, Masaharu Terauchi and Takashi Hirao, *Jpn. J. Appl. Phys.* **31**, 192 (1992).
31. Adurodija, F. O., Carter, M. J., Hill, R., *Sol. Energy Mat. Sol. Cells*, **37**, 203 (1995).
32. Parretta, A., Addonizio, M. M., Loreti, S., Quercia, L and Jayaraj, M. K., *J. Cryst. Growth*, **183**,196 (1998).
33. Firoz Hasan, S. M., Subhan, M. A., and Mannan, Kh. M., *J. Phys. D: Appl. Phys.* **32**, 1302 (1999).
34. Zeenath, N. A., Pillai, P. K. V., Bindu, K., Lakshmi, M. and Vijayakumar, K. P., *J. Mater. Sci.* **35**, 2619 (2000).
35. Bindu, K., Sudha Kartha, C., Vijayakumar, K. P., Abe, T. and Kashiwaba, Y., *Sol. Energy Mat. Sol. Cells*, **79**, 67 (2003).



36. Deepa, K. G., Ratheesh Kumar, P. M., Sudha Kartha, C., and Vijayakumar, K. P., *Sol. Energy Mat. Sol. Cells*, **90**, 3481 (2006).
37. Migliorato, P., Shay, J. L., Kasper, H. M. and Sigurd Wagner, *J. Appl. Phys.* **46(4)**, 1777 (1975).
38. Rincón, C., González, J. and Sánchez Pérez, G., *J. Appl. Phys.* **54(11)**, 6634 (1983).
39. Lange, P., Neff, H., Fearheiley, M. and Bachmann, K. J., *Phys. Rev. B*, **31**, 4074 (1985).
40. Lange, P., Neff, H., Fearheiley, M. and Bachmann, K. J., *J. Electron. Mater.* **14(6)**, 667 (1985).
41. Masayuki Tanda, Susumu Manaka, Jorge, R., Encinas Marin, Katsumi Kushiya, Hideki Sano, Akira Yamada, Makoto Konagi and Kiyoshi Takahashi, *Jpn. J. Appl. Phys.* **31**, L753 (1992).
42. Niki Shigeru, Makita Yunosuke, Yamada Akimasa, Obara Akira, Misawa Syunji, Igarashi Osamu, Aoki Kazuhiro and Kutsuwada Noboru, *Jap. J. Appl. Phys.* **33 (4A)**, L500 (1994).
43. Niki, S., Shibata, H., Fons, P. J., Yamada, A., Obara, A., Makita, Y., Kurafuji, T., Chichibu, S. and Nakanishi H., *Appl. Phys. Lett.* **67(9)**, 1289 (1995).
44. Rincón, C., Arsene, M. A., Wasim, S. M., Voillot, F., Peyrade, J. P., Bocaranda, P. and Albacete, A., *Mater. Lett.* **29**, 87 (1996).
45. Schön, J. H. and Bucher, E., *Appl. Phys. Lett.* **73(2)**, 211 (1998).
46. Mudryi, A. V. , Bodnar, I. V. , Gremenok, V. F., Victorov, I. A. , Patuk, A. I. and Shakin, I. A., *Sol. Energy Mat. Sol. Cells*, **53(3-4)**, 247 (1998).
47. Mudriy, A. V., Bodnar, I. V., Viktorov, I. A., Gremenok, V. F. , Yakushev, M. V., Tomlinson, R. D., Hill, A. E. and Pilkington, R. D., *Appl. Phys. Lett.* **16**, 2542 (2000).
48. Yakushev, M. V., Mudryi, A. V. and Tomlinson, R. D., *Appl. Phys. Lett.* **82**, 3233 (2003).
49. Yakushev, M. V., Mudryib, A. V., Feofanova, Y. and Tomlinsone, R. D. , *Thin Solid Films: Proceedings of Symposium B, Thin Film Chalcogenide Photovoltaic Materials, E-MRS Spring Meeting*, **431-432**, 190 ( 2003).
50. Mudryia, A. V., Gremenoka, V. F., Victorova, I. A., Zalesskia, V. B., Kurdesova, V. I., Kovalevskia, F. V., Yakushev, M. V. and Martin, R. W. , *Thin Solid Films: Proceedings of Symposium B, Thin Film Chalcogenide Photovoltaic Materials, E-MRS Spring Meeting*, **431-432**, 193 (2003).
51. Rega, N., Siebentritt, S., Beckers, I. E., Beckmann, J., Albert, J. and Lux-Steiner, M., *Thin Solid Films: Proceedings of Symposium B, Thin Film*

- Chalcogenide Photovoltaic Materials, E-MRS Spring Meeting, 431-432, 186 (2003).
52. Sho Shirakata and Hideto Miyake, *Phys. Stat. Sol. (a)*, **203**, 2897 (2006).
  53. Merdes Saoussen, Bechiri Lakhdar, Benabdeslem, Mohammed, Benslim Noureddine, Madelon Roger, Nouet Gerard, Sano Masatoshi and Ando Shizutoshi, *Jpn. J. Appl. Phys. Part 1*, **45**, 1495 (2006).
  54. Neumann, H., *Sol. Cells*, **16**, 317 (1986).
  55. Zott, S., Leo, K., Ruckh, M. and Schock, H.-W., *Proceedings of the 25<sup>th</sup> PVSC, Washington, D.C.*, p. 817 (1996).
  56. Shay, J. L. and Wernick, J. H., *Ternary Chalcopyrite Semiconductors: Growth, Electronic Properties and Applications*, Pergamon, Oxford, p. 118 (1975).
  57. Kazmerski, L. L. and Shieh, C. C., *Thin Solid Films*, **41**, 35 (1977).
  58. Varshni, Y. P., *Physica*, **34**, 149 (1967).
  59. Zott, S., Leo, K., Ruckh, M. and Schock, H. -W., *J. Appl. Phys.* **82**(1), 356 (1997).
  60. Mickelsen, R. A., Chen, W. S., Hsiao, Y. R. and Lowe, V. F., *IEEE Trans. Electron Devices*, **31**, 542 (1984).
  61. Medvedkin, G. A. and Magomedov, M. A., *J. Appl. Phys.* **82** (8), 4013 (1997)
  62. Zott, S., Leo, K., Ruckh M. and Schock, H. -W., *Appl. Phys. Lett.* **68**(8), 1144 (1996).
  63. Massé, G., *J. Appl. Phys.* **68**(5), 2206 (1990).
  64. Niki, S., Fons, P. J., Yamada, A., Kurafuji, T., Chichibu, S., Nakanishi, H., Bi, W. G. and Tu, C. W., *Appl. Phys. Lett.* **69** (5), 647 (1996).
  65. Neumann, H., Tomilson, R.D., Kissinger, W. and Avgerinos, N., *Phys. Stat. Sol. (b)*, **118**, K51 (1983).
  66. Tanino, H., *Phys. Rev. B*, **45**, 13323 (1992).
  67. Dagan, G., Abou-Elfotouh, F., Dunlavy, D. J., Matson, R. J. and Cahen, D., *Chem. Mater.* **2**, 286 (1990).
  68. Tseng B. -H., Lin S. -B., Hsieh K. -C. and Hwang H. -L., *J. Cryst. Growth*, **150**, 1206 (1995).
  69. Matsushita, H. and Takizawa, T., *Jpn. J. Appl. Phys.* **34**, 4699 (1995).
  70. Alberts, V. and Chenene, M. L., *J. Phys. D: Appl. Phys.* **32**, 3093 (1999).
  71. Dirnstorfer I., Burkhardt W., Meyer B. K., Ostapenko S. and Karg F., *Solid State Commun.* **116**, 87 (2000).
  72. Dean, J. P., *Phys. Rev.* **157**, 655 (1967).

73. Djessas, K., Yapi, S. and Massé, G., *J. Appl. Phys.* **8**, 4111 (2004).
74. Schön, J. H., Alberts, V. and Bucher, E., *J. Appl. Phys.* **81**(6), 2799 (1997).
75. Abou-Elfotouh, F., Kazmerski, L. L., Moutinho, H. R., Wissel, J. M., Dhere, R. G., Nelson, A. J. and Bakry, A. M., *J. Vac. Sci. Technol.* **A9**, 554 (1991).
76. Jayakrishnan, R., Deepa, K. G., Sudha Kartha, C. and Vijayakumar, K. P., *J. Appl. Phys.* **100**, 046104 (2006).
77. Lange, P., Neff, H., Fearheiley, M. and Bachmann, K. J., *Phys. Rev. B*, **31**, 4076 (1986).
78. Rincón, C. and Marquez, R. J., *Phys. Chem. Solids*, **60**, 1865 (1999).
79. Herberholtz, R., Walter, T., Muller, C., Pricdimeier, T., Schock, H. W., Saad, M., Lux. Steiner, M. Ch. and Alberts, V., *Appl. Phys. Lett.* **69**, 2888 (1996).
80. Walter, T., Herberholz, R., Muller, C. and Schock, H.W., *J. Appl. Phys.* **80**, 4411 (1996).
81. Igalson, M. and Schock, H. W., *J. Appl. Phys.* **80**, 5765 (1996).
82. Pallab Bhattacharya, *Semiconductor Optoelectronic Devices*, Second Edition, Pearson Education, Inc. p. 299 (2002).
83. Morgado, J., Barbagallo, N., Charas, A., Matos, M., Alcacer, L., Cacialli, F., *J. Phys. D: Appl. Phys.* **36**, 434 (2003).
84. Kobayashi, H., Ishida, T., Nakato, Y. and Mori, H., *J. Appl. Phys.* **78**, 3931 (1995).
85. Shewchun, J., Dubow, J. B., Wilmson, C. W., Singh, R., Burk, D. and Wager, J. F., *J. Appl. Phys.* **50**, 2832 (1979).
86. Kazmerski, L. L. and Sheldon, P., *Proc. 13th IEEE Photovoltaic Specialists Conf. IEEE*, New York, p. 541 (1978).
87. Kazmerski, L. L. and Wagner, S., *Current Topics in Photovoltaic*, eds. Coutts, T. J. and Meakin, J. D., Academic Press, New York (1985).

## CHAPTER 5

### Opto-electronic Characterization of $\beta$ - $\text{In}_2\text{S}_3$ Thin Films

---

*The photo-luminescence (PL) and photo-conductivity (PC) in  $\beta$ - $\text{In}_2\text{S}_3$  thin films prepared using Chemical Spray Pyrolysis (CSP) technique, as a function of the composition is studied in this chapter. A green luminescence because of the transition between vacancy of Sulphur defect level and vacancy of Indium ( $V_s - V_{In}$ ) defect level and a red luminescence because of the transition between interstitial Indium defect level and Oxygen replacing Sulphur ( $In_i - O_{V_s}$ ) defect level was identified in this system. Temperature dependent PL studies were used to calculate the thermal activation energy of  $In_i$ ,  $V_{In}$  and  $O_{V_s}$  defect levels. Stoichiometry dependent photosensitivity was exhibited by the films. From the excitation energy and temperature dependent PC studies it was observed that the  $V_{In}$  and  $In_i$  defect levels controlled the photoconduction mechanism. The lifetime of the carriers was determined to be  $\sim 24$  ms using AC-photo-conductivity. Conductance Atomic Force Microscopy showed that the grain boundaries were found to be more conducting than the grain and thus formed an additional conduction channel for the charge carriers. The photosensitive nature and broad luminescence makes this material an ideal material for opto-electronic devices like third generation solar cells, photo detectors and luminescent down converters.*

#### 5.1 Introduction

Starting from a II-VI compound, a variety of semiconductors can be built by replacing the divalent metal by other metals or combinations of them.<sup>1</sup> Replacement of the divalent metal by one of the Group III-B elements leads to a defect structure of the formula  $M_2X_3$  in which the non-metallic constituent X forms a cubic or hexagonal closed pack structure, where as part of the cation sites, (normally occupied in the Zincblende-, Wurtzite-, or similar lattices), remain vacant.<sup>2</sup> These III<sub>2</sub>-VI<sub>3</sub> compounds should be similar in some respect to

other Zincblende and Wurtzite-type materials. However unusual features are expected to be caused by the defect structure, such as a very strong scattering probability arising from the high defect concentration.<sup>1</sup> Different defect structures are found for several of the Group III- Group VI compounds.<sup>3</sup> Most of the III-VI compounds exist in several modifications: some of these are obtained by long time annealing and show an ordered arrangement of the cation vacancies possibly resulting in different transport properties in the ordered or disordered form.

Great diversity and many different stoichiometry are observed for the binary combinations of a Group III (Ga, In, Tl) and a Group VI chalcogen (S, Se, Te). Several structural types are found for these compounds including a defect Wurtzite structure for  $\text{Ga}_2\text{E}_3$ , a defect spinel for  $\text{In}_2\text{E}_3$  and layered structures for compounds of stoichiometry  $\text{ME}$ .<sup>4</sup> These chalcogenides are direct gap semiconductors with wide band gap like in II-VI compounds. However, their polytypism and the possibility of variety in stoichiometry, cause problems not observed in the simple II-VI materials. Currently there is a strong move to replace Cadmium with other elements. The replacement of n-type CdS layers in polycrystalline hetero-junction thin film solar cells, employing Copper Indium Diselenide ( $\text{CuInSe}_2$ ) or Copper Indium Gallium Diselenide  $\text{Cu}(\text{In,Ga})\text{Se}_2$  absorber layers, is of particular interest. In addition to “environmental issues” another factor for prompting search for new materials is that a higher band gap material allows more short wavelength photons to reach the absorber and generates photocurrent.

III-VI semiconductor materials such as Indium Sulfide ( $\text{In}_2\text{S}_3$ ) have received considerable attention for application in solar cells. With optimal physical properties,  $\text{In}_2\text{S}_3$  can meet the requirements of a window material or buffer layer for photovoltaic structures. It is an n-type semiconductor which can be successfully deposited by soft technique like chemical bath deposition (CBD) and the band gap can be varied between 2.0 and 2.45 eV, depending upon the composition.<sup>5</sup> Thin films of  $\text{In}_2\text{S}_3$  have been suggested as window material in  $\text{Cu}(\text{In,Ga})\text{Se}_2$  based solar cells. It has also been reported that there is no conduction band discontinuity at the  $\text{Cu}(\text{In,Ga})\text{Se}_2/\beta\text{-In}_2\text{S}_3$  interface.<sup>6</sup> Efficiencies of 15.7% have been obtained for devices employing  $\text{In}(\text{OH,S})$  layers, comparable to 16% obtained for the more standard CBD CdS buffer layers.<sup>7</sup> Hariskos et al. observed that the fill factor of these cells dropped with time when the cells were kept in the dark whereas upon illumination the degradation was reversed.<sup>7</sup> It has been suggested that the degradation is due to

absorption of some species (e.g., Oxygen, water) that reacts with the photo-generated electrons and holes. Similarly, hetero-structures based on  $\text{In}_2\text{Se}_3/\text{CuGaSe}_2/\text{SnO}_2$  and their photovoltaic effects have been studied.<sup>8</sup>

### 5.1.1 Crystal structure of $\beta\text{-In}_2\text{S}_3$

$\text{In}_2\text{S}_3$  crystallizes from its constituent elements at a temperature just above  $1000^\circ\text{C}$ , in the cubic spinel form and the lattice contains a large fraction of sites for unoccupied cations.<sup>9</sup>  $\beta$ - Indium Sulphide ( $\beta\text{-In}_2\text{S}_3$ ) is the stable modified tetragonal state of  $\text{In}_2\text{S}_3$  below  $420^\circ\text{C}$ .<sup>10</sup> In this state, the cation vacancies become ordered in the lattice.<sup>11, 12</sup> According to Hahn and Klinger this material has two modifications:  $\alpha$  and  $\beta$  and reported an irreversible transition from  $\alpha$  to  $\beta$  at about  $330^\circ\text{C}$ .<sup>13</sup> The  $\alpha$  modification is said to be a cubic closed pack lattice of Sulphur atoms, in which 70% of the Indium atoms are randomly distributed on octahedral sites and the remaining 30% on tetrahedral sites.

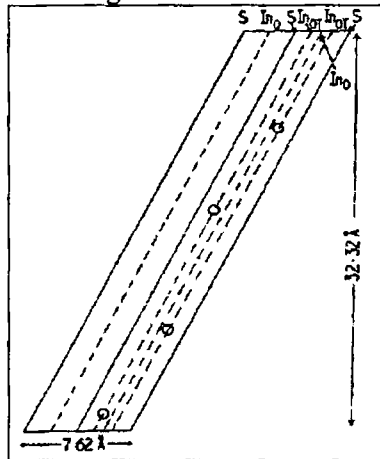


**Fig. 5.1:** Schematic view of secondary unit cell of the  $\beta\text{-In}_2\text{S}_3$  lattice showing location of tetrahedrally coordinated cation vacancies: S, Sulphur atoms;  $\text{In}_o$ , Indium in octahedral positions;  $\text{In}_{oT}$ , Indium in octahedral and tetrahedral positions; O, Indium vacancies at tetrahedral positions.

In an ideal spinel ( $\text{AB}_2\text{X}_4$ ) type, there will be 56 atoms in a unit cell where anions form the lattice framework and the metal ions occupy the tetrahedral and octahedral holes created by the anions.<sup>14</sup> There are 8 molecules in a unit cell in which the divalent 'A' atom occupies eight of the 64 tetrahedral sites and trivalent 'B' atoms occupy sixteen of the 32 octahedral positions. If 'A' and 'B' ions are similar then the spinel composition can be represented by  $\text{R}_3\text{X}_4$  where 'R' represents metal ions and 'X' that of Oxygen, Sulphur etc. The  $\beta$ -modification of  $\text{In}_2\text{S}_3$  is related to the spinel lattice where the cation vacancies

are randomly located on either the octahedral sites only or on both types of sites with eight of the seventy two possible cation sites in the three unit cells being vacant. Consequently spinel form of  $\text{In}_2\text{S}_3$  should have the composition  $\text{In}_3\text{S}_4$  ( $\text{R}_3\text{X}_4$ ) with some Indium vacancies.<sup>15</sup>

Rooymans carried out a more precise and quantitative structure determination of  $\beta\text{-In}_2\text{S}_3$  and modeled a crystal with ordered vacancies within a superstructure of tetragonal symmetry.<sup>11</sup> This model was later on confirmed by investigations of King.<sup>16, 6</sup> The unit cell consists of three spinel cubes stacked along the c-axis. By rotation the a- and b-axis through  $45^\circ$  a smaller unit cell can be obtained which belongs to a body-centered tetragonal Bravais- lattice with the parameters:  $a = b = 7.62 \text{ \AA}$  and  $c = 32.32 \text{ \AA}$ . This reduced unit cell contains 24 spinel-type octahedral sites, which are all occupied by Indium atoms. Of the 12 tetrahedral sites normally occupied in the spinel, only 8 are occupied by Indium whereas 4 remain empty. These 4 vacancies per unit cell are ordered along a four fold screw axis of symbol  $4_1$  parallel to the c-axis. The ordered modification can therefore be interpreted as a quasi-ternary compound consisting of In, S and vacancies or even as a quasi-quaternary one, when the difference between the two types of cation sites is taken into account. The chemical formula can be written as



where the symbols in the brackets describe the tetrahedral sites and  $\Box$  indicates vacancies. The unit cell contains four formula units of this kind with 16 molecules of  $\beta\text{-In}_2\text{S}_3$ .

Thus out of the total 48 ions, 8 In-cations are in tetrahedral coordination and 24 In-cations are in the octahedral coordination. In a stoichiometric crystal of  $\beta\text{-In}_2\text{S}_3$  there are a large number of cation vacancies, which in the ordered state form a part of the lattice. A small fraction of the cations may leave their ordered positions and occupy crystallographically ordered vacancies. This results in a number of quasi-interstitial cations and an equal number of disordered cation vacancies. The energy needed to transfer an Indium atom from a lattice site to an ordered vacancy is most probably much smaller than that needed to produce an interstitial cation, so that in a stoichiometric crystal of  $\beta\text{-In}_2\text{S}_3$  a considerable degree of disorder is always present.<sup>11, 13, 16</sup> Denoting a quasi-interstitial Indium atom by the symbol  $\text{In}\bullet(\Box_{\text{ord}})$  and a disordered vacancy by  $\text{In}\Box$  the Frenkel disorder can be formulated as



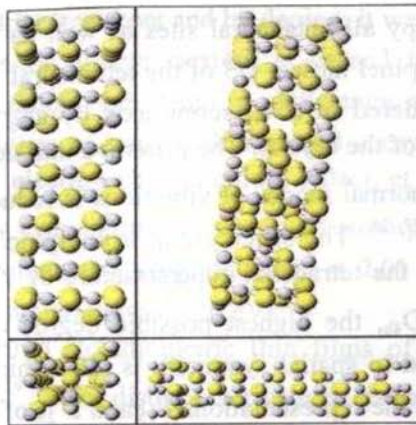


Fig. 5.2: Different views of the defect spinel  $\beta\text{-In}_2\text{S}_3$  crystal structure.

The total number of Indium atoms does not change by this process. For a strictly stoichiometric compound there is an equal concentration of  $\text{In}^{\bullet(\text{ord})}$  and  $\text{In}^{\text{vac}}$ , and thus also electrons and holes. The crystals always show n-type conductivity as the anion escapes during crystal formation leading to a surplus of Indium in the compound and causing the concentration of quasi-interstitial Indium atoms  $\text{In}^{\bullet(\text{ord})}$  which act as donors, to be larger than the concentration of Indium vacancies.

### 5.1.2 The band structure

A direct theoretical approach to the band structure of  $\beta\text{-In}_2\text{S}_3$  is hopeless because the tetragonal Brillouin zone contains 80 s-electrons and 112 p-electrons. Optical investigations have given energies of direct and indirect transitions in this material.<sup>2, 17</sup> There is sufficient controversy about the nature of the valence to conduction band transition at 2-2.2 eV in  $\beta\text{-In}_2\text{S}_3$ . A few authors associate it with an indirect electronic transition.<sup>17-19</sup> At the same time, there are publications treating it as direct allowed transitions.<sup>20, 21-25</sup> While some consider it as a direct forbidden transition.<sup>25</sup> From the close relationship to the Zincblende material, one would expect the direct transition of lowest energy at the center of the Brillouin zone. The conduction band minima above the valence band at points  $k \neq 0$  in the Brillouin zone may be leading to indirect transitions, while the spin-orbit splitting at  $k = 0$  must lie between 0.43 eV and 0.13 eV.<sup>2</sup> The room temperature stable phase of  $\beta\text{-In}_2\text{S}_3$  crystallizes in a defect spinel superstructure with space group  $I4_1/\alpha\text{md-D}_{4h}$  containing 16 molecules in the unit cell.



Indium atoms occupy all octahedral sites as well as 2/3 of the tetrahedral metal positions of the spinel lattice. 1/3 of the tetrahedral metal ion sites remain empty and they are ordered in a  $4_1$ , screw axis by alignment of three spinel blocks along the c-axis of the crystal. The primitive unit cell of  $\beta\text{-In}_2\text{S}_3$  chosen for the account of the normal modes of vibrations is reduced by one half along the c-axis unit cell.<sup>11, 27, 28</sup> The space group isomorphic to the point group of  $\beta\text{-In}_2\text{S}_3$  is  $D_{4h}$ . Since the tetragonal superstructure of  $\beta\text{-In}_2\text{S}_3$  is associated with the point group  $D_{4h}$ , the highest possible degree of degeneracy of any energy level with regard to spatial symmetry is two. This means that the three fold levels belonging to the representations  $\Gamma_{15}$  and  $\Gamma_{25}$  of the cubic point group  $O_h$  of the spinel split into a single and a two fold state. If spin is included the levels belonging to  $\Gamma_6$  and  $\Gamma_7$  remain doubly degenerate in the tetragonal crystal of point group  $D_{4h}$ , whereas the four fold degenerate state splits into two states of symmetry  $\Gamma_6$  and  $\Gamma_7$ .

$\text{In}_2\text{S}_3$  which belongs to the  $A_2^{III}B_3^{VI}$  compounds is a reddish wide band gap semiconductor material stable in air.<sup>29, 9</sup> The high photo-conducting property on powders and single crystals of this material was reported by Bube et al.<sup>3</sup> The powders showed a light-to-dark current ratio of about 100 at 3 ft-candles and  $6 \times 10^3$  V/cm, which were about  $10^{-2}$  to  $10^{-3}$  times as sensitive as standard CdS and CdSe powders. Temperature dependence of PC revealed that photocurrent decreased exponentially with temperature over a wide temperature range. Using the analysis of temperature quenching of photocurrent they showed that the onset of quenching corresponds to activation energy of about 0.1 eV, whereas the termination of quenching corresponds to energy of about 0.8 eV.<sup>30</sup> They concluded that an effectively continuous distribution of sensitizing levels may be present in this material. They reported that  $\text{In}_2\text{S}_3$  can be made to have high dark conductivity by incorporating halogen donors from  $\text{CdCl}_2$  or  $\text{NH}_4\text{Cl}$  or by heating the pure material in Nitrogen to above 1000 K. They also showed that elements of Groups I, II and IV behave as donor impurities. Gilles et al. reported that the photosensitivity of this material could be increased by Cu-doping and that a peculiar combination of deep donors and acceptors existed in this material.<sup>31</sup>

Rehwald and Harbeke carried out temperature dependent electrical resistivity and Hall measurements.<sup>2</sup> They concluded that the cation vacancies are ordered in this system and the small fraction of disordered cations and cation vacancies act as donors and acceptors, nearly compensating each other. They observed that, under heat treatment in air or vacuum, the compound losses

Sulphur. By Sulphur vapor treatment and by doping, it was demonstrated that the concentration and sign of charge carriers is caused by deviation from the stoichiometric concentration, i.e. from a deficiency in Sulphur. Thus the difference in concentration of ionized donors and acceptors increases slightly and results in a higher electron concentration. Palson et al. prepared  $\beta\text{-In}_2\text{S}_3$  thin films by reactively evaporating Indium in an atmosphere of Sulphur. They observed that the fundamental absorption starts at 2.01 eV and the activation energy for electronic conduction was 0.26 eV.<sup>26</sup>

Shazly et al. prepared stoichiometric thin films of  $\beta\text{-In}_2\text{S}_3$  by thermal evaporation technique.<sup>29</sup> Two distinct activation energies of 0.319 eV and 0.61 eV were obtained in as deposited films. After vacuum annealing these levels were identified to be at 0.166 eV and 0.515 eV. They concluded that the shallow defects were structure defect levels where as the deep levels were the characteristics of the material.  $\beta\text{-In}_2\text{S}_3$  and  $\beta\text{-In}_2\text{S}_3:\text{Co}^{2+}$  single crystals were grown by the chemical transport reaction method, using  $\text{In}_2\text{S}_3$ , S, and ZnS as the starting materials and  $(\text{ZnCl}_2 + \text{I}_2)$  as a transport agent by Kim et al.<sup>32</sup> The single crystals had tetragonal structure. The direct optical energy band gaps were found to be 2.639 eV and 2.175 eV for  $\beta\text{-In}_2\text{S}_3$  and  $\beta\text{-In}_2\text{S}_3:\text{Co}^{2+}$ , respectively. The indirect optical energy band gap of the single crystals at 298 K were found to be 2.240 eV and 1.814 eV for  $\beta\text{-In}_2\text{S}_3$  and  $\beta\text{-In}_2\text{S}_3:\text{Co}^{2+}$ , respectively.

Defect characterization of the semi-conducting thin films of  $\beta\text{-In}_2\text{S}_3$ , [prepared by chemical spray pyrolysis] using Thermally Stimulated Current (TSC) measurements revealed four trap levels with activation energies 0.1, 0.26, 0.43 and 0.82 eV in the band gap of this material.<sup>33</sup> Variation of their prominence was observed for the different stoichiometric ratios of In:S. The level at 0.1 eV was assigned to the defect level due to  $V_{\text{In}}$ . The level at 0.26 eV was tentatively assigned to Chlorine impurity while the one at 0.43 eV was identified as a 'native defect' whose prominence decreased when the Sulphur concentration increased or Indium concentration decreased as a result of the change in stoichiometric ratio between In & S in the spray solution. The defect level at 0.82 eV was identified as a neutral trap corresponding to the replacement of Sulphur by Oxygen. It was identified to be a 'giant trap', which was acting as a deep impurity level and was responsible for most of the electrical property of  $\beta\text{-In}_2\text{S}_3$ .

### 5.1.3 $\beta\text{-In}_2\text{S}_3$ an opto-electronic material

$\text{In}_2\text{S}_3$  single crystals and polycrystalline specimens synthesized from its constituent elements in a closed two-zone furnace system showed infra-red (IR)

emission at 90 K with spectral maxima at 0.79 and 0.88  $\mu\text{m}$ .<sup>9</sup> Springford studied the luminescence behavior of the  $\text{Ga}_2\text{S}_3\text{-In}_2\text{S}_3$  system and reported that the two emission bands in the  $\text{In}_2\text{S}_3$  system were associated with the complexes formed by neighboring anions in the vicinity of the two types of cation vacancy site in this material, one tetrahedrally and the other octahedrally coordinated.<sup>35</sup> Because of its high luminescence yield, its applications in important opto-electronic devices like, red and green phosphors for picture tubes of television has been patented.<sup>36-38</sup> Stable aqueous colloids of 2-3 nm  $\text{In}_2\text{S}_3$  nanocrystals prepared using the classical method of nano-particle stabilization by low molecular weight thiols exhibited relatively strong excitonic emission at 360-380 nm with a quantum yield of 1.5%.<sup>39</sup> The excitonic radiative lifetime was 350 ns, based on which it was concluded that direct allowed electronic transition was responsible for this emission. A novel in-situ oxidization-sulfurisation growth route via a self purification process was developed to synthesize  $\beta\text{-In}_2\text{S}_3$  dendrites.<sup>40</sup> It was found that the product was pure  $\text{In}_2\text{S}_3$  which showed strong quantum confinement of the excitonic transition.

$\beta\text{-In}_2\text{S}_3$  in powder form was chemically synthesized using  $\text{InCl}_3$  and Thioacetamide as precursors followed by annealing in Argon atmosphere in the temperature range 573–1123 K.<sup>41</sup> Optical band gap of the powder was determined to be 2.12 eV, from the reflectance studies as a function of wavelength. PL studies indicated a strong peak around 2.08 eV for all the samples annealed (Argon) in the range 573–1123 K.  $\text{In}_2\text{S}_3$  nanoparticles, embedded in a novel porous Phosphor Silica Xerogel, were synthesized by sol-gel processing.<sup>41</sup> Their fluorescence properties have been evaluated and compared with those of the un-doped Xerogel. A novel luminescent phenomenon was observed from  $\text{In}_2\text{S}_3$  nanoparticles embedded in the sol-gel Silica Xerogel. The PL of all the doped samples had high fluorescence intensities with two emission peaks: one at 440 nm while the other at 600 nm. The  $\text{In}^{3+}$  ions in the sol-gel Silica Xerogel were identified to be the cause for the sharp emission band. Sharma et al. carried out PL measurements on Manganese Indium Sulphide thin films.<sup>42</sup> A Gaussian shaped PL band, centered at 535 nm, was observed at 10 K. A study on the variation of  $\text{InCl}_3$  concentration in spray solution over the PL energy band position and shape suggests that varying  $\text{InCl}_3$  concentration in the solution or changing the  $\text{In}^{3+}$  composition in the film during growth did not affect PL maxima position in energy axis. But a reduction in the PL peak intensity was noticed with decreasing  $\text{InCl}_3$  solution concentration. Based on the luminescence data donor level height in the Manganese Indium

Sulphide energy gap was estimated and found to be around 20 meV; which on reduction of  $\text{InCl}_3$  concentration in solution was found to decrease marginally.

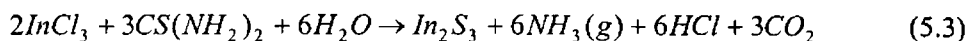
Junfeng et al. synthesized  $\beta\text{-In}_2\text{S}_3$  nanofibers via a hydrothermal method with AAO membrane as template.<sup>43</sup> XRD pattern indicated perfect crystallization of  $\beta\text{-In}_2\text{S}_3$ . SEM images showed that the  $\beta\text{-In}_2\text{S}_3$  nanofibers grew up from the channel ends of the AAO template. A broad emission peak at 375 nm (corresponding to 3.30 eV) was observed by them when the sample was excited using wavelength at 320 nm. Xuebo et al. demonstrated a template-free route for the preparation of hollow  $\text{In}_2\text{S}_3$  nanospheres by solvothermally treating solid  $\text{In}_2\text{S}_3$  spheres comprised of small particles, at 180 °C for 24 h.<sup>44</sup> Hollow  $\text{In}_2\text{S}_3$  nanospheres show an intense absorption between 318 and 512 nm, which is blue-shifted to shorter wavelengths relative to that of bulk  $\text{In}_2\text{S}_3$ . Hollow  $\text{In}_2\text{S}_3$  nanospheres also exhibit a strong PL. The green band centered at 518 nm was identified to be due to the band-to-band transitions and the orange emission centered at 624 nm originates from the Indium interstitial defect. These hollow  $\text{In}_2\text{S}_3$  nanospheres could be used as a distinctive multicolored phosphor and material for producing photo-electrochemical devices.

$\text{CuInS}_2/\text{In}_2\text{S}_3$  solar cells were fabricated using spray pyrolysis method and high short circuit current density and moderate open circuit voltage were obtained by adjusting the condition of deposition and thickness of both the layers. Consequently, a relatively high efficiency of 9.5% (active area) was obtained without any anti-reflection coating. The cell structure was  $\text{ITO}/\text{CuInS}_2/\text{In}_2\text{S}_3/\text{Ag}$ .<sup>45</sup> The CBD CdS buffer layers in  $\text{Cu}(\text{In,Ga})\text{Se}_2$  (CIGS) solar cells was replaced by  $\text{In}_x\text{S}_y$  thin film buffer layers prepared by ultrasonic spray pyrolysis at various substrate temperatures.<sup>46</sup> Their X-ray Diffraction measurements confirmed that the films contained primarily the tetragonal  $\text{In}_2\text{S}_3$  phase. X-ray Photoelectron Spectroscopy (XPS) measurements revealed the presence of low concentration of Chlorine impurity throughout the  $\text{In}_x\text{S}_y$  layer. By depositing the indium sulphide layer as buffer layer in the CIGS solar cell configuration, a maximum solar cell efficiency of 8.9% was achieved, whilst the reference cell with CdS/CIGS, on a similar absorber, exhibited 12.7% efficiency. Additionally, light soaking enhanced the efficiency of  $\text{In}_x\text{S}_y/\text{CIGS}$  cells primarily by improvements in fill factor and open circuit voltage.

## 5.2 Structural and morphological studies on $\text{In}_2\text{S}_3$ thin films

CSP is a simple, low-cost technique in which the deposition parameters can be easily varied. In the present work a solution containing the mixture of Indium

Chloride ( $\text{InCl}_3$ ) and Thiourea ( $\text{CS}(\text{NH}_2)_2$ ) were used as the precursor solution for spraying. Micro glass slides, with dimensions of  $37 \times 12 \times 1.4 \text{ mm}^3$ , [first cleaned with chromic acid followed by soap solution], were used as the substrates for film deposition. The In/S ratio in the solution was varied by varying the molar concentration of  $\text{InCl}_3$  and  $\text{CS}(\text{NH}_2)_2$ . Total volume of the solution sprayed was 400 ml and the rate of spray was 20 ml/min in all cases. Formation of  $\text{In}_2\text{S}_3$  resulted from the chemical reaction:



Detailed studies on the structural properties using XRD and its compositional dependence have been well established and reported earlier.<sup>49</sup> The samples showed  $\beta\text{-In}_2\text{S}_3$  phase with good crystallinity and preferential orientation along the (220) plane except for those having very low Sulphur concentration. The samples showed  $\beta\text{-In}_2\text{S}_3$  phase with orientation along the (220) plane at  $2\theta = 33.45^\circ$ . The  $d$  values coincide with that of  $\beta\text{-In}_2\text{S}_3$  in the standard JCPDS data card (25-390).

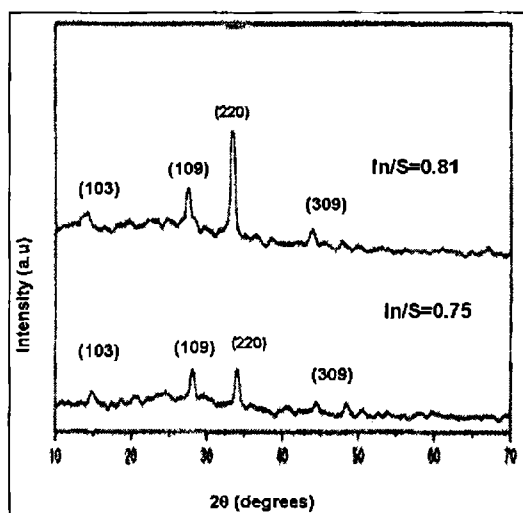


Fig. 5.3: XRD pattern of the films deposited with In/S=0.75 and In/S=0.81 which showed good optoelectronic properties.

The samples with an In/S = 0.75 showed good crystallinity and orientation along the (220) plane. As the Sulphur concentration in the spray solution was increased, the intensity of the peak corresponding to the (220) plane increased up to In/S = 0.81 and on further increasing the Sulphur concentration in the spray solution, the intensity of this peak decreased.<sup>47</sup> The grain size of the film was calculated from the peak at  $2\theta = 33.45^\circ$  using the Debye-Scherrer formula

$D = 0.9\lambda / \beta \cos \theta$ , where  $D$  is the diameter of the crystallites forming the film,  $\lambda$  is the wavelength of the Cu-K $\alpha$  line,  $\beta$  the FWHM in radians and  $\theta$  is the Bragg angle. The grain size varied from 20 to 200 nm, based on the sample stoichiometry. For films with In/S = 0.75 and In/S = 0.81 the grain size was found to be 30 nm and 80 nm respectively.

XPS analysis indicated that Indium and Sulphur were uniformly distributed throughout the depth of the sample (Fig. 5.4). The bottom portion of the spectra represents the surface of the film, and the top- the substrate. The binding energy values (Table 5.1) are in agreement with the reported values for In<sub>2</sub>S<sub>3</sub>.<sup>48</sup>

Element	Binding Energy (eV)
In 3d <sub>5/2</sub>	444.99
In 3d <sub>3/2</sub>	453.06
S <sub>2p</sub>	162.50

**Table 5.1:** Binding energy of Indium and Sulphur in the  $\beta$ -In<sub>2</sub>S<sub>3</sub> thin film obtained from XPS studies.

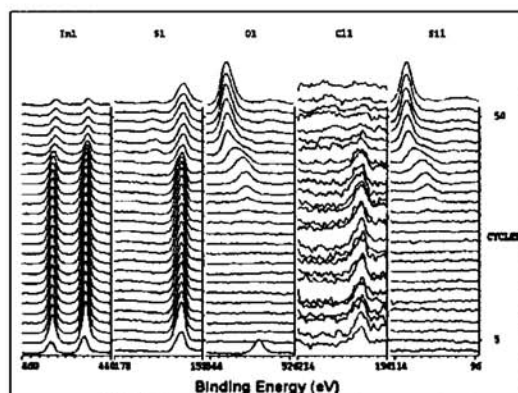


**Fig. 5.4:** XPS depth profile for sample with In/S = 0.81.

Binding energies of Indium and Sulphur clearly indicated the formation of In<sub>2</sub>S<sub>3</sub> [162.5 eV for S 2p, 444.9 eV for In 3 d<sub>5/2</sub> and 453.06 eV for In 3 d<sub>3/2</sub> respectively]. From the XPS pattern no obvious peaks of Indium oxides [529.8–530.5 eV for O 1s in In<sub>2</sub>O<sub>3</sub> and 531.8 eV for O 1s in In(OH)<sub>3</sub>] were observed. The binding energy peak corresponding to Oxygen in the sample was at 532.49 eV which proved that Oxygen was present only as a surface contaminant (532.5 eV), which corresponded to Sulfate. The decrease in the peak height of Sulphur at the surface of the film indicated that Oxygen substituted Sulphur at the top

layer. Chlorine in the elemental form was also present throughout the thickness of the sample which could have come from Indium Chloride used for film preparation.

Raman spectroscopy with polarized laser beams at different geometries with regard to the crystal orientation distinguishes between Raman-active modes of different symmetry. In total 36 modes should be observed by light scattering. Raman Bands at 235, 268, and 309  $\text{cm}^{-1}$  correspond to the  $\beta\text{-In}_2\text{S}_3$  defect spinel structure.<sup>49, 50</sup> Raman Bands corresponding to the  $\beta\text{-In}_2\text{S}_3$  defect spinel structure were poorly resolved due to the intense fluorescence background. In our samples the best Raman spectra were obtained from the sample with In/S = 0.81 (sample 3) and In/S = 0.75 (sample 4), as shown in Fig. 5.5. They were mainly broadened into a single band for sample with In/S = 0.81, indicating poor structural quality of the spinel structure in our samples. For sample 4, the bands at 309  $\text{cm}^{-1}$  and 367  $\text{cm}^{-1}$  were significantly improved. Based on our Raman analysis, it may be concluded that in sample with In/S = 0.81 there was a modification of the intrinsic point defects compared to sample with In/S = 0.75. It could also be concluded that the defect spinel structure was absent for sample with In/S = 0.81 which is characterized by the specific Raman lines whose position is mentioned above.

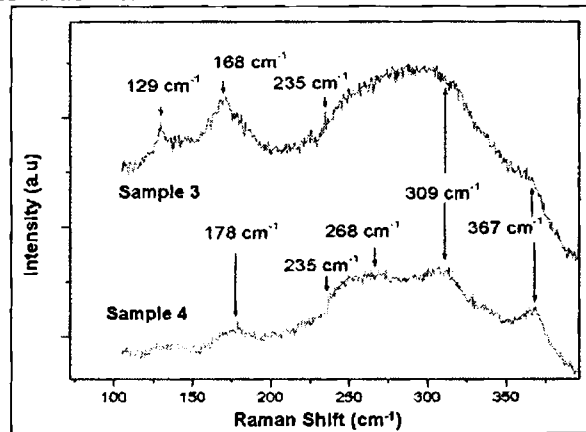


Fig. 5.5:  $\mu$ -Raman analysis of sample 3 with In/S = 0.81 and sample 4 with In/S = 0.75 at room temperature.

### 5.3 Optical absorption of $\beta\text{-In}_2\text{S}_3$ thin films

$\beta\text{-In}_2\text{S}_3$  thin films show optical absorption from the far IR region to the near UV region. A broad absorption band with peak at  $\sim 1400$  nm (0.89 eV) was prominent in all the samples studied. This absorption was found to be typically spread from 1650–1000 nm among the samples having different stoichiometry.

The main absorption started from around  $\sim 800$  nm (1.55 eV) and extended to the UV region. Figure 5.6 shows the typical absorption spectra for two  $\beta$ - $\text{In}_2\text{S}_3$  thin film samples.

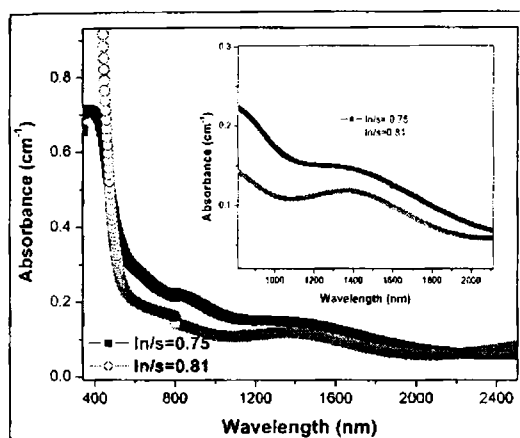


Fig. 5.6: Absorption spectra at 300 K of the samples in the wavelength region 375-2500 nm (inset represents the absorption spectra in the IR 900-2100 nm).

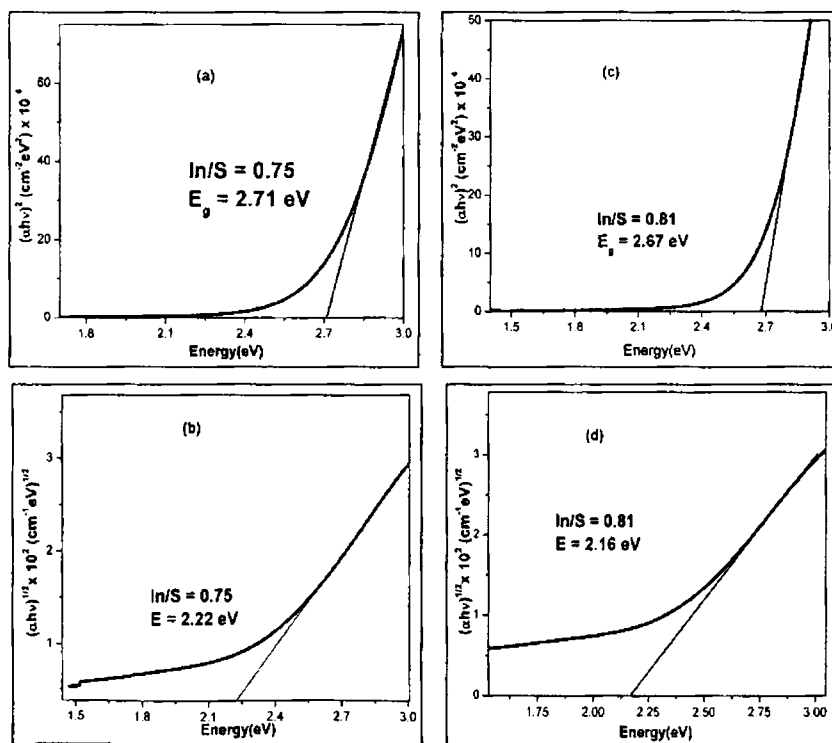


Fig. 5.7: (a, c) Plot of  $(ahv)^2$  versus  $h\nu$ , for samples with  $\text{In/S} = 0.75$  and  $\text{In/S} = 0.81$  respectively and (b, d) plot of  $(ahv)^{1/2}$  versus  $h\nu$  for samples with  $\text{In/S} = 0.75$  and  $\text{In/S} = 0.81$  respectively.



The optical absorption of  $\beta$ - $\text{In}_2\text{S}_3$  carry features related to direct and indirect transitions. For thin films deposited using spray pyrolysis, a direct band gap in the 2.5 - 2.8 eV range and an indirect transition in the 1.8 - 2.2 eV range were reported.<sup>17</sup> From the plot of  $(\alpha h\nu)^2$  versus  $h\nu$ , (Fig. 5.7(a) and (c)) direct band gaps of 2.71 eV and 2.67 eV were obtained for samples with  $\text{In/S} = 0.75$  and  $\text{In/S} = 0.81$  respectively. The graph of  $(\alpha h\nu)^{1/2}$  versus  $h\nu$  (Fig. 5.7(b) and (d)) indicated an indirect transition at 2.22 eV and 2.16 eV for these films respectively. Absorption tail and deep absorption band clearly indicated the presence of impurities /defect levels, which could be vital in deciding the opto-electronic properties of these thin films. This exercise was carried out in several samples and it was concluded that in our samples, there was an indirect transition centered around  $\sim 2.2$  eV and the band gap of the films was around  $\sim 2.7$  eV. The variation in band gap with In to S stoichiometry was proved earlier.<sup>49</sup>

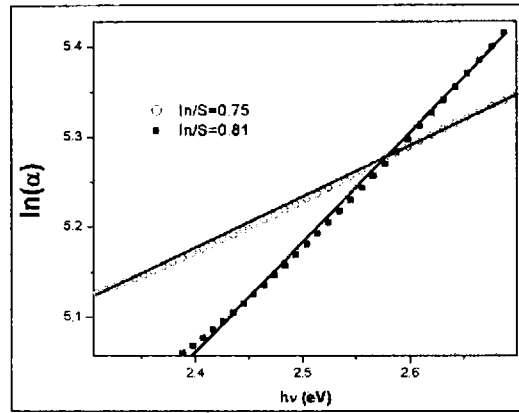


Fig. 5.8: Plot of  $\ln(\alpha)$  vs  $h\nu$  for samples fitted using relation (5.4).

From a plot of  $\ln(\alpha)$  vs  $h\nu$  (Fig. 5.8), it could be observed that the absorption coefficient ( $\alpha$ ) had an exponential tail (Urbach tail) with decreasing photon energy, below the band gap. It is well established that the broadening of the Urbach tail increases with increasing defect states in the film.<sup>51</sup> The Urbach tail width was calculated using the relation

$$\alpha = t(h\nu / \varepsilon) \quad (5.4)$$

where  $\alpha$  is the absorption coefficient,  $t$  is a constant and  $\varepsilon$  is the tail width. The tail width  $\varepsilon$  was obtained by taking the inverse of the slope of plot between  $\ln(\alpha)$  vs  $h\nu$  (Fig. 5.8). The Urbach tail width ( $\varepsilon$ ) was found to be 0.83 eV for sample with  $\text{In/S} = 0.81$  and 1.42 eV for sample  $\text{In/S} = 0.75$ . This

may be due to the difference in the defect structure of the films deposited due to the change in molarity of the spray solution. Broadening of the tail could be ascribed to the fluctuations in size of the crystallites in samples which was evident from XRD and AFM studies.

Thus, based on optical absorption studies, it could be concluded that the  $\beta$ - $\text{In}_2\text{S}_3$  thin films possessed a direct band gap typically around  $\sim 2.7$  eV. There was also an indirect transition whose magnitude was around  $\sim 2.2$  eV. The correlation between the direct and indirect optical absorption lead to hypothesis that an indirect valley may be located around  $\sim 0.5$  eV below the conduction band in this material. Correlation between the Urbach tail and the optical absorption indicated that there were defects in this system which may be giving rise to the IR absorption band centered around  $\sim 0.89$  eV whose density and band width varied with composition of the films.

#### **5.4 Defect analysis of $\beta$ - $\text{In}_2\text{S}_3$ thin films using PL**

For the PL measurements, samples with the In/S = 0.51, 0.59, 0.66, 0.72 and 1 (EDAX composition) were used. The samples [of area  $1 \text{ cm}^2$ ] were mounted on the cold finger of a liquid Helium cryostat (Janis Research Company CCS 100/202) and cooled to 15 K. Temperature was controlled with an accuracy of  $\pm 1$  K using a Lakeshore temperature controller (321 Auto tuning). Melles Griote Argon ion laser [488 nm with intensity of  $19.5 \text{ W cm}^{-2}$ ] was used to excite the sample. Unfocussed beam, of 0.63 mm diameter, was allowed to fall on the sample. Light emitted from the sample was collected using an optical fiber bundle, placed at  $90^\circ$  to the incident light, with the help of focusing lens. An optical fiber with a collimating lens at its end was coupled to a spectrophotometer (Ocean Optics USB2000) using SMA adapter. The spectra were recorded using the spectrophotometer with the help of the software "OOIbase32" (Ocean Optics).

PL spectra of  $\beta$ - $\text{In}_2\text{S}_3$  with In/S = 0.72 and band gap  $E_g = 2.76$  eV at 300 K, measured in the 550-900 nm wavelength range and 15-300 K temperature range, are depicted in Fig. 5.9. There were two bands, one of which was relatively sharp with an asymmetric Gaussian line shape, centered at 568 nm (A-band) corresponding to 2.19 eV. This band had maximum intensity at 15 K and the intensity decreased very fast, as temperature increased. The second band (B-band) was a very broad one, centered at 663 nm corresponding to 1.88 eV.

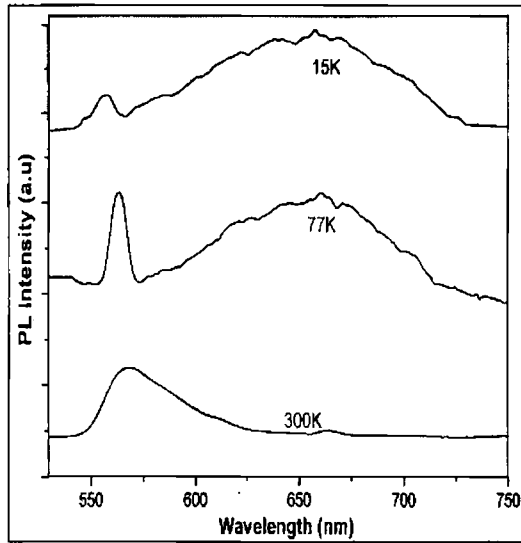


Fig. 5.9: PL spectra recorded for sample with In/S = 0.72.

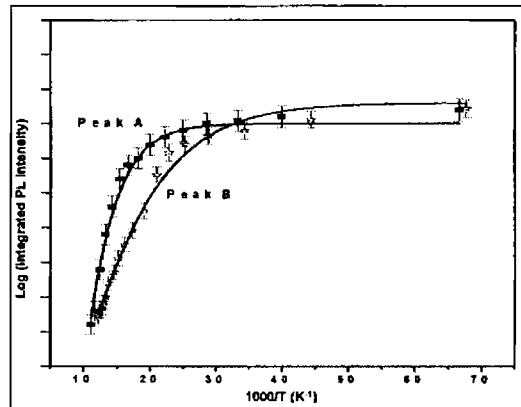


Fig. 5.10: Temperature dependence of log (Integrated PL intensity) for A- and B- bands fitted using relation (3.5).

In order to calculate the quenching energy of the PL emission, a plot between logarithmic (Integrated PL intensity) and  $1000/T$  was plotted. This was fitted using the relation (3.5), describing the thermal quenching of the emission line as shown in Fig. 5.10.

The  $\Delta E$  value for A- and B-bands was obtained to be 42 meV and 59 meV respectively.

In order to identify the defect levels responsible for the two bands, PL analysis of Sulphur rich and Sulphur deficient samples were carried out. As shown in Fig. 5.11, it was observed that A-band was absent for Sulphur rich sample while it was intense in the case of Sulphur deficient sample. This very

well proved that level corresponding to Sulphur vacancy was essential for the emission of A-band.

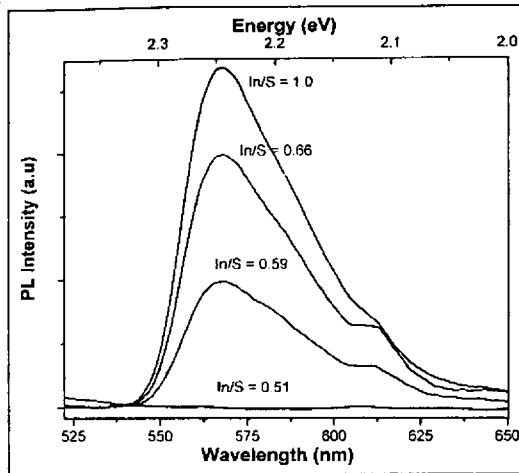


Fig. 5.11: Effect of increase in Sulphur content on A-band PL emission intensity.

From the optical absorption, it was observed that a level/band was present  $\sim 0.5$  eV below the conduction band which was giving rise to the indirect optical absorption at 2.2 eV. It had been reported earlier that Sulphur vacancy ( $V_S$ ) was acting as a donor (with activation energy of 0.43 eV) based on TSC studies.<sup>52</sup> Hence it could be now concluded that the PL emission at 2.19 eV was due to the recombination of electrons from this 'defect band'. On adding the peak energy of A-band emission (2.19 eV) and the thermal activation energy of the donor (0.43 eV), one gets 2.62 eV, which was lower than the band gap of 2.71 eV, by about 0.09 eV. Through TSC studies it was earlier identified that an acceptor level existed about 0.10 eV above the valence band, corresponding to Indium vacancy.<sup>52</sup> This vacancy level is intrinsic in  $\text{In}_2\text{S}_3$ .<sup>53</sup> Thus it became evident that the A-band emission was due to transitions from Sulphur vacancy ( $V_S$ ) donor level to the Indium vacancy ( $V_{\text{In}}$ ) acceptor level, which was 0.09 eV above the valence band.

Variation in the peak energy of A-band with temperature from 15-90 K was studied. It was seen that the peak energy of the emission had a blue shift by 28 meV, when the temperature was raised. Variation of band gap of  $\text{In}_2\text{S}_3$  with temperature from 15 K onwards was calculated with the help of Varshni's equation using constants  $\alpha = 6.842 \times 10^{-4}$  eV/K and  $\beta = 398$  K.<sup>54</sup> Results of the calculation are depicted in Fig. 5.12 along with the shift in peak energy of A-band with increase in temperature. The shift represents the change from the 0 K value obtained by extrapolation of a plot of peak energy versus temperature. It can be seen that the band gap decreased with increase in temperature while the

peak energy of the A-band increased. There were earlier reports stating that variations of band gap and PL peak energy emission would be opposite in nature, for emissions following the Cartesian Coordinate (CC) model of luminescence.<sup>55</sup>

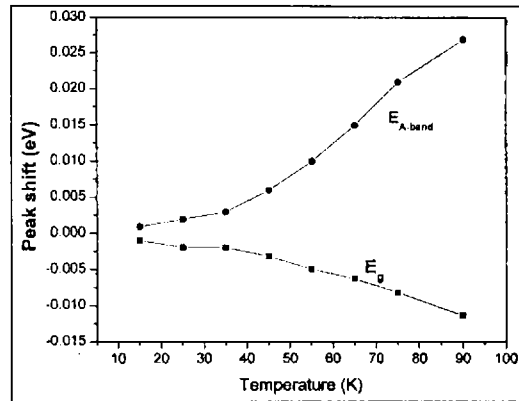


Fig. 5.12: Peak shift as a function of temperature for the A-band compared to the change in energy gap  $E_g$  derived from Varshni's equation.

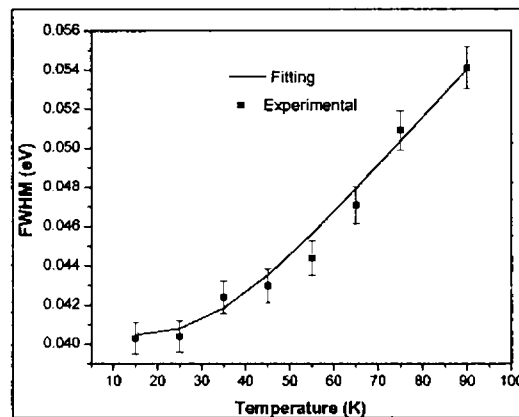


Fig. 5.13: Temperature dependence of FWHM for A band.

Figure 5.13 represents the temperature dependence of the full width at half maximum (FWHM) for A-band. It was found that the dependence followed the CC model equation<sup>55</sup>

$$W = W_0 [\coth\{h\nu_e / 2kT\}]^{1/2} \quad (5.5)$$

where  $W_0$  is a constant whose value is equal to  $W$  as the temperature approaches 0 K and  $h\nu_e$  is the energy of the vibration mode of the excited state. The fit was obtained with the parameters  $W_0 = 0.04$  and  $h\nu_e = 0.01$  eV. The  $h\nu_e$  value very well agreed with the value reported for other semiconductors like GaAs and GaSe, belonging to the same class of compounds as  $\text{In}_2\text{S}_3$ .<sup>2, 56</sup> The peak

energy shift and FWHM of A-band was found to follow the thermal quenching mechanism in the CC model.<sup>57</sup> Based on this model, the activation energy of 42 meV could be explained as the difference in the energies of the lowest excited state ( $V_s$ ) and the intersection point of this curve with the CC curve of the ground state ( $V_{in}$ ). Figure 5.14 represents the proposed CC model for the A-band luminescence.<sup>58</sup>

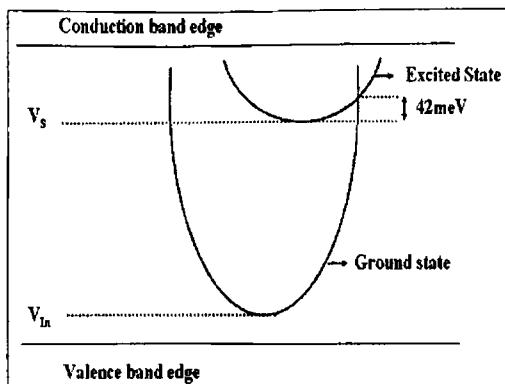


Fig. 5.14: CC model for the A-band luminescence.

Comparison of PL spectra of stoichiometric and Indium rich samples (Fig. 5.15) showed that B-band was absent in the spectra of stoichiometric sample while it was intense in the case of Indium rich sample. This readily proved that level due to Indium interstitial was essential for the emission of B-band to be exhibited by this system. It had been reported earlier that the level due to Indium interstitial was acting as a donor.<sup>52</sup> B-band was very intense and broadened at low temperature and intensity decreased rapidly as temperature increased. This rapid decrease in intensity could be attributed to the shallow nature of donor level because it became more occupied at low temperature, making the intensity of B-band high. But for A-band, which originated from a deep level with activation energy 0.43 eV, lowering of temperature did not cause such great increase in its intensity. Similarly on increasing the temperature, B-band vanished first while A-band did not (Fig. 5.9). The broad nature of the B-band at low temperature was suspected to be due to the presence of other PL emissions. ‘Multiple curve fitting’ of low temperature spectra of B-band revealed the presence of emissions at 612 nm (2.02 eV) and 707 nm (1.62 eV). Studies on the variation of these two emissions due to change in stoichiometry did not reveal the sources of emission. However it was found that the two peaks were not related to the 568 nm and 663 nm emissions.

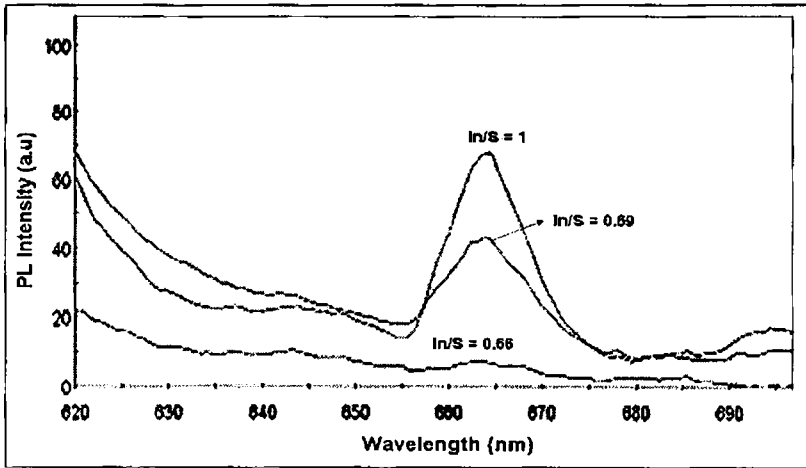


Fig. 5.15: B-band emission for samples with  $\text{In/S} = 1, 0.69$  and  $0.66$ .

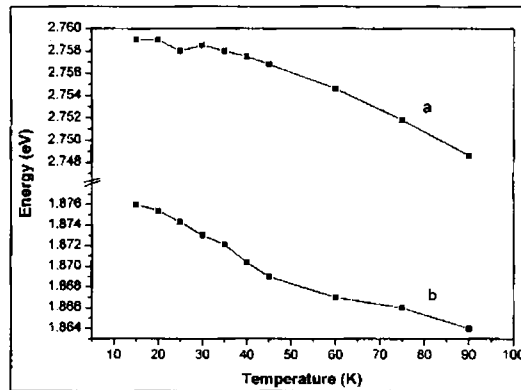


Fig. 5.16: Temperature dependence of the band gap and PL peak energy for B-band emission.

The observed shift of the peak energy position of B-band (Fig. 5.16) towards lower energies satisfied the temperature dependence of the ‘donor–acceptor pair (DAP)’ recombination. The magnitude of the observed shift of the peak energy was greater than the shift in band gap energy with temperature. PL studies of Zn-doped InP had also shown similar behavior and was attributed to recombination between substitutional acceptor and interstitial deep donor levels.<sup>59</sup> TSC measurements on similar samples could identify a level with activation energy of 0.82 eV corresponding to Oxygen replacing Sulphur vacancy ( $\text{O}_{\text{V}_s}$ ) and reported it to be an acceptor.<sup>52</sup> Optical absorption studies had also indicated the presence of defect band in this energy region, which were giving rise to the IR absorption band. With films in which there was full depth Oxygen (Fig. 5.17(a)) the B-band emission was prominent. But in films where there was only Oxygen

contamination at the surface like in film with  $In/S = 0.66$  (Fig. 5.17(b)) there was no B-band emission. Hence it could be concluded that Oxygen had a major role to play in controlling this red luminescence emission. XPS analysis (Fig. 5.17) on stoichiometric and Indium rich sample proved the existence of free Oxygen on the surface of all samples.

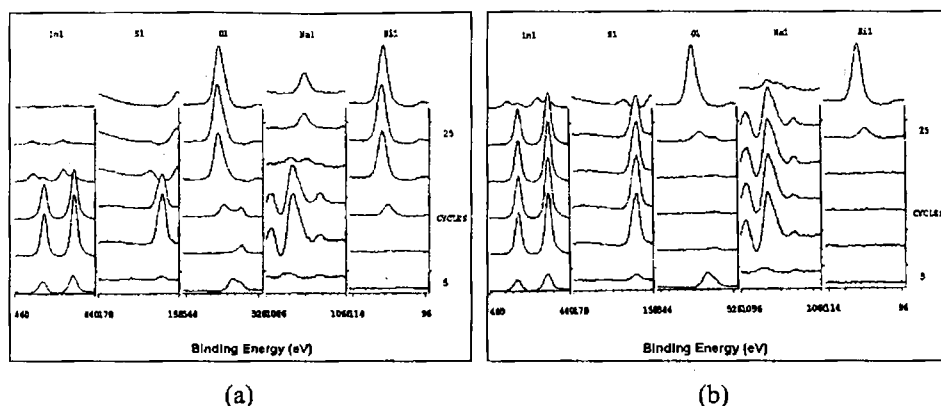


Fig. 5.17: XPS for samples (a) Stoichiometric  $In/S=0.66$  and (b) Indium rich  $In/S=1$ .

Hence it could be proposed that In interstitial ( $In_i$ ) formed a shallow donor level, 59 meV below the conduction band, and radiative transitions from this level to the acceptor level, formed by Oxygen replacing Sulphur vacancy ( $O_{Vs}$ ), caused the B-band emission. For B-band, the sum of PL quenching energy (59 meV), the PL peak energy (1.88 eV) and the thermal activation energy (0.82 eV) was found to be in good agreement with the band gap energy of 2.76 eV. To further verify the origin of B-band, PL spectra of  $\beta$ - $In_2S_3$  with  $In/S = 0.81$ , was measured in the 550-900 nm wavelength range and 11-300 K temperature range, using the 488 nm line of the Ar ion laser. The emissions obtained from samples with this stoichiometry typically were strong in the B-band emission.

The temperature dependence of this emission was as depicted in Fig. (5.18(a)). The PL spectrum was centered at  $\sim 680$  nm, with a higher energy shoulder at  $\sim 616$  nm and a low energy shoulder at  $\sim 733$  nm. In order to calculate the PL quenching energy, a graph between logarithmic value of integrated PL intensity and  $1000/T$  was fitted (Fig. 5.18(b)) using the relation (3.5) describing the thermal quenching of the emission line. The  $\Delta E$  value of the emission was obtained to be 45 meV. This was in good agreement with the reported activation energy of the donor level, corresponding to the interstitial Indium ( $In_i$ ) and supported our earlier assignment of this B-band emission.



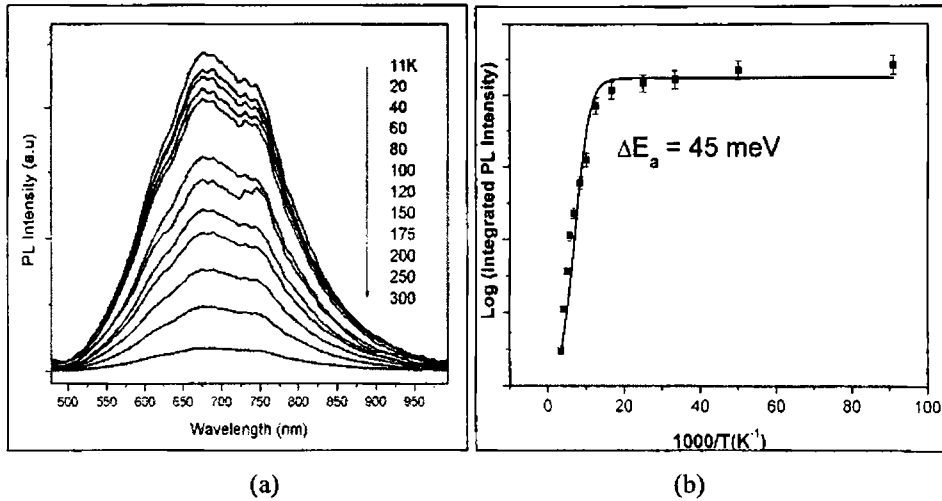
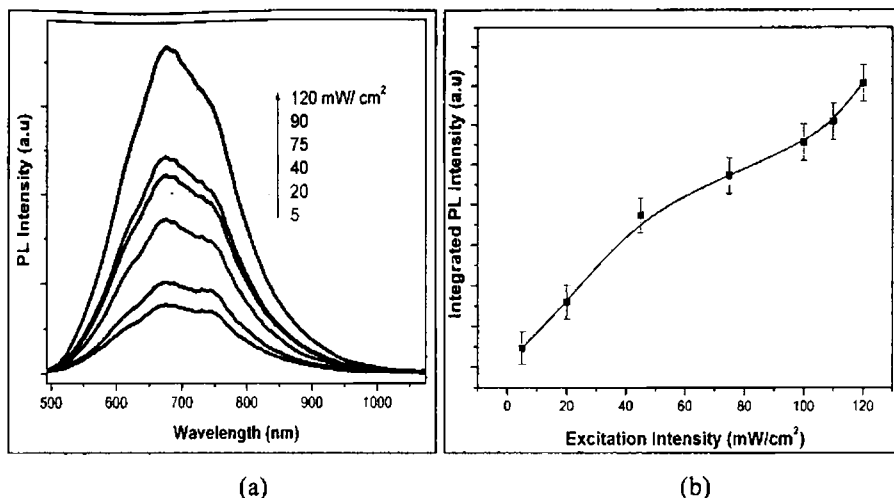


Fig. 5.18: (a) PL spectra for sample recorded from 11-300 K and (b) plot of logarithmic (Integrated PL intensity) vs  $1000/T$  fitted using relation (3.5).

The next set of measurements was done on this sample to analyze the variation of PL intensity due to the variation in excitation intensity (Fig. 5.19(a)) using 2.54 eV as the excitation energy. With the increase in excitation intensity, the emission at 680 nm became very strong, while the shoulder lobes lost prominence. In semiconductors, dependence of PL intensity on excitation intensity, in general, follows the relation (1.57) (section 1.2.5C).<sup>25</sup> The experimental data was fitted with  $\gamma=0.65$  and  $I_0=2500$  (Fig. 5.19(b)). As the value of  $\gamma$  was  $<1$ , it was concluded that this emission was due to a DAP recombination. According to the theory by Maeda, the temperature dependence of quenching is determined by the activation energy of the shallowest defect, and hence we assumed that the level with activation energy 45 meV was shallower among the pair.<sup>60</sup> This energy further agreed with the activation energy of the  $In_i$  donor level and hence was assigned to a DAP recombination with  $In_i$  acting as the donor. The activation energy of the acceptor could be estimated from the minimum peak energy at low excitation powers, assuming that the Coulomb and van der Waal term in relation (1.55) (section 1.2.5A) are negligible.<sup>61, 62</sup> At low excitation intensities, the emission peak was at 680 nm (1.826 eV). Hence in equation (1.55), this was used to calculate the acceptor level activation energy. At 300 K, for a band gap of 2.71 eV, and  $E_d = 45$  meV and  $h\nu = 1.826$  eV, the acceptor level was obtained to be 0.839 eV above the valence band. Interestingly, this energy range turned out to be within the energy range of the IR absorption band centered at  $\sim 1400$  nm (0.887 eV) (Fig. 5.6).



**Fig. 5.19:** (a) PL spectrum dependence on excitation intensity and (b) Plot of excitation intensity vs Integrated PL intensity fitted using relation (1.57).

We could thus clearly conclude, based on our PL studies that a dense acceptor band of width  $\sim 48$  meV was present in the film which was spread between 0.839 eV to 0.887 eV above the valence band. Intermediate bands show impurity photovoltaic effect and can effectively increase the efficiency of solar cells.<sup>63, 64, 65</sup> Thus the presence of this defect band can be one of the reasons as to why  $\beta$ -In<sub>2</sub>S<sub>3</sub> based solar cells showed appreciable efficiency. It was reported earlier that the activation energy of the substitutional defect level due to O<sub>Vs</sub>, may be at 0.82-0.88 eV.<sup>52</sup> This was in good agreement with the activation energy of the acceptor level, presently identified using PL. Thus we assumed that this thick level/ band is responsible for the IR absorption band due to the transition from the valence band to this level.

### 5.5 Effect of above band gap and sub-band gap excitation on the PL

Figure 5.20 compares the PL emission from the samples under 'above band gap' and 'near band edge' excitation. For the 'above band gap' excitation 325 nm (3.82 eV) line was used. For 'near band edge' excitation 488 nm (2.54 eV) line was used. The broad nature of the emission spectra suggested that the radiative transitions in In<sub>2</sub>S<sub>3</sub> occur at specific centers and do not take place between conduction and valence bands. The ground states of the emission centers may be assumed to be close to the Fermi level, based on the strong n-type semi-conduction shown by the films. It could be observed that there were two

emissions which were prominent in both ‘above band gap’ and ‘band edge’ excitations. Since the same PL emissions were observed with a small shift in peak position, it could be concluded that excitation from intermediate levels to the conduction band was taking place under the sub-band gap excitation, which was followed by the radiative transitions between the same set of defect levels which are active under intrinsic excitation. Else, peak positions under different excitation energies would have yielded different PL peak emissions.

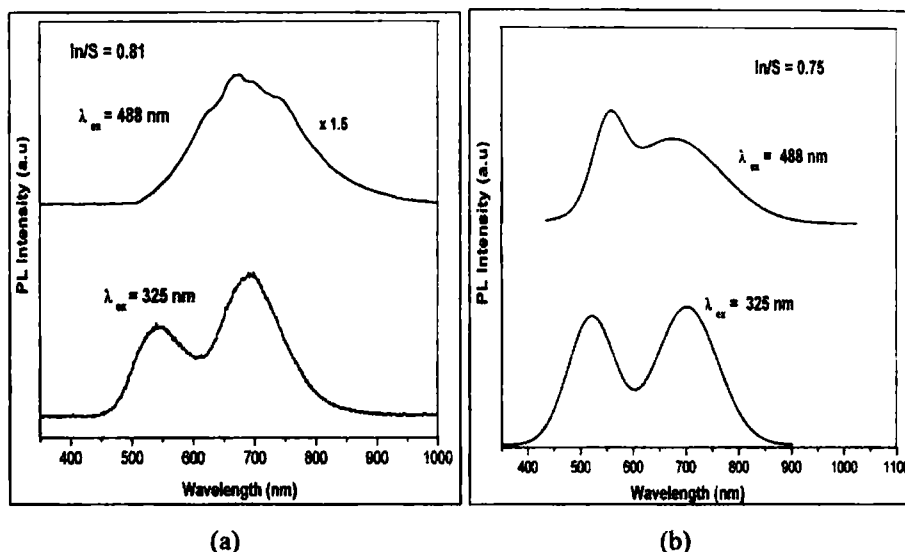


**Fig. 5.20:** Effect of above band gap and sub band gap excitation energy on PL emission at room temperature for sample (a)  $\text{In/S} = 0.81$  and (b)  $\text{In/S} = 0.75$ .

For sample with  $\text{In/S} = 0.81$ , under sub-band gap excitation (extrinsic excitation) with 488 nm, the PL peak was centered at  $\sim 680$  nm. The same sample under ‘above band gap’ excitation (intrinsic excitation) showed two broad peaks with a Gaussian profile. The highest energy PL peak was at 544 nm (2.28 eV) which was greenish in appearance. The lower emission was at 693 nm (1.79 eV) which was red in color. When the film stoichiometry was changed to  $\text{In/S} = 0.75$  both the green and red emissions were observed with extrinsic and intrinsic excitation. Under intrinsic excitation (325 nm) the peaks were centered at  $\sim 520$  nm (2.39 eV) with FWHM of 0.45 eV and at  $\sim 703$  nm (1.77 eV) with FWHM of 0.26 eV while under extrinsic excitation (488 nm) they were centered at  $\sim 557$  nm (2.23 eV) with FWHM of 0.29 eV and at  $\sim 679$  nm (1.83 eV) with a FWHM of 0.36 eV respectively. In general, it could be observed that under intrinsic excitation the green emission was shifted to higher energy side (small wavelength) while the red emission was shifted to smaller energy side (longer

wavelength). Table 5.2 summarizes the parameters of the PL emission and the excitation energy used.

Excitation Energy (eV)	Green Emission	Red Emission
3.82	Peak @2.39 eV FWHM=0.45 eV	Peak @1.77 eV FWHM=0.26 eV
2.54	Peak @2.28 eV FWHM=0.29 eV	Peak @1.83 eV FWHM= 0.36 eV

**Table 5.2:** Dependence of fundamental properties of the PL emission on the excitation energy in sample with In/S=0.75.

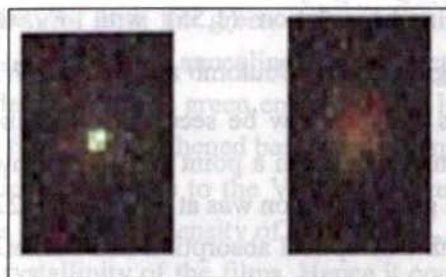


**Fig. 5.21:** The green and red emission from  $\text{In}_2\text{S}_3$  thin films under excitation of 325 nm.

Also under intrinsic excitation, the higher energy side of the green emission was broadened whereas the tail of lower energy side of the red emission was shortened. This shift of the green emission to high energy side under intrinsic excitation could be explained in terms of the effect of 'band filling'. When higher energy is used for excitation, all low lying states will get filled and PL transitions occur from filled higher energy states, which was another proof to the CC model of luminescence for the green emission.

Under the excitation of 488 nm in sample [with In/S=0.75] origin of the green emission was identified to be due to the  $V_S - V_{In}$  DAP recombination between  $V_S$  and  $V_{In}$ . From optical absorption, it was concluded that  $V_S$  lead to a defect band located  $\sim 0.5$  eV below the CB giving rise to indirect optical absorption at  $\sim 2.2$  eV. The  $V_{In}$  acceptor level was identified to be  $\sim 0.1$  eV above the VB<sup>52</sup> Using relation (1.55) with  $E_g = 2.71$  eV,  $E_A = 0.1$  eV,  $h\nu = 2.23$  eV and neglecting the Coulomb and van der Waal term,  $E_D$  was found to be 0.38 eV. This was calculated neglecting the thermal activation energy of 42 meV which was identified as the difference in the energies of the lowest excited state of ( $V_S$ ) and the intersection point of this curve with the CC curve of the ground state ( $V_{In}$ ).

Thus it could now be observed that the highest filled state of the  $V_S$  defect band was  $\sim 0.38$  eV below the CB. The position of the lowest filled level of  $V_S$  was earlier identified to be 0.42 eV from optical absorption presented here and the electrical studies reported by Rupa et al.<sup>52</sup> The difference between the highest and lowest states correspond to 42 meV which is in agreement with the thermal activation energy of 42 meV of the green emission obtained from temperature dependent PL studies (Fig. 5.10).<sup>58</sup>

Thus it was reasonable to assume that, under extrinsic excitation, recombination from the bottom of this  $V_S$  defect band to the  $V_{In}$  level was giving rise to the green emission. When the excitation energy was increased, the PL peak position shifted to higher energy. This could be possible only if the transitions start from higher level due to the filling of lower lying levels. Under intrinsic excitation using relation (1.55) with  $E_g = 2.71$  eV,  $E_A = 0.1$  eV,  $h\nu = 2.39$  eV and neglecting the Coulomb and van der Waal term  $E_D$  was found to be 0.22 eV. Thus it could now be seen that upon increasing the excitation energy, the transition started from a point 0.22 eV below the CB. This showed that the origin of the green emission was at a depth of 0.22 eV from the CB edge. Summing up the results of optical absorption and excitation intensity dependent PL studies one could conclude that the defect responsible for the green emission was spread from a depth of 0.22 eV below the CB to nearly  $\sim 0.5$  eV below to the CB. The existence of such a defect band in this compound was suggested electrically by Checinska et al. and through thermo-luminescence studies by Palson et al.<sup>9, 26</sup> Palson et al. also suggested that this band had a important role in the materials photosensitivity.<sup>26</sup> Rupa et al. had tentatively assigned the 0.22 eV defect level to Cl impurity.<sup>33</sup>

The red emission was shifted to lower energy when the excitation energy was lowered. This indicated that under sub-band gap excitation transitions were taking place to lower energy states of the defect band. It was established that the red emission was because of the  $In_i-O_{V_S}$  DAP recombination, where the  $O_{V_S}$  formed a defect band spread between 0.84 -0.89 eV above the VB. Absorption of high energy photons by the intermediate levels for the transition into the CB would be smaller in magnitude compared to the magnitude of absorption for the transition from VB to CB. The reverse would be true for absorption of low energy photons due to the density of absorption centers available. Hence under extrinsic excitation, ionization of the  $O_{V_S}$  level would be more prominent than under intrinsic excitation. Thus during recombination transitions will take place from the  $In_i$  defect level to ionized states of  $O_{V_S}$  which will be located deeper in

the band gap and hence the peak emission energy will shift to higher energy as the defect gets more and more ionized.

### 5.6 Effect of annealing in vacuum and air

Three samples of the same stoichiometry were prepared following the deposition procedure described earlier. One of the samples was subjected to vacuum annealing at a pressure of  $10^{-5}$  T for 1 hour at  $300^{\circ}\text{C}$ . Another sample was annealed in air for 1 hour at  $300^{\circ}\text{C}$ . The as prepared pure sample, showed PL emissions at  $\sim 540$  nm and  $\sim 690$  nm. When the samples were subjected to annealing in air/vacuum, it was observed that the emission intensity of the  $\sim 540$  nm emission decreased (Fig. 5.22). Figure 5.22 compares the PL spectra for the three samples. PL intensity of both the green and red luminescence decreased upon vacuum annealing, whereas air annealing lead to increase in the red PL emission intensity and decrease of the green emission. The luminescence model for this system could be further strengthened based on this annealing experiment. The green emission which occurs due to the  $V_S-V_{In}$  DAP recombination would be reduced when there is decrease in density of either  $V_S/V_{In}$ . Vacuum annealing resulted in increase in crystallinity of the films. Hence it could be expected that some of the defects were being annealed out. Hence this explained as to why the total luminescence intensity from the vacuum annealed samples was lower than that of the pure sample. Vacuum annealing can also remove adsorbed Oxygen from the film which would decrease the density of the  $O_{V_S}$  defect level and lead to decrease in the red emission of this system.

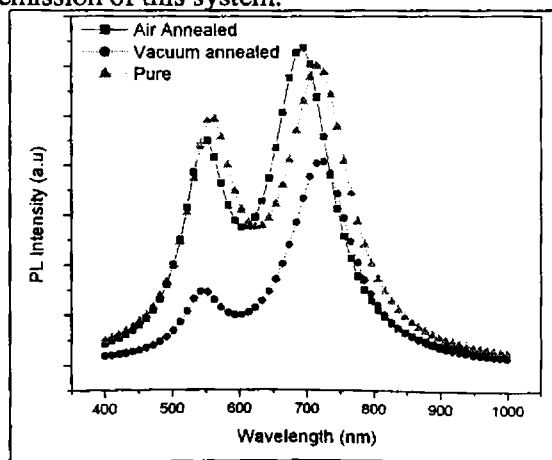


Fig. 5.22: Effect of annealing on the PL spectra for  $\text{In}_2\text{S}_3$  thin films.

Table 5.3 presents the EDAX results of the samples giving information on changes in chemical composition as result of the annealing process. From the EDAX measurements, it became clear that post deposition annealing in general increased the In-content while it reduced the Sulphur content of the films. It could also be observed that the content of the Cl impurity in the film increased as a result of the annealing. It could be seen from the EDAX results that the variation in S and Cl content were complementary and hence it was concluded that Cl was getting incorporated into the film as a result of the annealing by replacing Sulphur.

Sample	In	S	Cl	Cl/(In+S)
Pure	39.18	53.49	7.34	0.08
Air Annealed	40.47	48.30	11.23	0.13
Vacuum Annealed	39.90	50.55	9.55	0.11

**Table 5.3:** EDAX measurements of  $\text{In}_2\text{S}_3$  sample.

The intensity of PL emission around  $\sim 690$  nm was found to increase in air annealed samples. Oxygen is known to replace Sulphur vacancy site in  $\text{In}_2\text{S}_3$  and create an acceptor level around 0.82-0.88 eV above the valence band. It was earlier proved that the PL emission at  $\sim 690$  nm was due to radiative transition between the  $\text{In}_i$  and  $\text{O}_{V_s}$  defect levels. Hence it could be assumed that air annealing resulted in increase in density of the  $\text{O}_{V_s}$  defect level. It was well established that air annealing leads to full depth oxygen contamination in these sprayed  $\text{In}_2\text{S}_3$  thin films.<sup>47</sup> EDAX results had shown that the In-content was slightly increased for air annealed samples and hence a corresponding increase in density of  $\text{In}_i$  defect level could be assumed. An increase in density of these two defect levels would lead to an increase in PL emission intensity of the  $\text{In}_i$ -  $\text{O}_{V_s}$  DAP recombination. This was clearly observed in the PL spectra of the air annealed sample as shown in Fig. 5.22.

Thus it was realized that the luminescence intensity could be varied by subjecting the samples to post deposition annealing. To strengthen this idea, a film was prepared where the intensity of emission at 696 nm (red emission) was lower than that of the green emission by changing the In/S molar ratio in the spray solution. This sample was subjected to vacuum annealing for 1 hour. In agreement with our earlier hypothesis, the intensity of the emission at 696 nm was nearly quenched (Fig. 5.23). This verified our assignment of the 696 nm emission to the  $\text{In}_i$ - $\text{O}_{V_s}$  DAP.

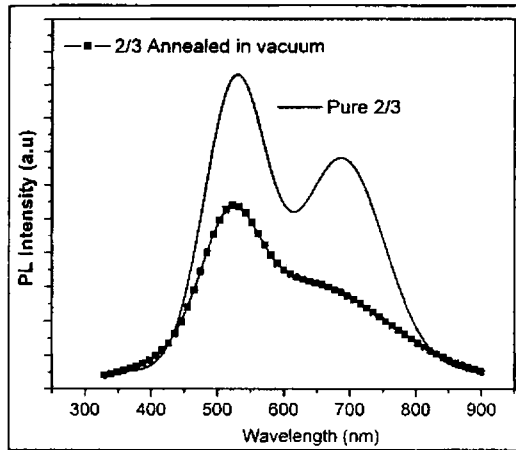


Fig. 5.23: PL spectrum for as prepared sample In<sub>2</sub>S<sub>3</sub> and after vacuum annealing.

### 5.6.1 Effect of rapid thermal quenching

PL measurement on samples, prepared with different rates of cooling after film deposition, was carried out. One of the samples (S1) was allowed to cool down naturally to the room temperature after post deposition annealing of 30 min on the substrate heater. The other sample (S2) was removed immediately once spraying was stopped and hence it was quenched to room temperature within a minute. S1 was found to be more crystalline than S2 from the XRD analysis because of which it could be expected that the defect concentration in S1 would be smaller than that in S2. Thus it could be expected that the total PL intensity in S1 would be smaller than that from S2.

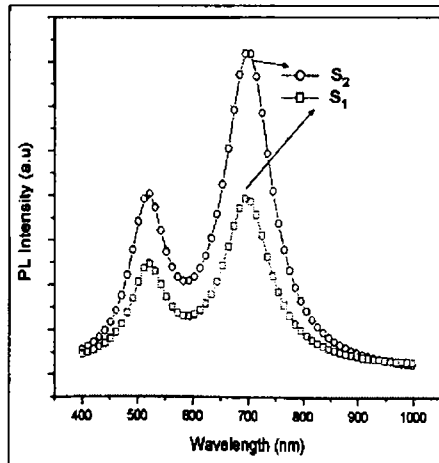


Fig. 5.24: PL spectra for slowly cooled (S1) and rapidly cooled sample (S2).



Figure 5.24 represents the PL spectra of the two samples. It was very evident that the PL emission intensity and FWHM of the peaks of the quenched sample S2 are larger than that of the sample S1. Table 5.4 provides the EDAX analysis results of the two samples. It was very clear that the films were deficient of Sulphur by birth and the deficiency was larger for the film which was quenched (S2). Easily, it could be now read that in sample S2 the defect concentration of  $V_s$  was larger because of which the PL intensity and FWHM was larger than S1. This strengthened our earlier hypothesis regarding the concentration of  $V_s$  defect level and the green emission at 540 nm. This also proved that rate of cooling after CSP was an important parameter controlling the optical properties.

Sample	In%	S%	Cl%	Cl/ In+S
S1	40.01	53.06	6.93	0.07
S2	40.62	51.42	7.96	0.08

**Table 5.4:** EDAX results for samples S1 and S2.

## 5.7 Photo-conductivity in $\beta$ - $In_2S_3$ thin films

### 5.7.1 General properties

The high photosensitivity in single crystal of this material was reported first by Bube et al. and later the effect of Cu-doping on photosensitivity was reported by Giles et al.<sup>3, 29</sup> The dependence of photosensitivity on substrate temperature and molar ratio in the spray precursor solution was reported by Teny et al.<sup>47</sup> It was observed that the photosensitivity to white light increased when Indium content in the precursor solution was reduced. Films sprayed at substrate temperature of 573 K were having higher photosensitivity, compared to the other substrate temperatures. However a detailed investigation on the photoconduction process in this material has not been yet reported.

Figure 5.25 shows the dependence of photosensitivity to white light of intensity  $100 \text{ mW/cm}^2$  on the film stoichiometry. It could be observed that photosensitivity of  $\sim 16000$  could be achieved when the In/S ratio was 0.54. But this high sensitivity was unstable and films lost their sensitivity in 72-96 hours. Stable sensitivity of  $\sim 1000$  (3-4 years now) could be achieved in films with In/S

sensitivity and hence the critical dependence of film chemistry on photosensitivity was realized.

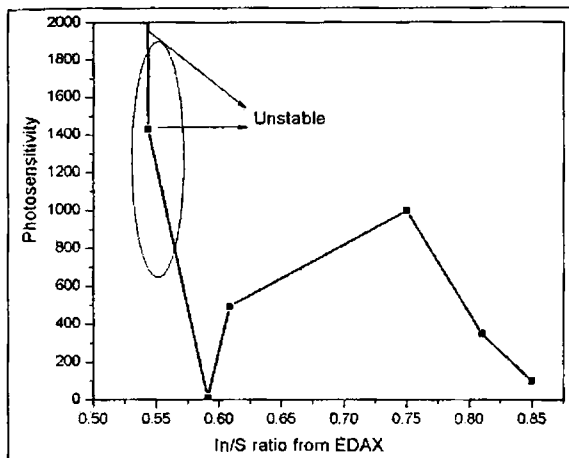


Fig. 5.25: Dependence of photosensitivity on the film composition.

Bias dependence of the photocurrent action spectrum in the thin film is depicted in Fig. 5.26(a). The peak position was unaffected but the magnitude of photocurrent increased as the bias increased. The photocurrent-voltage characteristics exhibit very strong wavelength dependence which could be exploited to develop tunable detectors. Figure 5.26(b) shows the photocurrent in the thin film for a series of wavelengths of equal intensity, from a halogen light source. At room temperature, at a given bias value, the photocurrent is quite distinct for different wavelengths. This wavelength dependence could be exploited to develop tunable detectors.

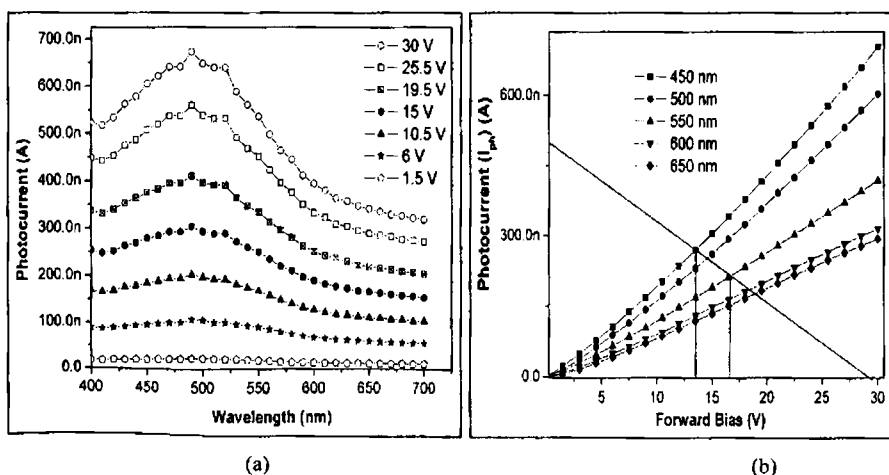


Fig. 5.26: (a) Bias dependence of photocurrent for the thin film at room temperature and (b) Photocurrent-Voltage characteristics for the device for various input wavelengths.

The lifetime of carriers is defined as the time spent by the excited carrier in the corresponding band before it recombines with a carrier of opposite type. Theoretically, it is defined as the time taken for the photocurrent to reduce to  $(1/e)^{\text{th}}$  of the saturated value. The carrier lifetime can be determined using the frequency dependence of photocurrent as described in section (2.5.2). Temperature dependence of lifetime for a film with  $\text{In/S} = 0.66$  is shown in Fig. 5.27. The lifetime decreased exponentially as temperature was raised. A decrease in lifetime suggests that the time of decay becomes fast as temperature increases. This leads to a reduction in time spend by the carrier in the conduction band which in turn lead to a decrease in photosensitivity.

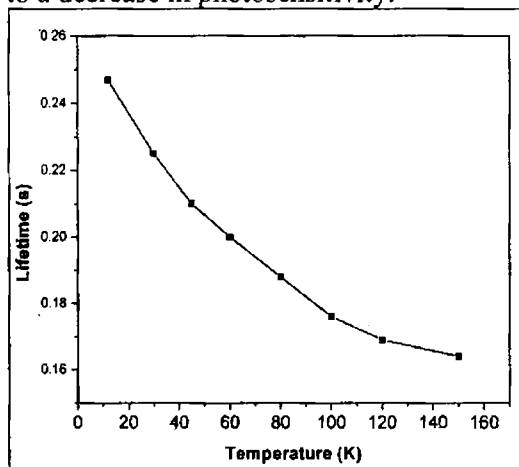


Fig. 5.27: Temperature dependence of lifetime in the  $\text{In}_2\text{S}_3$  thin films.

Figure 5.28 shows dependence of photocurrent on the excitation intensity for the two samples. The graph distinctly showed the difference in the response function of the two samples. For sample with  $\text{In/S} = 0.81$ , the photocurrent vs excitation intensity graph was typically “S shaped” with a non linear part between 20 to 80 mW. But the sample with  $\text{In/S} = 0.75$ , exhibited saturation in photocurrent beyond 50 mW. A curve fitting for the experimentally obtained values for light intensities and photocurrent using relation (1.97) (section 1.3.4E) for the samples of  $\text{In}_2\text{S}_3$  gives  $\gamma$  values, between 0.5 and 1.0. The value of  $\gamma$  lying between 0.5 and 1.0 has been explained theoretically by assuming that the Fermi level was between exponentially distributed trap levels for which the density of traps decreased exponentially with trap depth. Thus it could be concluded that the Fermi level for the  $\text{In}_2\text{S}_3$  thin film system was lying between an *exponentially distributed trap levels* where the density of traps decreased exponentially with

trap depth. The exponential behavior of such traps has already been reported in imperfect materials.<sup>68</sup> Thus the presence of an *exponential trap distribution* in the thin film of  $\text{In}_2\text{S}_3$  was realized.

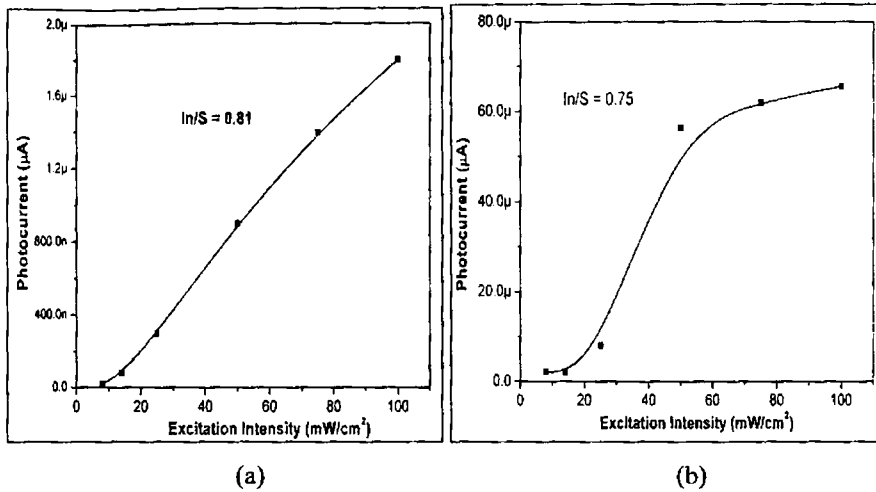


Fig. 5.28: Excitation intensity dependence of photocurrent under an applied bias voltage of 2 V for samples with (a)  $\text{In/S} = 0.81$  and (b)  $\text{In/S} = 0.75$ .

### 5.7.2 On the photo-conductivity in $\beta\text{-In}_2\text{S}_3$ thin films

Figure 5.29 exhibits the temporal response due to optical excitation using the 442 nm line (2.81 eV which is higher than the band gap of  $\text{In}_2\text{S}_3$ ) of the He-Cd laser at 20 mW in the sample with  $\text{In/S} = 0.81$  at 12 K and 300 K. There was increase in photosensitivity at low temperature which could be attributed to the presence of shallow traps in this system. At low temperatures, traps remain filled for longer times and enhance the minority carrier life. So larger numbers of free carriers are generated and the number depends upon the excitation energy/intensity and the temperature. As the temperature is raised, the traps would get thermal energy so as to release the trapped carriers into the conduction band there by decreasing the time period the carriers remain trapped and in effect the photosensitivity would decrease. Another proof to this model was the nature of the PC curve itself. At low temperature (12 K) the PC curve shows saturation while at higher temperatures (300 K) the photo-current shows the effect of carrier diffusion.

The process of diffusion is controlled by the density of minority carriers, a gradient of which can be generated by intrinsic photo-excitation. This strongly indicated that the traps are at equilibrium at low temperature where as at room temperature the traps were continuing to release the carriers. It was observed that

it takes nearly  $\sim 20$  minutes for PC to saturate at room temperature under the 'above band gap' excitation energy of 2.81 eV. Thus if the illumination time is increased, the photosensitivity at room temperature would become larger than that at 12 K because of the continuous release of carriers from the traps. The same photo-conducting properties were exhibited by the samples for excitation with 488 nm (2.54 eV). But there was no saturation of photocurrent for the same illumination period under extrinsic excitation (sub-band gap energy) at any of the studied temperatures.

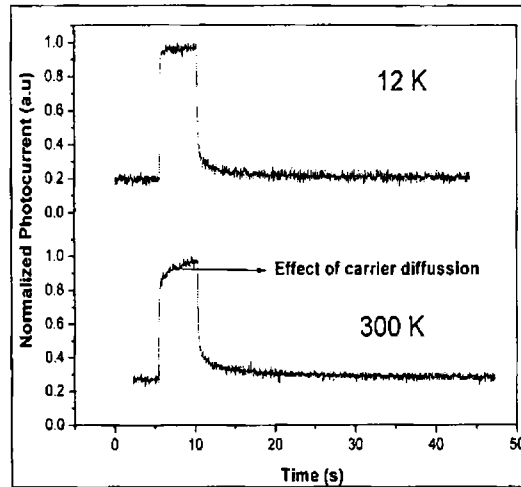


Fig. 5.29: Temperature dependence of PC under excitation of 2.81 eV for the illumination time of 5 s for a bias voltage of 5 V.

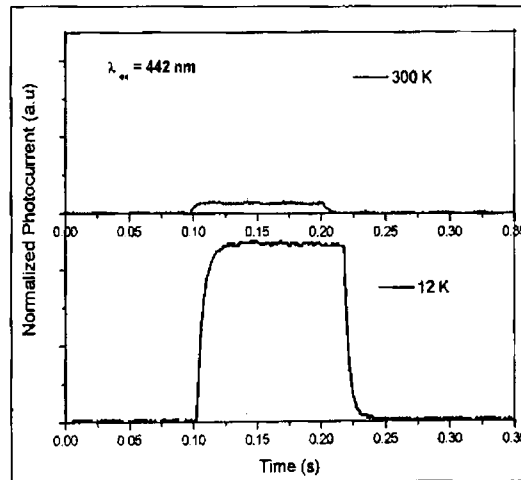


Fig. 5.30: Temperature dependence of photosensitivity in sample with  $In/S = 0.75$  under incident energy of 2.81 eV (442 nm).

When the stoichiometry was changed to the critical value of  $\text{In/S} = 0.75$  where films become highly photosensitive the nature of sensitivity was identical i.e. films were more sensitive at low temperature than at room temperature. The important difference was in the saturation of photocurrent. The response speed was fast for these samples and hence photocurrent was saturated both at room temperature and low temperature as shown in Fig. 5.30. The delay in the rise time and the decay time in temporal response observed in films with  $\text{In/S} = 0.81$  was absent. This indicated that shallow traps were absent/ reduced in density in films with  $\text{In/S} = 0.75$ . In other words the diffusion of minority carriers did not occur in films with the critical stoichiometry.

The temperature dependence of the photocurrent could be used to calculate activation energies of the shallow traps from the Arrhenius plot, as shown in Fig. 5.31. Temperature dependence of photocurrent could be fitted using the relation

$$I_{ph}(T) = I_0 / (1 + c_1 \exp(-E_{a1} / k_B T) + c_2 \exp(-E_{a2} / k_B T)) \quad (5.6)$$

where  $I_{ph}(T)$  is the photocurrent at a temperature  $T$ ,  $I_0$  is the photocurrent at temperature  $0 \text{ K}$ ,  $c_1$  and  $c_2$  are constants related to the capture cross section of traps/defect levels and  $E_{a1}$  &  $E_{a2}$  are the activation energy of the traps/defect levels responsible for the photoconduction.

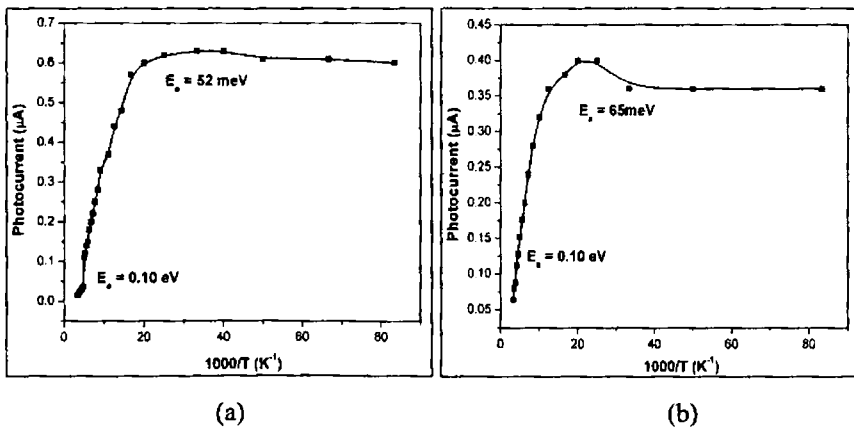


Fig. 5.31: Arrhenius plot of photocurrent versus  $1000/T$  for the film under excitation of (a) 2.81 eV (442 nm) and (b) 2.54 eV (488 nm).

Fig. 5.31((a) & (b)) shows the Arrhenius plots corresponding to excitation with 2.81 eV (442 nm) and 2.54 eV (488 nm) respectively for films with  $\text{In/S} = 0.81$ .  $E_{a1}$  &  $E_{a2}$  were found to be  $\sim 65 \text{ meV}$  and  $\sim 0.1 \text{ eV}$  under excitation of 488 nm while they were found to be  $\sim 52 \text{ meV}$  and  $\sim 0.1 \text{ eV}$  for 442 nm excitation.

The identified activation energies agreed with the established activation energies of  $In_i$  and  $V_{In}$  defect levels. Activation energies in the same range were obtained from the fitting of the Arrhenius plots for samples with  $In/S = 0.75$  using the same excitation energies.

It could be hence established that the same set of defect levels were controlling the photo-conducting properties under intrinsic and extrinsic excitation. These two defect levels were also found to be vital for the films to exhibit the green and red luminescence. Thus it could be assumed that the properties of PC and PL were being controlled by the intrinsic defects of this binary system. Bube et al. had identified that the onset of temperature quenching of photocurrent in single crystals of  $In_2S_3$  corresponded to 0.1 eV while the termination corresponded to energy of 0.8 eV. Thus an effective continuous distribution of sensitizing levels was assumed to exist in the material.<sup>3</sup> Correlating the excitation intensity dependent PC studies, the temperature dependent PC studies and PL studies indicate to the existence of a distribution for the  $In_i$ ,  $V_S$  and  $V_{In}$  defect levels in these thin films. This is based on the investigations carried out on the origin of broad luminescence and the extrinsic photosensitivity in this material by us. When the temperature dependence of sensitivity under excitation of 532 nm (2.33 eV) for films with  $In/S=0.75$  was measured it was observed that the photosensitivity of the material was high at low temperatures and decreased with increase in temperature.

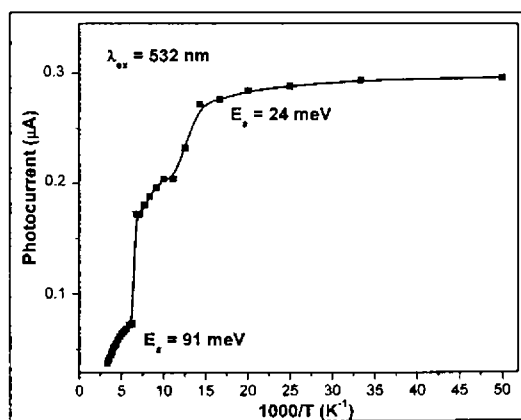


Fig. 5.32: (a) Arrhenius plot of photocurrent fitted using relation (5.6) to calculate thermal activation energy for sample with  $In/S = 0.75$  under photo- excitation with 2.33 eV (532 nm).

Figure 5.32 shows the Arrhenius plot of the photocurrent under this excitation energy, fitted using relation (5.6), which yielded  $E_{a1}$  &  $E_{a2}$  to be ~ 0.09 eV and 24 meV. The former activation energy could be assigned to the  $V_{In}$

acceptor level while the latter could not be assigned. Activation energies in the same range were obtained from the fitting of the Arrhenius plots for samples with  $In/S = 0.81$  using the same excitation energy.

Temperature dependent lifetime studies showed that the lifetime decreased exponentially with increase in temperature under this excitation energy. Since this excitation is extrinsic (below band gap energy) the result indicates that the excitation should be taking place from intermediate defect levels to the CB or from the VB to intermediate defect levels. The excitation intensity dependent studies showed that  $\gamma = 0.68$  which lead us to conclude that this excitation energy was perturbing a distribution of defect levels.

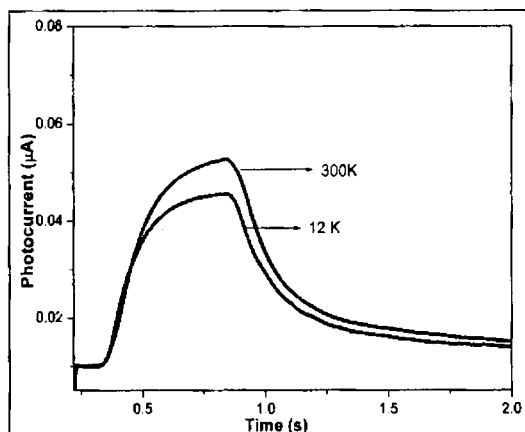


Fig. 5.33: Temperature dependence of photocurrent in sample with  $In/S = 0.81$ .

For sample with  $In/S = 0.81$  there was extrinsic photo-response to excitation wavelength of 632.8 nm (1.96 eV) as shown in Fig. 5.33. The interesting feature was that the photocurrent was larger at 300 K compared to that at 12 K i.e. the photosensitivity was larger at room temperature than at low temperature for this excitation energy. This indicated that the photo-conduction process under this excitation energy was different to that exhibited under excitation of 2.81 eV, 2.54 eV or 2.33 eV where the photosensitivity at room temperature was lower than that of the photosensitivity at cryogenic temperatures. Another interesting feature of this transient photocurrent was that the steep rise of photocurrent on illumination observed with intrinsic excitation was absent. The photocurrent rise and decay showed the effect of diffusion of carriers. The increase in photocurrent at room temperature compared to that at cryogenic temperatures could be explained on the basis of the effect of thermal release of carriers from the traps.<sup>71</sup> The temperature dependence of photocurrent could not be fitted using the relation (5.6) because of the anomalous dependence. Hence it was assumed



that there was a separate photoconduction channel for these red photons in this system. The excitation intensity dependent studies yielded  $\gamma = 0.78$  which indicated again to the distribution of states responsible for this photoconduction.

Most interestingly when the stoichiometry was changed to critical value of  $\text{In/S} = 0.75$  the films did not show any photo-response to this excitation energy. This clearly was a proof that the photoconduction channel for this excitation energy was absent for films with the critical stoichiometry.

Figure 5.34 shows the general nature of photocurrent (defined as difference between illuminated current and dark current) on temperature for the films under excitation using photons of energy 2.81 eV and 2.33 eV. Under excitation with 2.33 eV the photocurrent decreased rapidly up to 180 K and increased very gradually beyond this temperature. The dark current dependence on temperature is also simultaneously depicted in the Fig. 5.34. The dark current was nearly constant from 12 K to 120 K beyond which it increased. Under excitation with 2.81 eV ('above band gap' excitation) the photocurrent decreased from 12 K to 300 K. At this point we concluded that there were separate photoconduction channels in this material which were active depending on the excitation wavelength being intrinsic or extrinsic. Hence separate models had to be proposed to explain the experimentally observed photoconduction in this system.

Apart from the direct excitation of electrons from the valence band to the conduction band by energetic photons of 2.81 eV, electron transitions from the  $V_{\text{In}}$  acceptor levels [ $\sim 0.1$  eV above the valence band] into the conduction band, creating non-ionized  $V_{\text{In}}$  defect levels in the sample can also be induced by this excitation. Radiative recombination is an available recombination path with intrinsic excitation of 2.81 eV, because of the transitions from the  $V_{\text{S}}$  defect level to the non-ionized  $V_{\text{In}}$  acceptors available. The PC spectra was saturated at low temperatures but began to show growth and decay tails at higher temperatures (above 180 K). Growth and decay tails of the transient photocurrent have been associated with the presence of traps.<sup>72</sup> At low temperatures the traps remain filled and thus show no effect on the photocurrent. When the temperature is raised the traps get thermally emptied and increase the photocurrent. At the same time trapping/de-trapping at the trap levels leads to growth tail during rise time and the decay tail during decay which leads to the removal of the saturation of photocurrent. This agreed well with the theory that if traps determine the electron hole recombination then the PC will not show saturation.<sup>73</sup> So above 180 K when the traps are activated they do not allow photocurrent to saturate under intrinsic excitation.

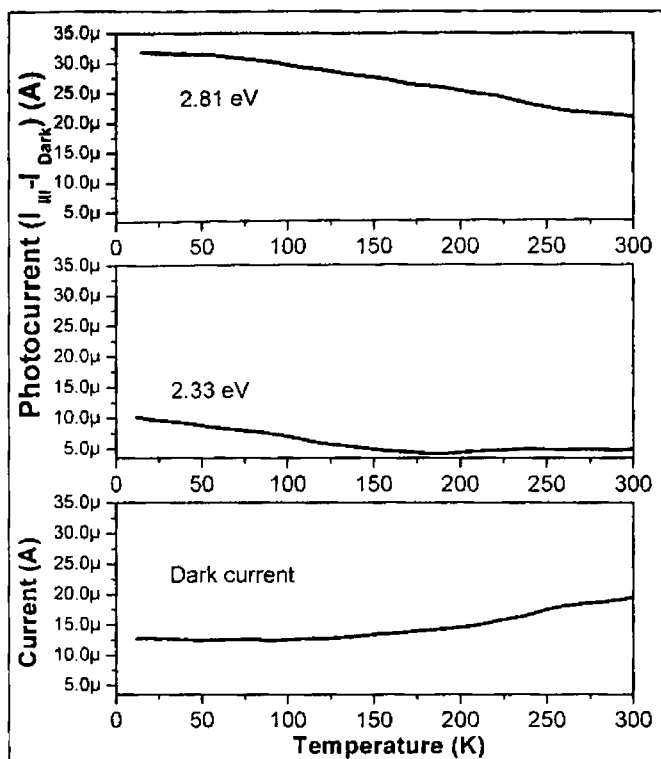


**Fig. 5.34:** Temperature dependence of dark and photo-current for the films. The photocurrent was measured under excitation of 442 nm (2.81 eV) and 532 nm (2.33 eV).

On the other hand under extrinsic excitation the photocurrent does not saturate in the studied temperature range. Energetic considerations preclude the creation of non-ionized  $V_{in}$  defect levels with direct excitation from VB to CB under extrinsic excitation of 2.33 eV. To explain the observed PC under this excitation energy we have to consider that electrons are either excited from defect levels other than the  $V_{in}$  defect level to the conduction band (CB) or the excitation was raising electrons from the valence band /  $V_{in}$  defect level to another intermediate impurity band. The existence of an indirect optical absorption typically around  $\sim 2.2$  eV in these films was realized. Correlating the optical absorption, the PL emission and the extrinsic PC, it was concluded that on excitation with 532 nm (2.33 eV) indirect optical absorption from the VB and or  $V_{in}$  defect level to the indirect valley because of  $V_s$  occur leading to the formation of non-ionized  $V_{in}$  defect levels.

Hence the PC under 2.33 eV excitation could be modeled (Fig. 5.35) as follows: Apart from the absorption taking place from intermediate defect levels to the CB optical absorption also raises electrons from the VB/  $V_{in}$  defect level to the indirect valley (process 1 and 2). It is to be noted that before the optical

absorption takes place the  $V_{in}$  defect level is filled with electrons from the valence band. The electrons reaching the indirect valley first fill the lower lying states and subsequently fill the higher lying states and finally reach the CB (process 3). The raising of electrons from  $V_{in}$  level now causes holes to be generated in this band (process 4) who are compensated by raising electrons from VB into this band (process 5). This enables further raising of electrons from the  $V_{in}$  level to the indirect valley (process 6). Because of this process the temporal response is always on the rise showing the effect of diffusion of carriers. It is also because of the filling up of indirect states and subsequent thermal transfer to the CB that the PC does not show saturation even at very low temperatures under extrinsic excitation of 2.33 eV.

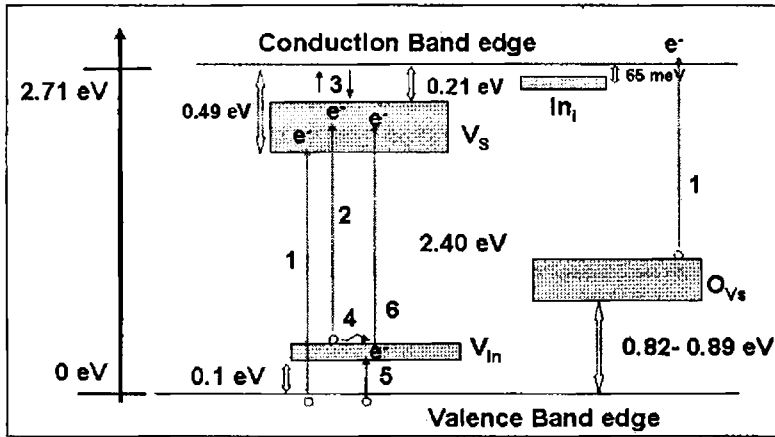


Fig. 5.35: Model for PC under excitation of 2.33 eV.

According to this model the photosensitivity to 2.33 eV should increase when the density of the  $V_{in}$  defect level is increased because it will lead to greater number of electrons being trapped at this center which can be raised by the extrinsic excitation. The photosensitivity to 2.33 eV increased in films when the films were made Indium deficient. The photosensitivity to 2.33 eV excitation was larger for films with  $In/S = 0.75$  compared to that for samples with  $In/S = 0.81$ . This observation strengthened our model.

The decay time for the photocurrent was calculated from the temporal response, by fitting the temporal dependence using relation<sup>73</sup>

$$V = V_0 + A \exp(t / \tau_1) + B \exp(t / \tau_2) \quad (5.7)$$

where A and B are constants describing the capture cross-section of the trapping centers,  $\tau_1$  and  $\tau_2$  are the decay times from the trapping centers, and  $V_0$

is the steady state voltage generated upon illumination with photons. From the curve fitting, it became evident that there were two decay times in this case.

Excitation Energy (eV)	$\tau_1$ (s)	$\tau_2$ (s)
2.81	0.073	6.432
2.54	0.095	6.583
2.33	0.152	7.452
1.96	0.265	7.767

**Table 5.5:** Photo-conductivity decay time obtained by fitting PC decay using relation (5.7).

Table 5.5 represents the PC decay time of the sample with  $In/S=0.81$ , when it was excited using the different excitation energies. Interestingly, the decay times in the first set varied by  $\sim 60\%$ . However the decay times in the second set were comparable. The presence of impurities, which act as trapping centers, could be the reason for such a behavior. To verify this idea, lifetime ( $\tau$ ) was measured using AC-PC and was found to be 30-40 ms for all of the excitation energies. Figure 5.36 represents the AC-PC plot of sample  $In/S = 0.81$  for two different photo- excitation energies, at a bias voltage of 5 V.

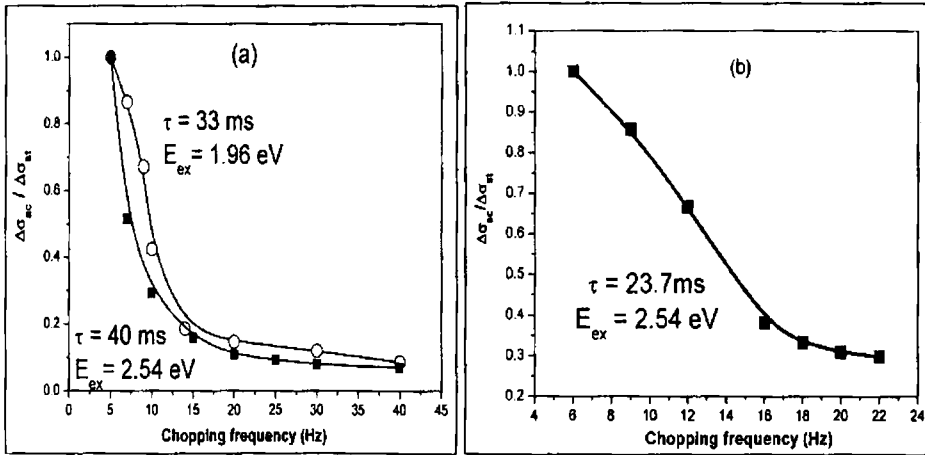


**Fig. 5.36:** AC-PC plot for sample with (a)  $In/S = 0.81$  and (b)  $In/S = 0.75$ .

The decay time was always longer than the lifetime and did not vary upon increasing the excitation intensity. Under the extrinsic photo-excitation, the decay time and lifetime were nearly of the same order. But still the decay time was larger, indicating presence of shallow traps. Even though the decay time increased from 73 ms to 265 ms when the excitation energy was decreased from

2.81 eV (442 nm) to 1.96 eV (632.8 nm), it was observed through AC-PC studies that the lifetime under the different excitation energies was nearly the same ( $\sim 40$  ms). It is known that, if the release of carriers to the conduction band is due to any thermal process, this can lead to an increase in decay time rather than the lifetime.<sup>74</sup> Hence we naturally assumed that, under the sub band gap excitation, the carrier generation process involved a thermal process also.

This was verified when the PC was measured at low temperature. Figure 5.33 represents the photo current measured for sample with  $In/S = 0.81$  at 12 K and 300 K under the sub-band gap excitation condition. The magnitude of photocurrent decreased as the temperature decreased. This supported our assumption that a thermal process was involved in the release of carriers when the sample was under the sub-band- gap excitation condition.

For sample with  $In/S = 0.75$ , extrinsic PC under excitation of 1.96 eV was absent. The PC decay obtained with 2.54 eV is shown in Fig. 5.37, and the decay time was obtained to be  $\sim 24$  ms, without a second decay time. Here, the lifetime ( $\tau$ ) measured using AC- PC (Fig. 5.36(b)) was also found to be  $\sim 24$  ms. Thus the decay time became almost equal to the carrier lifetime. This again indicated that some 'special' types of traps/ defects present in sample with  $In/S = 0.81$  were causing the PC on excitation using photons of 1.96 eV, and these were negligible in concentration or absent in the sample with  $In/S = 0.75$ . Again, the speed of response of this sample was faster compared to the former, which was evident from the time scales of the rise, and decay times for the sample (Fig. 5.37). Since the presence of traps leads to a decrease in speed of response owing to an additional time dependent process of trap filling (during the rise) and trap emptying (during decay) the above result prove that there are fewer traps present in sample with  $In/S = 0.75$  compared to that in sample  $In/S = 0.81$ .

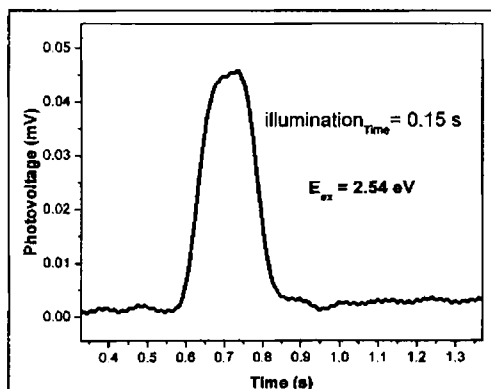


Fig. 5.37: PC decay curve for sample with  $In/S=0.75$  under excitation using 2.54 eV photons.

The temperature dependence of photosensitivity for different wavelengths revealed an important property for these films when the question as to why sensitivity for 632.8 nm excitation was larger at room temperature than at low temperature. Explaining this observation a model for the photoconduction under photo-excitation with 1.96 eV could be proposed as follows: On exciting the samples with 1.96 eV, the absorption causes transition from the 0.83-0.88 eV defect band to the conduction band edge. (It is also worth mentioning here that this acceptor level  $O_{V_s}$  was already filled with electrons from valence band). This was followed by the trapping and de-trapping of the electrons from the shallow  $In_i$  donor level ( $\sim 45$  meV below the conduction band) to the conduction band. The trapping and de-trapping is less active at lower temperatures because of which photosensitivity at lower temperature is reduced compared to room temperature. According to this model, when these donors / acceptors are low in concentration or when they are absent, such a PC behavior must be absent. The sensitivity to 632.8 nm was absent in sample with  $In/S=0.75$  having very low concentration of Indium. Again, this was the reason for the slow rise in photo current due to the excitation using 1.96 eV source (Fig. 5.33). This clearly proved that, by varying the atomic ratio, one could get either a red sensitive or blue sensitive film, making the material a good light sensor. Thus it could be proposed that the  $In_i$  defect level was controlling the speed of response for this system.

It could hence be concluded that, in the  $In_2S_3$  system, the defect centers played important role in controlling the opto-electronic properties. It was observed that there were two separate absorption channels for extrinsic excitation wavelengths of 532 nm (2.33 eV) and 632.8 nm (1.96 eV). The green photons were absorbed relatively in larger quantities from the  $VB/V_{In}$  defect level into the indirect valley located  $\sim 0.5$  eV below the CB while the red photons were absorbed from the  $O_{V_s}$  defect level to the CB. Based on the excitation intensity and temperature dependences, it could be assumed that in the  $In_2S_3$  system these two defect levels  $In_i$  and  $V_{In}$  were distributed exponentially in the band gap and were responsible for the photoconduction properties exhibited by the thin films prepared using CSP technique. It could be modeled that, in general, photo- excitation by these wavelengths was causing electrons to be raised from the valence band (VB) or intermediate defect bands to the conduction band (CB). The  $V_{In}$  defect level would act as an electron trap, enhancing the minority carrier lifetime and increasing the sensitivity of the films

which are In-deficient. This also explained as to why films prepared with low In-content were more photosensitive.

### 5.8 The role of $Cl^-$ impurity on the opto-electronic properties

In the  $In_2S_3$  thin film, four types of intrinsic defects are possible: (1) Indium vacancy ( $V_{In}$ ) (2) Indium interstitial ( $In_i$ ) (3) Sulphur vacancy ( $V_S$ ) and (4) Sulphur interstitial ( $S_i$ ). The first three defects were identified and characterized using PL technique in the present work. Earlier Rupa et al.<sup>75</sup> analyzed these defects using Thermally Stimulated Current measurements. The probability of formation of  $S_i$  defect level is very small as free Sulphur tends to escape rather than remaining as an interstitial and in all of the EDAX measurements the films were found to be Sulphur deficient. Naturally other defects which could be formed unintentionally had to be analyzed to fabricate device quality  $In_2S_3$  thin films. In this category, impurities of Chlorine and Oxygen had very high probability as the precursor solution contained  $InCl_3$  and for spraying air was used as the carrier gas. The role and position of  $O_2$  defects in this system was also identified in this work. The position of  $Cl^-$  impurity was not identified yet beyond speculation.<sup>33, 52, 76</sup>  $In_2S_3$  samples were prepared using Indium Nitrite  $In(NO_3)_2$  and  $CS(NH_2)_2$ . Chlorine was doped purposefully in the sample by adding Ammonium Chloride to the precursor spray solution.

Table 5.6 shows the effect of  $Cl^-$  doping on the stoichiometry of these films. It is to be noted that in all of the earlier samples studied, incorporation of  $Cl^-$  impurity occurred unintentionally. It could now be noted that, as the Chlorine content in the film increased, Indium and Sulphur content decreased. Earlier we had observed similar results when the effect of annealing was studied on the unintentionally doped films (section 5.6). The concentration decrease was larger for Sulphur compared to Indium.

Sample	[In](%)	[S](%)	[Cl](%)	[Cl]/{[In]+[S]}	Photosensitivity
In 5	39.42	59.86		-	21.142
In 8	40	57	3	0.03	18.284
In 4	37.79	49.82	12.5	0.14	25.367
In 7	38.11	51.31	10.58	0.12	9.427

**Table 5.6:** Photosensitivity values for the doped and un-doped films along with the samples EDAX results.

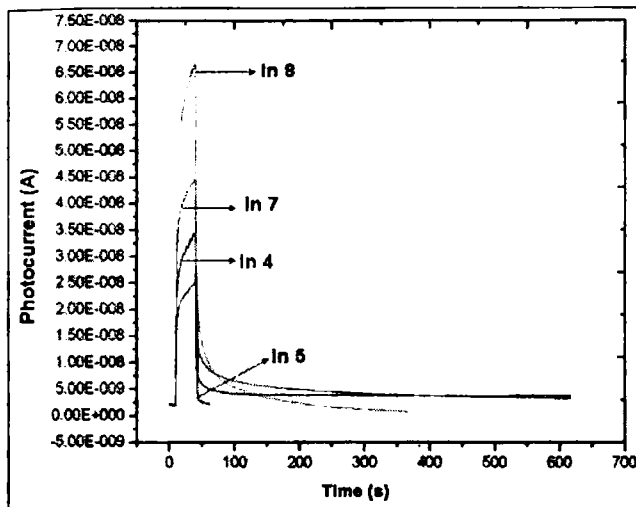


Fig. 5.38: PC spectra for doped and un-doped films.

These films showed very poor photosensitivity. It was not possible to pick up any PC under extrinsic excitation for this set of samples. PC measurements were carried out using a white light source. The transient PC curves for doped and un-doped films are shown in Fig. 5.38. The results indicated that, for this set of samples, the photosensitivity did not improve with increasing the doping concentration. However an important conclusion was obtained: The persistence of PC increased as the amount of Chlorine in the film increased.

Correlating Table 5.6 and Fig. 5.38 we conclude that the  $Cl^-$  impurity effectively generates a positive charge in the  $In_2S_3$  system and provides shallow electron trapping states which lead to persistence in the decay of photocurrent. In the earlier part of the work, it was concluded that shallow traps were responsible for the decay tail in the transient PC. Those films were born with  $Cl^-$  because  $InCl_3$  solution was used as the precursor for the thin film preparation. Sample In5 which did not contain any  $Cl^-$  impurity, did not exhibit the decay tail. Sample In4 which contained the maximum  $Cl^-$  content failed to return to its dark current value even 1200 seconds after the illumination was switched off. This conclusively proved that the incorporation of  $Cl^-$  impurity was responsible for the decay tail.

It can be assumed that during  $Cl^-$  doping, some of the  $Cl^-$  ions occupy the lattice sites normally occupied by  $S^{2-}$  ions. In that case, it will naturally lead to formation of positive ion vacancies (vacancy of  $In^{3+}$ ) which will act as electron traps. The creation of vacancies requires good deal of energy and hence the



quantity of  $Cl^-$  incorporated in the lattice will be strongly limited. The presence of vacancies, even though they occur in very small concentrations, also leads to the formation of localized levels in the forbidden energy gap. This was evident when the PL spectra of the un-doped sample (In5) and the film showing maximum  $Cl^-$  incorporation (In4) were compared (Fig. 5.39).

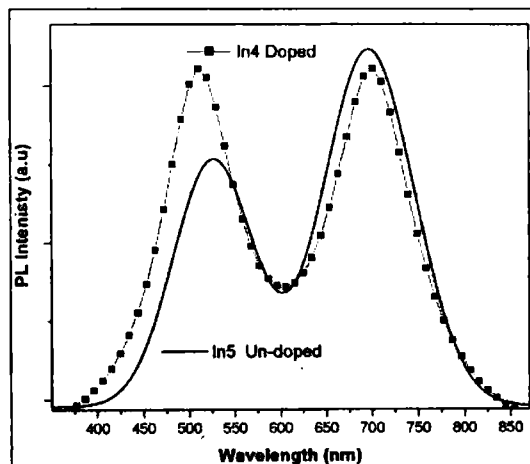


**Fig. 5.39:** Room temperature PL spectra for un-doped and doped samples of  $In_2S_3$ .

In sample In5 the red emission due to the  $In_i - O_{V_s}$  [DAP] recombination was more prominent than the green emission due to the  $V_s - V_{In}$  [DAP] recombination. After  $Cl^-$  doping,  $V_s - V_{In}$  [DAP] recombination gained prominence slightly greater than the  $In_i - O_{V_s}$  [DAP] recombination. Also the FWHM of the green emission increased in the doped sample. EDAX analysis showed that amount of Sulphur in the film was much reduced on doping. Thus effectively both the cation and anion vacancies increased which was reflected by the increase in the green PL emission intensity because of the  $V_s - V_{In}$  [DAP] recombination. It is already well known that the cation vacancy ( $V_{In}$ ) is ordered in the lattice as 1/3 of these sites are vacant by birth. PL proved that, in addition to these intrinsic vacancies,  $Cl^-$  doping promoted formation of  $V_{In^{3+}}$ , and this enhanced the green emission from this compound.

The general shape of the PL spectrum was found to be independent of the  $Cl^-$  impurity i.e. the red and green emission were present in  $In_2S_3$  films which had some  $Cl^-$  impurity and also in films which did not contain the  $Cl^-$  impurity. This proved that the  $Cl^-$  ions themselves are not the luminescence centers. But the  $Cl^-$  impurity disturbs the  $In_2S_3$  lattice in such a way that additional luminescence centers are created which alter the photo-response and luminescence efficiency of the system. This work now proves why  $Cl^-$  impurity

is essential to this system and why solar cells prepared using  $\text{In}_2\text{S}_3$  containing  $\text{Cl}^-$  impurity, show very good efficiency.<sup>45</sup>

### 5.9 Conducting grain boundaries of $\beta\text{-In}_2\text{S}_3$

Opto-electronic devices achieve performance close to the theoretical expectations, when high quality single crystal materials, are used. But it has always been found that the polycrystalline counterparts outperform their single crystal analogues.<sup>77</sup> The origin of the improved device behavior, such as in solar cells, is widely studied at present. Major difference in the structure of a polycrystalline film from that of a single crystal is the presence of “grain boundaries” which separate small single crystal regions within the film.<sup>78, 79</sup> A grain boundary becomes electrically active as a result of ‘charge trapping’ by gap states, localized between the two adjacent grains. Such interface states are possibly created by dislocations introduced by the crystallographic mismatch between the adjacent grains, or by the vacancies thereby leading to dangling bonds or by other interfacial defects.<sup>80</sup> A second possible origin of these states is due to dopant or impurity atoms, trapped at the interface, creating donor or acceptor levels. The electric field, generated by the charged interface, gives rise to a band-bending in the adjacent grains.<sup>81</sup> If the band-bending is strong enough for the GBs to become inverted, the spatial separation of photo-generated e-h pairs is helped and the minority carriers in the bulk of the grains are channeled along the continuous network of GBs as majority carriers, with minimal e-h recombination.<sup>79, 82</sup> The presence of the charged barrier has been successful in explaining the large photosensitivity exhibited by the polycrystalline films.<sup>79, 83</sup> Theoretically, it had been predicted that  $\Sigma 3$  grain boundaries in chalcopyrite represent a barrier without charged defects, whose presence would improve the photoconductive gain of this system.<sup>84, 85</sup> Susanne et al. identified neutral barriers in  $\text{CuGaSe}_2$  and reasoned that the Cu deficiency of the grain boundaries was responsible for this.<sup>86</sup>

As one turns from the single crystal to the polycrystalline film, it is also observed that the width of the exponential absorption tail and the related PC tail change considerably. The common explanation in literature for the phenomenon is that the narrow Urbach tail is widened by the disorder-induced exponential density of tail states.<sup>80, 87, 88</sup> The disorder may be in the bulk of the grains or in the grain boundaries (GBs). If it is in the former region, then one can adopt the conventional Seto-type mechanism for the inter-crystalline transport, where the GBs essentially play only the role of potential barriers between the grains.<sup>89, 90</sup> If

the disorder is mainly in the GBs, we have to assume that the extended absorption tail is associated with the GBs. In that case, the effective “band gap” of the GB should be smaller than that of the crystal/bulk of the grain and one would expect that sub-band gap photo excitation in polycrystalline materials will mainly take place along the network of the GBs. Interestingly; these carriers may help the electrical transport process taking place in the polycrystalline films.

The crystal structure of  $\beta\text{-In}_2\text{S}_3$  consists of sheets of Sulphur atoms between which there are sheets of Indium atoms, with some sheets having both tetrahedrally and octahedrally co-ordinated Indium atoms, while others only having the latter. Some tetrahedral sites are unoccupied, leaving the neighboring Sulphur atoms bonded only to three instead of the usual four Indium atoms. These vacant sites will, as a result, exhibit electron affinity and act as electron traps. Overlap of trapped electron wave functions between such highly ordered states can lead to sharp trapping levels.<sup>9</sup>

The material exhibited very high photosensitivity ( $\sim 10^3$ ) only for a specific In/S volume fraction in the spray solution.<sup>47</sup> But samples with other volume fractions were not so photosensitive. In fact, this result forced us to ask the question ‘from where does the photocurrent originate in  $\beta\text{-In}_2\text{S}_3$  thin films?’ The other related problems were that of defects which yield persistent photo-conductivity (PPC) and response to sub-band gap excitation in this system.<sup>76</sup> DX like centers are known to yield PPC.<sup>91-94</sup> It is generally believed that the point defect, accompanied with a strong structural relaxation due to the change in charge state, is the most probable candidate for PPC. The shallow states responsible for this are expected to yield band tails, leading to extended conduction.<sup>95</sup> Understanding the defects and the photoconduction process is essential for improving the functionality of the solar cells fabricated using  $\beta\text{-In}_2\text{S}_3$  thin films.

Sample No:	Molarity of In/S in spray solution	[In]/[S] from EDAX	Photosensitivity
1	0.015/0.0375	34.0/65.9	$\sim 25$
2	0.025/0.0375	34.2/56.5	$\sim 60$
3	0.025/0.1	40.0/49.54	$\sim 350$
4	0.015/0.1	39.6/52.5	$\sim 10^3$

**Table 5.7:** Sample names, their composition and photosensitivity.

The details of the molarity used in the spray solution and the results of the compositional analysis of the samples, using EDAX technique are given in Table 5.7. The band gap of the films were typically of the order of 2.6 - 2.7 eV. Photosensitivity [defined as  $(I_{ill} - I_{dark}) / I_{dark}$ ] was measured by illuminating the films with a halogen lamp, delivering  $100 \text{ mW/cm}^2$  on the sample surface. This set of samples was purposefully taken in order to understand the route of photocurrent in these thin films.

AFM analysis over an area of  $1 \mu\text{m}^2$  clearly showed the crystallite/grain structures of the samples distinctly (Fig. 5.40). AFM image of sample 1 showed agglomerated regions with no proper distinction between the grain and grain boundary. Each of the agglomerate contained a number of smaller grains. But this was not clearly visible at the available magnification. When the Sulphur content in the film increased, the agglomerations appeared with random distribution of grain size. In sample 4, however, the grains were densely packed with the grain size ranging from 50 to 80 nm. Smaller crystallites were well packed between the larger ones, without pores. A well-connected network of the grain boundaries was evident from the AFM analysis. The film could, hence, be called “grainy” with well-interconnected grain boundaries. Such a distribution was absent in all other samples. Sample 3 contained crystallites of  $\sim 110 \text{ nm}$ . Though the film was continuous for this stoichiometry, there were voids between the crystallites.

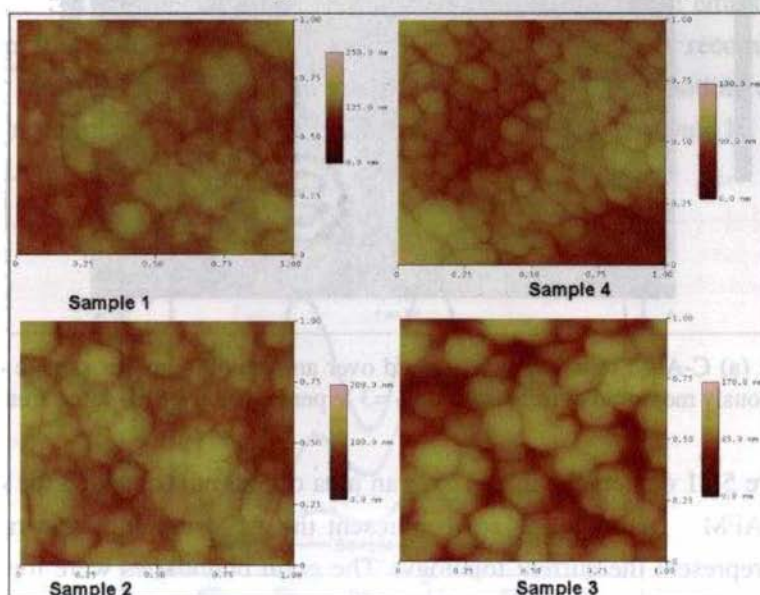


**Fig. 5.40:** AFM surface topology of the samples over an area of  $1 \mu\text{m}^2$  with varying In/S stoichiometry.

In sample 3, we were able to detect extrinsic PC under sub-band gap illumination of 488 nm, 532 nm and 632.8 nm. However in sample 4, the extrinsic PC was obtained only for the excitation using 488 nm and 532 nm. In spite of sample 4 being more photosensitive, it did not respond to 632.8 nm excitation. Also the speed of response of sample 4 was much higher than that of sample 3. The lifetime of the carriers measured using AC-PC was  $\sim 20$  ms in sample 4 whereas in sample 3, it was  $\sim 0.2$  s.<sup>69</sup> It is already proved that the 'current images' obtained using Conductance Atomic Force Microscopy (C-AFM), provided local two-dimensional cross- sections of the three-dimensional photoconduction network.<sup>90</sup> C-AFM data was taken in 'contact mode' using a commercial Nanoscope [4 (DI) AFM system], having Co-Cr coated Silicon tip. The current sensitivity of the system was 1000 pA/V and the cantilever length was 250  $\mu\text{m}$ . Silver electrodes were used as the counter electrode to the local contact provided by the C-AFM tip. Local I-V measurements were also performed by applying a DC bias on the sample while doing the C-AFM scanning. The range of the bias was from -10V to +10V. A 2 mW diode laser, operating at 632 nm, was used for all of the C-AFM and AFM measurements.

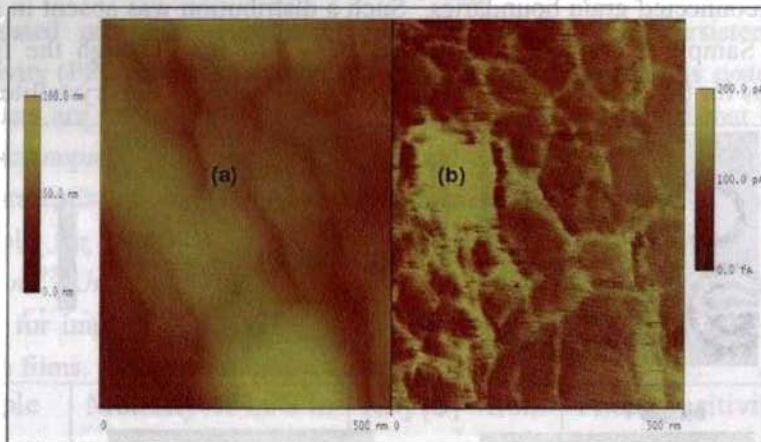


**Fig. 5.41:** (a) C-AFM topography measured over an area  $500 \text{ nm}^2$  for sample 4 and (b) Simultaneously measured current map at  $V_B = 3 \text{ V}$  performed over the same area.

Figure 5.41 depicts the image over an area of  $500 \text{ nm}^2$  obtained for sample 4 using C-AFM (left [Fig. 5.41(a)] represent the AFM topology and right [Fig. 5.41(b)] represent the current topology). The grain boundaries were found to be conducting in the sample 4, while in the other samples, no conducting grain boundaries could be detected using C-AFM. Even though the AFM laser was left 'on' while doing the C-AFM experiment, our PC studies showed that 632.8 nm did not produce any photoconduction in sample 4. Since current propagates

through a film by selecting path of least resistance, the C-AFM analysis proved that the grain boundaries provide an alternate current path in  $\beta\text{-In}_2\text{S}_3$  thin films. Our results clearly indicated that the GBs themselves provided a parallel route for the flow of charge carriers in sample 4. Thus it could be assumed that this conducting channel could be one of the reasons for the high photosensitivity of sample 4, as it could provide an easy path for the photo-generated minority carriers. None of the other samples showed the presence of a conducting grain boundary.

Since PL is the best tool to search for shallow traps / defects, we carried out PL analysis of these samples. PL emissions were obtained from the films, which were even visible to the naked eye (Fig. 5.42) at room temperature itself. In sample 4, the highest emission peaks were at  $\sim 517$  nm (green emission, 2.40 eV) and  $\sim 696$  nm (red emission, 1.78 eV). Origin of the green and red luminescence in this system had been identified earlier in this work.<sup>69</sup> In the case of sample 3, the higher energy emission was shifted to  $\sim 540$  nm (2.30 eV) while the lower energy emission was at the same position, as in the former sample. Again for the former sample, the PL emission intensity was larger (along with a broadening of the rising edge of the  $\sim 517$  nm peak towards the higher energy side) which proved the presence of higher defect concentration. In sample 3, where the intensity of the red emission was low (compared to sample 4), PC response to red illumination improved. As stated earlier, the red emission in  $\beta\text{-In}_2\text{S}_3$  thin films was identified to be due to the  $\text{In}_T\text{-O}_V$ , DAP recombination. Hence it was naturally assumed that if these DAP recombination could be reduced in sample 4; PC due to the excitation using 632.8 nm could be induced/enhanced.

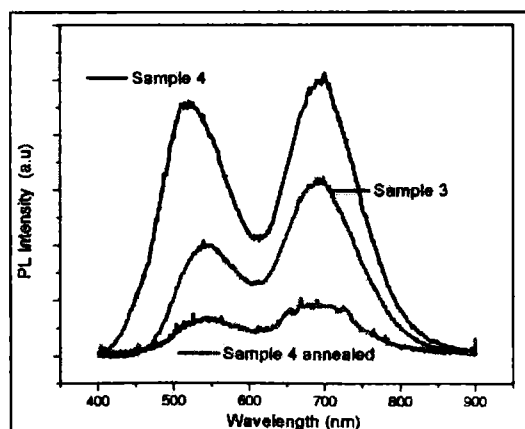
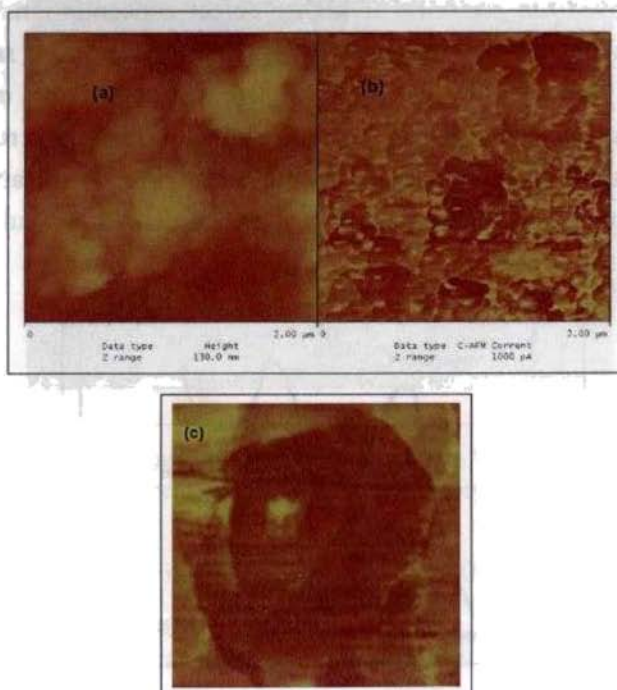


**Fig. 5.42:** PL emission from different samples using 325 nm as excitation wavelength, at 300 K.



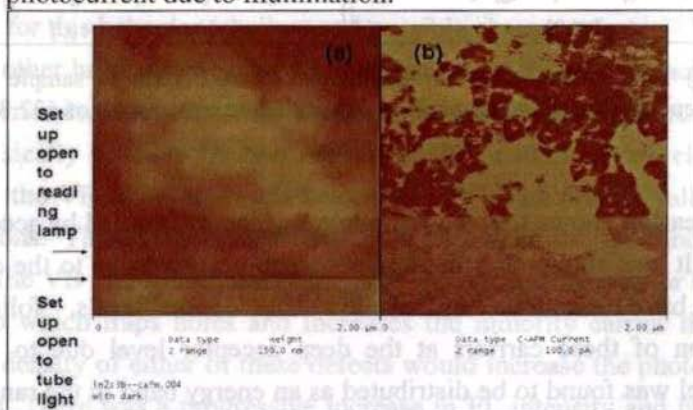
Sample 4 was then subjected to vacuum annealing for 1 hr at 300 °C with the idea of removing the adsorbed Oxygen, which would lead to a decrease in the concentration of acceptor type  $O_v$  defect level, resulting in a less intense red luminescence emission. Figure 5.42 also shows the PL spectrum of sample 4 after vacuum annealing [green line]. [The annealed sample 4 is named sample 5 here after]. As expected, intensity of the red luminescence decreased considerably. Annealing also resulted in the improvement of grain size and crystallinity of the films. This could have resulted in annealing out of the band tails, which is reflected in the decrease in the ascending and descending tails of PL emission for sample 5 (Fig. 5.42).

Figure 5.43(a) shows the AFM and CAFM topology of sample 5. It was observed that there were agglomerations throughout the film, resulting from the grain gathering. Different to the sample 4, now the sample 5 had larger grains and each of the grains showed a conducting central region (Fig. 5.43(b)). Thus it could be concluded at this point that, after vacuum annealing, the grain boundary material and the grain center material had the same photo-conducting nature. Now the current percolation network had an additional path through the grain centers.



**Fig. 5.43:** (a) AFM image for sample 5 (b) C-AFM image for sample 5 and (c) enlarged picture of a single grain from sample 5.

The photosensitivity of the films was  $<10$  after vacuum annealing. This was because of the decrease in dark resistance of the films. Sample 4 had a resistivity of  $15 \text{ K}\Omega \text{ cm}$  and after annealing, the resistivity reduced to  $15 \Omega \text{ cm}$ . Figure 5.44 shows the real time AFM (Fig. 5.44(a)) and C-AFM current map (Fig. 5.44(b)) analysis demonstrating the effect of light on this system. Starting at the bottom of the picture scan was done keeping the AFM system in the dark. It is to be noted that during this stage and later on the AFM laser was always switched on. The left side of Fig. 5.44 represents the AFM topology and the right represents the C-AFM topology. It can be noted that when only the AFM laser is on the contrast between the grain and the grain boundary is low. Later on when the tube light is switched on (indicated by the first arrow) and later on when an additional reading lamp was switched on (indicated by the second arrow) the contrast between the grain and grain boundary becomes very sharp and the presence of the conducting path right through the center of each grain becomes visible. This is because of the increase in photocurrent due to illumination.



**Fig. 5.44:** Photo conductivity studied using C-AFM: First the sample is kept in dark and C-AFM data is taken. After 10 s of scanning in the dark the samples were exposed to white light in a room (a) shows the CAFM topology and (b) the simultaneous current map.

An analogues representation of the same phenomenon is represented by the plot between photocurrent and illumination time. This experiment very clearly proved that in the samples the photoconduction was associated with a more photoconductive material that is segregated on the grain boundaries. This is first time that a more photoconductive grain center has been observed in any material. Further, sample 5 also exhibited response to the sub-band gap excitation using  $632.8 \text{ nm}$ , as shown in Fig. 5.45(a). (It should be noted here that before vacuum annealing this sample did not show any response to excitation with  $632.8 \text{ nm}$ ).



The photocurrent required more than 20 minutes to reach the original dark current value. It could be now realized that, while taking the C-AFM measurements, we had left the diode laser switched on which had to be one of the reasons for the sample 5 to exhibit enhanced GB current due to its improved extrinsic response.

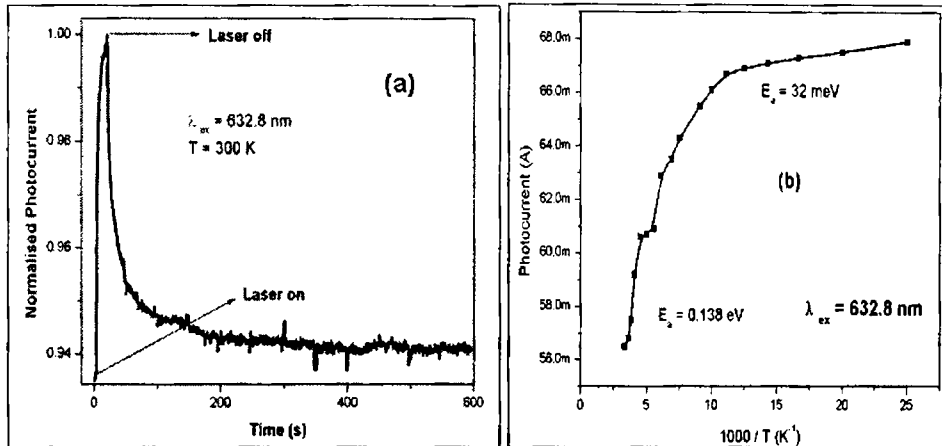


Fig. 5.45: (a) PPC under excitation wavelength of 632.8 nm in sample 5 and (b) temperature dependence of photocurrent under excitation wavelength of 632.8 nm in this sample.

We had earlier shown that the red luminescence was caused by acceptor type defects.<sup>58, 69</sup> It was shown that the luminescence occurred due to the capture of conduction band electrons by shallow  $In_i$  donor levels, followed by recombination of these carriers at the deep acceptor level due to  $O_{V_s}$ . This acceptor level was found to be distributed as an energy band in the range 0.835–0.887 eV, above the valence band edge and the model for photoconduction due to extrinsic excitation with 632.8 nm was well established.<sup>69</sup>

As the total PL intensity of the sample decreased, the PPC increased. It has been established that as the band bending increases, the e-h recombination tend to become minimal. The intensity ratio of the red emission to the green emission in sample 4 was  $\sim 1.1$  before and after annealing while in sample 3 it was  $\sim 1.5$ . Thus it was concluded that the PPC is associated to the defects in the system. If the defect states are present on the GBs they would induce GB potential barriers resisting lateral conductivity. When film is illuminated with photons of energy capable of raising electrons from these states into the CB discharging of these states would occur which would induce a conductivity increase by lowering the barriers. When the illumination is switched off, electrons from the bulk use the thermal energy to surmount the remaining potential barrier, refill the grain-

boundary states, and resume their equilibrium distribution. During this process the barrier height, and consequently the trapping process lifetime, increases resulting in PPC.

The temperature dependence of photocurrent can be used to calculate activation energies of shallow traps from its Arrhenius plot as shown in Fig. 5.45(b). The temperature dependence of photocurrent under sub-band gap excitation of 632.8 nm was fitted using the relation (5.6). A shallow trap with activation energy of  $\sim 37$  meV and a deep trap with activation energy 0.138 eV were obtained from the temperature dependence of photocurrent using sub-band gap excitation of 632.8 nm. These were close to the activation energy of the  $In_i$  donor level which plays the role of the shallow trap, enhancing the photoconduction under excitation of 632.8 nm and the  $V_{in}$  acceptor level respectively. This indicated that the  $In_i$  donor which may be in the  $In_i^+$ ,  $In_i^{++}$  or  $In_i^{+++}$  ionized states in the  $\beta$ - $In_2S_3$  system are responsible for the PPC under illumination of 632.8 nm: going by the generally accepted nature of defects responsible for this behavior (shallow and possible charge states).

On the other hand photosensitivity can increase if there is an increase in the minority carrier concentration in the valence band of this n-type material. This can be physically possible by two means (A) if on illumination electrons are raised from the VB to defect levels below the CB which are not fully occupied with electrons. Thus these levels will trap the electrons and increase hole lifetime in the VB and subsequently increase the photosensitivity or (B) if there is hole trap which traps holes and increases the minority carrier lifetime. An increase in density of either of these defects would increase the photosensitivity of the films. There was a progressive increase in PL intensity and full width at half maximum of the samples (Fig. 5.42) as the photosensitivity increased which validates this model. The specific defect responsible for this increase in photosensitivity has not been identified but may be assumed to be some unintentional dopants from the substrate or the precursor solution. This may be most probably the defects like  $Cl_i$  or  $Cl_{Vs}$ .

The grain boundary material was found to be more conductive than the grain material in  $\beta$ - $In_2S_3$  thin films. Since there was response to excitation with 632.8 nm in samples with and without conducting grain boundaries it became clear that the effect of conducting grain boundaries alone could not be responsible for the extrinsic PC under excitation of 632.8 nm. Had there been such a nexus the annealed samples should not have shown response to extrinsic excitation with 632.8 nm. PPC was observed in samples with and without conducting GBs but

was enhanced significantly when GB conductivity highly improved. The enhancement was at the loss of sensitivity and response speed.

## 5.10 Conclusions

The use of PL and PC in the defect analysis of  $\beta\text{-In}_2\text{S}_3$  has revealed very interesting opto-electronic applications for this material. The material was identified as a good luminescent material having a green emission centered around  $\sim 540$  nm and a red emission centered around  $\sim 690$  nm. The luminescence intensity of these two emissions was found to be competitive to one another. But nevertheless tunability for the emission could be achieved by varying the stoichiometry, post deposition annealing conditions or by a bias (not included in this thesis<sup>78</sup>). It was observed that the intrinsic defects of this system controlled both the luminescence and PC properties. Using PC and PL, the position of the  $\text{In}_i$  donor level,  $V_S$  donor level,  $V_{In}$  acceptor level and  $O_{V_S}$  acceptor level were identified. The defects in this system were identified to have an exponential distribution in the band gap based on the photo-response and temperature dependence of photoconduction to intrinsic and extrinsic excitation.

Green emission from  $\text{In}_2\text{S}_3$  was identified to be due to the transition from the excited states of the  $V_S$  level to the  $V_{In}$  level. Mechanism of this emission could be explained on the basis of the CC model of luminescence. The red emission from the films was identified to be due to transition from the  $\text{In}_i$  donor level to the  $O_{V_S}$  defect level above the VB. The presence of the  $\text{In}_i - O_{V_S}$  DAP was identified to be the cause of extrinsic PC i.e., sensitivity to red photons. Hence the important role of the defect levels in determining the opto-electronic properties of  $\text{In}_2\text{S}_3$  was realized. Presence of the  $V_S\text{-}V_{In}$  DAP was identified to be cause of the extrinsic PC under excitation using green photons. The presence of a defect band located between  $\sim 0.84 - 0.89$  eV above the valence band was also identified, based on optical absorption and PL studies. It was hence possible to propose that the photocurrent from photovoltaic devices, based on  $\beta\text{-In}_2\text{S}_3$  thin films having these defects, would be large because of the extrinsic photo-response exhibited by this material. This material would hence become the natural choice for fabrication of third generation solar cells.<sup>64</sup> Because of the luminescence phenomenon associated with this system it can also find application as a “luminescence down converter” in solar cells, where absorption of higher energy photons takes place and it is re-emitted as photons of lower energy.

$\beta$ - $In_2S_3$  thin films were very sensitive to light illumination levels and showed sensitivity dependence on the incident wavelength. Sensitivity in general was higher at low temperatures and decreased as temperature was raised. Smart devices based on  $\beta$ - $In_2S_3$  thin films could be fabricated which could be used as photo-detectors. The wavelength sensitivity of these devices showed bias dependence. It was found that the differential bias voltage controlled the wavelength sensitivity of the device. Thus depending upon the differential bias voltage, the wavelength sensitivity of the device could be tuned. The sensor exhibited an average sensitivity of 17.5 mV/ nm in the wavelength range of 325 nm – 650 nm.

It was also found that the grain boundary material is more conductive than the grain in our  $\beta$ - $In_2S_3$  thin films prepared using CSP technique and this type of PC has a strong dependence on the stoichiometry of the sample. The red photo-response of these films could be improved by vacuum annealing of the samples, and this proposes a technique to improve sub-band gap photo-response of these films. This will naturally lead to the improvement in the efficiency of optoelectronic devices like solar cells, based on this material, as it creates carriers by absorbing sub-band gap photons.

## 5.11 Reference

1. Welker, H. and Ergeb, D., *Exakt. Naturwissenschaften* **29**, 275 (1956).
2. Rehwald, W. and Harbeke, G., *J. Phys. Chem. Solids*, **26**, 1309 (1965).
3. Richard H. Bube and William H. Mc. Carroll, *J. Phys. C: Solid State Phys.* **10**, 333 (1959).
4. Greenwood, N. N. and Earnshaw, A., *Chemistry of the Elements*, Pergamon press, Oxford, ch.7, p. 286 (1984).
5. Govender, K., Boyle, D. S. and O'Brien, P., *J. Mater. Chem.* **13**, 2242 (2003).
6. Bernede, J. C., Barreau, N., Marsillac, S. and Assmann, L., *Appl. Surf. Sci.* **195**, 222 (2002).
7. Hariskos, D., Ruckh, M., Ruble, U., Walter, T., Schock, H. W., Hedstorn, J. and Stolt, L., *Sol. Energy Mater. Sol. Cells*, **41-42**, 345 (1996).
8. Djessas, K., Yapi, S., Masse, G., Ibannain, M. and Gauffier, J. L., *J. Appl. Phys.* **95**, 4111 (2004).

9. Garlick, G. F. J., Springford, M. and Checinska, H., Proc. Phys. Soc. **82**, 16 (1963).
10. Wha-Tek Kim and Chang Dae Kim, J. Appl. Phys. **60**, 7 (1986).
11. Rooymans, C. J. M., J. Inorg. Nucl. Chem. **11**, 78 (1959).
12. Goodyear, J. and Steigmann, G. A., Proc. Phys. Soc. **78**, 491 (1961).
13. Hahn, H. and Klinger, W. Z., Anorg. Chem. **260**, 97 (1949).
14. Wycoff, R. W. G., Crystal Structure, (Interscience Publishers, NY), vol **II**, Chapter VIII (1948).
15. Goswami, A., Talele, G. D. and Badachhape, S. B., Indian J. Pure and Appl. Phys. **14**, 716 (1976).
16. King, G. S. D., Acta Cryst. **15**, 512 (1962).
17. Kim, W. T. and Kim, C. D., J. Appl. Phys. **60**, 2631 (1986).
18. Kambas, K., Physica B (Amsterdam), **160**, 103 (1989).
19. Kim, C. D., Lim, H., Park, H. L., Park, H. Y., Kim, J. E., Kim, H. G., Kim, Y. G. and Kim, W. T., Thin Solid Films, **224**, 69 (1993).
20. Nosaka, Y., Ohta, N. and Miyama, H., J. Phys. Chem. **94**, 3752 (1990).
21. Becker, R. S., Zhou, G. D. and Elton, J., J. Phys. Chem, **90**, 5866 (1986).
22. Herrero, J. and Ortega, J., Sol. Energy Mater. **17**, 357 (1988).
23. Hodes, G., Engelhard, T., Turner, J. A. and Cahen, D., Sol. Energy Mater. **12**, 211 (1985).
24. Kambas, K., Anagnostopoulos, A., Ves, S., Ploss, B. and Spyridelis, J., Phys. Stat. Sol. (b), **127**, 201 (1985).
25. Yoshida, T., Yamaguchi, K., Toyoda, H., Akao, K., Sugiura, T., Minoura, H. and Nosaka, Y., Proc. Electrochem. Soc. **97-20**, 37 (1997).
26. George, J., Joseph, K. S., Pradeep, B. and Palson, T. I., Phys. Stat. Sol. (a), **106**, 123 (1988).
27. Van Landuyth, J., Hatwell, H. and Amelinckx, S., Mater. Res. Bull. **3**, 519 (1968).
28. Keramida, V., Deangeli, S. and White, W. J., Solid State Chem. **15**, 233 (1975).
29. El. Shazl, A. A., Abd Elhady, D., Metwally, H. S. and Seyam, M. A. M., J. Phys. Condens. Matter **10**, 5934 (1998).
30. Bube, R. H., J. Phys. Chem. Solids, **1**, 234 (1957).
31. Gilles, J. M., Hatwell, H., Offergeld, G. and Van Cakenberghe, J., Phys. Stat. Sol. II, **K73** (1962).

32. Sung-Hyu Choe, Tae-Hwan Bang, Nam-Oh Kim, Hyung-Gon Kim, Choong-II Lee, Moon-Seog Jin, Seok-Kyun Oh and Wha-Tek Kim, *Semicond. Sci. Technol.* **16**, 98 (2001).
33. Pai, R. R., John, T. T., Kashiwaba, Y., Abe, T., Vijayakumar, K. P. and Kartha, C. S., *J. Mater. Sci.* **40**, 741 (2005).
34. Springford, M., *Proc. Phys. Soc.* **82**, 1029 (1963).
35. *Jpn. Patent Appl. Chem. Abstr.* **91**, 67384a (1979).
36. *Jpn. Patent Appl. Chem. Abstr.* **96**, 113316h (1979).
37. *Jpn. Patent Appl. Chem. Abstr.* **95**, 107324X (1981).
38. Dattatri Nagesha, K. Xiaorong Liang, Arif Mamedov, A. Gordon Gainer, Margaret Eastman, A. Michael Giersig, Jin-Joo Song, Tong Ni, and Nicholas Kotov, A., *J. Phys. Chem. B*, **105**, 7490 (2001).
39. Yujie Xiong, Yi Xie, Guoan Du, Xiaobo Tian, and Yitai Qian, *J. Solid State Chem.* **166**, 336 (2002).
40. Gorai, S., Guha, P., Ganguli, D., Chaudhuri, S., *Mater. Chem. Phys.* **82**, 974 (2003).
41. Zi Ping Ai, *Opt. Mater.* **24**, 589 (2003).
42. Sharma, R. K., Lakshmikumar, S. T., Gurmeet Singh and Rastogi, A. C., *Mater. Chem. Phys.* **92**, 240 (2005).
43. Xiaoyi Zhu, Junfeng Ma, Yonggang Wang, Jiantao Tao, Jun Zhou, Zhongqiang Zhao, Lijin Xie, Hua Tian, *Materials Research Bulletin*, **41**, 1584 (2006).
44. Xuebo Cao, Li Gu, Lanjian Zhuge, Wenhui Qian, Cui Zhao, Xianmei Lan, Wenjun Sheng, Dan Yao, *Colloids and Surfaces A: Physicochem. Eng. Aspects*, **297**, 183 (2007).
45. Teny Theresa John, Meril Mathew, Sudha Kartha, C. and Vijayakumar, K. P., Abe, T. and Kashiwaba, Y., *Sol. Energy Mater. Sol. Cells*, **89**, 27 (2005).
46. Ernits, K., Brénaud, D., Buecheler, S., Hibberd, C. J., Kaelin, M., Khrypunov, G., Müller, U., Mellikov, E. and Tiwari, A. N., *Thin Solid Films*, **515**, 6051 (2007).
47. Teny Theresa John, Bini, S., Kashiwaba, Y., Abe, T., Yasuhiro, Y., Sudha Kartha, C. and Vijayakumar, K. P., *Semicond. Sci. Technol.* **18**, 491 (2003).
48. Yu S-H, Shu L, Wu Y-S, Yang J, Xie Y and Qian Y-T, *J. Am. Ceram. Soc.* **82**, 457 (1999).
49. Lutz, H. D. and Haueseler, H., *Z. Naturf.* **26a**, 323 (1971).
50. Herrmann, H., *Phys. Stat. Sol. (b)*, **82**, 513 (1977).
51. Chakrabarti, S., Ganguli, D. and Chaudhuri, S., *Physica E*, **24**, 333 (2004).

52. Rupa Pai, Teny Theresa John, Kashiwaba, Y., Abe, T., Vijayakumar, K. P. and Sudha Kartha, C., *J. Mat. Sci.* **39**, 1 (2004).
53. Raynor, G. V. A., *Handbook of Lattice Spacing and Structure of Metals and Alloys vol 4* (Oxford: Pergamon) p. 698
54. Varshni, Y. P., *Physica*, **34**, 149 (1967).
55. Hwang, C. J., *Phys. Rev.* **180**, 827 (1969).
56. Klick, C. C. and Schulman, J. H., *Solid State Physics*, vol 5: ed Seitz, F. and Turnbull, D. (New York: Academic) p. 100 (1957).
57. Shigetomi, S, Kari, H. and Nakashima, I. I., *J. Appl. Phys.* **74**, 4125 (1993).
58. Jayakrishnan, R., Teny Theresa John, Sudha Kartha, C., Vijayakumar, K. P., Abe, T. and Kashiwaba, Y., *Semi. Cond. Sci. Tech.* **20**, 1162 (2006).
59. Aydinli, A., Gasanly, N. M., Yilmaz, L. and Serpenguzei, A., *Semicond. Sci. Technol.* **14**, 599 (1999).
60. Maeda, K., *J. Phys. Chem. Solids*, **26**, 595 (1965).
61. Shen, W. Z., Shen, S. C., Chang, Y., Tang, W. G., Yip, L. S., Lam, W. W. and Shih, I., *Infrared Phys. Technol.* **37**, 509 (1996).
62. Zott, S., Leo, K., Ruckh, M. and Schock, H. W., *J. Appl. Phys.* **82**, 356 (1997).
63. Luque, A. and Marti, A., *Phys. Rev. Lett.* **78**, 5014 (1997).
64. Keevers, M. J. and Green, M. A., *J. Appl. Phys.* **75**, 4022 (1994).
65. Green, M. A., *Third Generation Photovoltaics: Advanced Solar Energy Conversion*, Springer, New York, Chap. 8. (2003).
66. Bube, R. H., *Photo electronic Properties of Semiconductor*, Cambridge University press, (1959).
67. Bube, R. H. and Groove, W. M., *J. Appl. Phys.* **38**, 3515 (1967).
68. Bube, R. H. and Redfield, D., *J. Appl. Phys.* **66**, 3074 (1989).
69. Leroux, M., Grandjean, N., Beaumont, B., Nataf, G., Semond, F., Massies, J. and Gibart, P., *J. Appl. Phys.* **86**, 3721 (1999).
70. Goldys, E. M., Godlewski, M., Langer, R., Barski, A., Bergman, P. and Monemar, B., *Phys. Rev. B*, **60**, 5464 (1990).
71. Jayakrishnan, R., Tina Sebastian, Teny Theresa John, Sudha Kartha, C. and Vijayakumar, K. P., *J. Appl. Phys.* **102**, 043109 (2007).
72. Fan, H. Y., *Phys. Rev.* **92**, 1424 (1953).
73. Saitoh, H. G., Park, K. H., Park, B. N., Lim, H. J., Min, S. K., Park, H. L. and Kim, W. T., *Jpn. J. Appl. Phys., Part 2*, **32**, L476 (1993).
74. Rose, A., *Phys. Rev.* **12**, 362 (1951).

75. Rupa Pai, PhD Thesis, Cochin University of Science and Technology (2001).
76. Jayakrishnan, R. Sudha Kartha, C., and Vijayakumar, K.P., Proceedings of the National Conference on Luminescence Application (NCLA), p. 269 (2007).
77. Visoly-Fisher, I., Cohen, S. R. and Cahen, D., Appl. Phys. Lett. **82**, 4 (2003).
78. Salzman, J., Uzan- Saguy, C., Meyler, B. and Kalish, R., Phys. Stat. Sol. (a) **176**, 683 (1999).
79. Shalish, I., Kronik, L., Segal, G., Yoram Shapira, Zamir, S., Meyler, B. and Salzman, J., Phys. Rev. B, **61**, 15573 (2000).
80. Blatter, G. and Greuter, F., Phys. Rev. B, **33**, 3952 (1986).
81. Orton, J. W. and Powell, M. J., Rep. Prog. Phys. **43**, 81 (1980).
82. Doron Azulay, Oded Millo, Isaac Balberg, Hans-Werner Schock, Iris Visoly-Fisher, David Cahen, Sol. Energy Mater. Sol. Cells, **91**, 85 (2007).
83. Azulay, D., Millo, O., Silbert, S., Balberg, I. and Naghavi, N., Appl. Phys. Lett. **86**, 212102 (2005).
84. Persson, C. and Zunger, A., Phys. Rev. Lett. **91**, 266401 (2003).
85. Persson, C. and Zunger, A., Appl. Phys. Lett. **87**, 211904 (2005).
86. Susanne Siebentritt, Sascha Sadewasser, Mark Wimmer, Caspar Leendertz, Tobias Eisenbarth and Martha Ch. Lux-Steiner, Phys. Rev. Lett. **97**, 146601 (2006).
87. Evans, P.V. and Nelson, S.F., J. Appl. Phys. **69**(6), 3605 (1991).
88. Orton, J. W., Kipperman, A. H. M. and Beun, J. A., J. Phys. D: Appl. Phys. **9**, 69 (1976).
89. Orton, J. W., Goldsmith, B. J., Chapman, J. A. and Powell, M. J., J. Appl. Phys. **53**, 1602 (1982).
90. Carbone, A. and Mazzetti, P., Phys. Rev. B, **51**, 13261 (1994).
91. Biernacki, S. W., Solid State Commun. **88**, 365 (1993).
92. Istratov, A. A. and Vyvenko, O. F., J. Appl. Phys. **80**, 4400 (1996).
93. Wright, H. C. , Downey, R. J. and Canning, J. R., J. Phys. D, **1**, 1593 (1968).
94. Baum, D., Jiang, H. X. and Honig, A., J. Lumin. **40**, 119 (1988).
95. Azulay, D., Balberg, I., Conde, J. P., Chu, V. and Millo, O., Phys. Rev. B, **71**, 11304 (2005).



## CHAPTER 6

### Summary and Outlook

---

*The conclusion of this thesis can be divided into three areas: 1) the fabrication of a low temperature photo-luminescence and photo-conductivity measuring unit 2) photo-luminescence in the chalcopyrite  $\text{CuInSe}_2$  and  $\text{CuInS}_2$  system for defect and composition analysis and 3) photo-luminescence and photo-conductivity of  $\text{In}_2\text{S}_3$ . This thesis shows that photo-luminescence is one of most essential semiconductor characterization tool for a scientific group working on photovoltaics. Tools which can be robust, non-destructive, requiring minimal sample preparation for analysis and most informative of the device applications are sought after by industries and this thesis is towards establishing photo-luminescence as "THE" tool for semiconductor characterization. The possible application of photo-luminescence as a tool for compositional and quality analysis of semiconductor thin films has been worked upon by this thesis. Photo-conductivity complement photo-luminescence and together they provide all the information required for the fabrication of an opto-electronic device.*

The requirements for thin film semiconductor solar cell device structures are simple in comparison to other electronic and opto-electronic structures. The development of a viable thin film technology has been battered with difficulties, some fundamental, others originating from empiricism during the drive to demonstrate high efficiency devices. Three well known factors are that:

- (a) Grain boundaries influence recombination, current transport and diffusion / segregation. The influence of grain boundaries on the device response and local device behavior have to be understood in terms of local charge states and chemical profiles;
- (b) Point defects in thin film solar cells are not understood. In conventional semiconductors the conductivity and field profiles are engineered by controlled doping with well understood centers. In thin film solar cells this is achieved empirically, without knowing the identity of the active

centers, without knowing important compensating species and even at expense of sacrificing stability.

- (c) Electron affinity of absorbers makes contacting an issue for some material system. Understanding band line-ups in conjunction with device theory is yet to be evolved.

## 6.1 Summary

No single experimental diagnostic approach is capable of yielding all the diverse information relevant to the development of thin film solar cells. PL investigations can be used to characterize a variety of material parameters. In this thesis, the main objective of the work was to establish PL spectroscopy as a characterization tool for the thin films prepared in our laboratory for photovoltaic applications. PL spectroscopy provided a rapid non-destructive method to characterize the electronic properties of the polycrystalline semiconductors used in thin film photovoltaics. Shallow impurities and defects were identified using the temperature and excitation intensity dependence of the PL spectrum.

Instrumentation for PL was assembled from commercially available components, as there are few complete commercial systems available. For optical excitation, high intensity laser sources were first selected. Laser sources were selected on the basis of the materials prepared in our laboratory. A sample holder was designed for mounting the samples. Optics for focusing the laser onto the sample surface, and to collect the PL signal was assembled using fiber optics and lens arrangement. Two grating spectrometers were used in the detection part. The first spectrometer works in the 330 nm to 1100 nm range. It is fitted with a Si Charge Coupled Device (CCD) array detector. The second spectrometer works in the 900 nm -1730 nm wavelength range. It has an InGaAs linear array detector. CCDs achieve parallel detection of the entire spectrum at once, permitting long integration times to achieve high signal-to-noise ratio, and very fast data acquisition for samples with adequate PL intensity. A liquid Helium closed cycle cryostat was used to do PL analysis of samples at low temperature. Modifications of the cryostat windows were carried out in order to collect signals from samples mounted in the cryostat. Spatially resolved PL for quality and compositional uniformity required scanning of the excitation spot over the sample and collecting emission from each illuminated point of the sample. For this a stepper motor controlled XYZ translator was fabricated and was used to

scan the laser spot. The system was completed with the addition of a desktop computer for instrument control and data acquisition and analysis. The spectral resolution of the system is found to be 4 meV experimentally. The PL system was attached with additional accessories for PC measurement. AC-PC measurements were carried out to measure the lifetime ( $\tau$ ). Thus a complete defect characterization system was fabricated which could be used to characterize different kinds of samples which are prepared in our lab for photovoltaics.

Free exciton  $FE_A$  emission, which is the highest band-edge emission energy, was used to identify the composition of the  $CuInS_2$  thin films. Stoichiometric films yield  $FE_A$  emission at 1.55 eV, the In-excess films show  $FE_A$  emission at 1.56 eV and the Cu-excess films yield  $FE_A$  emission at 1.53 eV. Variation in PL peak positions as a function of the concentration of the precursor solution was characterized. The specific concentration of the precursor solution to yield a stoichiometric chalcopyrite  $CuInS_2$  polycrystalline thin film could be standardized based on the peak position of the free exciton  $FE_A$  emission. Excitons bound to defects also were found to yield PL emission but it was not possible to predict the composition accurately based on these emissions. The presence of  $FE_A$  emission from a film itself was an indication of good crystallinity and ordering in the film.

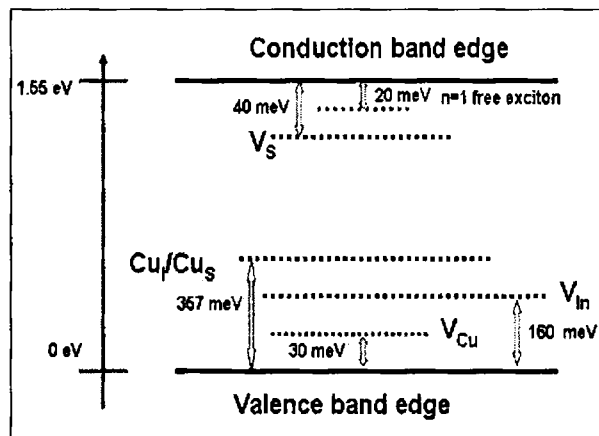


Fig. 6.1: Band level diagram for  $CuInS_2$  based on the PL studies in this work.

The spatial variation in  $FE_A$  emission hence could be used to correlate/monitor sample quality and uniformity. Spatial fluctuation in intensity and peak position of the  $FE_A$  emission can be used to study non-uniformity in growth process or the deposition technique itself. Using samples prepared under the same set of experimental conditions it was observed that the spatial distribution profile

varied from sample to sample. A change in precursor solution also created a spatial distribution in  $FE_A$  emission intensity which arose due to change in composition of the films. Spatial uniformity in composition of the films was tested using PL and it could be used to predict homogeneity in the films. PL was used as a tool to standardize the substrate temperature for the deposition of  $CuInS_2$  thin films through spray pyrolysis. Intrinsic defects like vacancy of Sulphur  $V_S$ , vacancy of Indium  $V_{In}$ , vacancy of Copper  $V_{Cu}$ , Copper interstitials  $Cu_i$  and Copper in Sulphur anti-site  $Cu_S$  could be identified. Figure 6.1 shows the proposed electronic level diagram for  $CuInS_2$  from the present studies.

A combination of the Chemical Bath Deposition (CBD) technique and the Sequential Evaporation of Elemental (SEL) layers was used to deposit  $CuInSe_2$  thin films. To optimize and establish a suitable process for the production of  $CuInSe_2$  films for photovoltaic applications their PL properties were characterized. The characterization has enabled in establishing that CBD growth process leads to films with larger defect concentrations and hence making them unsuitable for device applications. This work also indicates an attractive perspective for the SEL grown  $CuInSe_2$  films. PL analysis of samples prepared using sequential physical vapor evaporation showed that the films were stoichiometric, repeatable and homogenous. The line widths of the In-rich films were the least where as the Cu-rich films had large line widths based on which the composition of the films could be distinguished.

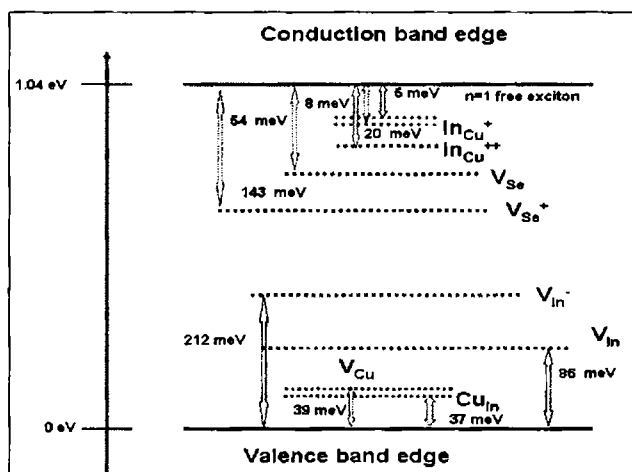


Fig. 6.2: Energy band diagram for  $CuInSe_2$  based on PL studies in this work.

The position of point defects like  $V_{In}$ ,  $V_{In}^-$ ,  $V_{Cu}$ ,  $In_{Cu}^+$ ,  $In_{Cu}^{++}$ ,  $V_{Se}$ ,  $V_{Se}^+$ ,  $Cu_i$  and  $Cu_{In}$  were identified using PL. Figure 6.2 shows the energy band diagram for  $CuInSe_2$  based on the PL studies carried out in the present work. Characteristics of bound

exciton emission ( $BX$ ), free-to-bound and bound-to-free emissions ( $e, A^0$ ) & ( $D^0, h$ ) and donor-acceptor pair recombination emissions were identified. Anomalous increase in PL intensity with increase in temperature could be modeled on the basis of presence of two competitive trapping centers. On ITO/CuInSe<sub>2</sub> hetero-structures selective tuning of the donor acceptor pair transition and the conduction band to acceptor transition could be demonstrated by varying either of the two parameters- excitation intensity or temperature. Figure 6.2 shows the proposed electronic level diagram for CuInSe<sub>2</sub> from the present studies.

Polycrystalline thin films of In<sub>2</sub>S<sub>3</sub> presented a unique challenge to PL characterization. The high concentration of grain boundaries, defects and impurities typical of thin film PV produced broad line widths, and the spectra was dominated by radiative recombination through defects and impurities. Because of the absence of band edge emissions from the sample a correlation between the composition and PL emission could not be drawn. A number of opto-electronic applications for the material could be suggested based on the optical and electrical properties investigated for this interesting material. The origin of two strong visible emissions- a green and another red were identified and the defect mechanism to tune the intensity of the emission was realized. Green emission from In<sub>2</sub>S<sub>3</sub> was identified to be due to transitions from the excited states of the V<sub>S</sub> level to the V<sub>In</sub> level. The mechanism of this emission could be explained on the basis of the Cartesian Coordinate (CC) model of luminescence. The red emission from the films was identified to be due to transitions from the In<sub>i</sub> donor level to the O<sub>V<sub>S</sub></sub> defect level above the VB. The material was also found to highly photosensitive whose origin was due to the presence of extrinsic impurities. The presence of the halogen impurity Cl<sup>-</sup> was found to deter the photoconduction mechanism with out changing the luminescence peak position. Hence the role of this impurity as a co-activator in this material was realized. Grain boundaries which are normally considered to be scattering centers were found to provide an alternate photoconduction network in this material. Hence it may lead to establishing that a conducting grain boundary material is essential for better device performance. This could answer why polycrystalline materials out-perform their single crystal counterparts specifically in PV applications. Figure 6.3 shows the energy band diagram for sprayed  $\beta$ -In<sub>2</sub>S<sub>3</sub> thin films. It is proposed that there are defects bands within the energy gap of this material which makes it attractive for third generation solar cells specifically.



artificially created in other materials, but are an intrinsic property of  $\beta\text{-In}_2\text{S}_3$ . Thus a very good PV material was realized out of  $\beta\text{-In}_2\text{S}_3$ . Future research on this material should be towards device fabrication exploiting these interesting properties. Most interestingly the C-AFM analysis showed that this material can be processed to have a conducting grain center surrounded by an insulating grain material. Such structures have not been reported in literature so far. Future research should be streamed towards understanding the composition of these respective regions using state of the art imaging and composition analysis tools. They may hold interesting properties which are yet to be discovered.

### 6.3 Reference

1. Jeong, M. S., Kim, Y. -W., White, J. O., Suh, E. -K., Cheong, M. G., Kim, C. S., Hong, C. -H. and Lee, H. J., *App. Phys. Lett.* **79**, 3441 (2001).
2. Liu, J., Perkins, N. R., Horton, M. N., Redwing, J. M., Tischler, M. A. and Kuech, T. F., *Appl. Phys. Lett.* **69**, 3519 (1996).
3. Crowell, P. A., Young, D. K., Keller, S., Hu, E. L. and Awschalom, D. D., *Appl. Phys. Lett.* **72**, 927 (1998).
4. Vertikov, A., Kuball, M., Nurmikko, A. V., Chen, Y. and Wang, S. Y., *Appl. Phys. Lett.* **72**, 2645 (1998).
5. Jeong, M. S., Kim, J. Y. Kim, Y. -W., White, J. O. Suh, E. -K., Hong, C. -H. and Lee, H. J., *Appl. Phys. Lett.* **79**, 976 (2001).